FAILURE MODES OF SILICON NITRIDE ROLLING ELEMENTS WITH RING CRACK DEFECTS

YING WANG

A thesis submitted in partial fulfilment of the requirements of Bournemouth University for the degree of Doctor of Philosophy

March 2001

Bournemouth University
In collaboration with
SKF Engineering and Research Centre, The Netherlands

ABSTRACT

High quality silicon nitride ceramics have shown some advantages for rolling element bearing applications. In particular hybrid bearings (silicon nitride rolling elements and steel races) have the ability to withstand high loads, severe environments and high speeds. However, the difficulties of both sintering and machining the material may result in surface defects, such as surface ring cracks. It is difficult to detect surface ring cracks during high volume production processes and hence it is crucially important to understand their influence and the fundamental mechanism of the failures they cause.

The purpose of this study is to examine the contact fatigue failure modes of silicon nitride rolling elements with surface ring crack defects. In this study, new experimental and computational techniques are developed to measure and model the interaction of the surface with pre-existing crack defects. A rolling contact fatigue test method is devised for positioning the ring crack in the contact path. Rolling contact fatigue tests are conducted using a modified four-ball machine in a hybrid ceramic/steel combination. A three-dimensional boundary element model is used to determine the stress intensity factors and to carry out the crack face contact analysis.

Research shows that the RCF life performance of silicon nitride bearing elements is dependent upon the crack location and fatigue spall happens only at a few crack orientations. The spalling fatigue failure is not only influenced by the original ring crack propagation but also strongly influenced by the subsequent crack face contact. Secondary surface cracks play an important role in the formation of a fatigue spall. The crack gap and crack face friction coefficients significantly affect the formation of secondary surface cracks. Numerical calculation results are consistent with the experimental observations. A quantitative three-dimensional boundary element model has been developed, which can be used to determine the geometry of acceptable surface ring cracks.

PUBLICATIONS RESULTING FROM THESIS

[1] "Rolling contact fatigue failure modes of lubricated silicon nitride in relation to ring crack defects"
By Y. Wang and M. Hadfield
Wear Journal, 225-229, 1284-1292, 1999, ISSN 0043-1648

[2] "The influence of ring crack location on the rolling contact fatigue failure of lubricated silicon nitride: experimental studies"
By Y. Wang and M. Hadfield
Wear Journal, 243, 157-166, 2000, ISSN 0043-1648

[3] "The influence of ring crack location on the rolling contact fatigue failure of lubricated silicon nitride: fracture mechanics analysis"
By Y. Wang and M. Hadfield
Wear Journal, 243, 167-174, 2000, ISSN 0043-1648

[4] "Ceramic surface ring crack fatigue failure during rolling contact"
By Y. Wang and M. Hadfield
Submitted to *Proc. Roy. Soc. Lond. A*

[5] "Boundary element analysis of surface ring crack in silicon nitride bearing elements"
By Y. Wang and M. Hadfield
International Conference on Tribology in Environment Design 2000, p297-304, Professional Engineering Publishing, ISBN 1 68058 2664

[6] "Ring crack propagation in silicon nitride under rolling contact"
By Y. Wang and M. Hadfield
13th International Conference on Wear of Materials, Vancouver, British Columbia, Canada 22-26 April 2001

ACKNOWLEDGEMENTS

The author wishes to acknowledge the help, support and encouragement that I received whilst undertaking my PhD study.

My very grateful thanks are expressed to Dr. M. Hadfield, my supervisor, who has provided a constant source of encouragement, inspiration and strength. Every step in the progress of my work reflects his solid support and patient help.

I would also like to thank Dr. R. T. Cundill at SKF Engineering and Research Centre for his support and advice.

My appreciation also goes to all the staff I have worked with so closely at Bournemouth University, especially Mrs. Christine Thwaites (former Departmental Secretary) and laboratory staff.

A special thanks also goes to my parents and my wife for their support and encouragement.

CONTENTS

LIST OF FIGURES

LIST OF TABLES

NOMENCLATURE

A_0	surface area of ceramic ball
A	area of contact track
a	radius of contact circle
Δa	crack increment
Δa_{max}	maximum crack increment
c	material constant (Paris equation)
da/dn	rate of change of crack length with respect to the loading cycles
E_1	elasticity modulus of ceramic ball
E_2	elasticity modulus of steel ball
E	elasticity modulus
E^*	effective elasticity modulus
f	mean frictional coefficient of Hertzian contact
f_c	frictional coefficient of crack face contact
h	height of the segment which cuts through the contact track
K_I	mode I stress intensity factor
$K_I^{P'}$	approximation of mode I stress intensity factor at point P' along the crack front
K_{II}	mode II stress intensity factor
$K_{II}^{P'}$	approximation of mode II stress intensity factor at point P' along the crack front
K_{III}	mode III stress intensity factor
$K_{III}^{P'}$	approximation of mode III stress intensity factor at point P' along the crack front
K_{IC}	fracture toughness
K_{eff}	effective stress intensity factor
K_{eff}^{max}	maximum effective stress intensity factor
K_{eff}^{min}	minimum effective stress intensity factor
K_{eq}	equivalent stress intensity factor
K_{max}	maximum stress intensity factor
K_{min}	minimum stress intensity factor
ΔK	difference of K_{max} and K_{min}
ΔK_{eff}	difference of K_{eff}^{max} and K_{eff}^{min}
ΔK_{th}	fatigue crack propagation threshold
l	crack depth
L	applied load (shaft load)

m	material constant (Paris equation)
ΔN	fatigue cycles
P	contact load
p_0	maximum contact pressure
$p(x,y)$	Hertzian contact pressure
$q(x,y)$	tangential traction
r	coordinate in local crack front coordinate system
R	radius of ring crack circle
R_1	radius of ceramic ball
R_2	radius of steel ball
R^*	effective radius
R_σ	ratios of K_{max} to K_{min}
S	strain energy density factor
S_{min}	minimum strain energy density factor
u^P	displacement of crack faces at point P
u_n^P	projection of u^P on normal direction of the local crack front coordinate system
u_t^P	projection of u^P on 1st tangential direction of the local crack front coordinate system
u_b^P	projection of u^P on 2nd tangential direction of the local crack front coordinate system
(x,y)	Cartesian coordinate system with origin at the centre of Hertzian contact circle
(x,y,z)	Cartesian coordinate system with origin at the centre of Hertzian contact circle
α	angle of the crack path (line P_1P_2 in figure 3.53) to the ball surface
β	angle of the chord of ring crack to the central line of the contact track
δ	distance of the centre of the ring crack circle to the central line of the contact track
ϕ	angle of an element position on crack faces
ϕ_0	half angle of ring crack arc AB
φ	contact angle
μ	shear modulus of elasticity
ν	Poisson's ratio
ν_1	Poisson's ratio of ceramic ball
ν_2	Poisson's ratio of steel ball
θ	polar angle in the local crack front coordinate system

ρ	contacted crack probability
σ_{max}	maximum affecting stress
σ_{min}	minimum affecting stress
ω	angle of an element position on crack front

The following notation is used in appendices.

E'	effective elastic modulus
G	dimensionless material parameter
h_{min}	minimum film thickness
H_{min}	dimensionless minimum film thickness parameter
L	stress cycle factor
R_A	radius of driving ball
R_P	radius of planet ball
R_x	effective radius in x (motion) direction
R_y	effective radius in y (motion) direction
u	mean surface velocity
U	dimensionless speed parameter
W	dimensionless load parameter
η_0	viscosity
ξ	pressure viscosity
λ	lambda ratio
σ^*	composite r.m.s. roughness

ABBREVIATIONS

BEM	Boundary Element Method
BEASY	Boundary Element Analysis System
DBEM	Dual Boundary Element Method
EHL	Elasto-Hydrodynamic Lubrication
HIP	Hot Isostatically Pressed
RCF	Rolling Contact Fatigue
SEM	Scanning Electron Microscope
SIF	Stress Intensity Factor
UV	Ultra Violet
WC	Tungsten Carbide

CHAPTER 1

INTRODUCTION

1.1 GENERAL BACKGROUND

Ceramic materials such as silicon nitride applied to rolling element bearings show some practical advantages over traditional bearing steels (Hamburg et al. 1981, Miner et al. 1981, Bhushan and Sibley 1981 and Aramaki et al. 1988). Silicon nitride has been found to have the optimum combination of properties suitable for this application. Hybrid rolling element bearings, i.e. precision angular contact ball-bearings using ceramic rolling elements are now offered as standard components within the ball bearing manufacturing industry.

Quality control of the ceramic ball surfaces has reached a satisfactory position and high volume inspection is practical. Surface cracks, however, are found on ceramic balls (Cundill 1990) and are difficult to detect, hence there is an important need to assess their influence and fundamental failure mechanism.

At present there is little information on failure mechanics and the mechanisms of ceramic rolling elements with such surface defects. In this thesis, new experimental and computational techniques are developed to measure and model the interactions of the surfaces with pre-existing cracks. The techniques are applied to study the influence of surface ring crack defects on the stresses and consequent failure processes in lubricated rolling contacts.

The concentrated contact analysis focuses on a hybrid ceramic/steel combination. A modified four-ball machine is employed which correctly models ball motions and precisely defines ball load. The upper ball is ceramic with surface ring cracks. Rolling contact fatigue tests are devised for positioning the ring crack in the contact path. In this way many stress cycles are applied to a fixed contact area on the upper ball and hence fatigue experimentation time is reduced. It is found that the fatigue life under rolling contact loading is markedly sensitive to the location of the ring crack on the contact track. Only a few locations on the contact track can lead to fatigue failure. A boundary element model is used to determine the stress intensity factors along the crack front. Consequently, a relationship between the crack location

and crack propagation is established.

To interpret the failure processes and accurately predict the fatigue life, a three-dimensional contact mechanics approach is adopted to model crack face contact behaviour and subsequent effects. It is found that the ring crack fatigue failure involves three possible periods and each stage corresponds differently in relation to the cracking behaviour. The findings of the research provide sufficient quantitative insight into the process of surface fatigue to enable performance prediction and rational design of a hybrid ceramic rolling contact bearing.

1.2 OBJECTIVE AND SCOPE OF RESEARCH WORK

The main objective of the study presented in this thesis is to investigate experimentally and model analytically the fatigue failure mechanisms and durability of silicon nitride rolling elements which have ring crack defects. The scope of this study includes: (1) subsurface and surface characterisations of surface ring cracks, (2) experimental studies of the influence of surface ring cracks on the RCF performance and failure modes of the ceramic balls, and (3) analytical modelling of the concentrated contact volume with surface ring cracks.

1.3 OUTLINE OF THESIS

In Chapter 1, general background and previous research work related to this subject are described. Chapter 2 describes the main programme of experimental testing. Section 1 describes test materials. Section 2 is concerned with crack geometry studies. Section 3 describes experimental methods and procedure. Section 4 outlines experimental observations during fatigue testing. In the final section, Scanning Electron Microscopy (SEM) analysis is described.

In Chapter 3, experimental results are presented. Section 1 presents the rolling contact fatigue (RCF) performance with ring crack locations. The effect of viscosity and crack location on the fatigue life is addressed. Section 2 describes the RCF performance with surface line defects. Section 3 describes surface observations of crack failure processes. Section 4 describes subsurface observations of crack propagation. Section 5 presents the investigation of micro-crack wear patterns in

rolling contacts. Crack characterisations are presented in Section 6.

The analysis of ring crack propagation is described in Chapter 4. Section 1 describes ring crack geometry modelling and loading configuration. Section 2 presents boundary element modelling. Section 3 is concerned with the calculated results of the stress intensity factors. The influence of crack geometry, loading conditions and crack positions on SIF is described. Section 4 describes life prediction of spalling fatigue failure. The predicted crack propagation path is described in Section 5.

Contact analysis of crack faces is described in Chapter 5. A three-dimensional crack face contact model is developed to investigate the failure mechanisms of ceramic surface ring crack in rolling contact. The calculated results based on the model are discussed and compared with the experimental observations. Discussion, conclusions and recommendations for further research topics resulting from this present study are outlined in Chapter 6.

1.4 LITERATURE SURVEY

1.4.1 Surface ring crack

Quality control of the ceramic ball surface has reached a satisfactory standard and high volume inspection is practical. Surface ring cracks, however, are commonly found on ceramic balls (Cundill 1990) and are difficult to detect. These ring cracks are circular extending for approximately one-quarter to one-third of the circumference of a circle, and they decrease the rolling contact fatigue performance substantially. Ring cracks caused by manufacturing pressing faults or blunt impact loads are the most common type found on ceramic ball surfaces. Lateral and radial surface cracks are less common and occur due to poor sintering mixture or a sharp indention load (Ueda 1989).

There have been a number of experimental studies of brittle fracture under contact loading. A typical experiment involves pressing an indenter into the surface of the solid with a progressively increasing load and observing the pattern of fracture which develops under the contact. Under a blunt indenter, a well-defined cone shaped crack pops in when the normal load reaches a critical magnitude (Roesler 1956,

Chaudhri and Phillips 1990). Tillett (1956) and Roesler (1956) detail numerous historical observations of ring cracking being visible once the surface tensile stress is much greater than that required for fracture in bulk tensile test specimens. This has been attributed to the small volume acted upon by the contact-induced tensile stress. A number of theoretical models have been developed which can predict both the fracture load and the subsequent length of the cracks (Frank and Lawn 1967, Wilshaw 1971, Mouginot and Maugis 1985). The development of the cone crack from the ring crack in the strongly inhomogeneous Hertzian stress field was investigated by Frank and Lawn (1967). The mode I stress intensity factor at the cone crack front was calculated by modelling it as a two-dimensional plane strain crack in an infinite medium loaded by the stresses acting on the location of the cone crack in the corresponding uncracked body. It was assumed that the inclined sides of the cone crack followed trajectories of the minimum principal stress so that it was perpendicular to the maximum principal stress. This model predicts that the crack propagation arrests at a depth which is related to the applied load. The partial cone cracks can be generated if the indenter slides over the surface under the action of a combined normal and tangential load (Lawn 1967 and Bethune 1971). The cracks are initiated at the trailing edge of the contact, and propagate almost perpendicular to the surface.

Warren (1978) used a similar two-dimensional approximation and considered the effect of ring crack initiation some distance outside of the circle of contact. The model was combined with experiments to measure the fracture toughness of carbides based on the initiation of the ring crack. Mouginot and Maugis (1985) also used the two-dimensional approximation to analyse cracks generated by both spheres and flat punches. Li and Hills (1991) fully analysed circular crack initiation and propagation using a numerical calculation method. A finite element method was used. They found that the mode II stress intensity factor was about one-tenth of the mode I stress intensity factor. A review paper by Warren et al. (1995) discussed ring crack initiation and propagation using analytical techniques. The first two stages of surface defect growth show that surface flaws develop into complete rings. In the final phase the crack develops into a cone.

Ring crack initiation load of HIP silicon nitride bearing balls was

experimentally studied by Ichikawa et al. (1995a), Ichikawa et al. (1995b), Ohgushi and Ichikawa (1996). Initiation of a ring crack was detected using acoustic emission. The ring crack initiation load showed considerable scatter and ranged from 3 KN to 6 KN (corresponding to the maximum Hertz contact pressure of 14 GPa and 18 GPa). The ring crack initiation load is much smaller than the crushing load, and approximately follows two-parameter Weibull distribution with a shape parameter ranging from 9-11.

Impact cracking of silicon nitride balls, during ball finishing or by subsequent handling, is a cause for concern since a surface crack is the type of defect most likely to cause failure in a hybrid rolling element bearing. Ring cracks formed prior to, or during, the final lapping or polishing stage are particularly difficult to detect. Such cracks are not visible with optical techniques even at high magnifications except after processing with high sensitivity fluorescent penetrants. Impact cracking of silicon nitride balls was investigated by Cundill (1997), leading to a parameter for assessing impact resistance. Some material types were found to be more resistant to impact cracks than others. The types of silicon nitride densified by sintering followed by hot isostatic pressing and by gas pressure sintering have the best impact resistance. For ball sizes of 6.35 mm, the maximum contact pressure of 20-25 GPa was required to form surface ring cracks; for ball sizes of 12.7 mm, 10-15 GPa was required; for ball sizes of more than 20 mm, 10-12 GPa was required.

1.4.2 Fatigue crack propagation

Fatigue crack propagation is always involved in rolling contact fatigue failure. Many efforts have been completed to relate crack propagation behaviour with RCF life performance. The rolling and sliding wear processes have attracted the interest of many researchers over the past few decades. A general review of ceramic wear is given by Kato (1990) and a more specific overview of delamination wear arising from rolling and sliding contact is given by Suh (1977). The bulk of that research was focused on the experimental aspects of wear. Only a few attempts have been made to develop analytical models for predicting the wear process. The importance of determining analytical models for wear mechanisms has been

discussed by Braza et al. (1989b). Wear modes must be described mechanistically to better understand how they occur and to develop formulae for wear material removal. Fracture mechanics has been applied to the analysis of wear modes in a number of studies. Fleming and Suh (1977), Hills and Ashelby (1979), and Rosenfield (1980) have presented a fracture mechanics approach to delamination wear. They analysed a subsurface crack parallel to the surface of a half-plane subjected to a Hertzian surface load. The stress intensity factors at the crack tips were calculated from an approximate stress field induced by the contact load in a crack-free half-plane. Keer et al. (1982) presented an improved analysis for delamination and surface cracks. They calculated the stress field in the half-plane under surface Hertzian contact stresses using dislocation theory to model the cracks.

Keer and Bryant (1983), Bryant et al. (1984) analysed cracks at an angle to a surface acted on by a Hertzian contact load. In Keer and Bryant, lubrication pressure was considered as a crack opening force; in Bryant et al. sufficient lubrication was taken to exist in the crack such that the crack face friction was zero. The analyses were further extended in Miller et al. (1985) to include the effects of subsurface inclusions and asperity perturbations on the pitting crack. Finally, Bower (1988) thoroughly analysed the surface pitting crack, summarising the effects of crack face friction and lubrication pressures on crack propagation, and including loading history dependence when regimes of slip and stick were considered for the crack. In all of these analyses, mode II stresses were the main cause of crack propagation. This caused crack propagation to be highly dependent on the coefficient of friction between the crack faces.

Several attempts have been made to explain the wear mechanisms in brittle materials. Braza et al. (1989b) discussed mechanical aspects of wear without regard to tribochemical effects. In the case of brittle materials, cracks may occur on the surface due to tension or subsurface cracks parallel to the contact path due to shear. Friction in rolling and sliding contact can arise from asperity interlock, adhesion or abrasion by debris trapped between the contacting surface and viscous drag of the lubricant. Keer and Worden (1990) presented a qualitative model to describe the micro-chipping wear mode in ceramic rollers. It is stated that microchipping cracks

can form as a result of the stress distribution due to a Hertzian contact. Because the direction of principal stresses varies rapidly at an indentation contact, cracks propagating at the surface will link or branch to turn parallel to the surface, thus providing a mode for wear material removal. A strong dependence was seen relating the wear particle size with the coefficient of friction. Thomsen and Karihaloo (1996) modelled near-surface cracks in zirconia ceramics which are subjected to contact loading. It is concluded that frictional contact may have a significant influence, especially upon the sliding mode (mode II) deformation of the closed crack. In the analysis for a phase-transforming material, the friction contact between the crack faces may even be of greater importance, since the transformation zones at the crack tip(s) showed a marked closing effect on the tips, thus exerting significant compressive stresses there. These compressive stresses would, in turn, induce frictional stresses opposing the sliding deformation of the crack tips.

Fatigue crack propagation in ceramics has been studied in two modes: long crack and short crack studies. The long crack studies (typically with crack length about 3 mm) were done with through cracks in pre-cracked specimens, such as single-edge-notched specimens in three and four-point bending or tapered double-cantilever beam specimens, or compact tension specimens. Crack lengths were monitored optically or by measuring the resistance of a conducting coating. Linear elastic stress-intensity solutions for the various specimen geometry are given in standard handbooks (Tada et al. 1985). Short crack experiments (typically with cracks less than 250 μm in length) were done by bending beams using surface cracks introduced from a notch or by indentation. Stress intensity factors for such surface cracks can be obtained from linear elastic solutions for three-dimensional semi-elliptical surface cracks in bending (and /or tension) (Newman and Raju 1986). The long crack propagation studies gave results that could be described by the Paris law, but the exponent m varied between 12 and 40, which is much larger than the values of 2-4 typical of metals. The short crack studies gave much greater crack growth rates than the long crack studies at equivalent applied stress intensity values. Also, the crack growth takes place in the short crack studies at stress intensities below the threshold value required in long crack studies (Ritchie and Dauskardt 1991).

Studies of cyclic fatigue in ceramics using long crack techniques are clearly important in understanding basic fatigue phenomena in ceramics and data obtained in such experiments may apply to design considerations in some circumstances. However, the same problem arises as with other uses of long crack data. Namely, ceramics having only the naturally occurring short cracks are generally used for load-bearing applications. Thus fatigue data for short cracks is needed.

Results on small fatigue cracks in ceramics, however, are very limited. In contrast to long crack results, the small cracks grow at progressively decreasing growth rates with increase in size, until finally linking together as the density of cracks across the specimen surface increases; the specimen then fails.

Dauskardt et al. (1992) investigated the ambient-temperature subcritical growth behaviour of both long and micro-structurally small cracks during cyclic-fatigue loading in a SiC-whisker-reinforced alumina ceramic composite. Based on long crack experiments using compact tension specimens, cyclic fatigue crack growth rates are found to be sensitive to the applied stress intensity range and load ratio. The long crack fatigue threshold, ΔK_{th}, was found to be in the order of 60% of K_c, similar to behaviour in other ceramic materials. Cyclic fatigue crack growth rates for small surface cracks are found to occur at applied stress-intensity levels significantly smaller than the nominal long-crack threshold ΔK_{th}.

Reece and Guiu (1991) studied the influence of environment on the cyclic fatigue behaviour of a high-purity alumina bioceramic using the repeated indentation technique. Tests were conducted in the presence of water, a variety of alcohols, toluene and simulated physiological fluid environments. The results show that these environments do not have any detectable effect on the damage produced by single indentations, but those containing water cause a significant degradation in cyclic fatigue resistance which cannot be quantified in terms of subcritical crack growth behaviour in static fatigue.

A study of contact fatigue in silicon nitride was reported by Lee and Lawn (1999). The contacts were made using WC spheres, principally in cyclic but also in static loading, and mainly in air but also in nitrogen and water. Damage patterns were examined in three silicon nitride microstructures: (i) fine – almost exclusively

fully-developed cone cracks; (ii) medium – well-developed but smaller cone cracks, plus modest subsurface quasi-plastic damage; (iii) coarse – intense quasi-plastic damage, with little or no cone cracking. In the fine and medium microstructures strength degradation was attributable primarily to chemically assist slow growth of cone cracks in the presence of moisture during contact, although the medium material showed signs of enhanced failure from quasi-plastic zones at large number of cycles. The coarse microstructure, although relatively tolerant of single-cycle damage, showed strongly accelerated strength losses from mechanical degradation within the quasi-plastic damage, especially in water.

Fatigue cone crack propagation in Si_3N_4 under cyclic fatigue loading was reported by Hu et al. (1996). The tungsten ball contacted with a disk-shaped silicon specimen and the tests were run under a maximum contact pressure of 15.01 GPa and 17.02 GPa. Unlike the so-called quasi-static Hertzian cone crack, the fatigue Hertzian cone crack propagation eliminates the dynamic effect on unstable crack propagation. The crack propagates following the path of pure mode I type. The multiple cracks and crack kinking were presented.

Mechanisms of cyclic fatigue in ceramics have not yet been definitely established. The possible mechanisms have been classified into two categories: intrinsic and extrinsic (Ritchie and Dauskardt 1991, Ritchie et al. 2000). The intrinsic mechanism would involve the creation of a fatigue-damaged microstructure ahead of the crack tip that would produce a crack-advance mechanism operating uniquely in cyclic fatigue. Possible mechanisms are alternating crack tip blunting and resharpening or, for whisker-reinforced composites, whisker breakage. Extrinsic mechanisms may not involve a change in the crack propagation mechanism under cyclic fatigue conditions. Instead, the unloading may change the value of the crack tip shielding. Thus cyclic fatigue might reduce the crack tip shielding effect of transformation toughening or crack tip bridging.

1.4.3 Failure modes

Many test-rig types (see appendix 1) are used to investigate rolling contact fatigue of silicon nitride bearing materials. Typically, in such tests, a detector

coupled with a shutdown device is used to monitor the vibration of the assembly. When a preset vibration level is exceeded, indicating the formation of a spall or excessive uneven wear, the test is automatically stopped and the lifetime of the test is recorded. Alternatively, the tests are suspended at different durations to study the wear rate. The RCF performance and failure modes were influenced by the test-rig type and studied by Hadfield and Stolarski (1995a). Several failure modes of silicon nitride in rolling contact have been reported, i.e. spalling, delamination and rolling contact wear.

1.4.3.1 Spalling

Spalling describes a specific form of surface damage and it is the most common mode of failure in rolling contact fatigue tests. Silicon nitride spalls in a manner similar to bearing steels, which is, in fact, one of the reasons for silicon nitride being a good candidate for replacing bearing steels. Other structural ceramics, for example, SiC, typically fail by catastrophic fracture due to their low fracture toughness or severe wear by micro-fracture. Catastrophic failure can cause damage to the entire bearing assembly.

The fatigue life of high-speed-ball bearings with hot-pressed silicon nitride balls was investigated by Parker and Zaretsky (1975). A five-ball fatigue test machine was employed to perform fatigue tests. Lubricated contact was studied with 12.7 mm diameter balls, Hertz stresses ranging from 4.3 to 6.2 GPa, a shaft speed of 9600 rpm and a contact angle 30°. There was no evidence of a wear mode of failure, only fatigue spalls similar to those found on steel. Life predictions showed that ceramic-steel contact compared equally to steel-steel contact. Edge cracking was not detected on any region near spalled areas or along the contact path.

Lucek and Cowley (1978) investigated the failure mode of hot-pressed ceramic using a disc-on-rod machine. All failures were of a spalling non-catastrophic nature and test loads varied from 4.1 to 5.5 GPa. Standard tests conducted with test rods of roughness 0.1μm R_a and non-standard tests conducted with various grades of ceramic, lubricants and roughness have been conducted by Hadfield and Stolarski (1995c). The results inferred that silicon nitride tested under various tribological conditions fails in a

non-catastrophic spalling mode.

Silicon nitride hybrid bearings were tested by Morrison et al. (1984), using 12.7 mm diameter balls, M50 steel rings and a brass cage. Contact pressure ranged between 1.95 and 2.44 GPa, and the film parameter was approximately 3.5 for all tests. Spalling was identified as the only mode of failure with no cases of the silicon nitride balls fracturing. Statistical analysis showed that bearing life varies in accordance with a power law model.

Experimental work performed by Fujiwara et al. (1989), examined the dynamic and static load rating of silicon nitride as a bearing material. The ball-on-plate machine was employed. Steel balls revolving around an inner race were loaded against a flat test piece. The maximum contact stress was 6.4 GPa, the rotational test speed was 1400 rpm and the lubricant was a turbine mineral oil. Spalling was identified as the most common long-term mode of failure; two other modes that occurred in very short times were 'cave-in' and peeling.

Lucek (1990) reported the rolling contact fatigue performance of hot-pressed silicon nitride using a rod type machine. Peak contact stress of 6.4 GPa and synthetic turbine oil at ambient temperature provided boundary lubrication. The specimen speed was set at 3600 rpm or 8600 stress cycles per minute. Results showed that the predominant fatigue failure mechanism in silicon nitride involves the slow growth of circumferential crack from the edges of the contact path driven by tensile stresses. Spalling occurred when material in the compressive zone was insufficiently supported.

The results of extensive testing carried out on perfect and artificially pre-cracked silicon nitride balls were presented by Hadfield et al. (1993a), Hadfield et al. (1993b) and Hadfield et al. (1993c). The cracks were artificially induced and tests were conducted using a modified four-ball machine at maximum contact stresses of 6.4 GPa and spindle speed of 5000 rpm. The lubricants investigated were high viscosity mineral oil, low viscosity synthetic oil and high penetration kerosene. The failure mode was spalling in a non-catastrophic way. Experimental results showed that the artificially produced cracks failed in a non-catastrophic way, the pattern of failure was strongly influenced by the lubricating fluid and the final failure mode was spalling.

Burrier (1996) studied the rolling contact fatigue performance using 11 silicon

nitride bearing materials. Tests were conducted using a ball-on-rod machine at maximum contact stresses of 5.93 GPa and rod rotation speed of 3600 rpm. Research showed that the materials exhibited differences in life-span of several orders of magnitude and failure mode was spalling fatigue. Silicon nitride materials can exhibit a wide range of rolling contact fatigue endurance. Under the relatively high stress conditions, fatigue durability increased dramatically as the microstructure tended toward finer, more equiaxed grains and a uniform, minimum distribution of second phases.

1.4.3.2 Delamination

Studies of delamination fatigue failure on perfect and artificially pre-cracked silicon nitride balls were carried out using a modified four-ball machine by Hadfield et al. (1993a), Hadfield et al. (1994), Hadfield and Stolarski (1995b), Hadfield et al. (1993c). The silicon nitride balls were in rolling contact with a steel ball to simulate the rolling condition of a hybrid bearing. The cracks were artificially induced being in the forms of ring cracks or radial and lateral cracks. Testing under high compressive cyclic stress and various tribological conditions resulted in delamination failure. Scanning electron microscope observations enabled the delamination failures to be classified by the location of crack initiation and subsequent propagation. For ring-cracked balls, failure occurred by spalling. For radial and lateral cracked balls, failure occurred in three ways: (1) lateral crack induced spalling, (2) radial crack induced surface bulging, and (3) radial crack induced delamination. The failure mode was also sensitive to the lubricant used because lubricant could penetrate into the subsurface cracks to produce significant hydrostatic pressure.

In the case of surface delamination, adjacent radial cracks were propagated and connected, the delamination area showed typical fatigue striations. Residual stress measurement by x-ray diffraction indicated compressive stress in the delaminated area. In the case of surface bulging, ferrous debris originating from the upper steel ball was trapped under the ball surface. The steel debris, suspended in the pressurized lubricant, was forced up through the ball surface.

A recent study by Hadfield (1998) showed that the ring cracks did not develop into conics but failed due to delamination. The surface ring cracks were found on silicon nitride as purchased from manufacturers and were not produced artificially. The critical depth of the ring crack defect is 5 to 20 μm. Porosity was the dominant property which controlled wear mode and performance.

1.4.3.3 Rolling contact wear

Rolling contact wear is the most common type found on the contact path and it has been reported by a number of researchers. Preliminary work using a modified four-ball machine to assess hot-pressed silicon nitride as a rolling bearing material was reported by Scott and Blackwell (1973). Unlubricated contact was studied at different temperatures at 1500 rpm and a maximum Hertzian stress of 5.8GPa. Lubricated contact was also studied at 7.7 GPa and ambient temperature. Under unlubricated conditions upper ball wear after 30 minutes was measured as 0.6 mg, and the wear track on the ball surface retained modest surface quality. For lubricated contact, failure occurred to the upper ball after 20 seconds, the failure mode being wear and fracture. A silicon nitride upper ball was tested in contact with an En31 steel lower ball and this increased the time of failure to 70 seconds.

Wear properties of silicon nitride in dry rolling-sliding contact were studied by Akazawa and Kato (1988) using a ring-on-roller test machine. Under no lubrication and a maximum Hertzian pressure of 1.1 GPa, results showed thin flake-like wear particles that were rich in oxygen and depended on the roughness of the contact surfaces. Braza et al. (1989a) carried out rolling and sliding wear mechanism experiments. This work involved the use of a large diameter cast iron roller contacting with a smaller diameter silicon nitride roller with an internal steel pin lubricated with a standard lubrication oil. Contact pressure was small, i.e., 1.37 GPa, and three types of silicon nitride were tested: hot pressed, pressureless sintered and reaction bonded. The wear rate for the reaction bonded type was higher, the wear mode being by 'grain pullout'. The other two types had similar wear rates, the mode of wear being submicron chipping. Rolling contact friction coefficients were 0.0056 and all similar. Dry rolling tests by Kim et al. (1986) on several ceramics concluded

that the silicon nitride wear rate was the smallest. A ring-on-disc testing machine was used, with the maximum Hertz stress ranging from 2.5 GPa to 5 GPa. A relation between wear rate and mechanical properties was attempted without success, suggesting that a combination of material properties and roughness was needed. Brittle fracture was concluded to be the dominant wear mode.

Allen (1994) studied the effect of composition and physical properties of silicon nitride on rolling wear and fatigue performance using a ball-on-rod machine. Three commercial bearing materials were tested at maximum contact pressure of 6.4 GPa. Wear and fatigue properties were compared to physical properties and material composition. It was found that a high fracture toughness was not required for high fatigue life and wear resistance. Grain boundary composition did not appear to affect the wear mechanism of these hot-isostatically-pressed materials. Chao et al. (1998) reported transient wear of silicon nitride in lubricated rolling contact. A ball-on-rod test machine was used, with the maximum Hertz stress ranging from 5 to 6.5 GPa. Wear rate and behaviour were dependent on the initial surface roughness.

1.5 STATE OF ART RESULTING FROM LITERATURE SURVEY

Surface ring cracks are commonly found on silicon nitride balls and fatigue failure is initiated from those cracks. The presence of surface cracks on silicon nitride balls necessitates the understanding of failure modes of rolling elements with such surface cracks. Currently, there is little fundamental understanding of damage, failure modes and mechanism. Detailed failure processes initiated from surface ring cracks have not been adequately explained. Since the size of surface ring crack is very small (0.2 mm in radius) and the contact radius has the same dimensional scale, slight changes in geometric orientation on the contact track will result in a significant change in rolling contact fatigue life. The influence of crack location on rolling contact fatigue life has not been fully considered and crack propagation behaviour in rolling contact has not been adequately studied at this stage. The crack face contact effect in rolling contact has not been dealt with. Clearly, much effort must be devoted to these aspects.

CHAPTER 2

EXPERIMENT METHODOLOGY

This chapter presents specifications related to experimental research. Test materials are described with regard to silicon nitride ceramic balls, steel balls and lubricants. Specimen preparation and procedures for crack geometry studies are described. The rolling contact fatigue test method is described with respect to the test machine, crack position method and test procedure. In-test surface observation and post-test analysis, using light microscopy and scanning electron microscopy are also described.

2.1 TEST MATERIALS

2.1.1 Silicon nitride ball

Pure silicon nitride exists in two crystallographic forms: α and β, both of which have a hexagonal crystal structure. The α phase has a unit cell approximately twice as large the β phase. Silicon nitride materials are classified according to the processing techniques used to prepare the solid form. The categories include sintered, hot-pressed, reaction-bonded and hot isostatically pressed. It is important to recognise that the composition, microstructure, and properties of silicon nitrides vary strongly depending on the processing route used in the fabrication of the product (Appendix 2). Silicon nitride typically has higher fracture toughness than the other non-transforming monolithic ceramics. This is attributed to the whisker-like interpenetrating morphology of the β- Si_3N_4 grains which deflect the crack and thus increase the fracture resistance (Faber and Evans 1983). In the so-called self-reinforced silicon nitrides, this unique microstructure has been further exploited to increase the fracture toughness to 10 MPa $m^{1/2}$ (Li and Yamanis 1989).

Silicon nitride balls used for this research are manufactured by a hot isostatic pressing (HIP) of 'green' preformed powder. Preformed 'green' ball blanks are produced by compaction after blending, milling and agglomeration operations. Geometry of preformed blanks may be soft machined by standard operations at this stage. Densification of ball blanks is achieved by HIP at pressures of 200-300 MPa and temperatures of 1750-1900 °C. Densification of silicon nitride is preferred to

other methods such as hot-pressing, gas pressure sintering and pressureless sintering, as greater control and superior quality of material properties is available. Ball blanks are ground and polished to 12.7 mm diameter. Standardised procedures are adopted to ensure consistent quality of material and geometry. Average roughness (R_a) of the silicon nitride ball surfaces is typically 0.01μm and ball roundness is within ball bearing tolerances. Typical physical and mechanical properties are listed in table 2.1 (Jahanmir 1994).

Table 2.1 Typical properties of commercial bearing Si_3N_4.

Grade (manufacturer)	NBD-200
Material fabrication process	Hot-isostatic pressing
Density (g /cm^3)	3.16
Young's modulus (GPa)	320
Poisson's ratio	0.26
Fracture toughness (MPa m$^{1/2}$)	5.46
Hardness (Vickers indentation) (GPa)	16.6 (at 10 kg)
Thermal expansion coefficient (10^{-6} / K), 20-800 °C	2.9
Thermal conductivity (Watt / m K)	29.3 (at 20°C)

2.1.2 Steel ball

The steel ball is carbon chromium steel. The diameter and surface roughness are 12.7 mm and 0.02 μm R_a, respectively. The hardness of the steel balls is on average 839 H_v. The elastic modulus and Poisson ratio are 210 GPa and 0.3, respectively.

2.1.3 Lubricant

Four test lubricants are used in rolling fatigue tests and are listed in table 2.2. Base oil (Shell Tapla 20) is a highly refined straight naphthenic mineral oil with high oxidation stability, low carbon-forming tendencies and natural detergent properties. Gas Turbine oil is a low viscosity synthetic lubricant with additives. The cylinder and gear lubricants are a highly refined mineral oil with additives. Low and high

viscosity oils are used to examine possible effects of viscosity and increased film thickness.

Table 2.2 Physical and chemical properties of test lubricants

Lubricant	Viscosity @ 40°C (cSt)	Pour point (°C)	Flash point (°C)
Base Oil	94.6	-33	216
Gas Turbine Oil	25	-54	250
Cylinder Oil	1040	-6	260
Gear Oil	680	-6	200

2.2 RING CRACK GEOMETRY STUDIES

2.2.1 Specimen preparation

Manufacturing processing faults or blunt impact load often cause surface cracks on the ceramic balls due to their brittle characteristic. Surface cracks are extremely difficult to observe on ceramic surfaces even under high microscopic magnification. Other non-destructive test techniques such as X-ray radiography and ultrasonics are of restricted use for screening operations. To enable quick and effective surface crack screening, a fluorescent dye penetration technique is used.

In preparation for the fluorescent dye penetration examination, the sample is thoroughly cleaned with acetone in an ultrasonic bath. It is important to remove any surface grease and debris. The sample is heated up to 500° for one hour to burn out the oil within the crack. The sample is then soaked for a period of time in a dye penetrant. After soaking and draining the sample is immersed in a dye remover for a short time; this process removes any dye from the ball surface. The sample is then washed thoroughly and then dried carefully leaving no wash marks on the surface. The sample is then ready for examination, dye present within surface cracks may be observed under microscopic analysis with an ultraviolet light source. It is important to inspect the sample as quick as possible due to fluorescent degradation.

2.2.2 Surface inspection

The purpose of surface inspection is to obtain the crack geometry characteristic on the ball surface. Light microscope techniques are used to observe the ball surface. A customised manipulator (Appendix 3) positions each ball without manual contact interference. Figure 2.1 illustrates typical defect images found on the ceramic ball surface. Most of the defects are ring cracks. Ring crack radius and length are measured from light microscope observations.

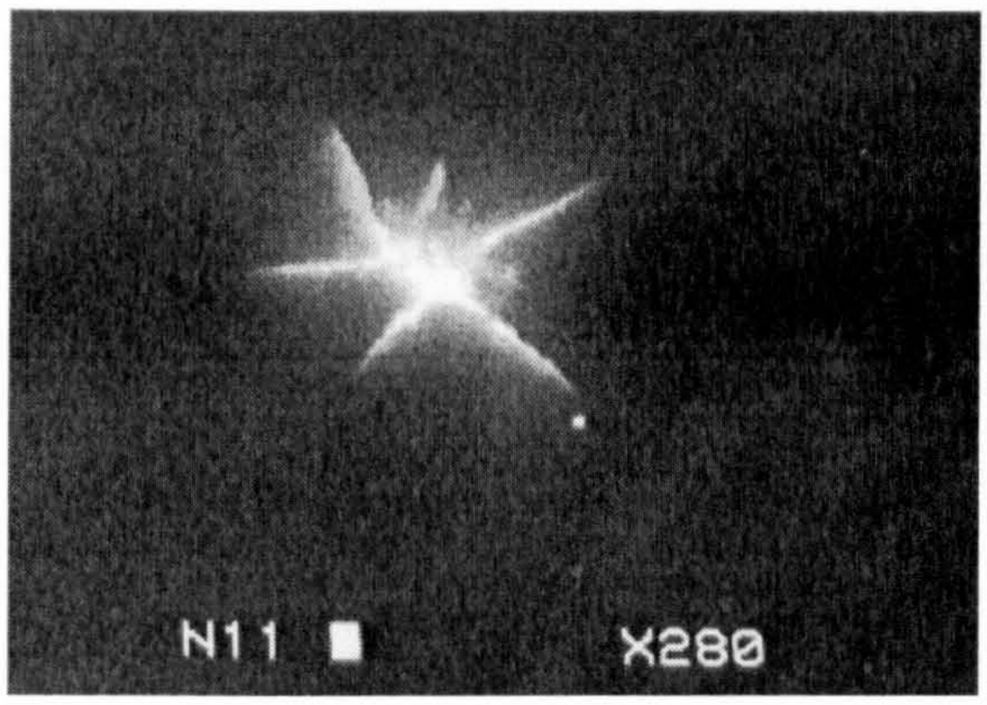

(a) Star defect

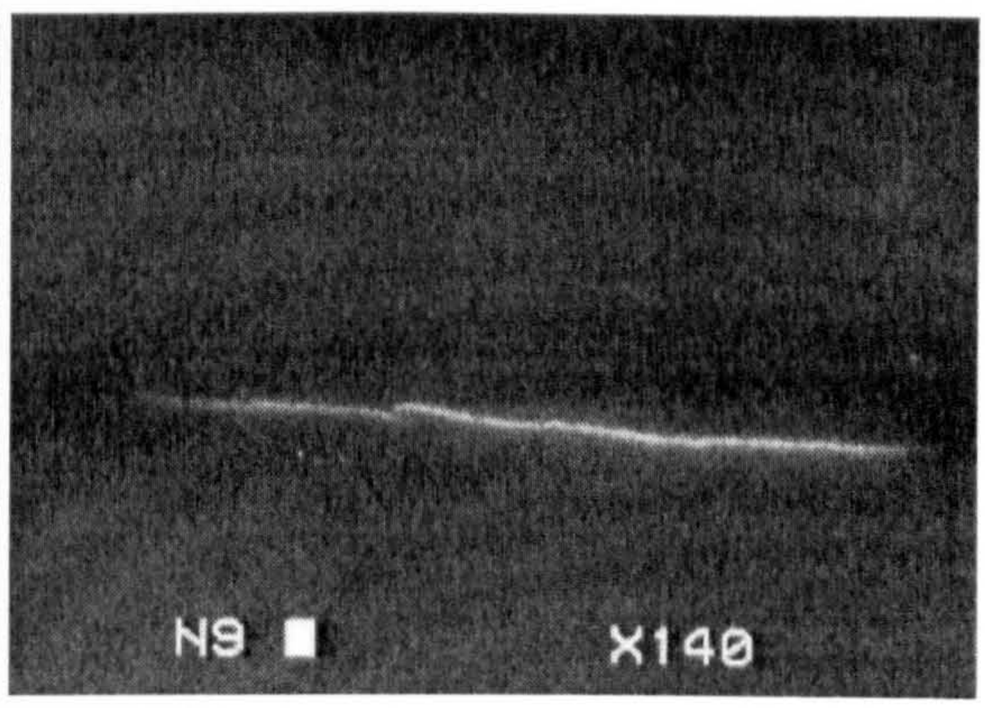

(b) Pressing defect

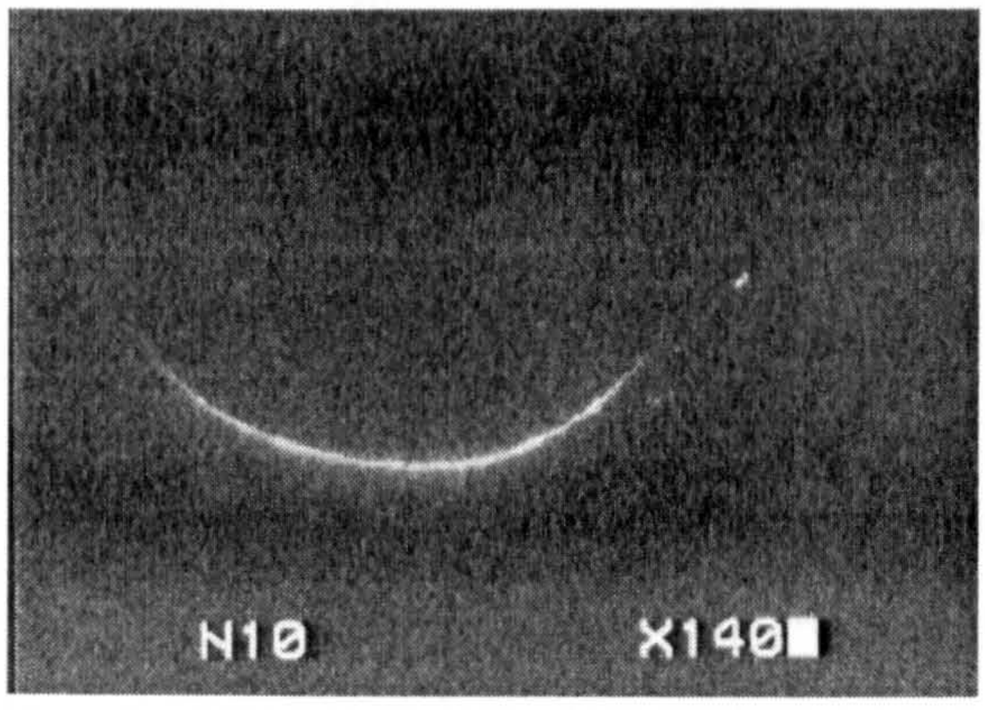

(c) Single ring crack

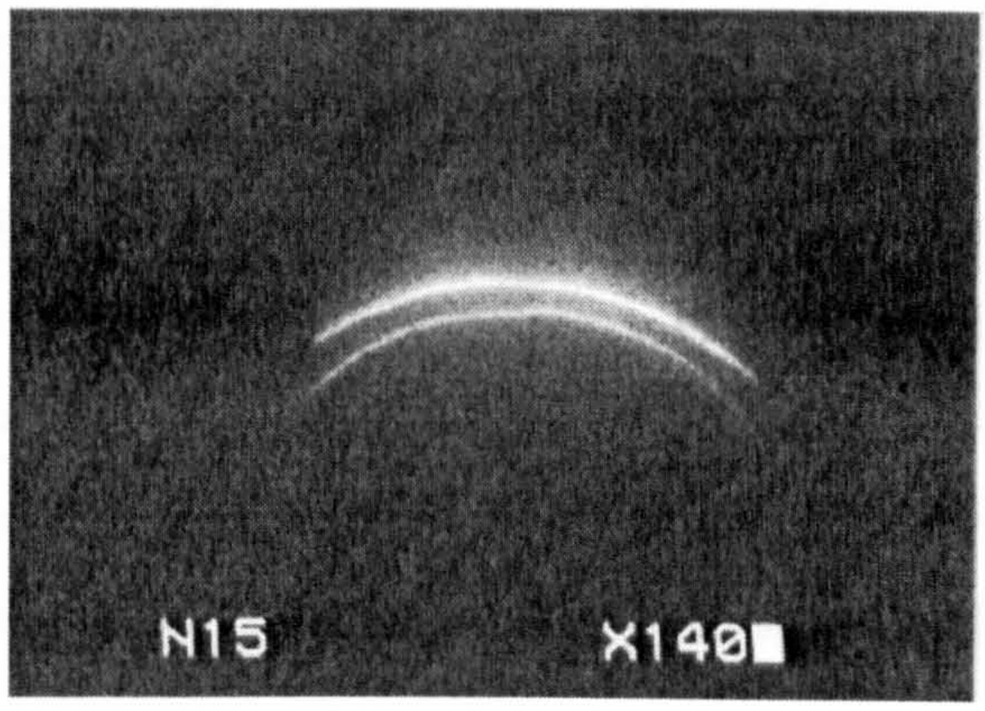

(d) Double ring cracks

Figure 2.1 Typical surface defects found on ceramic ball surfaces.

2.2.3 Subsurface observations

To study the subsurface geometry of the surface ring crack, the cracked ball is sectioned near the crack and then polished gradually across the ring crack to examine

the profile of the crack path. The polished sample is then inspected with a light microscope; various techniques are used to improve visual appearance. Light microscopy is employed to examine the silicon nitride ball surface and characterise ring crack defects.

It is difficult to section and polish ceramics due to high hardness and moderate toughness of the material. A 'Sturers' cutting machine incorporating a diamond wheel with sample rotation facility is used to section ceramic balls. Sample feed rate is set at 0.2 millimetres per minute, the cutting wheel head is lubricated with water. Once sectioned, the sample is mounted by means of a mounting machine. Silicon carbide paper (400, 600 and finally 800) is used to grind and smooth the sample surface. The surface is polished by using a polishing cloth and diamond paste (9, 6 and 3 μm). At the final polishing stage, a light microscope is required to examine the sample for scratches.

2.3 ROLLING CONTACT FATIGUE TESTING

2.3.1 Test equipment

The rolling contact fatigue tests are performed using a Plint TE92/HS Rolling Tribometer as shown in Figure 2.2. The equipment consists of a bench-mounted test machine and control interface. The computer is connected via the serial port to the micro-controller interface. The control software is installed on the PC. All test parameters are set up through menu-led utilities and a control panel generated on a colour monitor. Test data is stored on the hard disc.

Tests are defined by a series of steps, each step containing load, speed and temperature set-points, data recording and alarm level information. Set-points can be adjusted by step change or ramp. The test sequence is followed unless interrupted by the operator or an alarm.

The core of the machine is two rigid vertical columns which ensure accurate location of the drive spindle with respect to the normal loading axis. The test adapters are mounted on a cross beam which is guided by linear bearings on the columns and loaded by a pneumatic actuator. The load actuator assembly includes an in-line force measurement for direct feedback control of load.

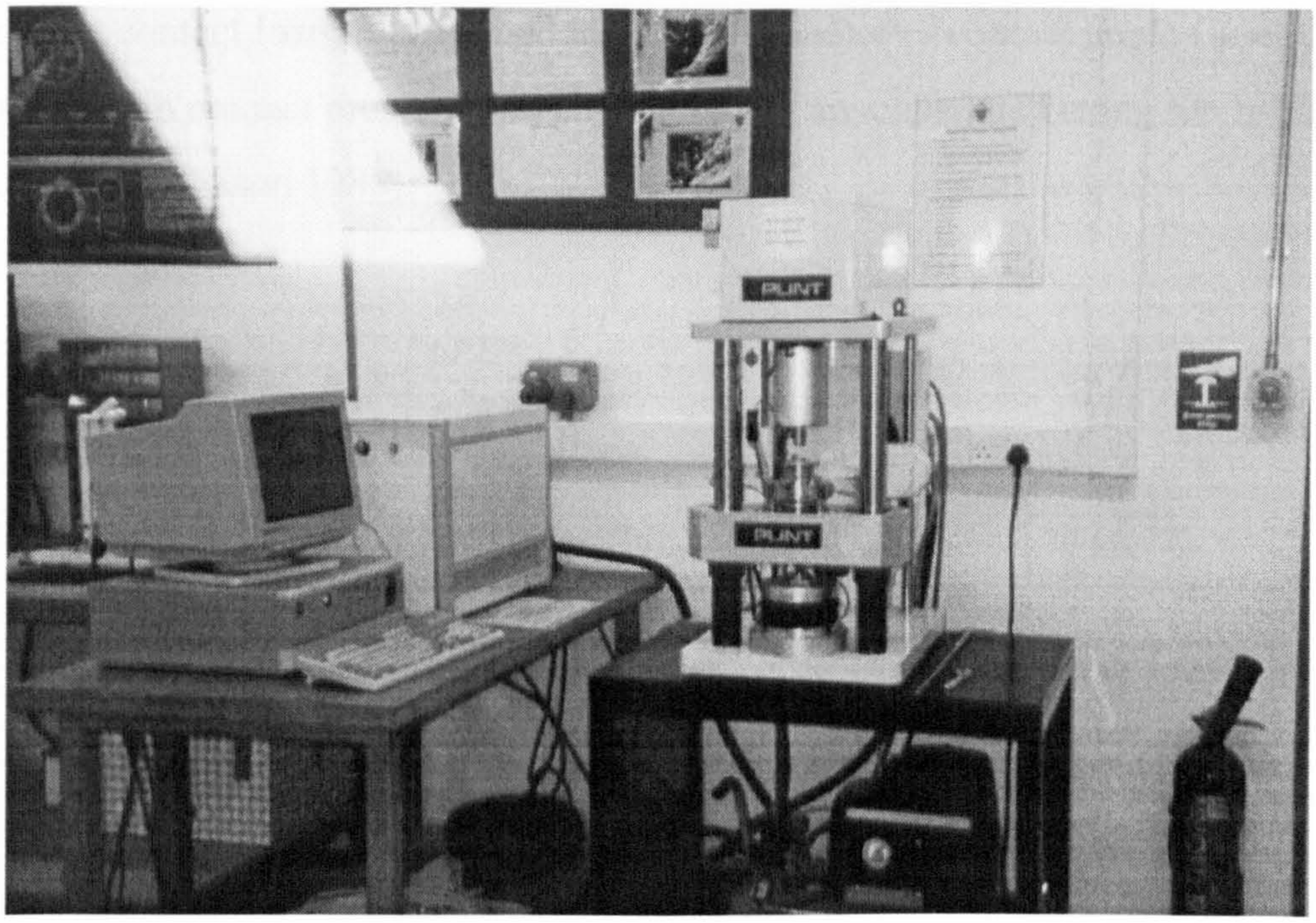

Figure 2.2 Rolling contact fatigue test bench.

This machine is employed as it simulates rolling elements and precisely defines the contact load. It consists of an assembly that simulates an angular contact rolling element bearing. The stationary steel cup represents a bearing outer-race, three lower balls represent the rolling elements within a bearing-race and the upper ball represents the inner-race. The upper-ball is assembled to a drive shaft via a collet and contacts three lower-balls when the machine is stationary. The contacting positions between the upper ball and lower balls are immersed in lubricating oil. The tests are terminated automatically at a set number of drive-shaft revolutions measured by a tachometer. A vibration sensor automatically stopped tests at a pre-determined potentiometer sensitivity and light emitting diode duration (2 seconds).

2.3.2 Ring crack location within the contact path

Figure 2.3 shows the loading geometry of the test machine and the geometric attitude of a crack on the contact track. The contact load is given by

$$P = \frac{L}{3\cos\varphi} \tag{2.1}$$

where P is contact load, L is applied load (shaft load), φ is contact angle ($\varphi = 35.3^{o}$). The maximum contact pressure and contact radius are calculated using the following expressions (Johnson 1985):

$$p_0 = \left(\frac{6PE^{*2}}{\pi^3 R^{*2}} \right)^{1/3} \tag{2.2}$$

$$a = \left(\frac{3PR^{*}}{4E^{*}} \right)^{1/3} \tag{2.3}$$

$$E^{*} = \left(\frac{1-\nu_1^2}{E_1} + \frac{1-\nu_2^2}{E_2} \right)^{-1} \tag{2.4}$$

$$R^{*} = \left(\frac{1}{R_1} + \frac{1}{R_2} \right)^{-1} \tag{2.5}$$

where p_0 is maximum contact pressure, P is contact load, a is contact radius, $E_{1,2}$ and $\nu_{1,2}$ are the Young's modulus and Poisson's ratios of the ceramic ball and steel ball, and $R_{1,2}$ is the radius of the ceramic ball and steel ball respectively.

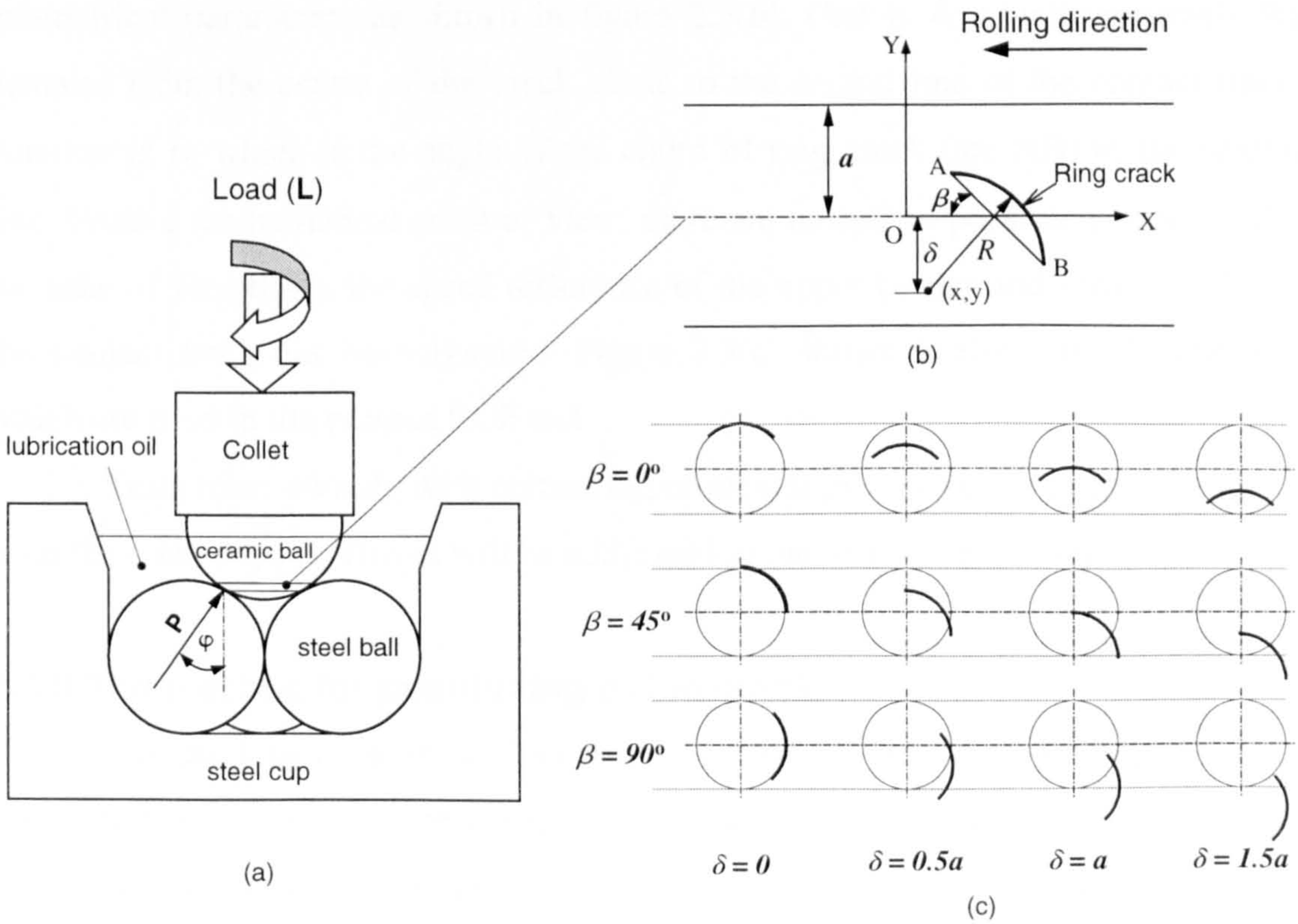

Figure 2.3 Loading configuration and ring crack locations on the contact path.

Surface ring cracks distribute randomly on the ball surface and the cracks can occur in any positions when two balls contact together. Therefore, the probability for the crack being in the contact area is calculated using the expression

$$\rho = A / A_0 \tag{2.6}$$

in which ρ is contacted probability, A is area of contact track, A_0 is area of ball surface. The A is approximately given by

$$A = 4\pi a R_1 \sin\varphi \tag{2.7}$$

where a is the contact radius, R_1 is the radius of the ceramic ball.

If R_1 = 6.35 mm, a = 0.21 mm, $\varphi = 35.3^\circ$, hence ρ = 0.02. As can be seen from the calculated result, the probability is only two percent, so it is not possible to be certain that a crack will be on the contact track if the ceramic ball is put randomly into the collet.

The geometric attitude of the crack location is described using two geometrical parameters as shown in figure 2.3(b). One is δ, which represents the distance from the centre of the crack circle to the central line of the contact track. Another is β, which is the angle of the chord of ring crack (arc AB) to the central line. From a mathematical point of view, there are unlimited possible positions. For the sake of simplicity, the speed difference of the upper border and lower border of the contact track has been ignored. Figure 2.3(c) shows twelve typical locations, which are used in the present RCF test.

Tests must comply with certain experimental procedures to ensure the crack is on the contact path. This is will be addressed in the following section.

2.3.3 The method for positioning a ring crack

The crack orientation on the contact path is very important in fatigue testing due to the contact circle size being close to the crack. Fatigue life is considerably dependent on the crack orientation. The key to studying the influence of crack location on fatigue failure is to locate the crack on the target position. To do this, a

crack location tool is used in the experiment as shown in figure 2.4.

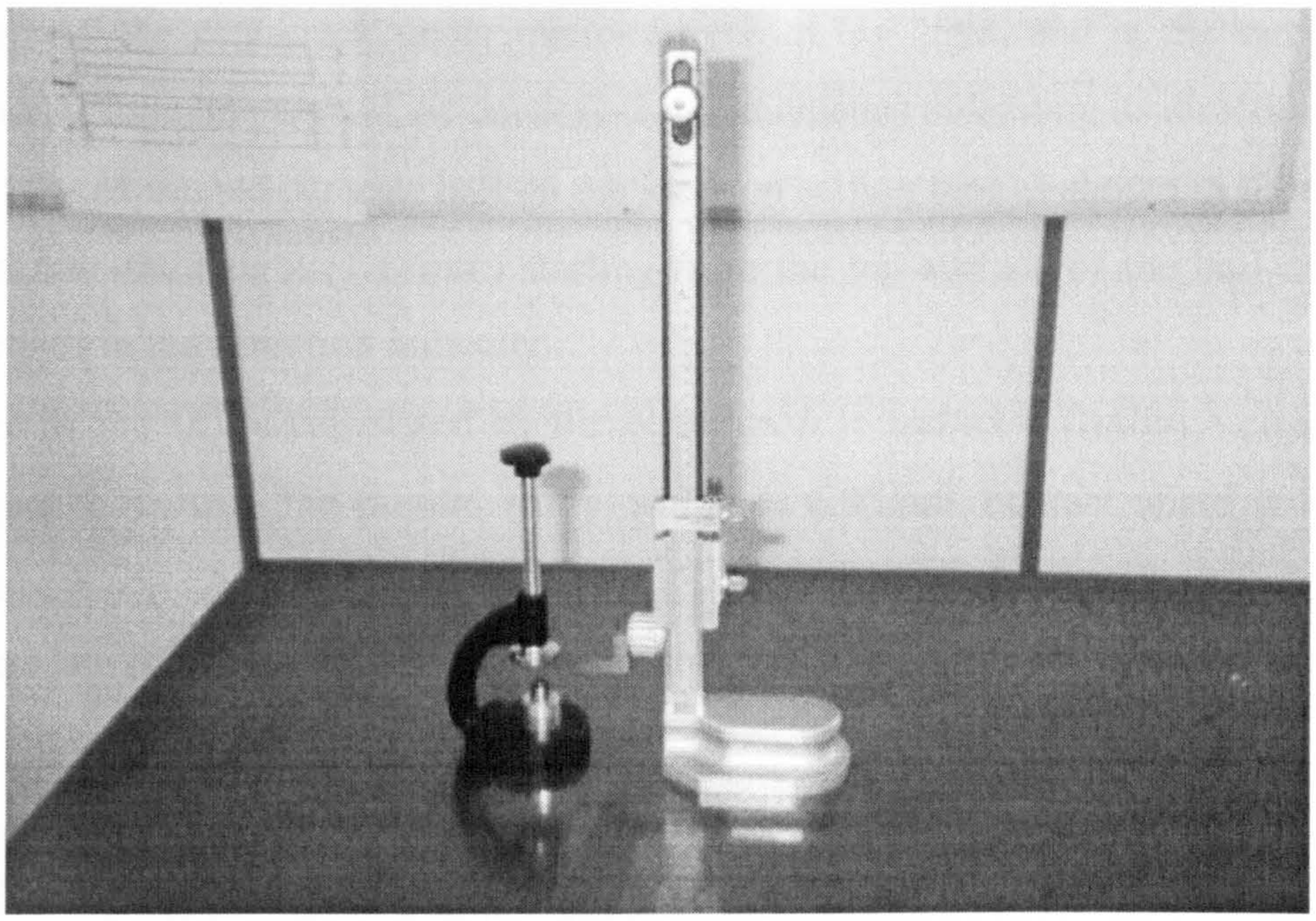

Figure 2.4 Crack location determination rig.

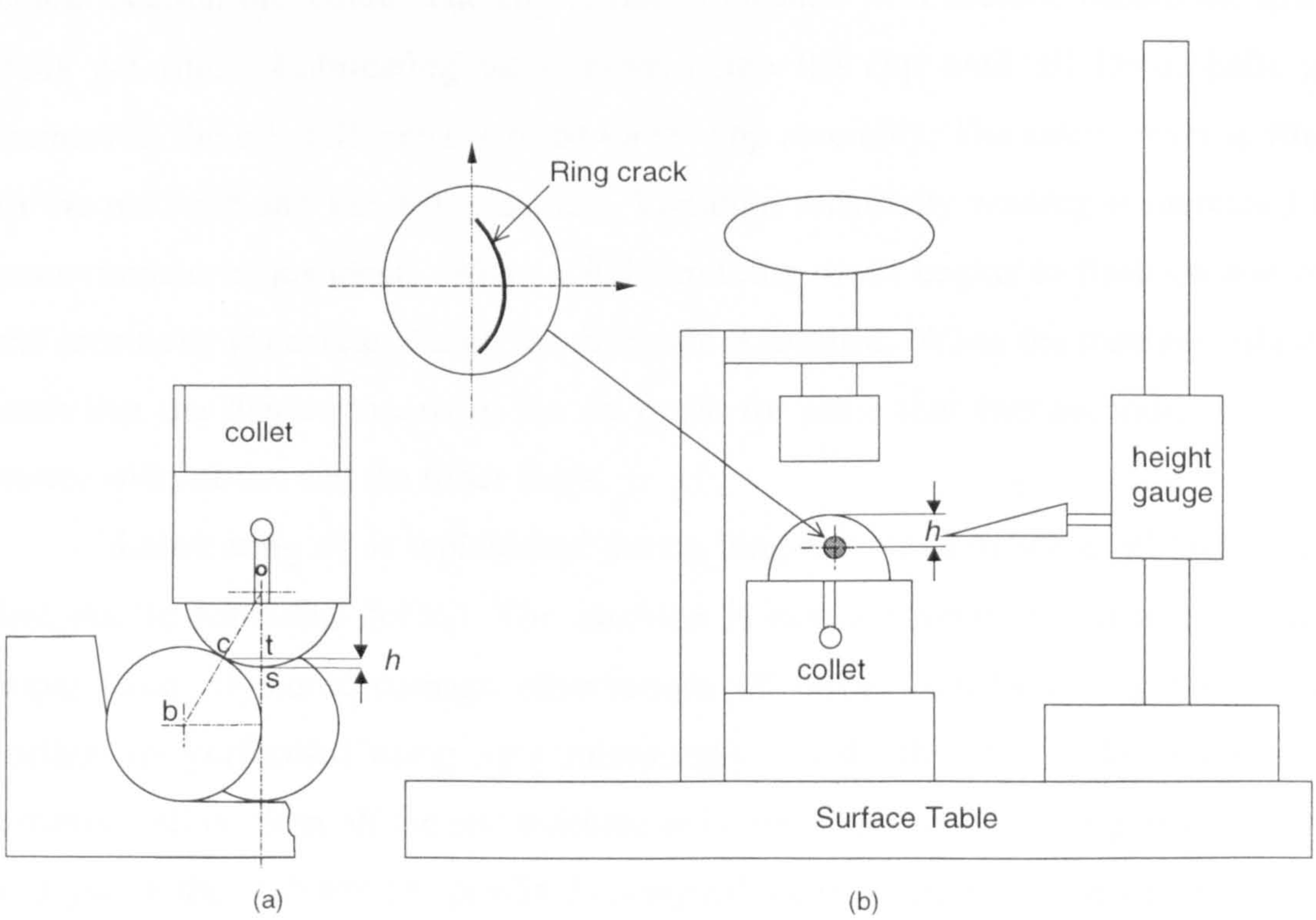

Figure 2.5 Schematic showing how a crack is located on the target location.

Figure 2.5 presents the schematic showing how a crack is located on the target location. Test preparations must be done in terms of the following procedures:

(1) Observe the ring crack under microscopy with UV light, and at the same time, draw a circle line around the crack (1-2 mm diameter) indicating its direction.

(2) Put the examined ceramic ball on the location setting tool as shown in figure 2.4.

(3) Measure the height (1.17mm) starting from the top surface of the ball and turn the ball in the direction indicated.

(4) The height (h) is calculated by the equation $h = radius - (radius \times cos\varphi)$ (see figure 2.5(a)). In the present study, $radius$ = 6.35mm, contact angle φ =35.3°, hence h = 1.17mm.

(5) Press the ball into the collet (figure 2.5(b)).

2.3.4 Test procedure

The collet assembly is pressed into the drive spindle after completing the crack location procedure. The cup is finally cleaned with acetone before the lower balls are fitted. Lubricating oil is poured into the cup until all lower balls are immersed, the oil spill cover is fitted on the cup assembly. The safety cover is fitted to the machine and the test is started. Vibration sensitivity reading is increased by potentiometer adjustment. When a light emitting diode begins to flash on and off, the sensitivity is decreased until the off mode is reached. When the machine vibrates such that the diode remains in the on mode for more that two seconds, the drive motor will cut-out and the timer stops.

Lubricating oil is replenished during long-term tests as some oil lubricant is lost due to rotational force. The machine is run overnight if necessary without supervision. Dynamic damage observations of surface cracks during the fatigue testing are performed using light microscopy. To do this, the collet holding the ceramic ball is taken off the test machine at intervals during the testing time, cleaned and put on the platform (Appendix 3) designed for supporting microscopy detection. After each observation, the collet is returned to the test machine to continue the fatigue test until failure or expiry of the suspending time (180 hours).

After test completion, the collet is taken off the machine and the upper

ceramic ball is pushed out of the collet and cleaned in acetone. Balls requiring further analysis are stored in a desiccator, other samples are stored in a sample file. All machine components are cleaned in 'genclean' after test completion; the steel cup is inspected for surface damage and replaced if necessary.

2.4 SURFACE CRACK OBSERVATIONS DURING TESTING

2.4.1 Apparatus

A light microscope (Olympus BX60) is employed to inspect surface crack propagation behaviour. The information on crack propagation can be directly obtained from the image even though there is a limitation in magnification. Various techniques are used to improve visual appearance. Illuminated light intensity, dark field and Normasky interference are examples of light microscope techniques. The ultra-violet light illumination is also used to identify the original crack and the propagated crack.

2.4.2 Observation procedure

The collet is taken off the test machine at interval testing times and then is thoroughly cleaned with acetone in an ultrasonic bath for 20 minutes. The sample is then dried carefully leaving no wash marks on the ball surface. The sample is then ready for examination. The collet is put on the platform designed for supporting microscopic observation to observe the crack (Appendix 3). After each observation, the collet is returned to the test machine to continue the fatigue test.

2.5 SURFACE SEM STUDIES

2.5.1 Sample preparation

Sample preparation is directly related to the quality of the electron microscopic analysis. Good electrical conductivity is required to prevent 'charging' of the specimen which may result in variation in brightness or signal strength. Sample cleanliness from dust or grease is important to maximise image clarity and chemical analysis. It is also important to make the sample mechanically stable for remote manipulation within the microscope.

Selected ball samples which have been analysed with a light microscope, are

mounted on special metallic stubs. Ball samples are attached to the stubs with conductive adhesive. A conductive path is necessary from the sample and stub to the goniometer to prevent electron charge saturation. Silver paint is spread on the metallic stub, adhesive and sample to increase conductivity.

Ceramic materials have low electric conductivity and hence require a thin coating of conductive material. The type of coating influences the image quality and resolution; for ceramic balls gold is the most suitable material. A diode splutter method of coating is employed. The coating should be as thin as possible to avoid charging in the electron microscope. The sample is coated in a clean vacuum to improve the consistency and reduce debris on the surface.

Coating the sample to ensure high distribution and adhesion especially for spherical samples is time consuming. The sample is placed in a vacuum chamber pumped out to 0.1 torr pressure. Argon is then released into the chamber and the vacuum is increased to 0.2 torr. Pressure is released to 0.1 torr whilst flooding the chamber with argon gas. The chamber is pumped out again and the process of argon flooding is repeated. Finally, the chamber is sealed and pumped out to 0.7 torr pressure. Electric power is applied to the gold diode and gas is released from the chamber to control the charging rate and position. After approximately 5 minutes the power is stopped and vacuum is released, the sample is placed in a desiccator ready for analysis.

2.5.2 Machine description

A Scanning Electron Microscope (SEM), PHILIPS SEM505, is used for fatigue surface analysis. High resolution and large depth of field are features of SEM analysis. The basic principle of the scanning electron microscope is the use of a fine probe of electrons interacting with a specimen to produce a variety of signals and images. The electron probe is produced by an electron gun and focused along an electron column by condenser lenses.

The microscope may be considered as five distinct systems: electron gun source, condenser system, scanning system, detection facility and display system.

CHAPTER 3

EXPERIMENTAL RESULTS

This chapter presents results of rolling contact fatigue (RCF) tests. The aim of the experimental studies is to investigate failure modes of pre-cracked ceramic elements under various tribological conditions. The influence of ring crack location on the RCF performance is tested and described in Section 3.1. The rolling contact fatigue performance is tested with various load ranges. Low and high viscosity oils are used. The RCF performance with surface line defects is tested and results are described in Section 3.2. The influence of lubricant properties on line defect failure is considered.

Surface observations of crack failure processes are carried out and results are described in Section 3.3. Results from low viscosity oil lubrication are described in Section 3.3.1 and results from high viscosity oil lubrication are described in Section 3.3.2. Subsurface observations of crack propagation are discussed in Section 3.4. The investigation of micro-crack wear patterns in rolling contacts is discussed in Section 3.5.

Light microscopy is employed to examine the ball surfaces and characterise ring crack defects. A dye-pentrant method is utilised to enhance the detection of surface ring cracks. Ring crack characterisations are described in Section 6. Surface appearances are described in Section 3.6.1. Subsurface geometry of the ring crack is studied and geometric equations are described in Section 3.6.2.

3.1 RCF PERFORMANCE WITH RING CRACK LOCATION

3.1.1 Low viscosity oil lubrication

Two parameters δ and β were used to describe the crack orientations within the contact path and were discussed in Chapter 2, Section 2.3.2. Twelve typical locations were described. Synthetic turbine oil is used to examine the effect of crack locations on RCF performance. Test conditions are described in table 3.1. All of the tests are conducted at a speed of 5000 rpm. The oil temperature variation (in 24

hours) during testing is shown in figure 3.1.

Table 3.1 Experimental test conditions (low viscosity lubricant)

Test No.	Contact Pressure (GPa)	Crack Locations
1	5.58	$\beta = 0^{\circ}, \quad \delta = 0$
2	5.58	$\beta = 0^{\circ}, \quad \delta = 0.5a$
3	5.58	$\beta = 0^{\circ}, \quad \delta = a$
4	5.58	$\beta = 0^{\circ}, \quad \delta = 1.5a$
5	5.58	$\beta = 45^{\circ}, \quad \delta = 0$
6	5.58	$\beta = 45^{\circ}, \quad \delta = 0.5a$
7	5.58	$\beta = 45^{\circ}, \quad \delta = a$
8	5.58	$\beta = 45^{\circ}, \quad \delta = 1.5a$
9	5.58	$\beta = 90^{\circ}, \quad \delta = 0$
10	5.58	$\beta = 90^{\circ}, \quad \delta = 0.5a$
11	5.58	$\beta = 90^{\circ}, \quad \delta = a$
12	5.58	$\beta = 90^{\circ}, \quad \delta = 1.5a$
13	6.63	$\beta = 90^{\circ}, \quad \delta = 0.5a$
14	7.58	$\beta = 90^{\circ}, \quad \delta = 0.5a$
15	8.35	$\beta = 45^{\circ}, \quad \delta = a$

Results (Tests 1 to 12) are plotted in the bar chart shown in figure 3.2. As can be seen from the results, silicon nitride balls do not always fail although the cracks are exactly in the contact region and the contact loading traverses the crack. The rolling contact fatigue performance is the function of parameters β and δ for a given contact load and lubrication regime. The fatigue life changes with the change of β and δ.

The rolling contact fatigue life decreases as the β increases. When $\delta = 0$, the fatigue life is 24 hours (1.626×10^7 fatigue cycles) for $\beta = 90^{\circ}$, 40.7 hours (2.758×10^7

fatigue cycles) for $\beta = 45^{\circ}$, and 180 hours (1.215×10^{8} fatigue cycles) no failure for $\beta = 0^{\circ}$. When $\delta = 0.5a$, the fatigue life is 72 hours for $\beta = 90^{\circ}$ and 180 hours no failure for $\beta = 45^{\circ}$ and $\beta = 0^{\circ}$. When $\delta = a$ or $\delta = 1.5a$, no fatigue failures happen for $\beta = 0^{\circ}$, $\beta = 45^{\circ}$ and $\beta = 90^{\circ}$ in 180 hours of fatigue testing.

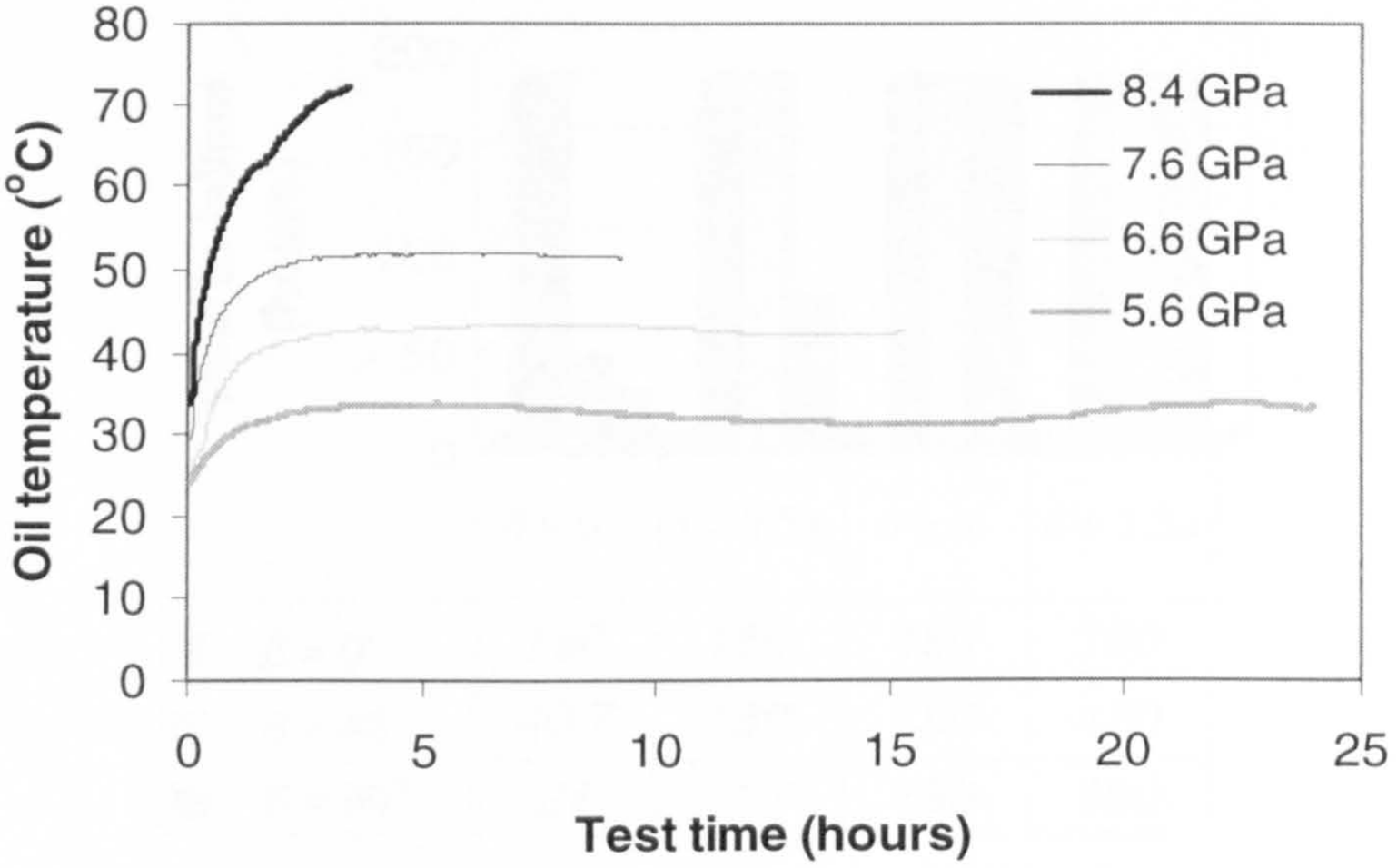

Figure 3.1 Temperature variation in a day at various contact pressures (turbine oil).

The rolling contact fatigue life increases as the δ increases. When $\beta = 0^{\circ}$, no fatigue failures happen for $\delta = 0$, $\delta = 0.5a$, $\delta = a$, $\delta = 1.5a$ in 180 hours of fatigue testing. When $\beta = 45^{\circ}$, the fatigue life is 40.7 hours for $\delta = 0$ and 180 hours no failure for $\delta = 0.5a$, $\delta = a$ and $\delta = 1.5a$. When $\beta = 90^{\circ}$, the fatigue life is 24 hours for $\delta = 0$, 71.7 hours for $\delta = 0.5a$ and 180 hours no failure for $\delta = a$ and $\delta = 1.5a$.

The contact loading is increased to 8.35 GPa (Test 15) to attempt low cycle failure modes. There is no fatigue spall in the fatigue cycles of 2.84 million for $\beta = 45^{\circ}$ and $\delta = a$. Due to this loading being too high, it is not easy to keep the test running without frequent changes of the lower steel balls, so the test is suspended.

It can be seen from the results of the experiment on twelve typical locations, that only three locations lead to fatigue failure when maximum contact pressure is 5.58 GPa. The previous calculation shows that the probability of the surface ring crack

being in the contact region is only 2 percent. Furthermore, the failure probability of surface ring crack is to be 0.5 percent only if the ball is put into the collet randomly. This may explain why the fatigue life is too discrete to correlate the fatigue performance with such properties as density and hardness etc.

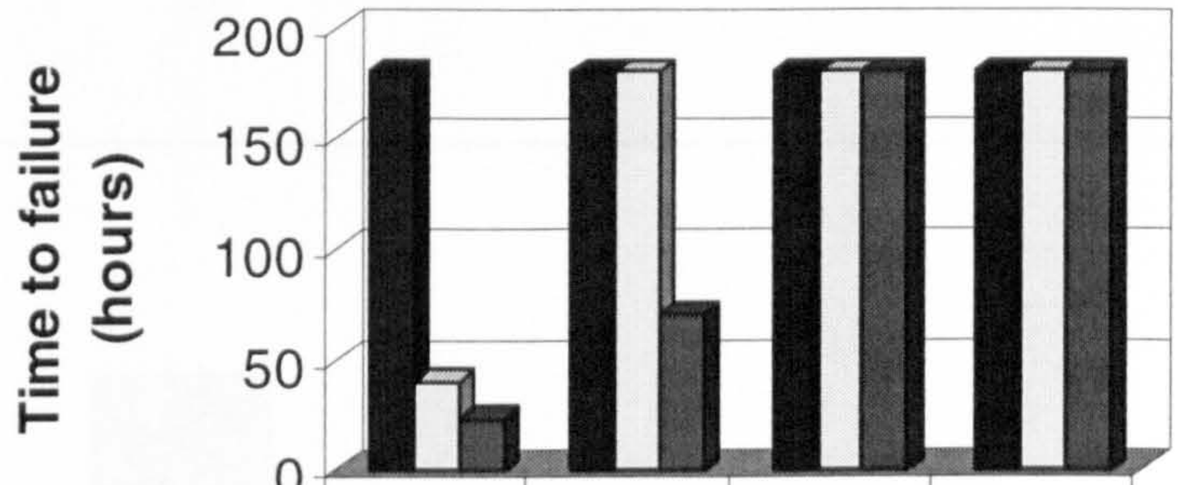

	$\delta = 0$	$\delta = 0.5a$	$\delta = a$	$\delta = 1.5a$
■ $\beta = 0°$	180	180	180	180
□ $\beta = 45°$	40.7	180	180	180
■ $\beta = 90°$	24	71.7	180	180

Figure 3.2 Fatigue life of 12 typical crack locations under test conditions.

The reason for differences in rolling contact fatigue performance is that different crack locations have different stress intensity factor values, which govern the crack propagation behaviour, when $\delta = 0$ and $\beta = 90^{\circ}$, K_I and K_{eq} reach maximum value compared with other crack locations (see Chapter 4, Section 4.3.3). When stress fields are activated, surface ring cracks propagate along specific lines. The magnitude of the stress intensity factors decides whether the crack propagates and how fast it will grow. When $\delta = 0$, both K_I and K_{eq} along the crack front at the location of $\beta = 90^{\circ}$ are higher than those for $\beta = 45^{\circ}$ and $\beta = 0^{\circ}$. The K_I and K_{eq} at the location of $\beta = 0^{\circ}$ are then the lowest. Hence, the fatigue performance is different for these test conditions. Crack propagation is a necessary condition for a fatigue spall of silicon nitride bearing elements because the crack does not always grow toward the ball surface. Detailed stress intensity factor calculation will be discussed in Chapter 4.

Figure 3.3 presents the comparison of fatigue life for three crack locations at increased load. The crack location is $\beta = 90^{o}$ and $\delta = 0.5a$. It is obvious that the fatigue life decreases with the increase of contact stresses. Oil temperature variation in a day during testing is shown in figure 3.1. As temperature gradually increases with contact load, film thickness reduces due to the effects of the viscosity.

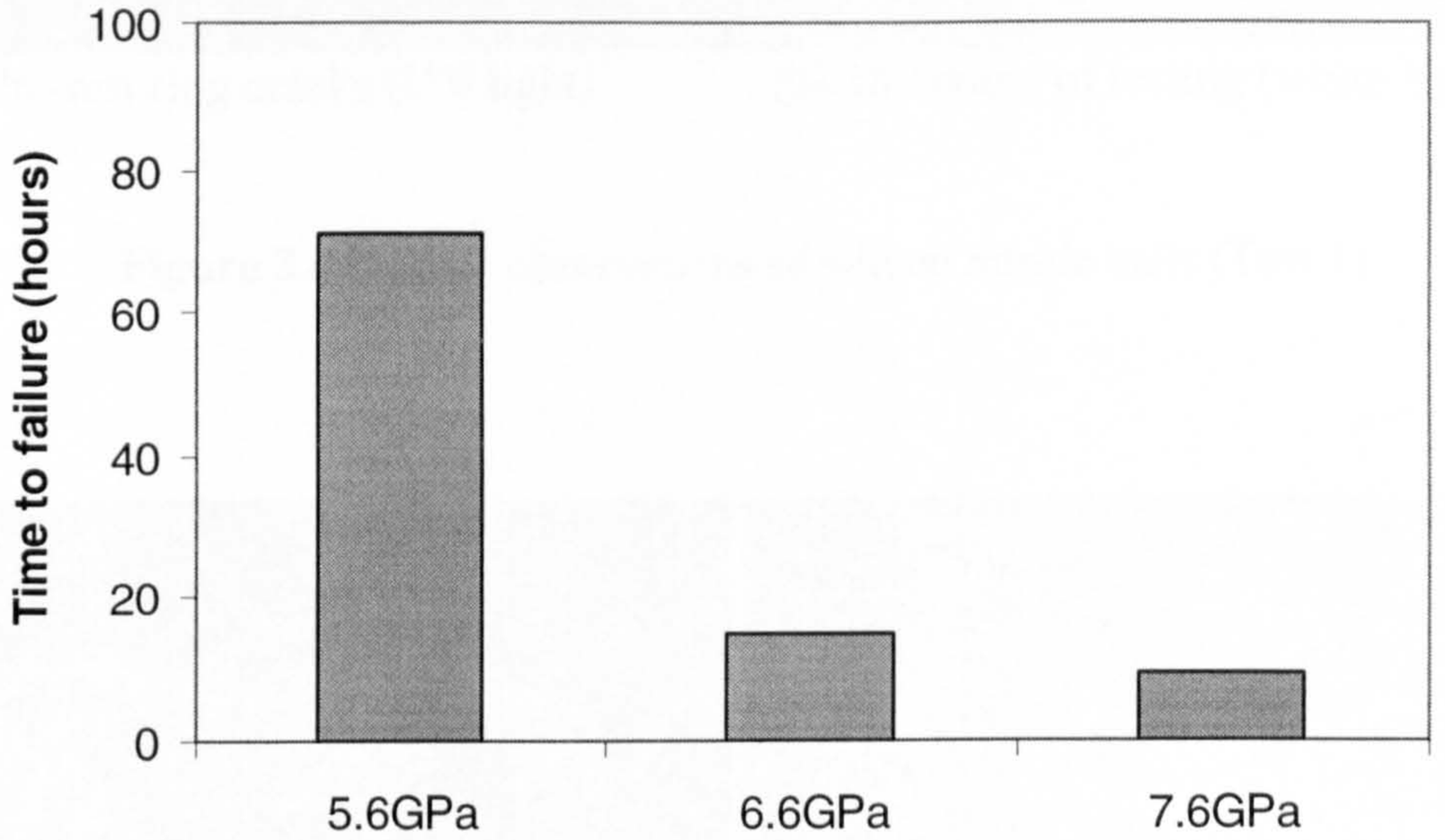

Figure 3.3 RCF performance at different contact stresses in the same crack location.

In general, surface ring cracks are not visible without an UV light source. The cracks are only to be detected using the dye-penetrant method under ultra-violet light. During the fatigue tests, however, the cracks become visible under normal light conditions. Some examples are given in the following discussion. Detailed surface damage analyses during rolling contact are discussed in Section 3.3.

Figure 3.4(a) shows a surface ring crack image before testing and this crack is used for Test 1. Figure 3.4(b) shows the crack location on the contact path. The wear track is clear, and the crack is obvious. Figure 3.5(a) is the ring crack image before test (Test 7), and figure 3.5(b) shows the surface image after 180 hours of testing.

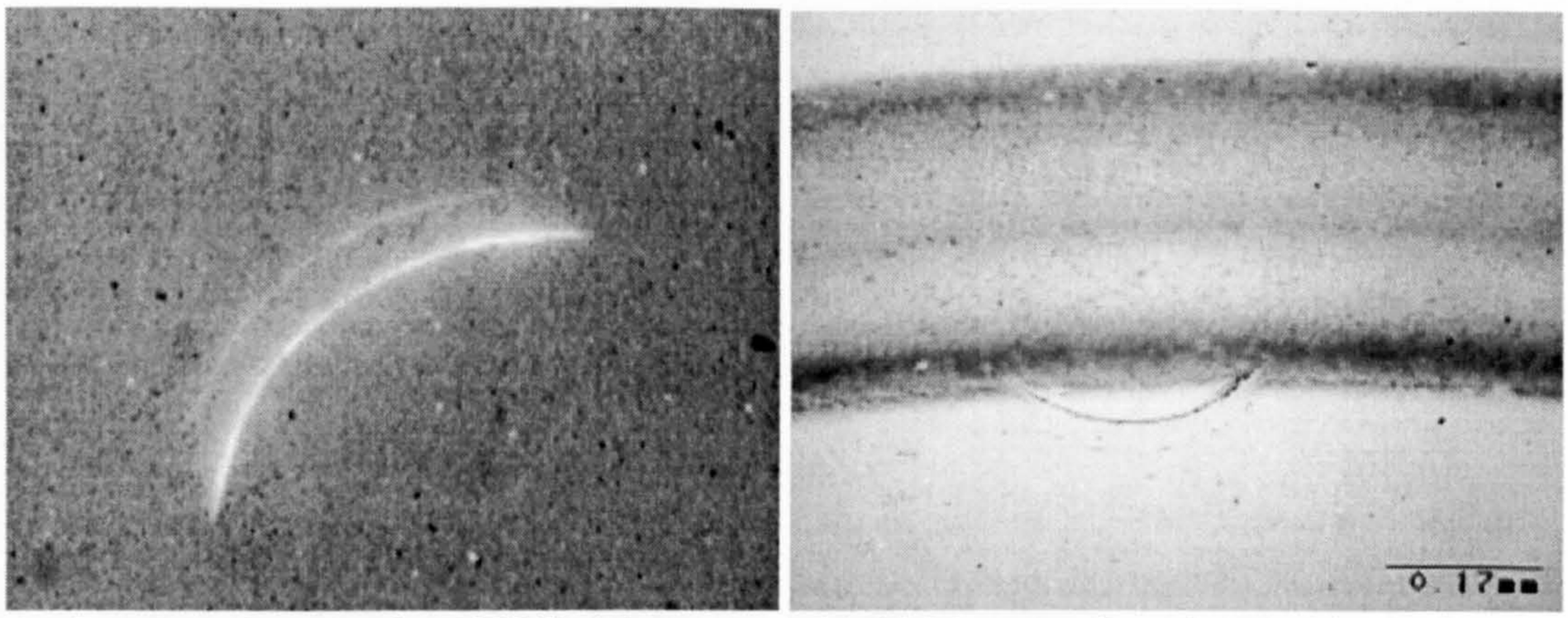

(a) Pre-test ring cracks (UV light) (b) 180 hours of testing (white light)

Figure 3.4 Surface observations of silicon nitride balls (Test 1).

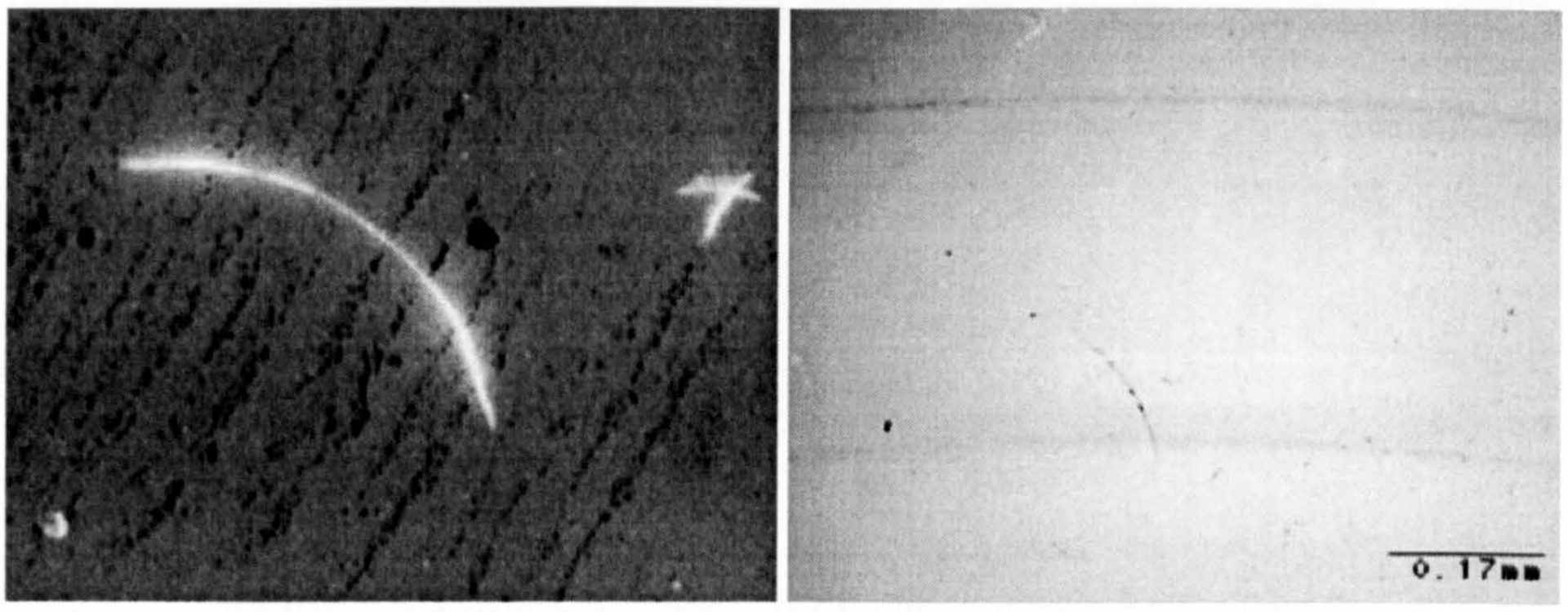

(a) Pre-test ring crack (UV light) (b) 180 hours of testing (white light)

Figure 3.5 Surface observations of silicon nitride balls (Test 7).

Figure 3.6(a) and figure 3.6(b) show the ring crack image before testing and during testing (17 hours) used in Test 9 respectively. Figure 3.6(c) shows an optical image of a fatigue spall. The SEM image is shown in figure 3.6(d). The spalling shape of rolling contact fatigue looks like an ellipse. The longer semi-axis is always parallel to the rolling direction, and the short axis is perpendicular to the rolling direction. The short semi-axis approximates to the magnitude of the contact radius under the applied load.

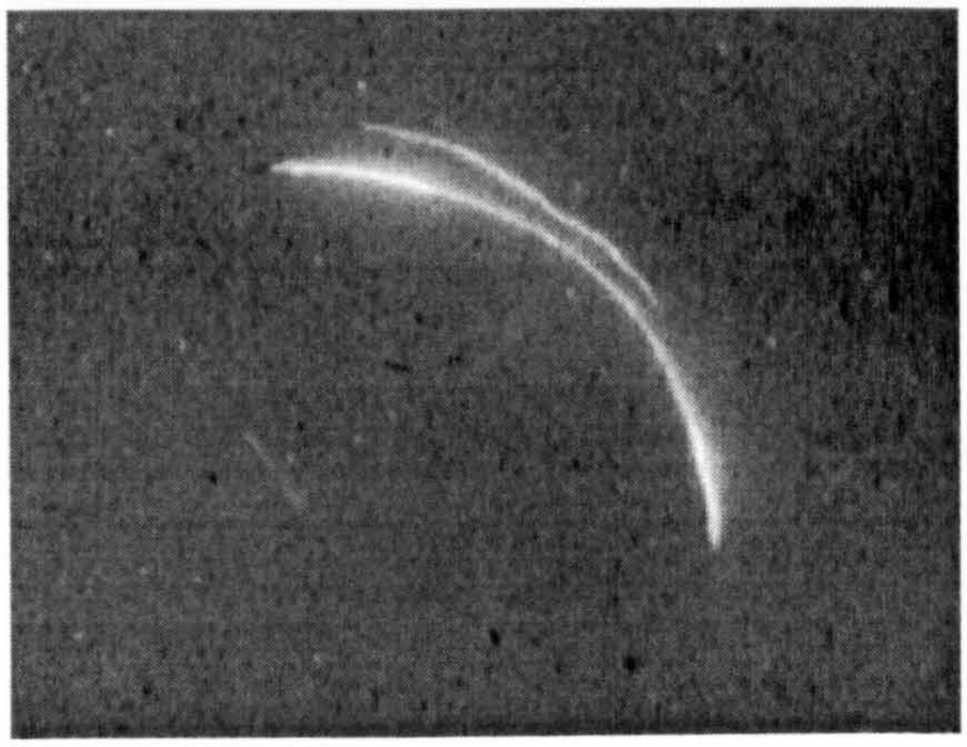

(a) Pre-test ring cracks (UV light)

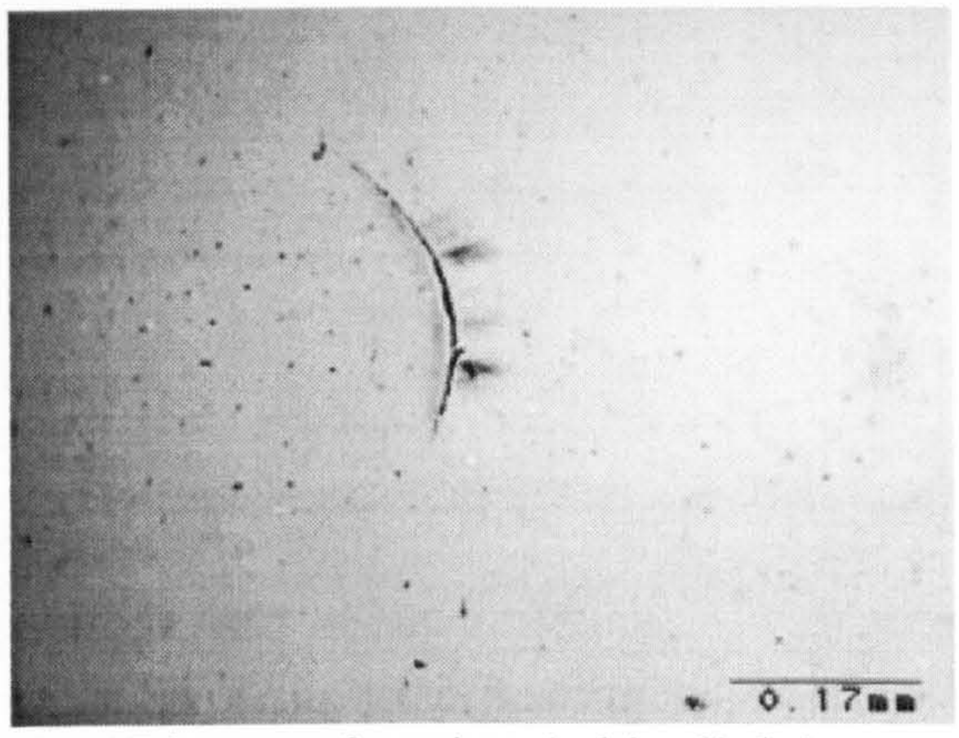

(b) 17 hours of testing (white light)

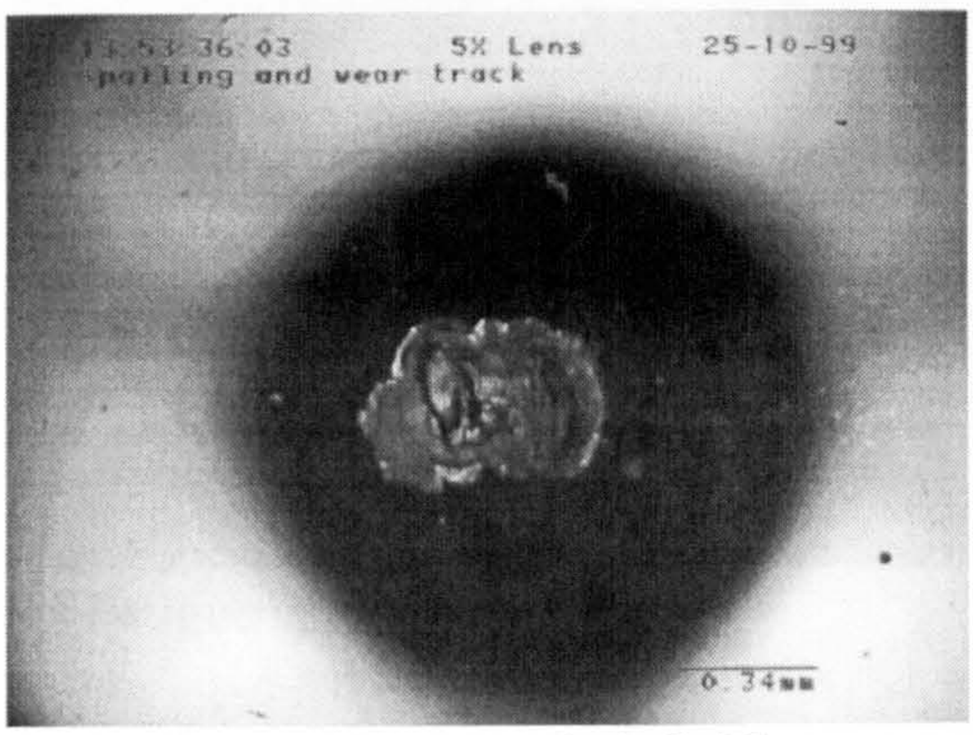

(c) Spall optical image (dark field)

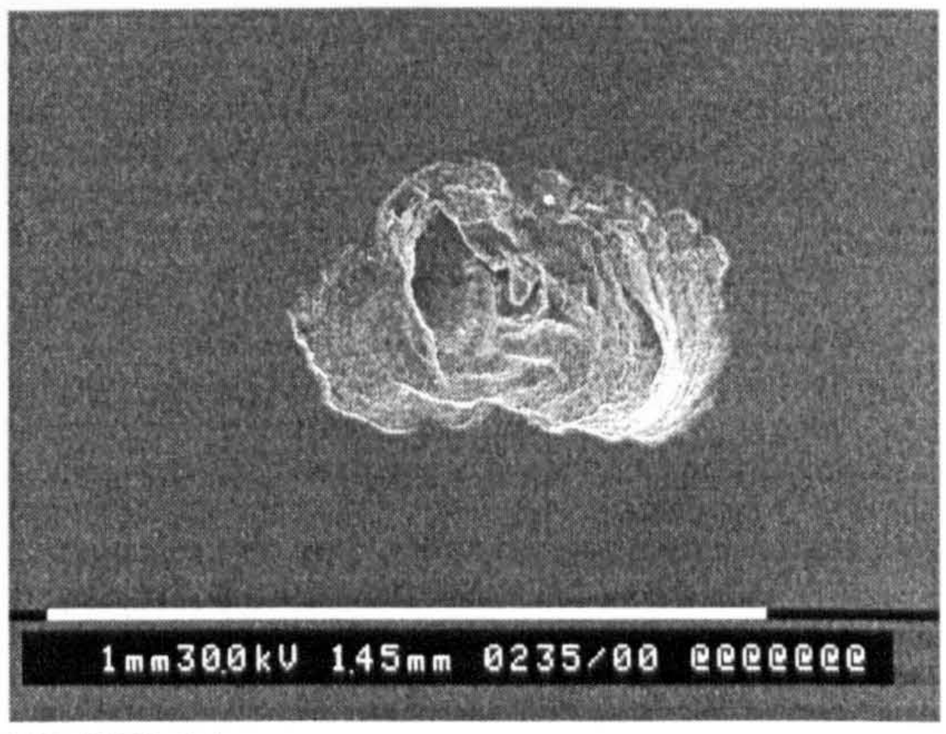

(d) SEM image

Figure 3.6 Surface observations of silicon nitride balls (Test 9).

Observations of silicon nitride ball surfaces from Test 10 are shown in figure 3.7. The test condition is contact stress = 5.58GPa, $\delta = 0.5a$ and $\beta = 90^{o}$. Figure 3.7(a) shows this surface ring crack image with UV light before the testing. This crack has a radius of 0.225 mm and is 0.314 mm long. As the fatigue test proceeds (22 hours of testing) the crack becomes visible with normal light as shown in figure 3.7(b). The contact track is very clear and three arrows indicate the ring crack. Figure 3.7(c) is an optical micrograph, and figure 3.7(d) is a spall SEM micrograph. As can be seen, the spalling contours always resemble an ellipse no matter how δ and β change. The contour shape seems to be directly related to the geometry of the contact region.

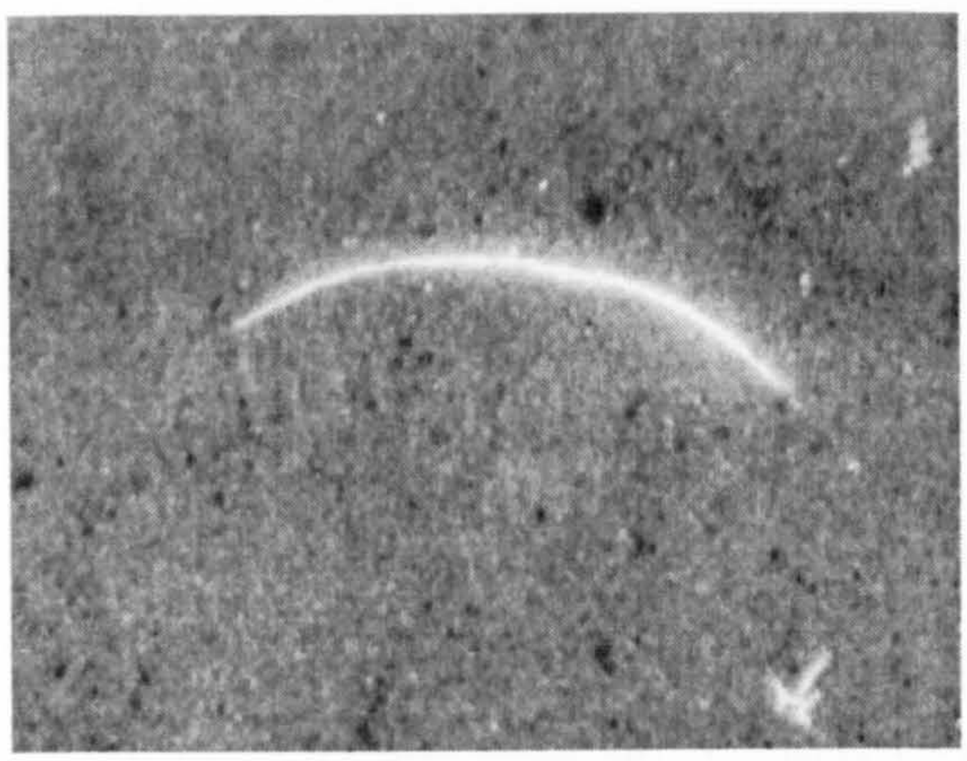

(a) Pre-test ring crack (UV light)

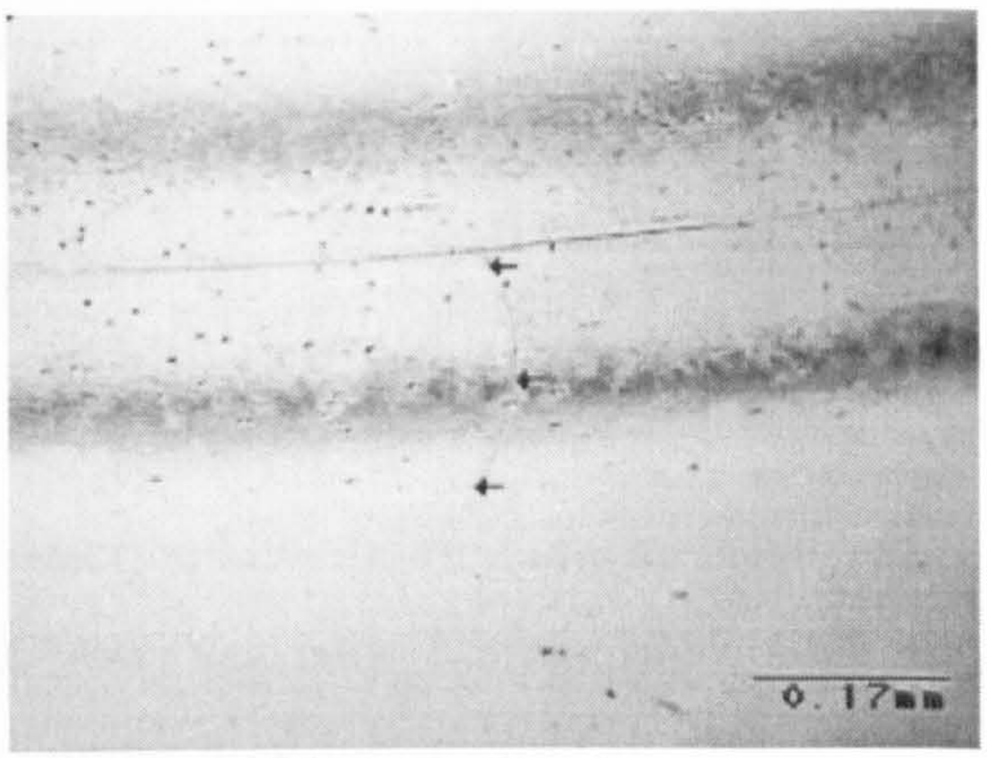

(b) After 22 hours of testing

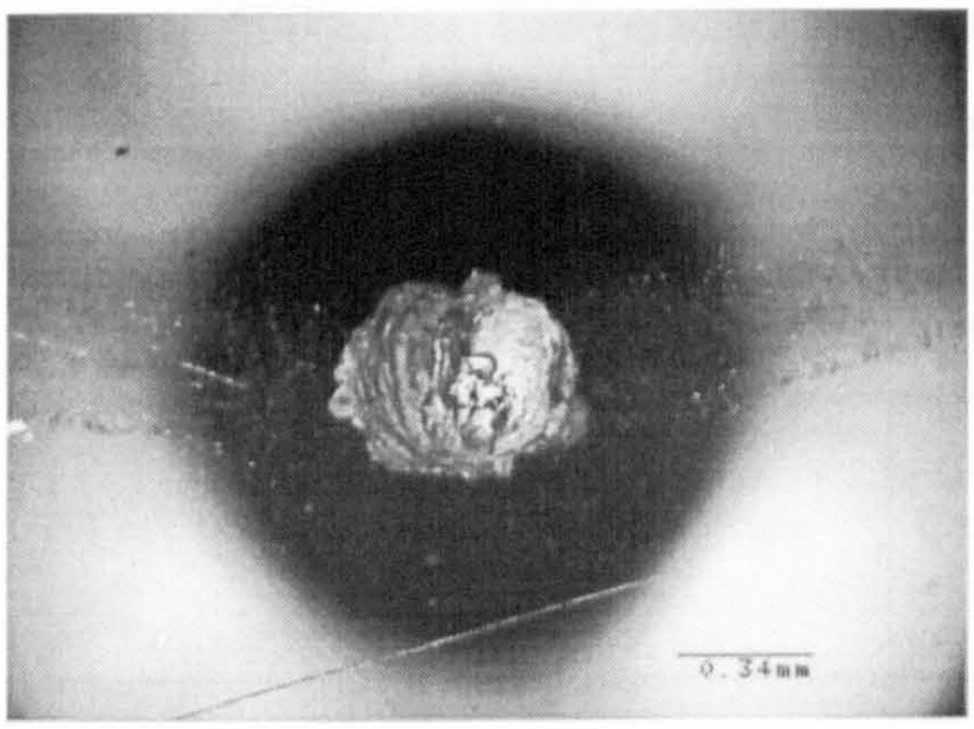

(c) Fatigue spall optical image

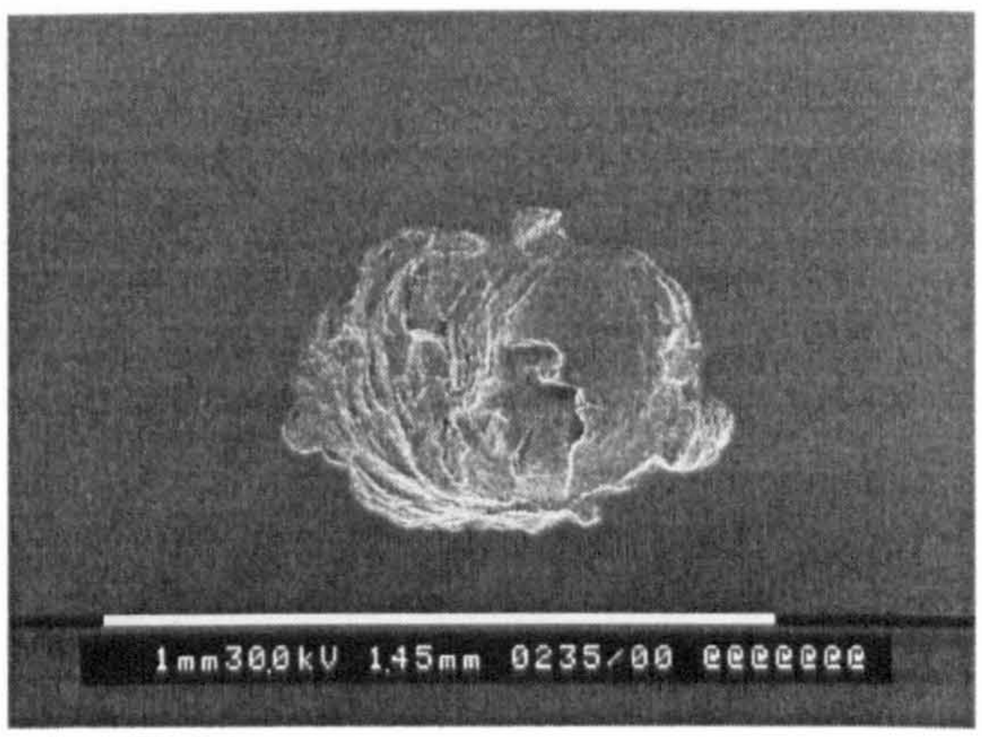

(d) SEM image

Figure 3.7 Surface observations of silicon nitride balls (Test 10).

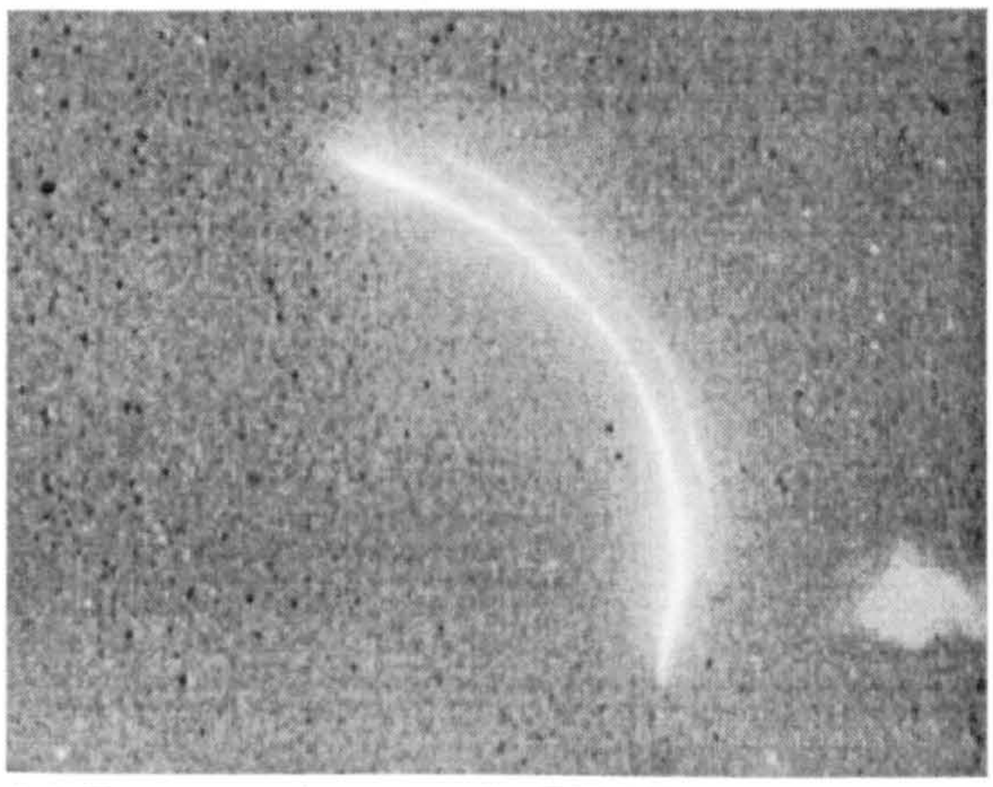

(a) Pre-test ring crack (UV light)

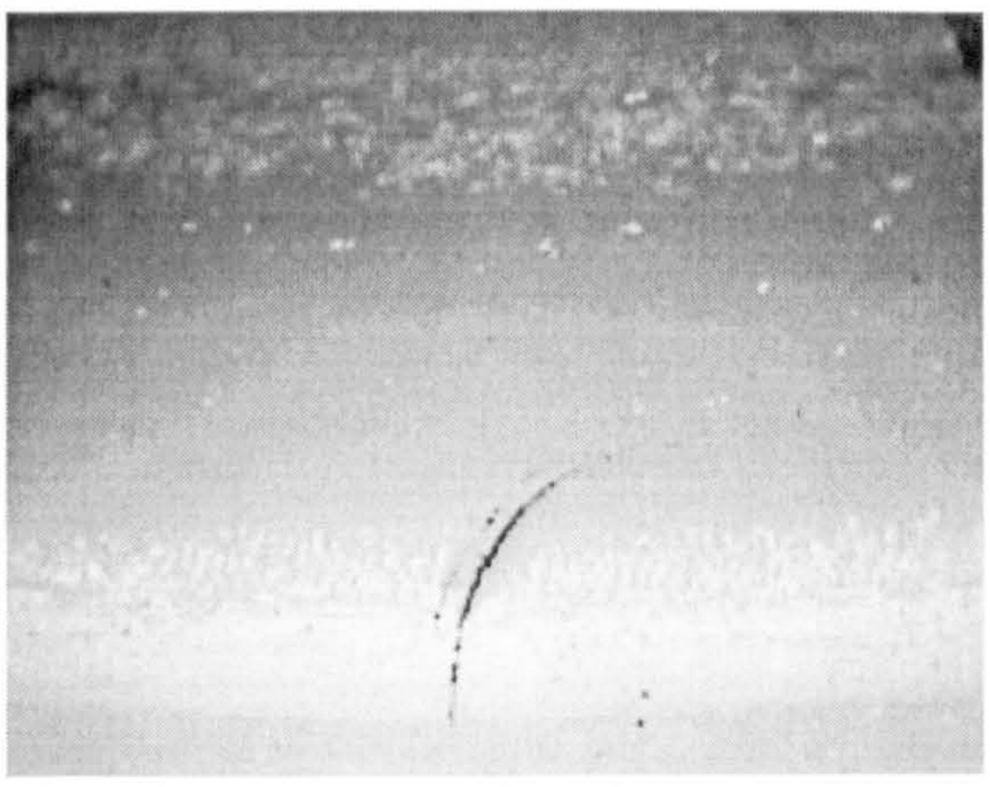

(b) After 4.2 hours of testing

Figure 3.8 Surface observations of silicon nitride balls (Test 15).

Figure 3.8(a) shows a ring crack image before testing, and figure 3.8(b) shows the image after 4.2 hours of testing (Test 15, maximum contact pressure 8.35 GPa, $\delta = a$, $\beta = 45^{\circ}$).

3.1.2 High viscosity oil lubrication

Results from the previous section describe how the ring cracks behave in the different crack locations operating with low viscosity lubrication oil. A high viscosity lubricant, gear oil, is used to examine how lubrication oil affects failure modes. Test conditions are described in table 3.2. All of the tests are conducted at a speed of 5000 rpm. Temperature variation during testing is shown in figure 3.9. As in low viscosity oil, temperature increases with contact load.

Table 3.2 Experimental test conditions (high viscosity lubricant)

Test No.	Contact Pressure (GPa)	Crack Locations	lubricant
A	5.58	$\beta = 90^{\circ}$, $\delta = 0$	Gear oil
B	5.58	$\beta = 90^{\circ}$, $\delta = 0.5a$	Gear oil
C	5.58	$\beta = 90^{\circ}$, $\delta = a$	Gear oil
D	5.58	$\beta = -90^{\circ}$, $\delta = 0$	Gear oil
E	6.63	$\beta = 90^{\circ}$, $\delta = 0.5a$	Gear oil
F	6.63	$\beta = 45^{\circ}$, $\delta = 0$	Gear oil
G	7.58	$\beta = 45^{\circ}$, $\delta = 0.5a$	Gear oil
H	6.63	$\beta = -90^{\circ}$, $\delta = 0$	Cylinder oil

The first three tests examine the influence of δ on fatigue life. The result is shown in figure 3.10. It is clear that rolling contact fatigue life increases as the δ increases. This result confirms the sensitivity of spalling fatigue failure mode to the

crack locations even with high viscosity oil lubrication.

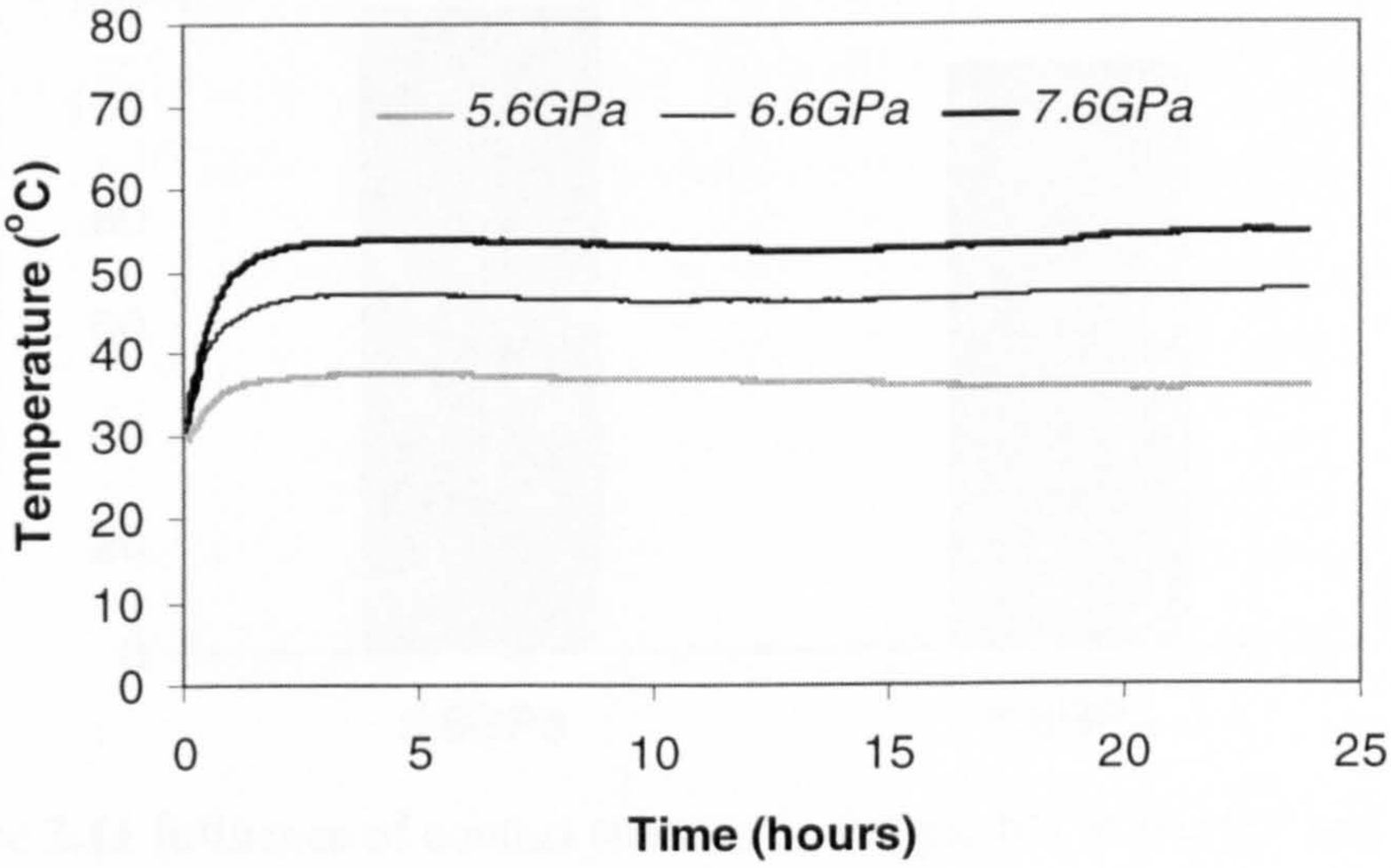

Figure 3.9 Temperature variation in a day at various contact pressures (gear oil).

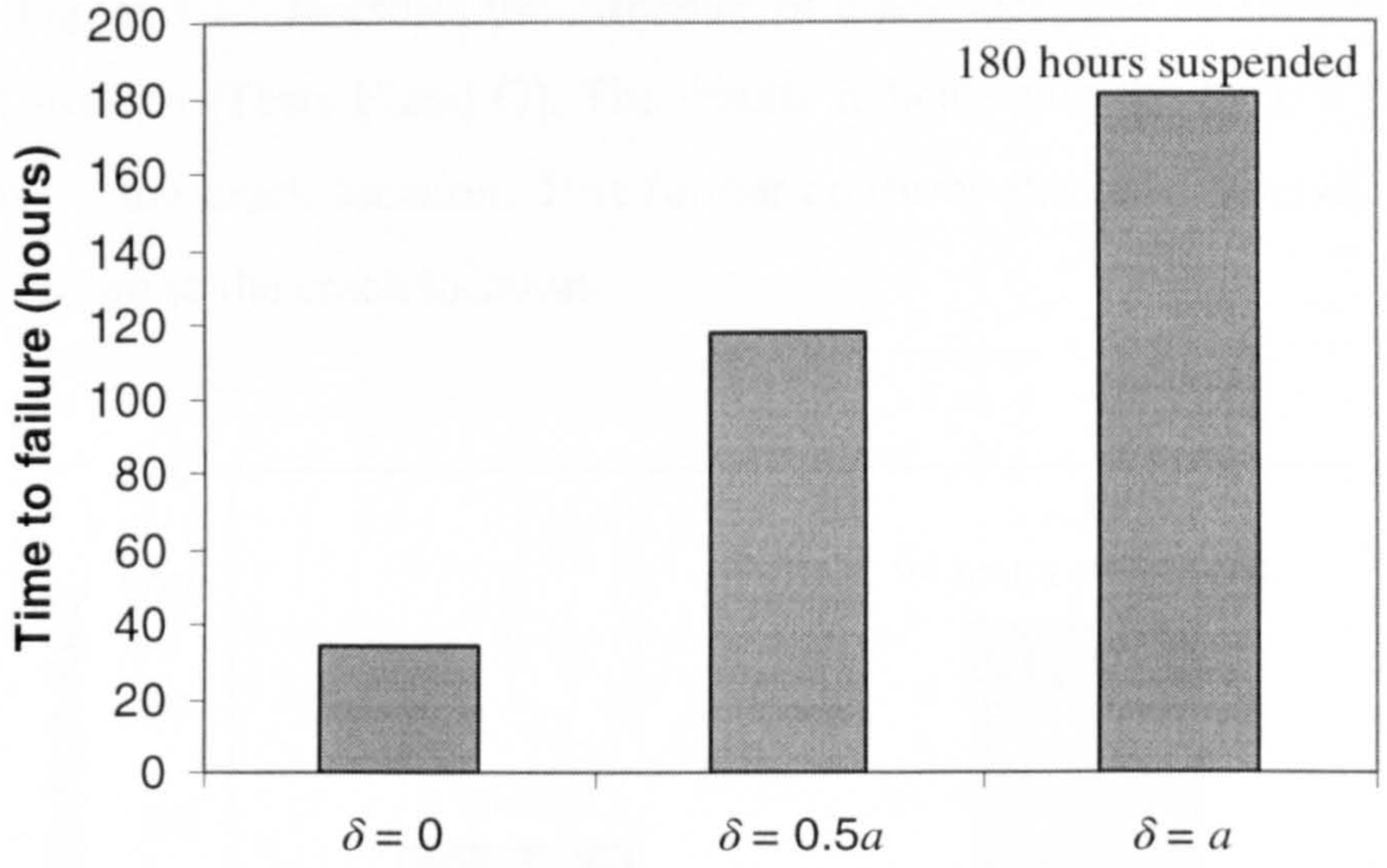

Figure 3.10 Influence of δ on fatigue life at the contact pressure of 5.6 GPa.

Figure 3.11 describes the influence of contact stresses on the fatigue life at $\beta = 90^{\circ}$ and $\delta = 0.5a$ (Tests B and E). The results show that increasing contact stress reduces fatigue life.

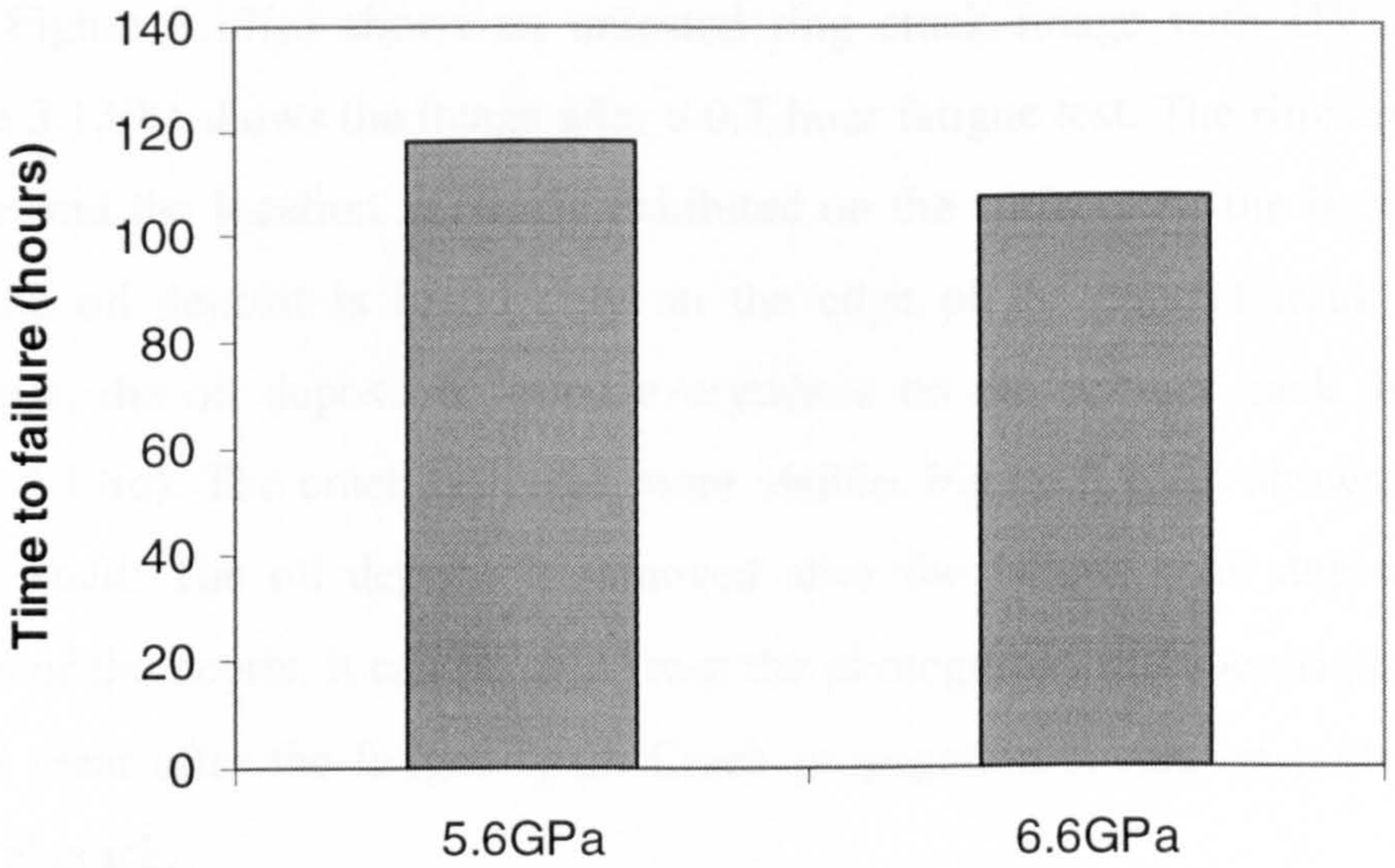

Figure 3.11 Influence of contact stresses on fatigue life at $\beta = 90^{o}$ and $\delta = 0.5a$.

Figure 3.12 describes the influence of crack locations on fatigue life at high contact stresses (Tests F and G). The results indicate that the fatigue failure mode depends on the crack location. This further confirms the sensitivity of the spalling fatigue failure to the crack location.

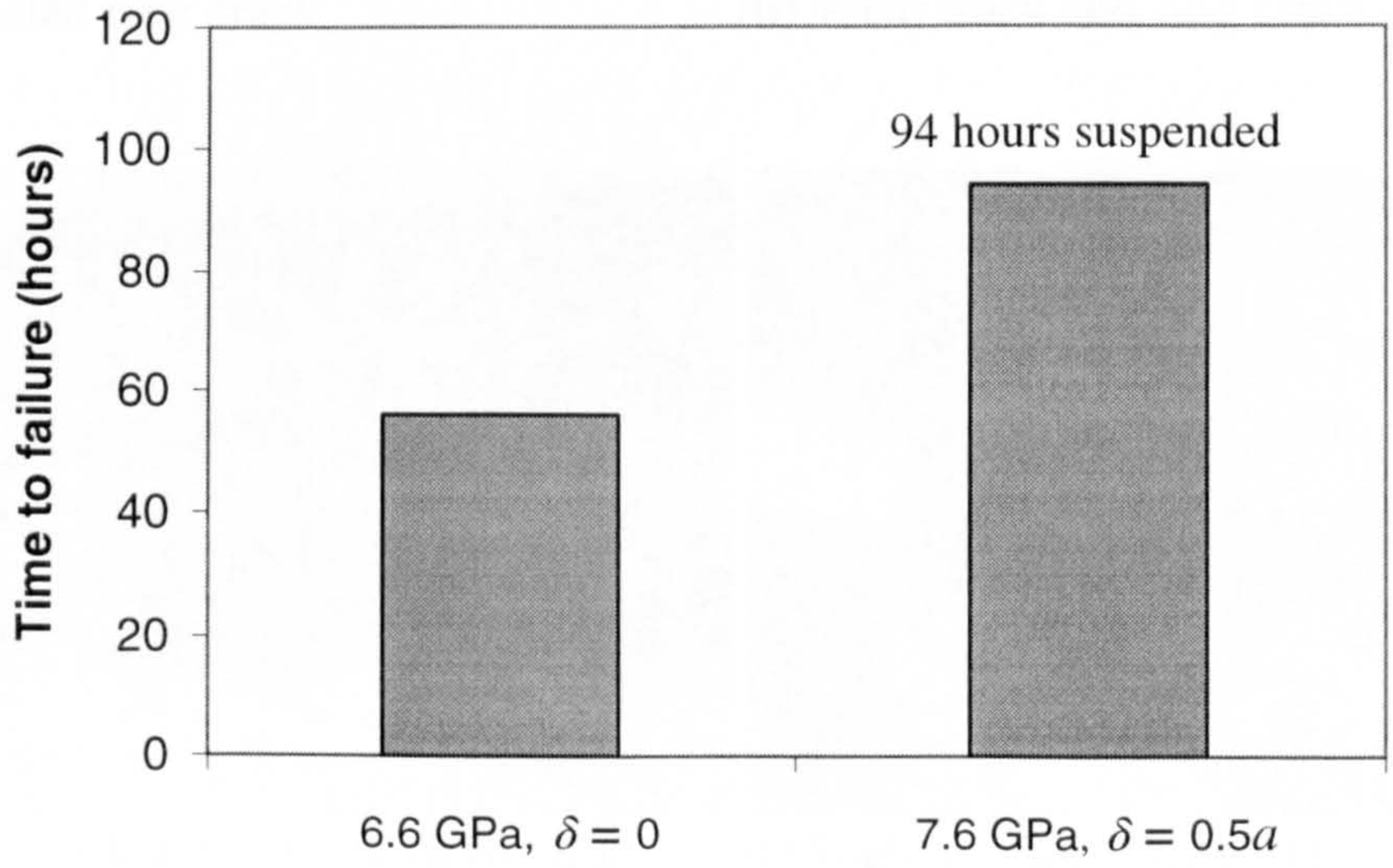

Figure 3.12 Influence of crack locations on RCF performance at $\beta = 45^{o}$.

Dynamic observations of fatigue damage from Test B are shown in figure 3.13. Figure 3.13(a) shows an untested ring crack image with UV light source. Figure 3.13(b) shows the image after a 0.7-hour fatigue test. The ring crack becomes visible and the location is clearly exhibited on the surface. At the beginning of the test, the oil deposit is found only on the edge of the contact track. As the test proceeds, the oil deposit is found everywhere on the contact track and shown in figure 3.13(c). The crack becomes more visible. Figure 3.13(d) shows an overview of the spall. The oil deposit is removed after the fatigue spall due to machining effects of the debris. It can be seen from the photographs that the original ring crack is still clear after the fatigue spall. Crack propagation occurs on both sides of the original crack.

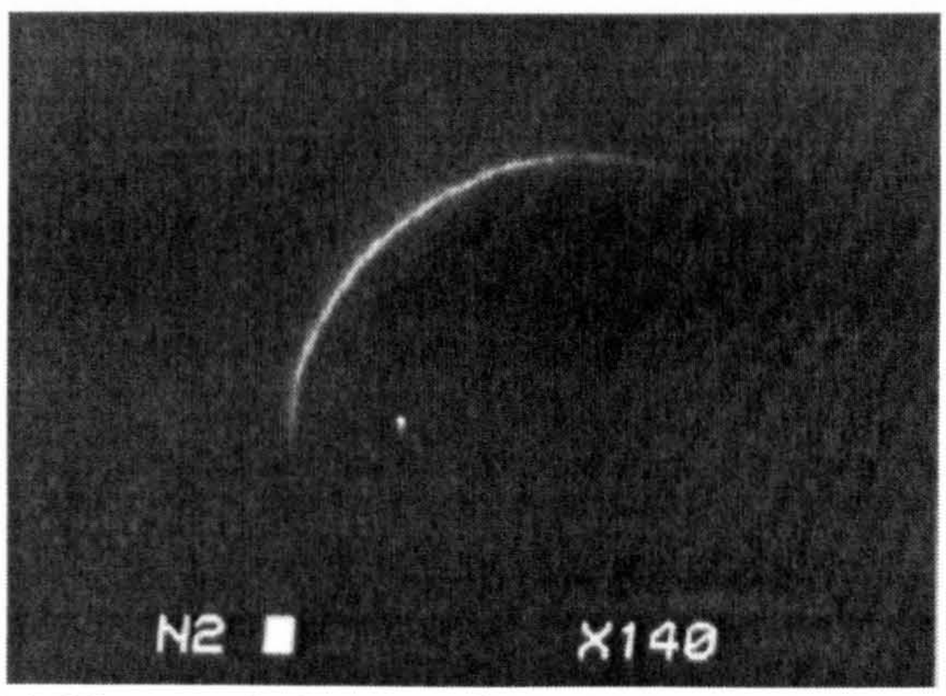

(a) Untested ring crack

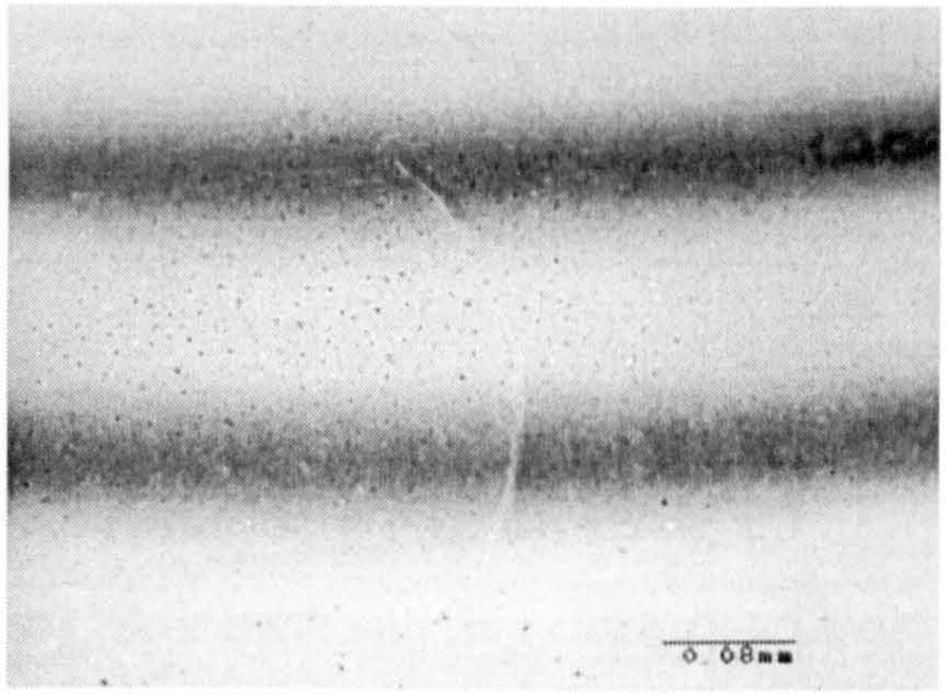

(b) Wear track and ring crack (0.7 hrs)

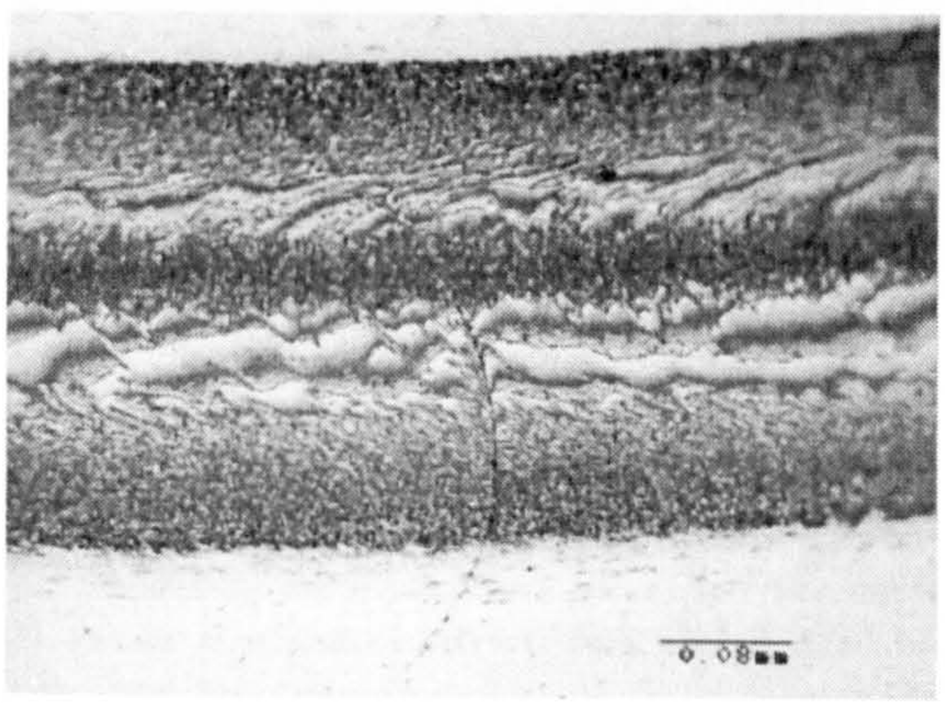

(c) Wear track and ring crack (47 hrs)

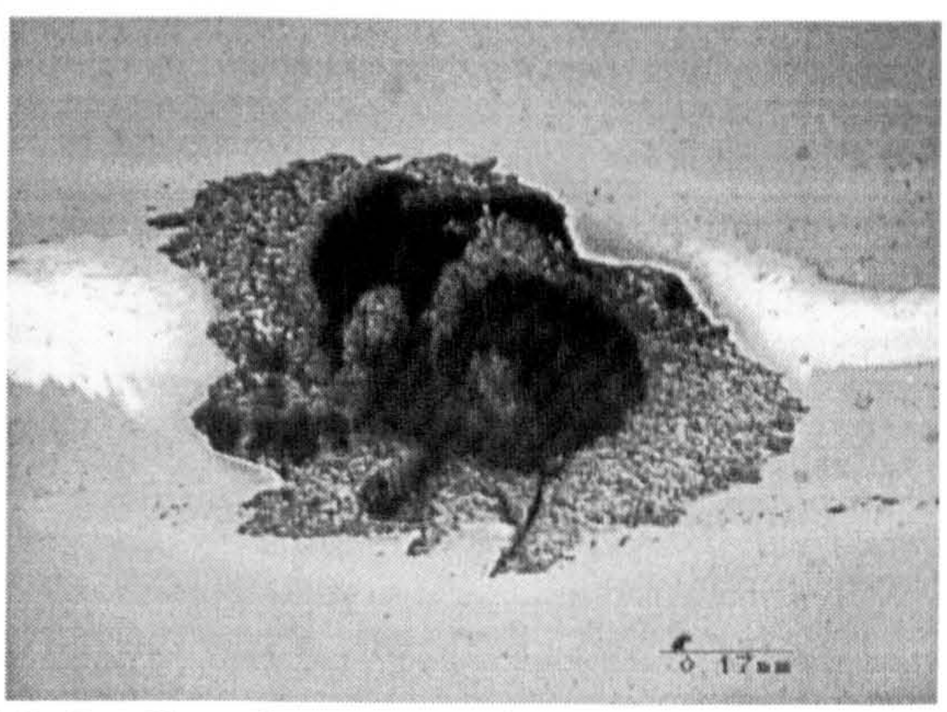

(d) Spall and wear track (117 hrs)

Figure 3.13 Surface observations of silicon nitride balls (Test B).

Figure 3.14 shows a series of observations from Test E. This test differs from Test B in that the load is different. The maximum contact pressure is increased from 5.6 GPa to 6.6 GPa, and the crack is kept in the same location. Figure 3.14 (a) shows the image after a 0.5 hour test. The oil deposit appears on the contact track. Unlike in Test B, the pattern of the contact path is changed after several hours of fatigue testing. Figure 3.14(b) shows the image after 22.5 hours of testing. As can be seen, the substances deposited become bright except the outer edge. This bright deposit material can be removed using polishing powder or diamond paste. Figure 3.14(c) shows an image after 93.5 hours of testing. After the spall the bright deposit disappears as shown in figure 3.14(d). The contact path is still in a good condition.

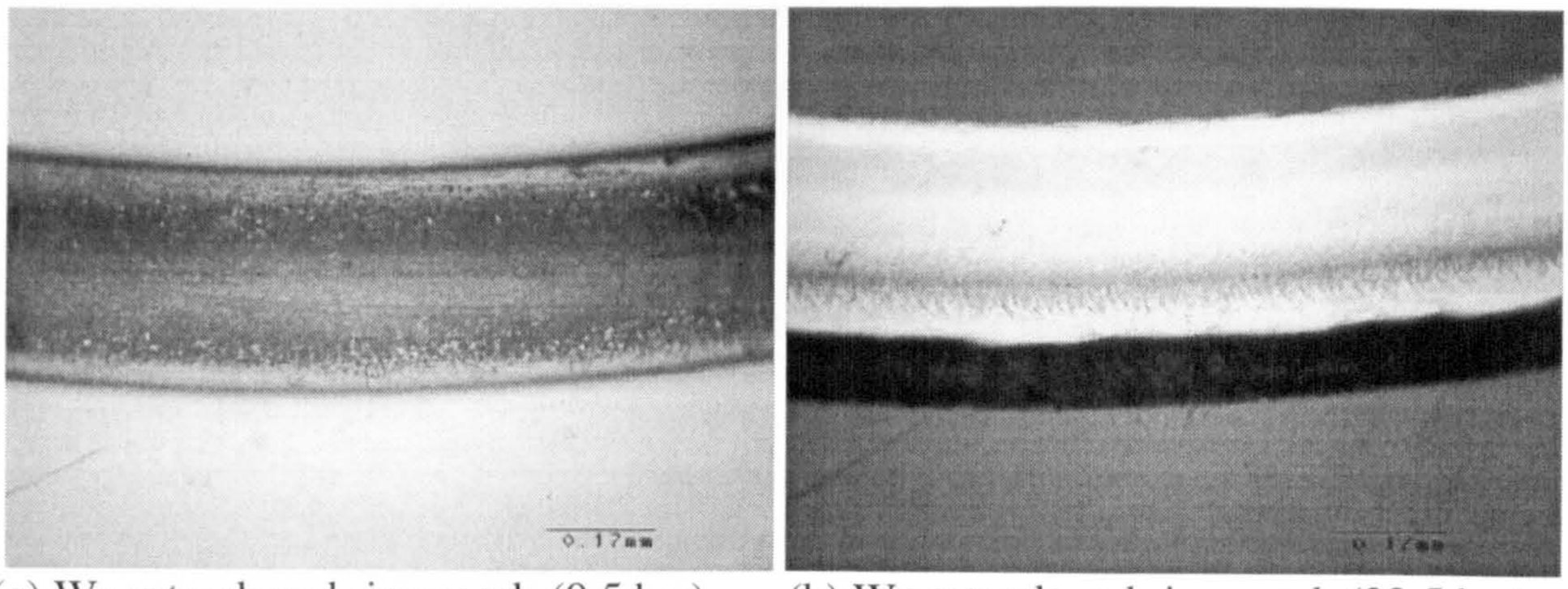

(a) Wear track and ring crack (0.5 hrs)

(b) Wear track and ring crack (22.5 hrs)

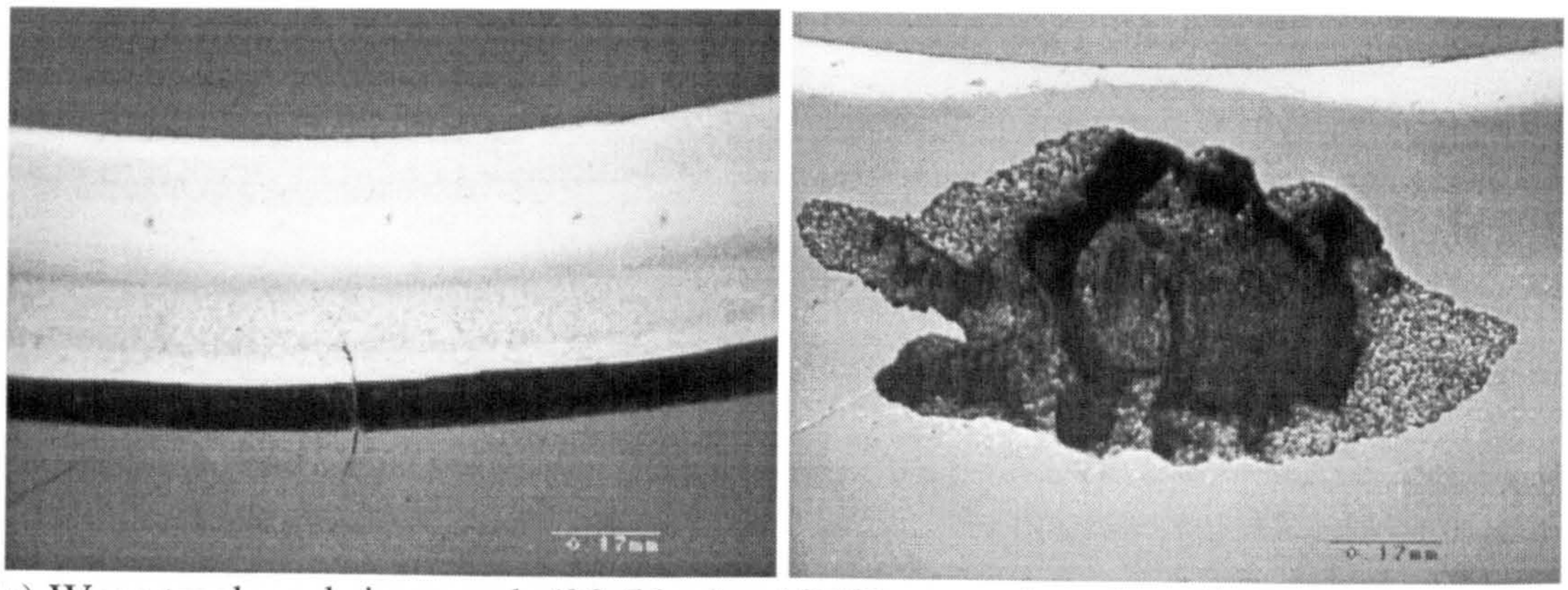

(c) Wear track and ring crack (93.5 hrs)

(d) Wear track and spall (107 hrs)

Figure 3.14 Surface observations of silicon nitride balls (Test E).

The surface damage process at high load (Test G) is shown in figure 3.15. Figure 3.15 (a) shows the contact path after 52 hours of testing. A bright substance covers the contact track. The crack is clearly shown on the contact path. The contact track is in a good condition. Figure 3.15(b) shows the image after 72 hours of testing. The bright material is being removed starting from the outer edge of the contact path. The pattern of the deposit material is different from that after 52 hours of testing. The wear occurs along the original ring crack. After 94 hours of testing, more bright material is removed from the edge of the contact track and the wear occurs on the contact track shown in figure 3.15(c). Figure 3.15(d) shows an optical micrograph after deposit substances removed.

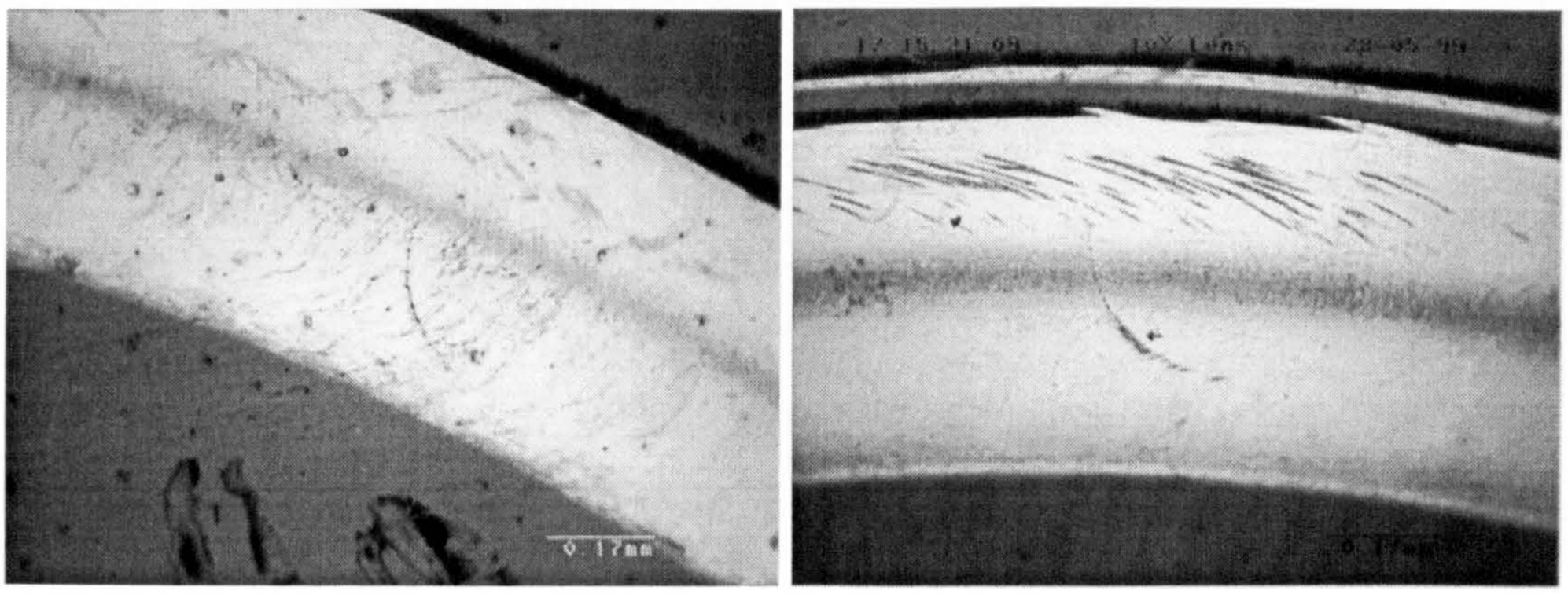

(a) Wear track and ring crack (52 hrs)

(b) Wear track and ring crack (72 hrs)

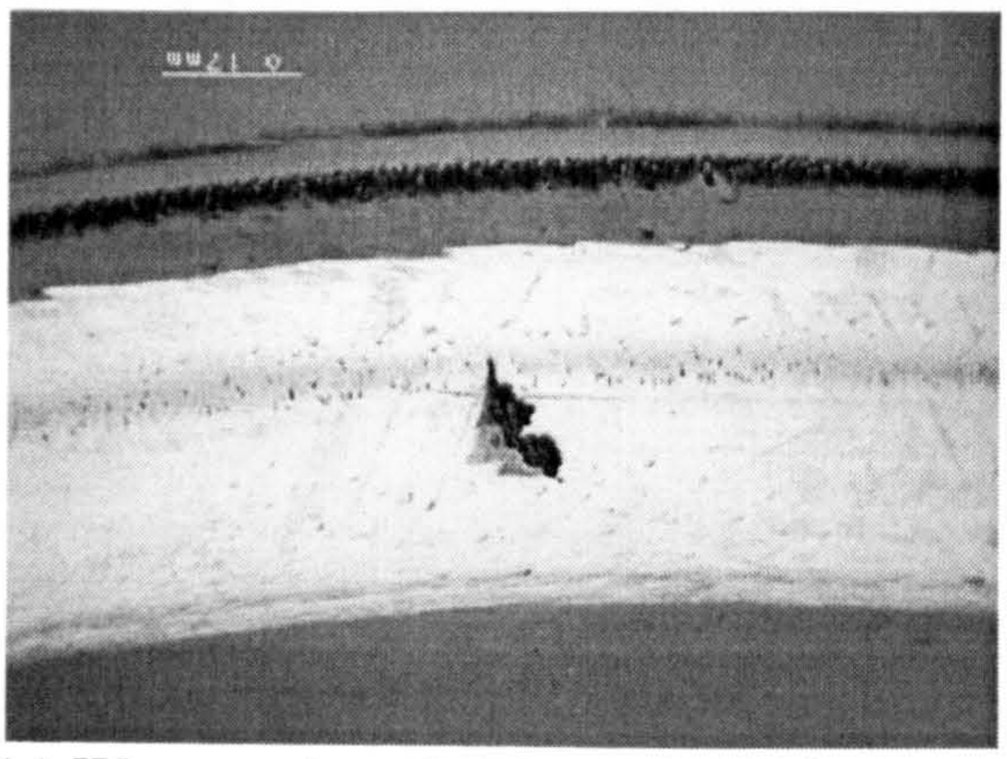

(c) Wear track and ring crack (94 hrs)

(d) After deposit removed (94 hrs)

Figure 3.15 Surface observations of silicon nitride balls (Test G).

Figure 3.16 illustrates surface images from Test H. The cylinder oil is adopted as a lubricant. The composition of the oil has been described in Chapter 2, Section 2.1. The fatigue failure modes are shown to be the same as with the other lubrication oils apart from a different fatigue life performance (2.8 hours in this case). Figure 3.16(a) shows an overview of the fatigue spall and the SEM micrograph is shown in figure 3.16(b). The delaminated failure characteristic is found and shown in figure 3.16(c). Figure 3.16(d) illustrates a fractography of fatigue crack propagation initiated from the original ring cracks. The circle undulations are clearly displayed on the micrographs.

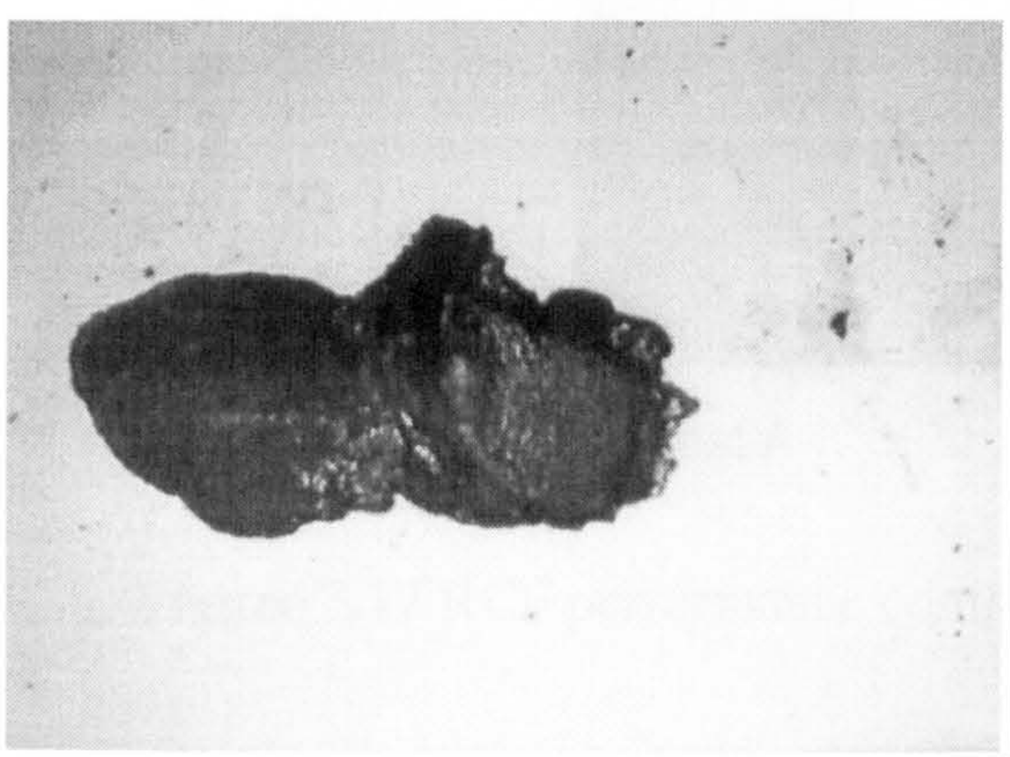

(a) Overview of a spall

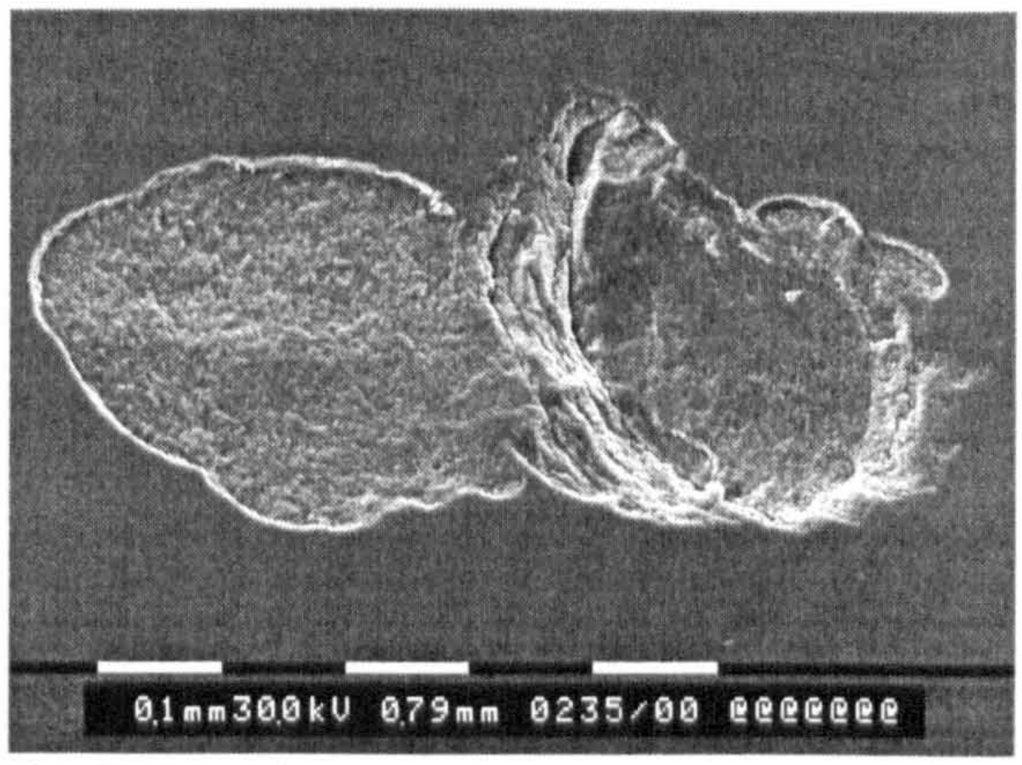

(b) SEM micrograph

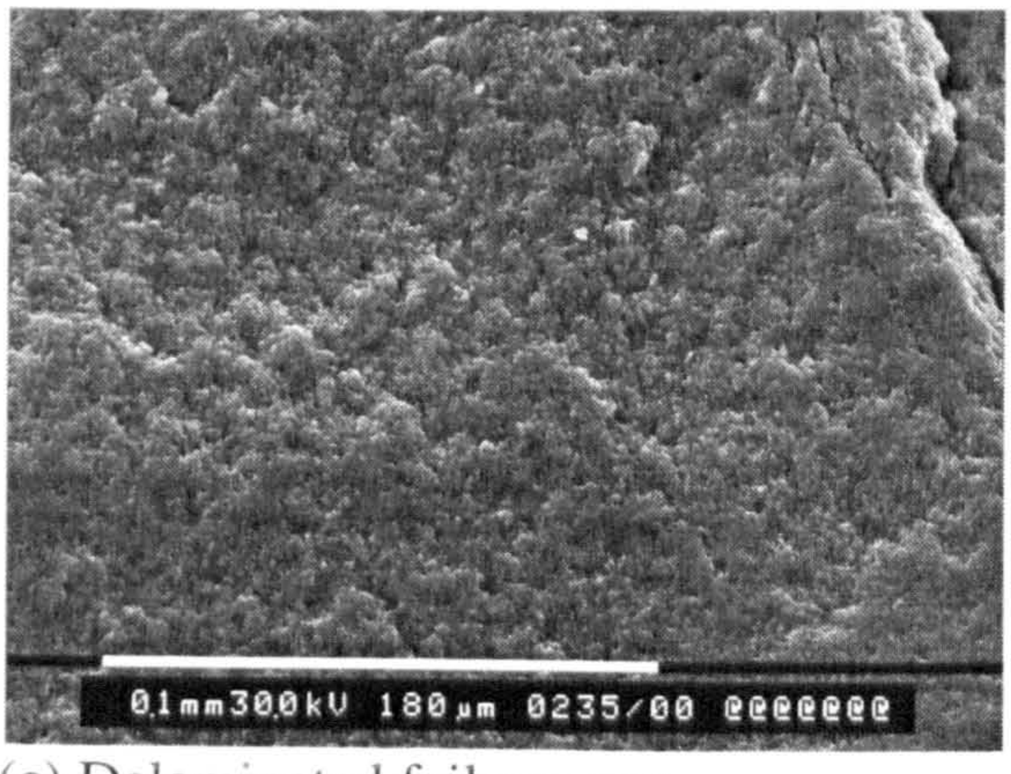

(c) Delaminated failure area

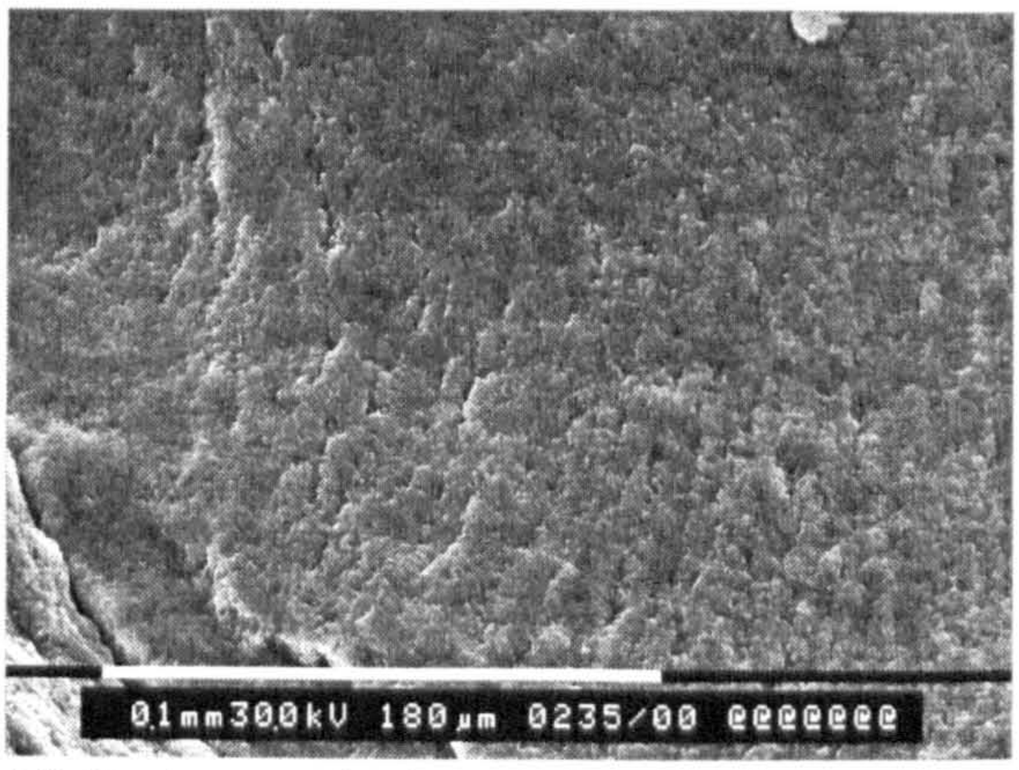

(d) Fatigue striations

Figure 3.16 Surface observations of silicon nitride ball (Test H).

Tests A and D are designed to study the influence of surface traction direction (rolling direction) on fatigue failure modes. Test conditions are described in table 3.2 and the result is shown in figure 3.17. The results indicate that the spalling fatigue failure will occur independently of the rolling directions.

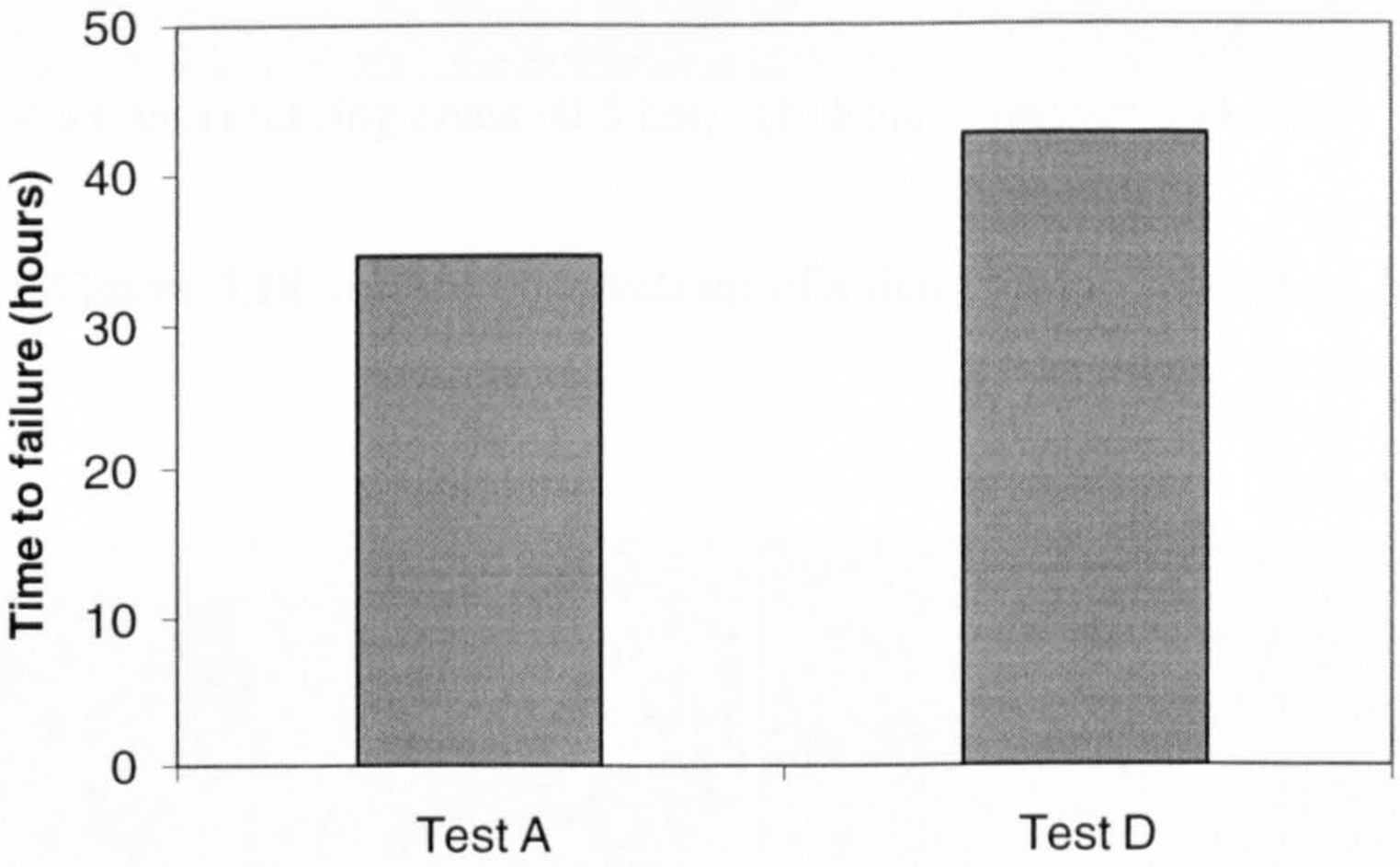

Figure 3.17 RCF performance comparison of different traction directions

Fracture surface shows that the failure mode is fatigue spall. The spall size is similar and the shape is elliptical. Figure 3.18 shows the surface damage processes from Test A. Figure 3.18(a) shows the ring crack and contact path after 0.5 hours of testing. The crack location is clear and lubricant deposit tends initially towards the edge of the contact path. Figure 3.18(b) is the spall image after 34.6 hours of testing. The lubricant deposit is removed after spall.

The surface observations from the reversed rolling direction (Test D) are shown in figure 3.19. As in Test A, the lubricant deposit tends initially towards the edge of the contact path and gradually covers the whole contact path. The surface after 28.5 hours of testing is shown in figure 3.19(a). Figure 3.19(b) shows a spall image after 42.7 hours of testing.

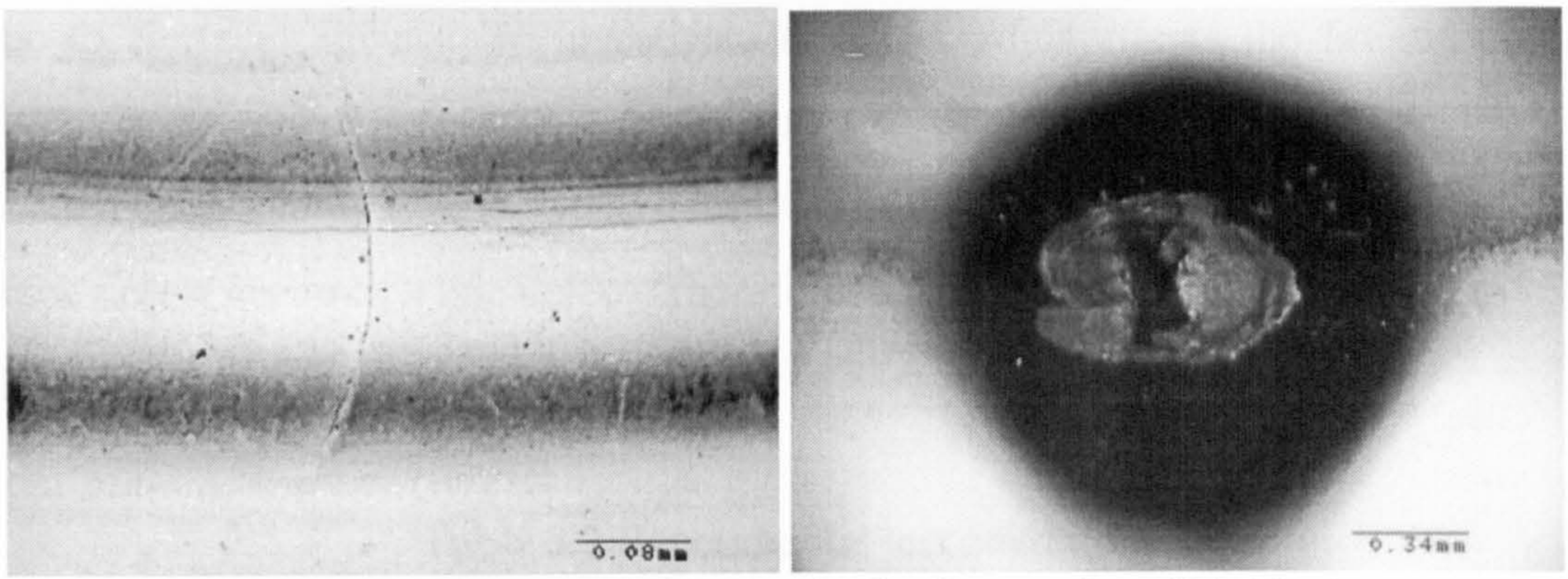

(a) Contact path and ring crack (0.5 hrs) (b) Spall overview (34.6 hrs)

Figure 3.18 Surface observations of silicon nitride balls (Test A).

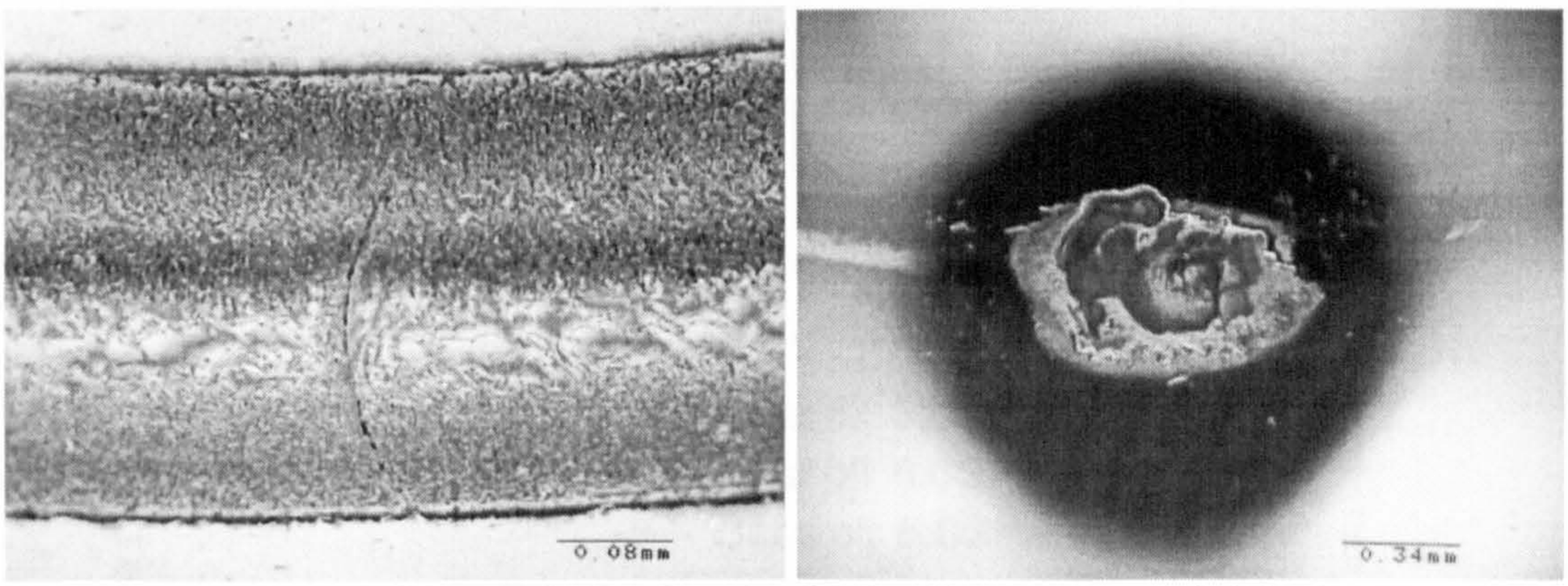

(a) Contact path and ring crack (28.5 hrs) (b) Spall overview (42.7 hrs)

Figure 3.19 Surface observations of silicon nitride balls (Test D).

3.2 RCF PERFORMANCE WITH SURFACE LINE DEFECTS

Results from the previous sections describe the rolling contact fatigue performance with surface ring crack defects. The fatigue test is performed on ceramic balls with surface ring crack defects. The results describe the surface ring crack behaviour in the different crack locations. The radius of ring cracks, commonly found on the commercial ceramic ball surface, is in a range of 0.2 to 0.25 mm. It is difficult to find surface ring cracks with the radius of more than 0.3 mm

due to Hertzian contact. To investigate how the radius affects the fatigue failure modes a line defect (pressing defect) is used to examine the radius effect. From a mathematical point of view, when the radius of a ring crack approaches ∞, the ring crack defect becomes a line defect. Therefore, a line defect can be considered to be a special type of ring crack.

Table 3.3 Experimental test conditions

Test No.	Contact Pressure (GPa)	Crack Locations (for line defects)	lubricant
I	5.58	$\beta = 90^{o}$	Gear oil
II	6.63	$\beta = 90^{o}$	Gear oil
III	6.63	$\beta = 90^{o}$	Base oil

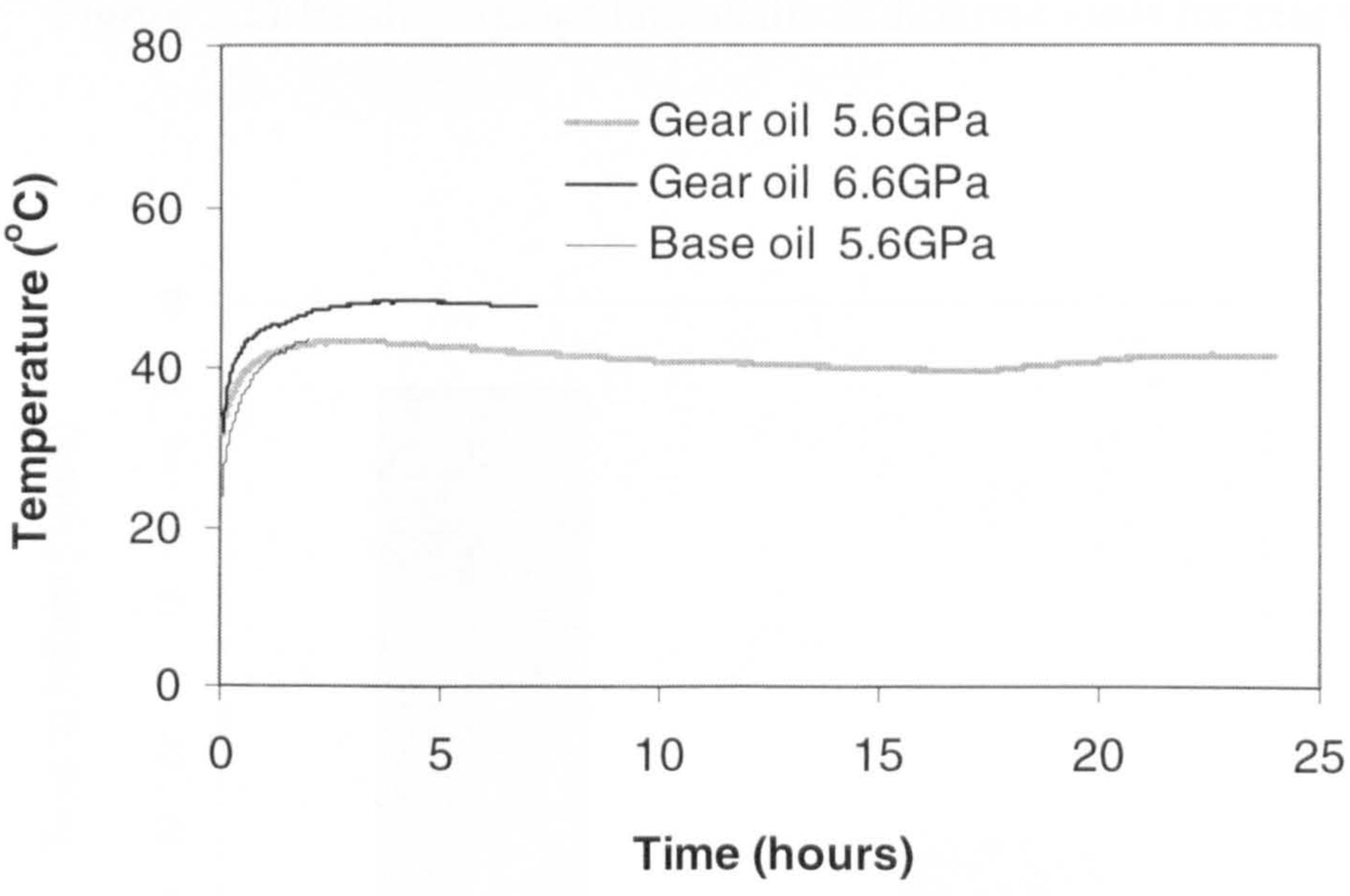

Figure 3.20 Oil temperature variation during testing.

Test conditions are described in table 3.3. Two kinds of lubricant oil are adopted to examine how surface defects affect rolling contact fatigue failure modes. Temperature variation during testing is shown in figure 3.20.

Test results are described in figures 3.21 and 3.22. It is clear that the fatigue life decreases with the increase of the maximum contact pressure (see figure 3.21). Rolling contact fatigue performance is considerably influenced by lubricant properties and is shown in figure 3.22.

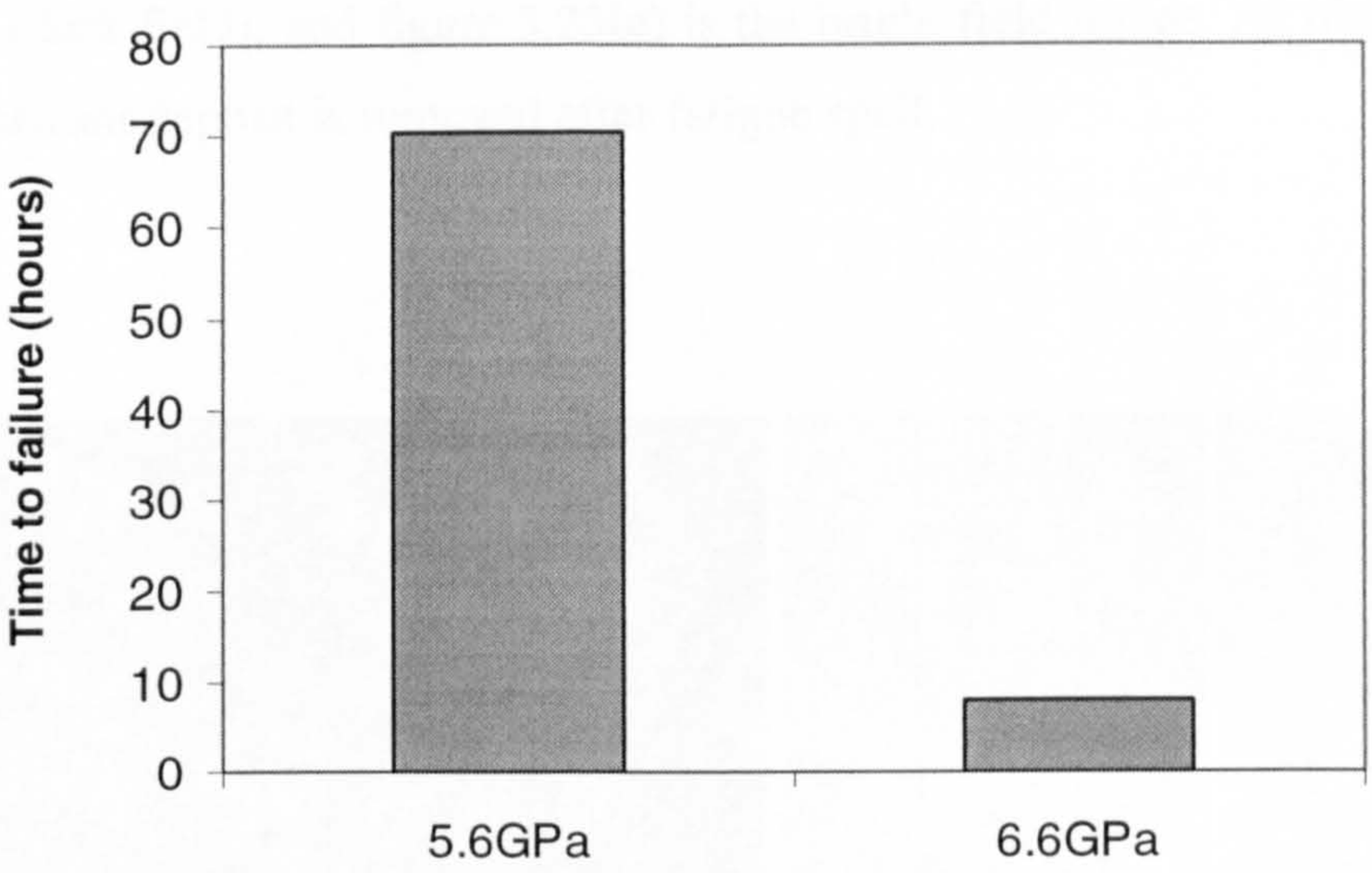

Figure 3.21 Rolling contact fatigue life at different loads for gear oil

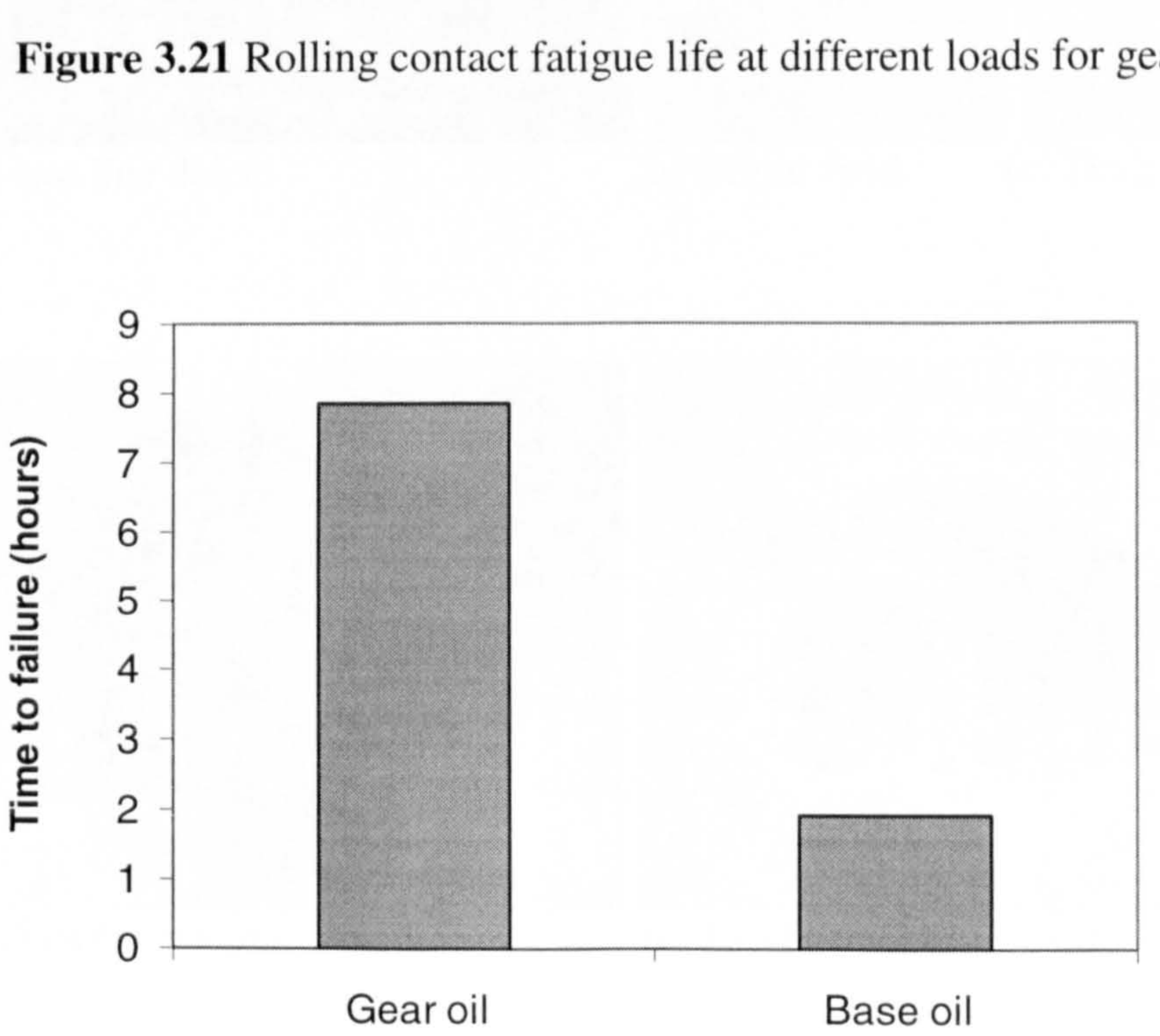

Figure 3.22 Rolling contact fatigue life at the same load for different oils

Dynamic observations of surface damage processes are described in figures 3.23 to 3.25. Surface observations from Test I are shown in figure 3.23. A line defect is shown in figure 3.23(a). Figures 3.23(b) and 3.23(c) are dark and bright field images respectively. It is obvious that the ball surface is perfect and the line defect can not be seen without an UV light source. Figure 3.23(d) shows an optical spall image (dark field), and figure 3.23(e) is the bright field image. As discussed above, the lubricant deposit is removed after fatigue spall.

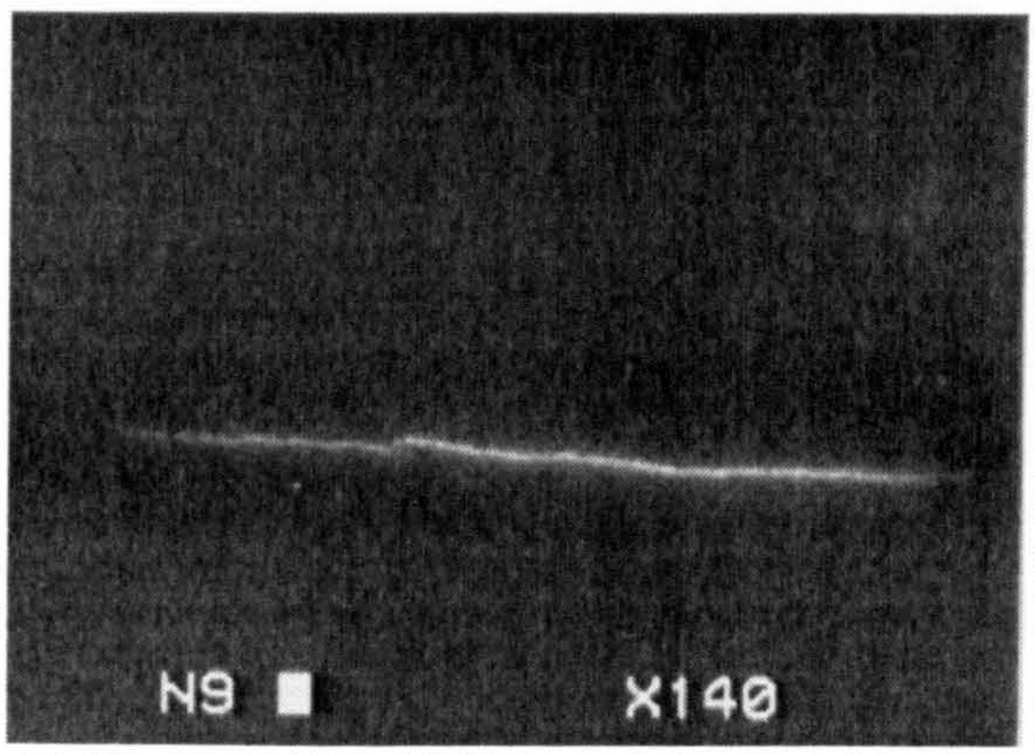

(a) Pre-test line defect

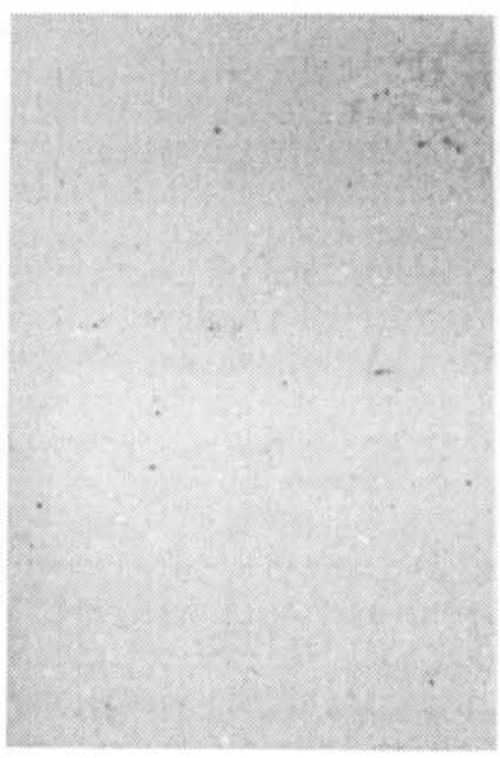

(b) Bright field

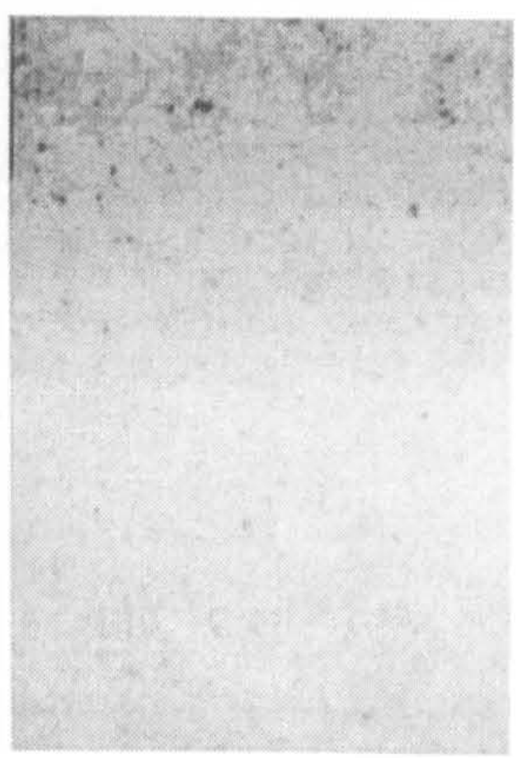

(c) Dark field

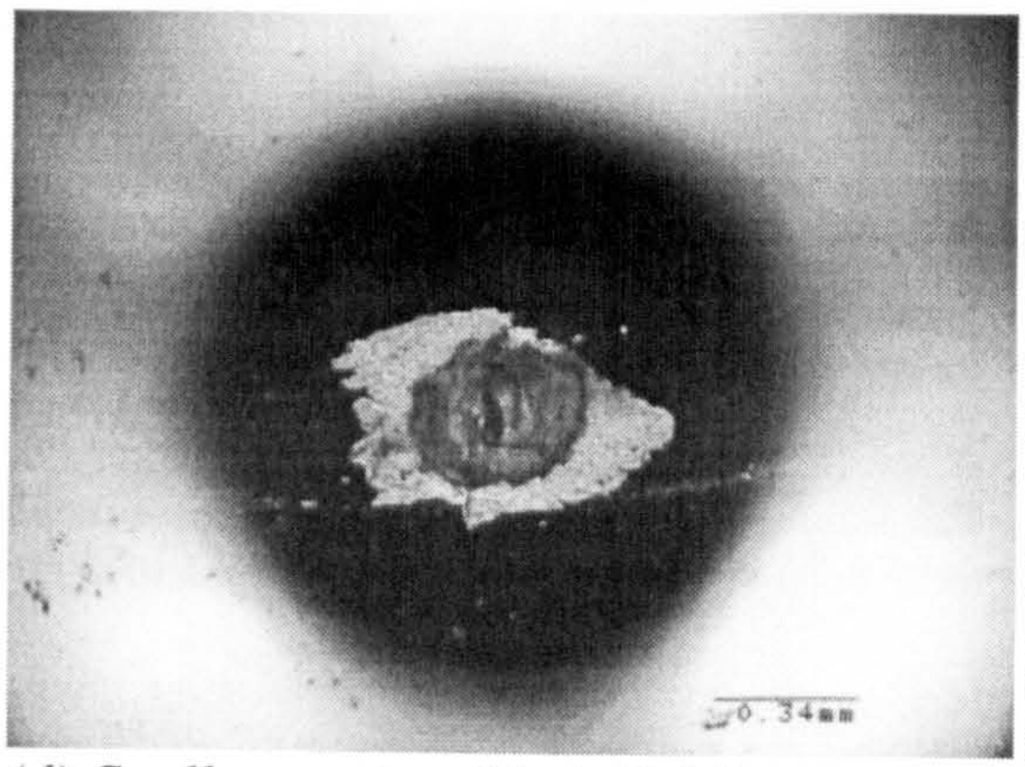

(d) Spall overview (dark field)

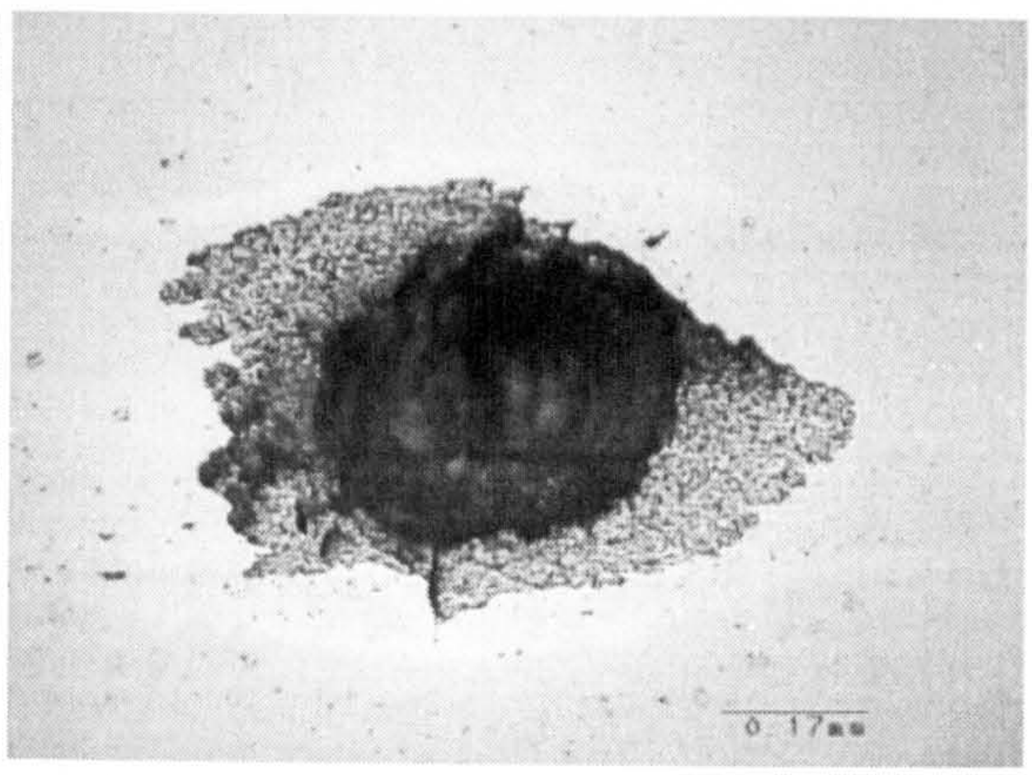

(e) Bright field (70.3 hrs)

Figure 3.23 Surface observations of silicon nitride balls (Test I).

Surface observations from Test II are shown in figure 3.24. Figure 3.24(a) shows an untested line defect under UV light illumination. The image in the same position is shown in figures 3.24 (b) and (c). The defect can not be seen under a normal light source. Figure 3.24(d) is an overview after 1.4 hours of testing. The dark field image of fatigue spall is shown in figure 3.24(e).

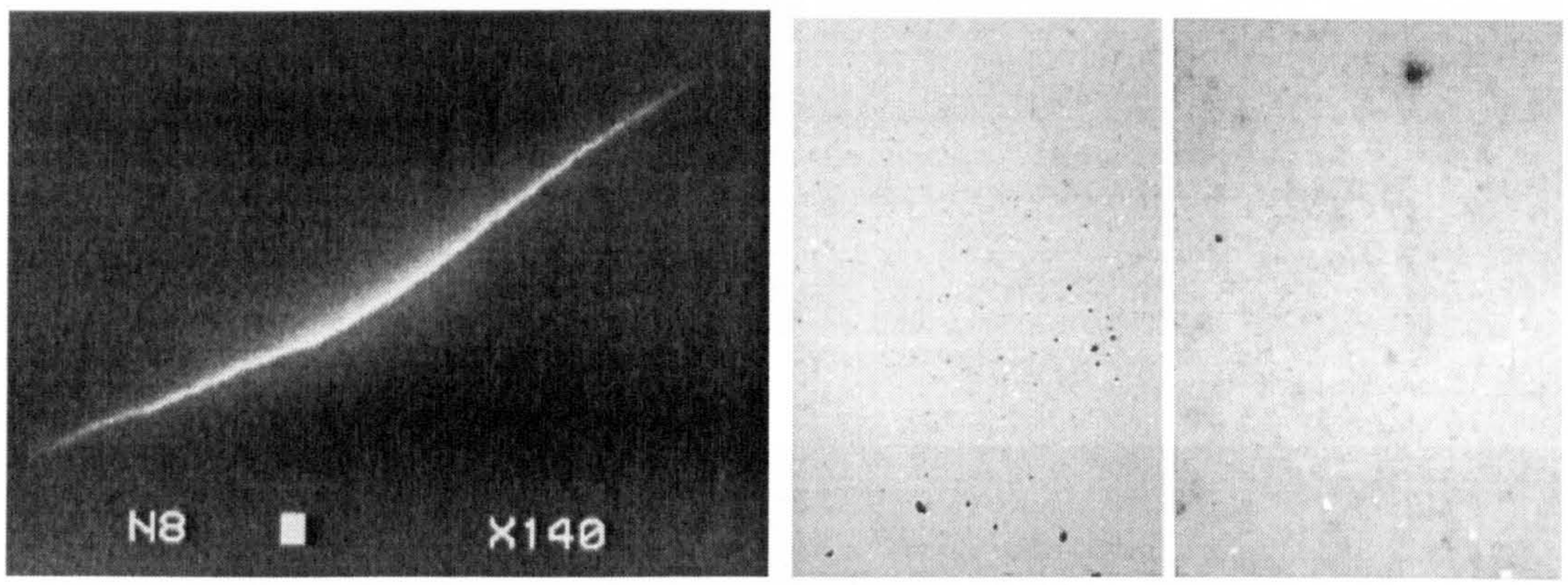

(a) Pre-test line defect (b) Bright field (c) Dark field

(d) Contact path and line defect (1.4 hrs) (e) Fatigue spall overview (7.8 hrs)

Figure 3.24 Surface observations of silicon nitride balls (Test II).

Figure 3.25 shows surface damage micrographs from Test III. The optical micrograph of the fatigue spall is shown in figure 3.25(a) and the SEM micrograph in figure 3.25(b). The upper edge of the spall is shown in figure 3.25(c), and lower

edge is shown in figure 3.25(d). The central part is shown in figure 3.25(e). High magnification is shown in figure 3.25(f). These surface images clearly describe how a spall is generated in rolling contact. Aspects of the mechanics of the fatigue failure processes will be discussed in Chapter 5.

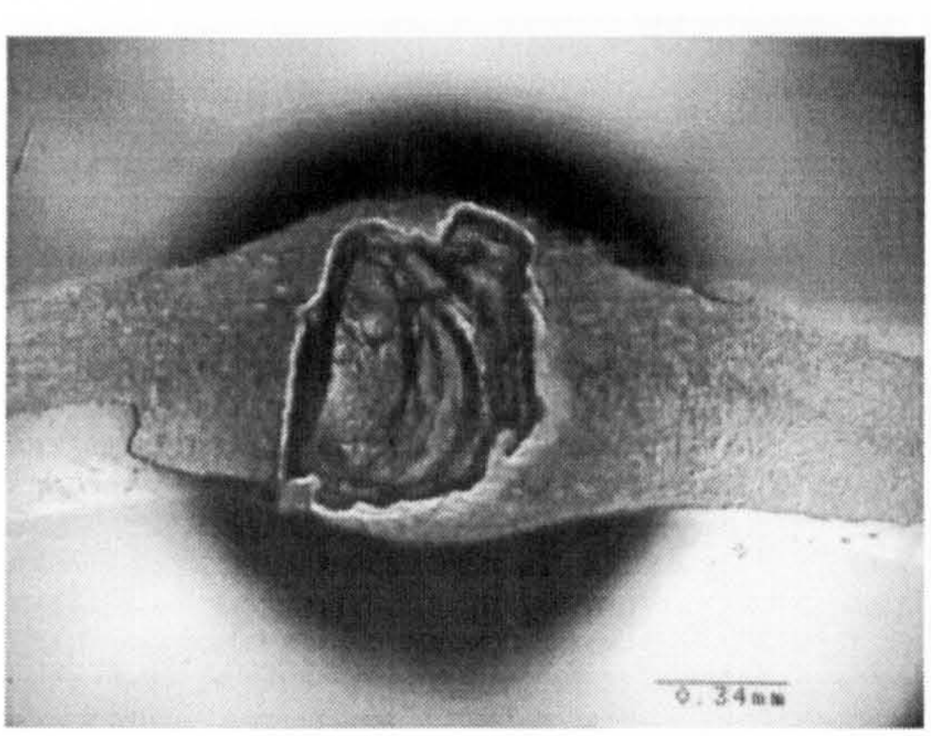

(a) Spall optical image

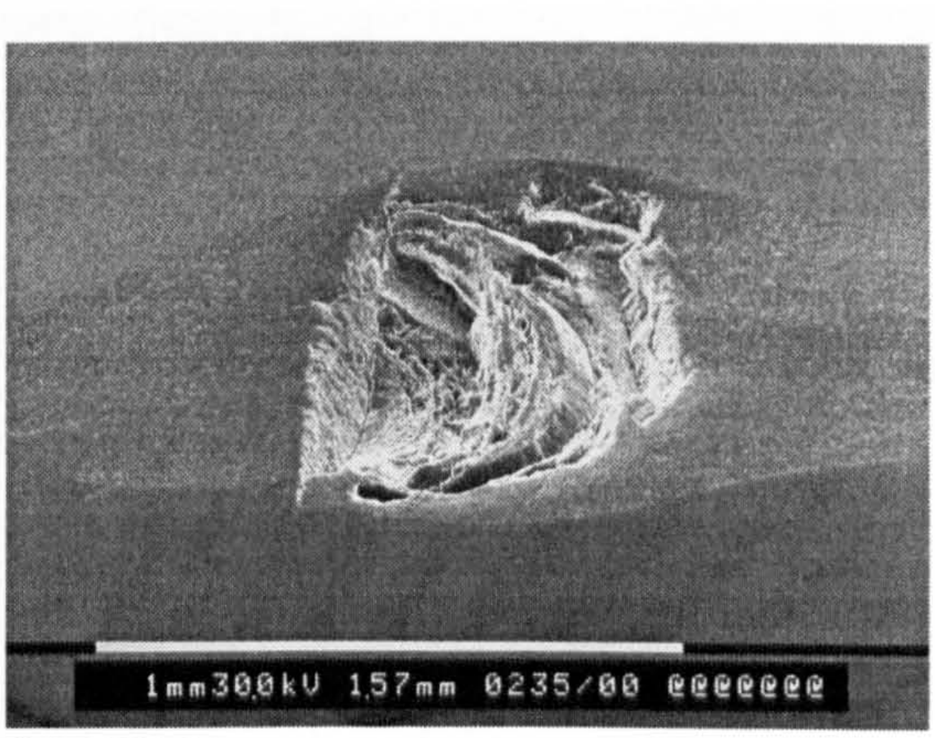

(b) SEM image

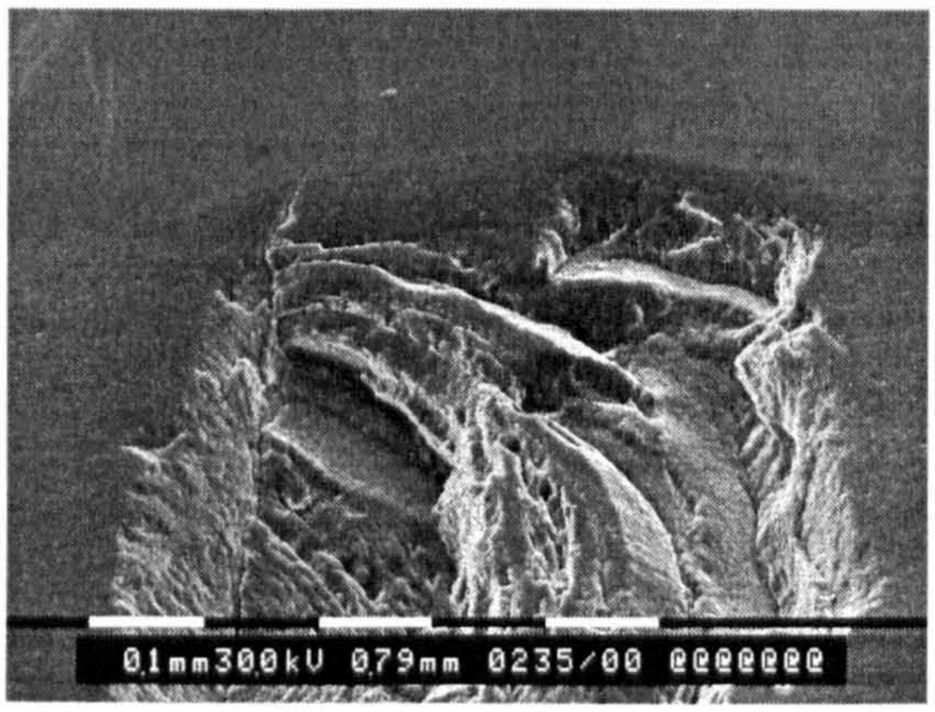

(c) Upper edge

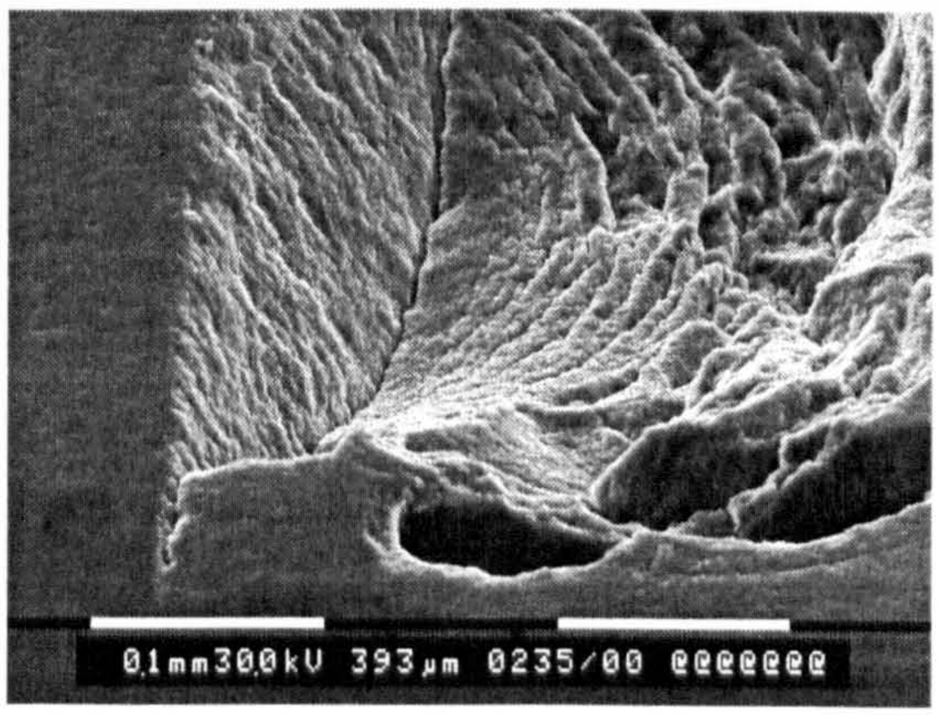

(d) Lower edge

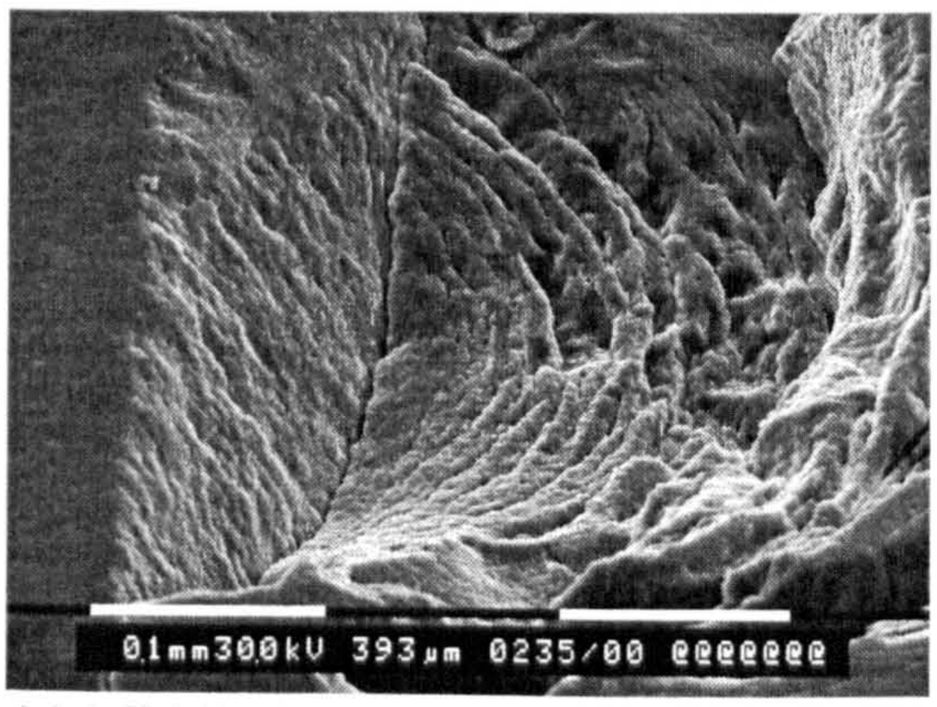

(e) Middle part.

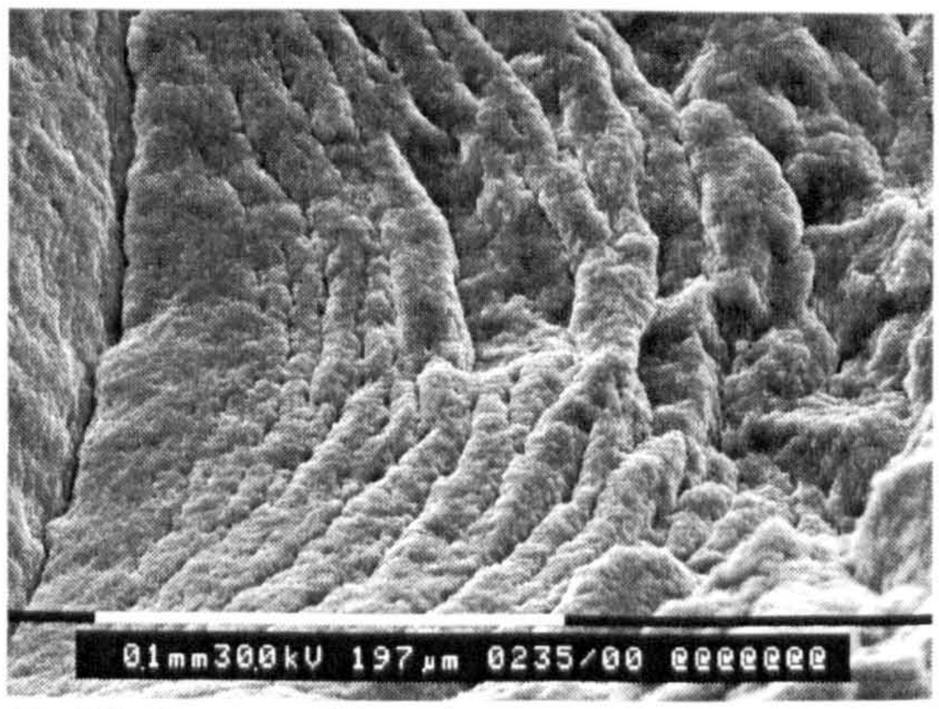

(f) High magnification.

Figure 3.25 Surface observations of silicon nitride balls (Test III).

3.3 SURFACE OBSERVATIONS OF CRACK FAILURE PROCESSES

3.3.1 Low viscosity oil lubrication

In previous sections, some micrographs have been shown to demonstrate fatigue spall and crack positions. Detailed investigations of failure processes of surface ring cracks are described in this section.

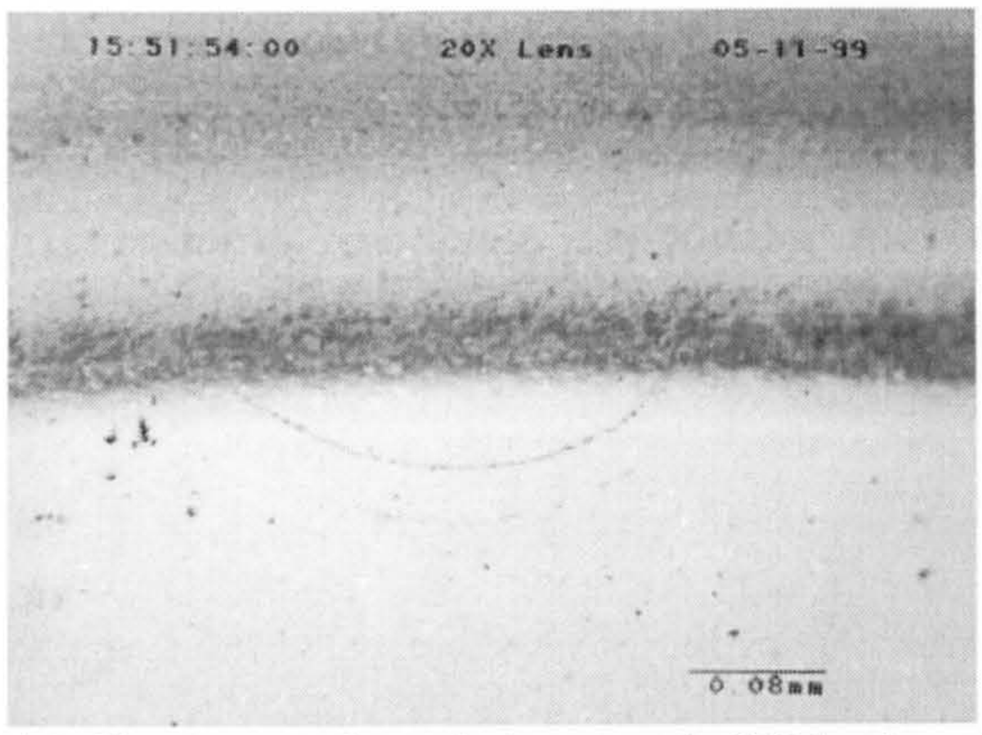

(a) Contact path and ring crack (50 hrs)

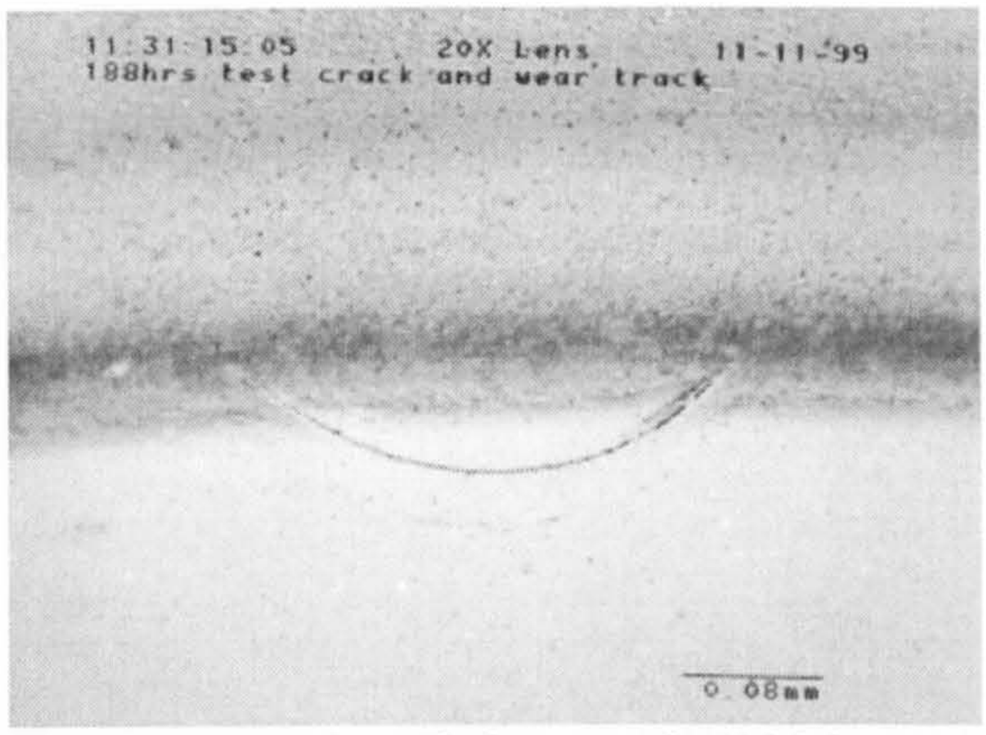

(b) Contact path and ring crack (180 hrs)

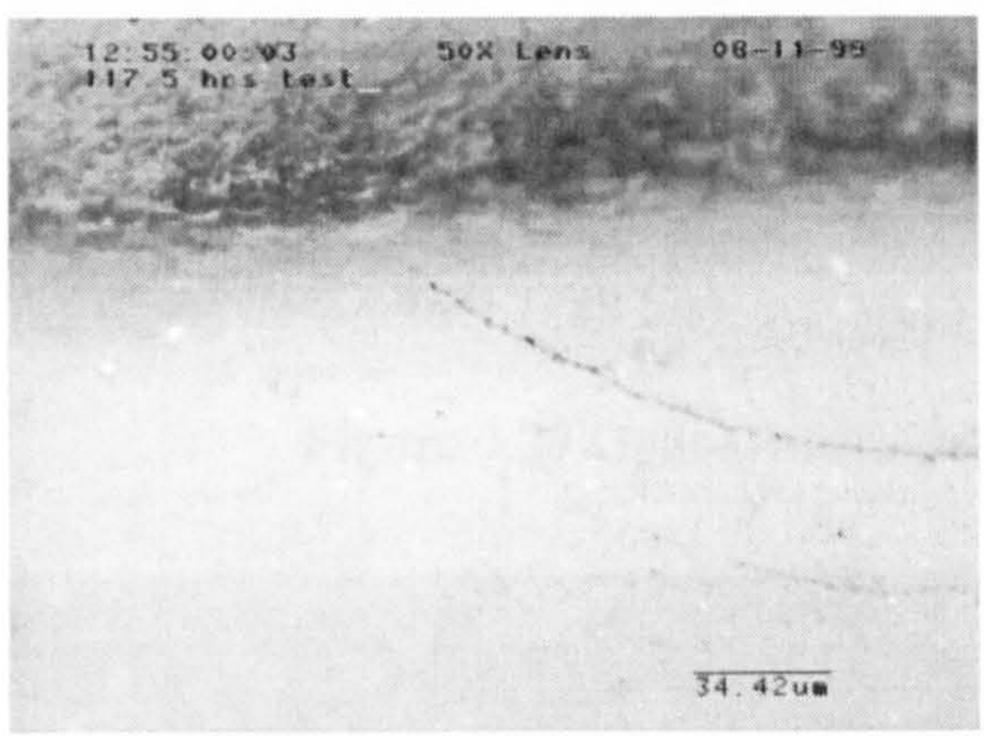

(c) Left part detailed view (117 hrs)

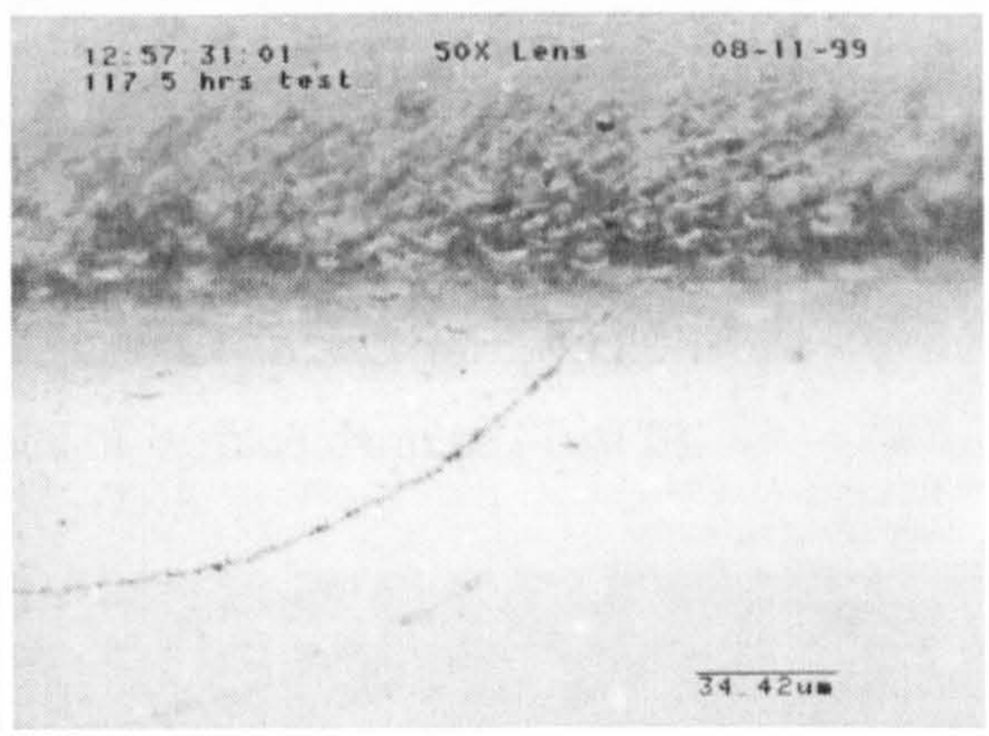

(d) Right part detailed view (117 hrs)

Figure 3.26 Optical micrographs of surface damage (Test 1).

A dynamic observation of surface damage is carried out for Test 1. Figure 3.26 shows micrographs of surface damage. The crack can not be seen without UV light. During the fatigue test, however, surface ring cracks become visible under white light illumination. This is due to the loss of materials caused by crack face friction. Figure 3.26(a) shows a surface after 50 hours of testing. The longer the test runs the more obvious is the crack. Figure 3.26(b) is the surface after 180 hours of testing. Comparison of figures 3.26(a) and 3.26(b) reveals that the crack does not propagate along the ring crack circle. Detailed surface images after 117 hours of

testing are shown in figures 3.26(c) and 3.26(d). Microcracks are found near the edge of the contact track. These micro-cracks are distributed in a regular pattern.

The results of surface examinations from Test 3 are shown in figure 3.27. The observation of the contact path, figure 3.27(a), shows that the ring crack is not easy to see under a white light source. In contrast, the crack can be detected easily under the UV light illumination, figure 3.27(b). No evidence of crack growth is found along the original ring circle on the surface. The observations from this test provide experimental evidence supporting the mode I stress intensity dominating crack propagation.

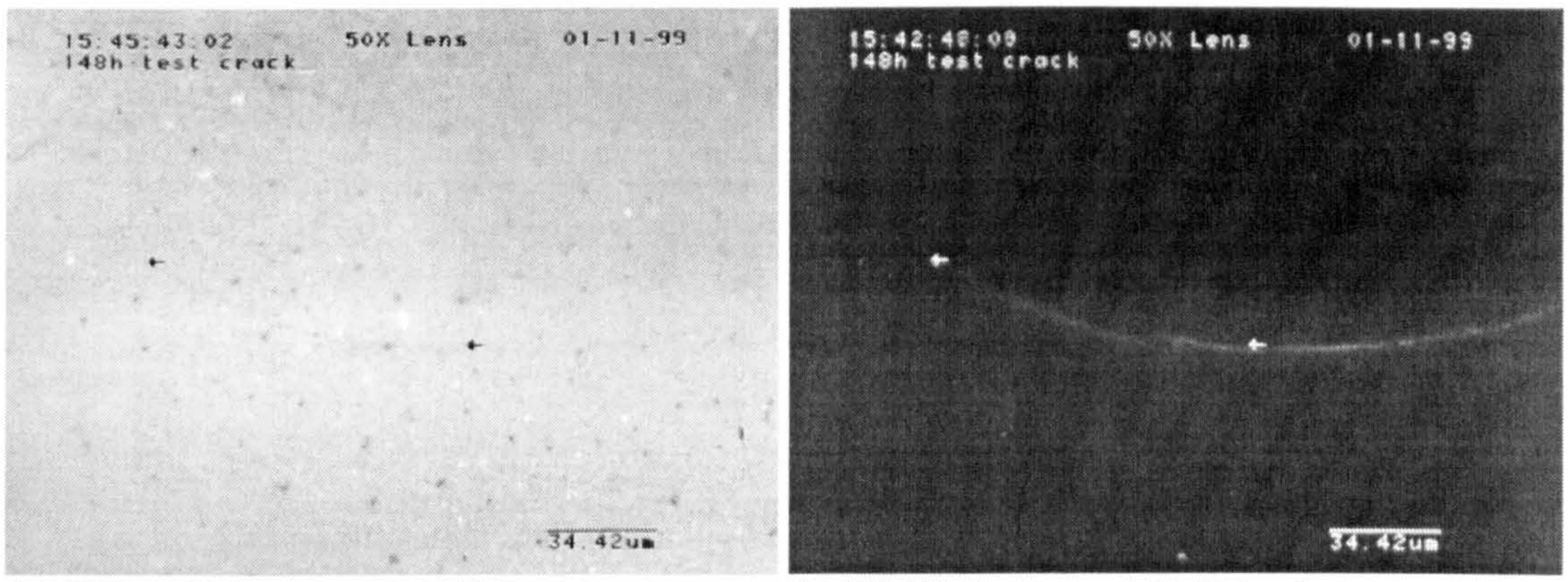

(a) White light source (148 hrs) (b) UV light source (148 hrs)

Figure 3.27 Optical micrographs of surface damage (Test 3).

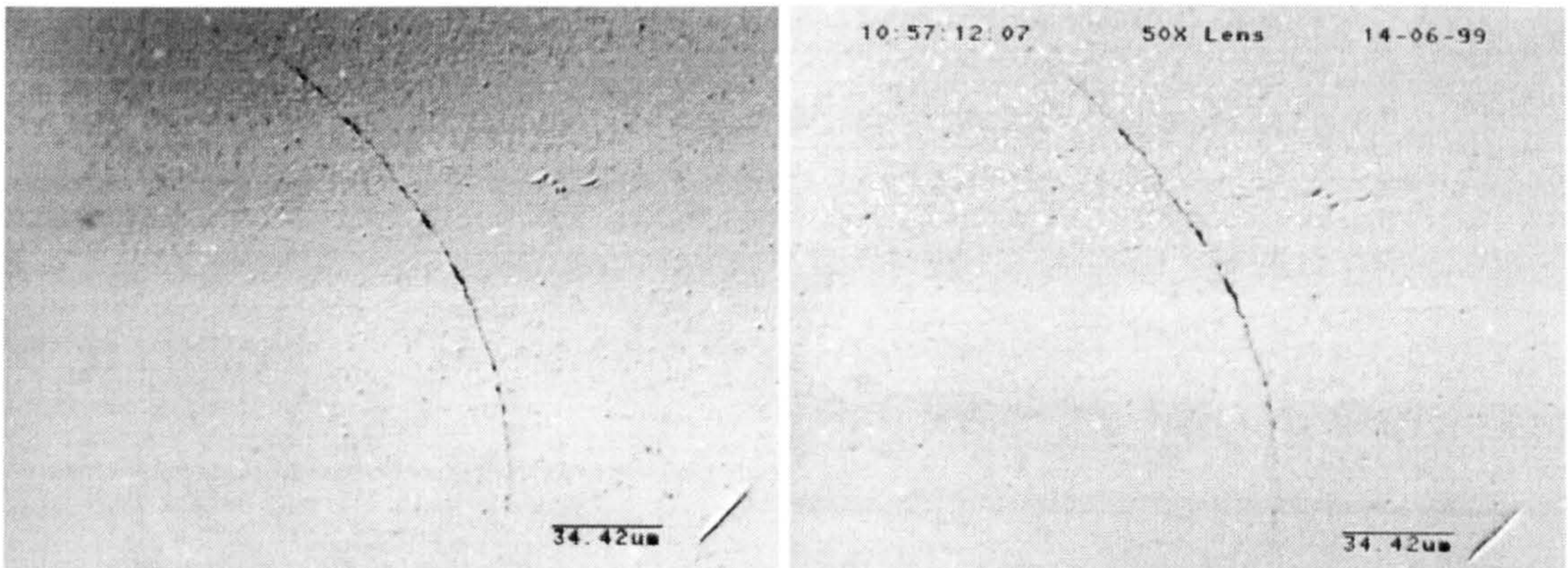

(a) Contact path and ring crack (102 hrs) (b) Contact path and ring crack (180 hrs)

Figure 3.28 Normaski micrographs of surface damage (Test 7).

Results from Test 7 are shown in figure 3.28. Figure 3.28(a) shows the ring crack after 102 hours of testing and figure 3.28(b) after 180 hours of testing. Comparison reveals that there is no significant change in the ring crack and contact

path. The crack still stays at the original crack length. The ceramic ball surface is still in a good condition even though it has been subjected to 180 hours of testing (121 million stress cycles).

The observations from Test 9 provide evidence supporting the assumption of crack gap enlargement. The results are shown in figure 3.29. As discussed above, the ring cracks are not visible using a normal light source but become visible as the tests proceed. Figure 3.29(a) is a ring crack after 8 hours of fatigue testing and figure 3.29(b) is the same ring crack after 17 hours of fatigue testing. No evidence of crack growth is found along the original ring circle on the surface. The observations reveal that the crack gap is proportional to the test time and it is possible to reach a value of 0.5 μm.

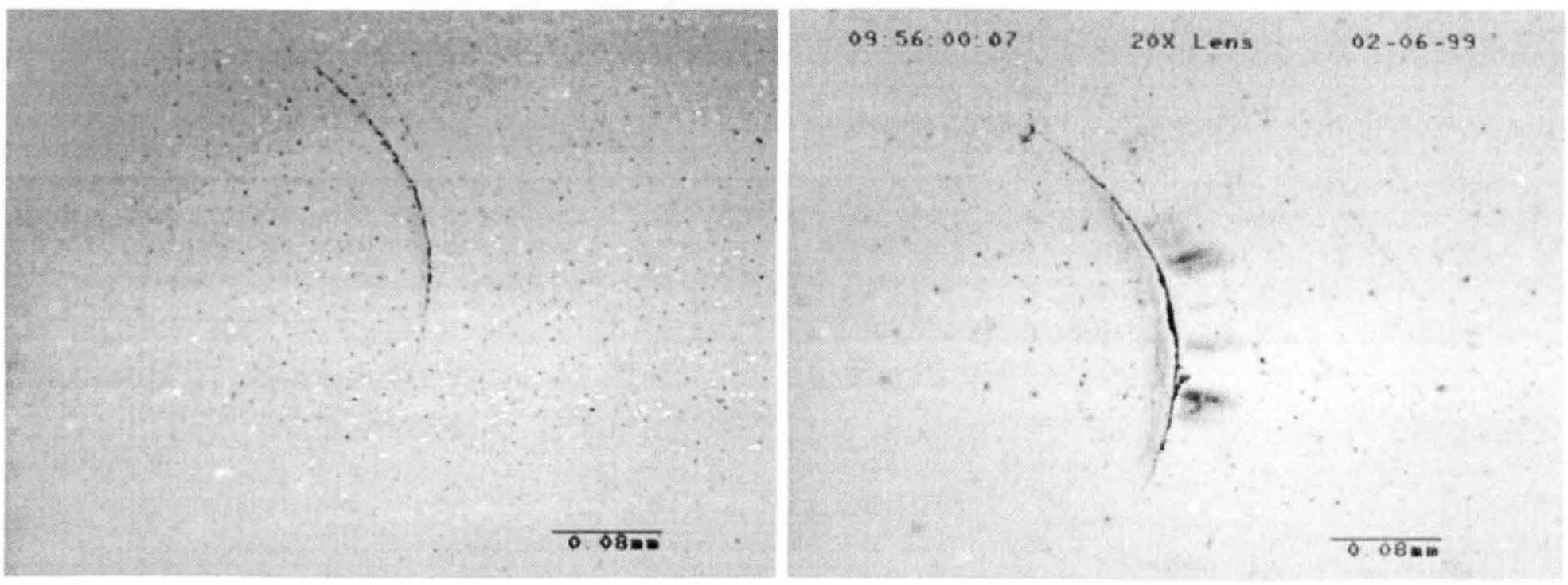

(a) Contact path and ring crack (8 hrs) (b) Contact path and ring crack (17 hrs)

Figure 3.29 Optical micrographs of surface damage (Test 9).

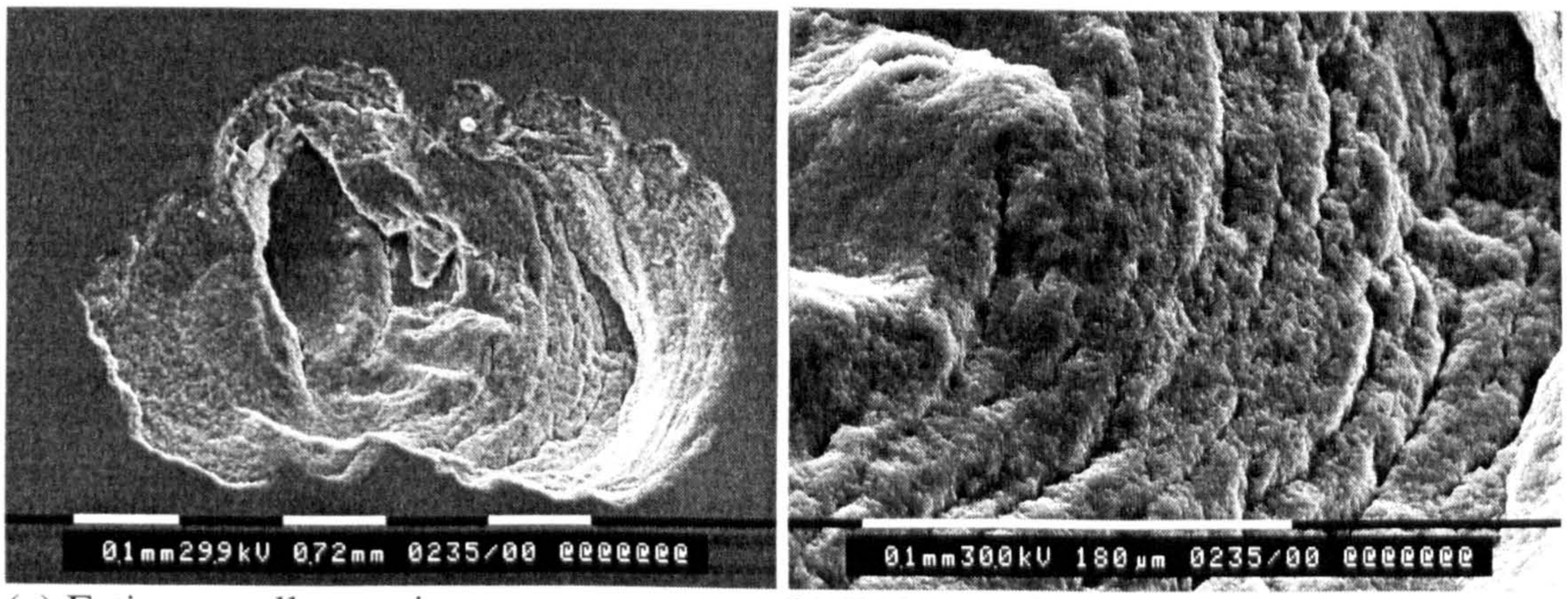

(a) Fatigue spall overview (b) Fatigue striations

Figure 3.30 SEM micrographs of surface damage (Test 9).

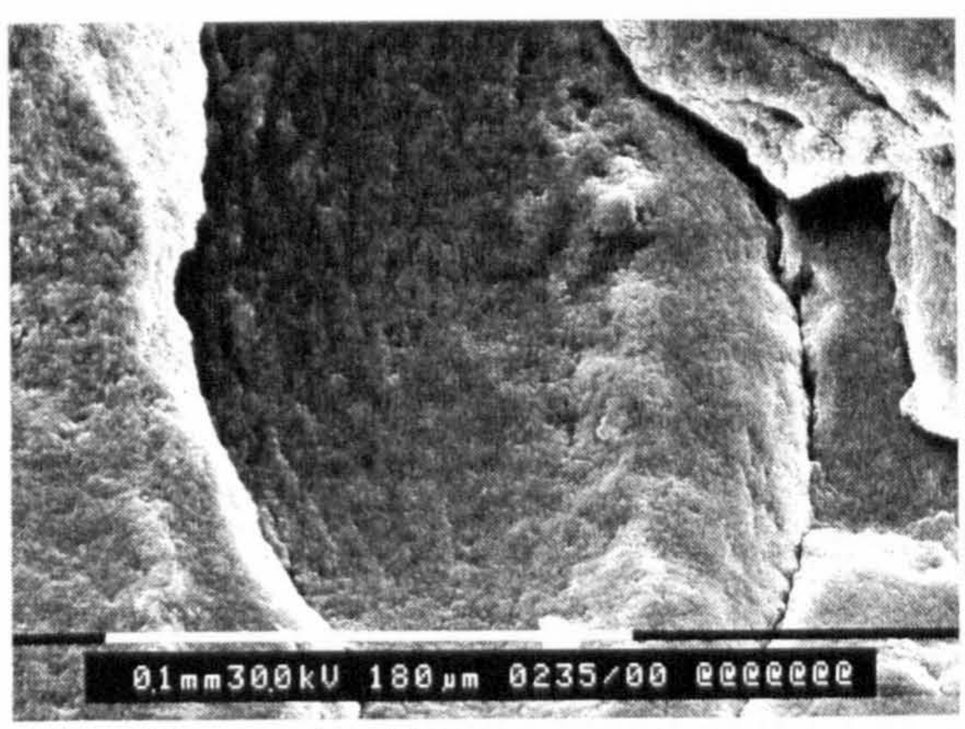

(c) Left part detail

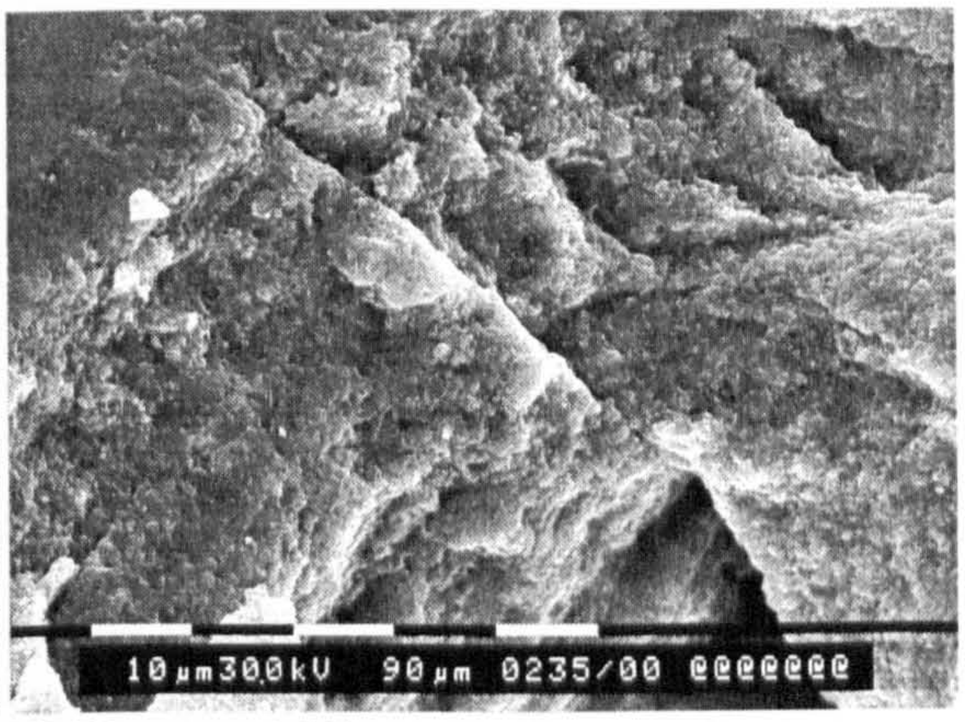

(d) Upper middle area

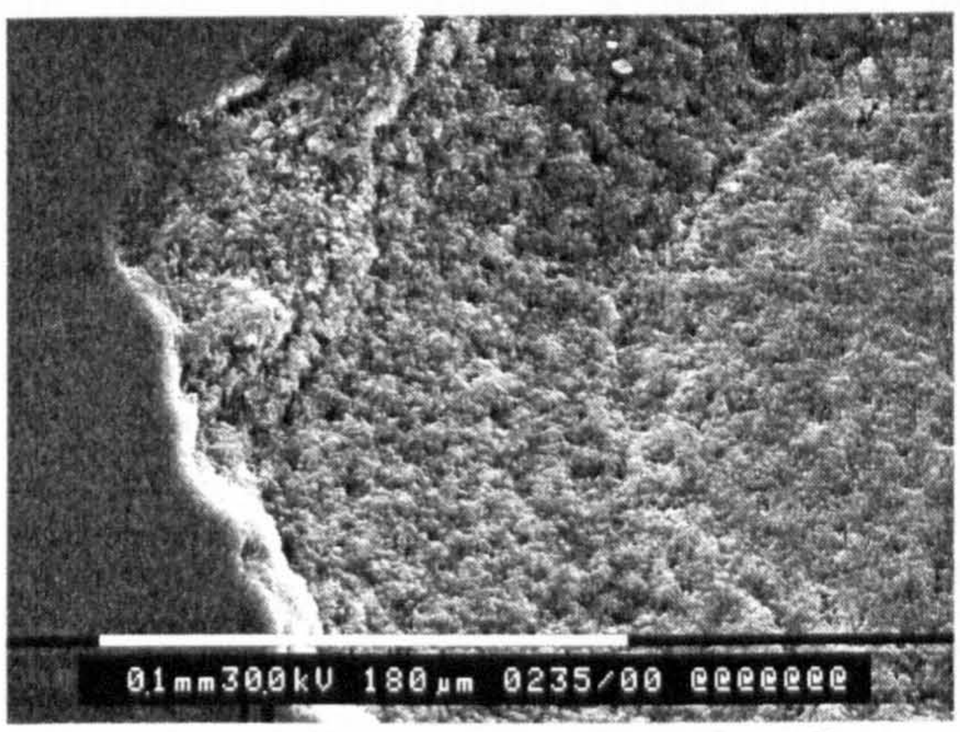

(e) Peeling failure at the edge of spall

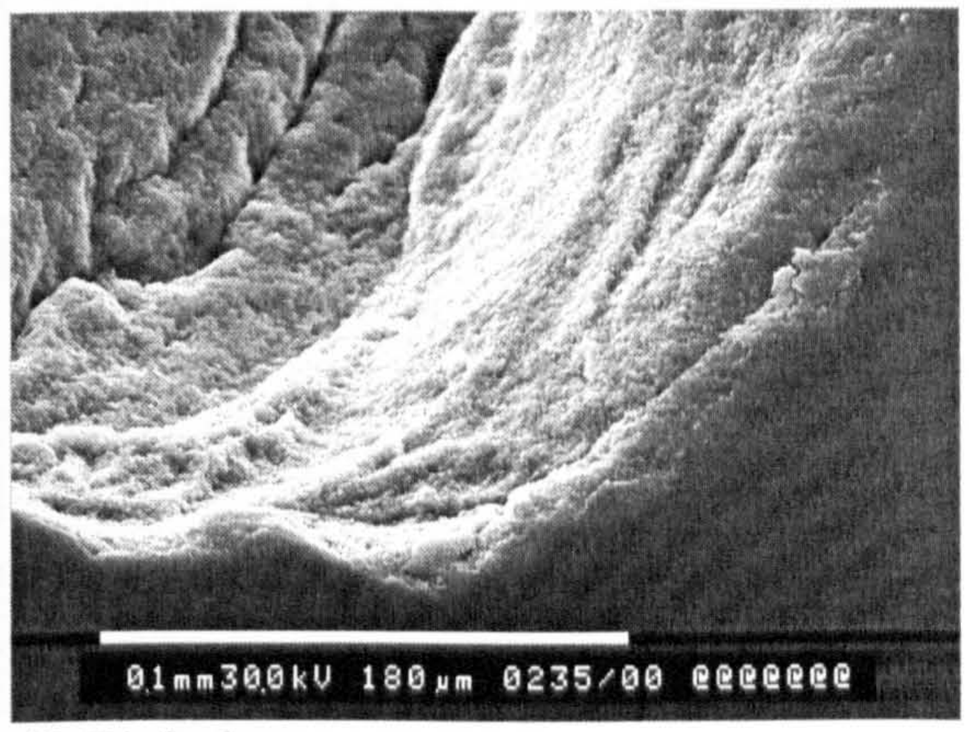

(f) Right bottom corner

Figure 3.30 Continued

Detailed SEM investigation of the test ball is carried out. Figures 3.30(a) to 3.30(f) show micrographs from Test 9. Figure 3.30(a) is an overview of a fatigue spall. The ring crack is still clear. Fatigue crack propagation initiates from the original ring crack and grows outwards in both directions. The propagation striations on the right side are shown in figure 3.30(b). The original ring crack propagation forming a striation-like pattern is clearly displayed on fatigue fracture surfaces. Unlike the striations found on metal fatigue surfaces (e.g. aluminium alloy), striations formed in ceramics under rolling contact show apparent branch cracks. The branch crack geometry always takes the shape of the pre-existing crack fronts. The mechanisms of ring crack growth must somehow be related to the formation of fatigue striations. The mechanics of the subsequent branch crack formation will be described in Chapter 5. Figure 3.30(c) shows the propagation area formed on the left side. Fatigue crack propagation initiates from the site of the original conic face in

which the subsurface branch cracks are formed. This subsurface branch crack formed on the lower crack face propagates in the opposite direction to the original ring crack growth. From optical observation, there is no significant evidence for the crack growth along the original ring crack circle. Figure 3.30(d) illustrates the upper area on which the original ring crack is clearly seen. The symptom of subsequent surface cracks is clearly seen on both sides of the original ring cracks. The SEM observation confirms that the crack gap may reach 0.5 μm. Figure 3.30(e) illustrates a peeling failure mode found at the left edge. Figure 3.30(f) is the micrograph from the right bottom corner, which shows the secondary surface cracks and the brittle fracture.

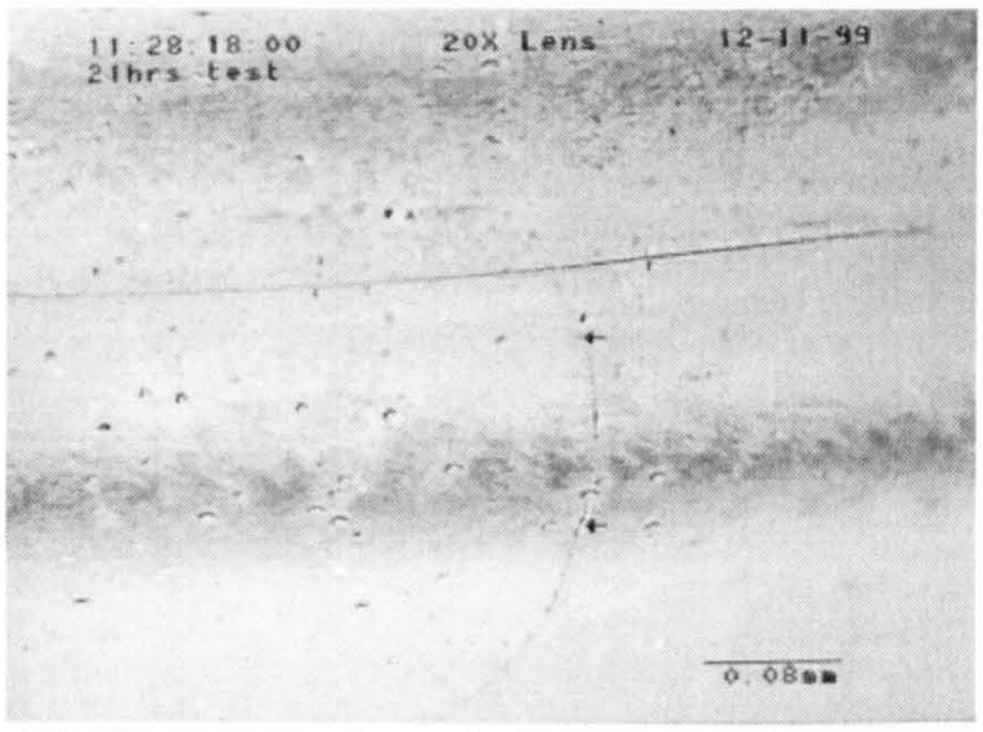

(a) Contact path and ring crack (21 hrs)

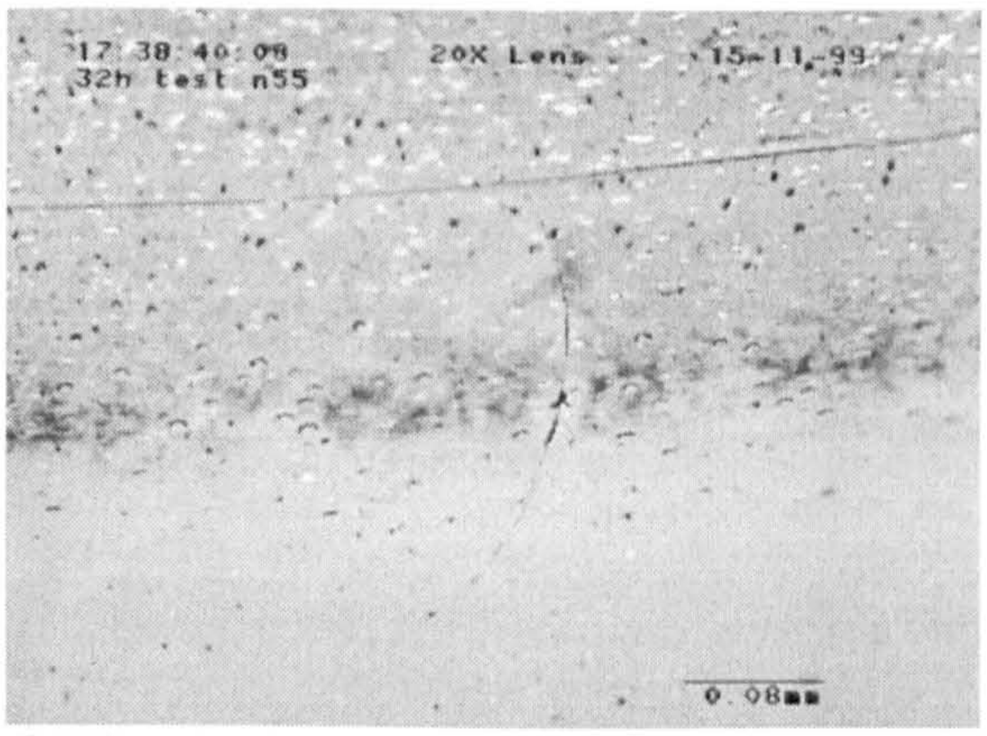

(b) Contact path and ring crack (32 hrs)

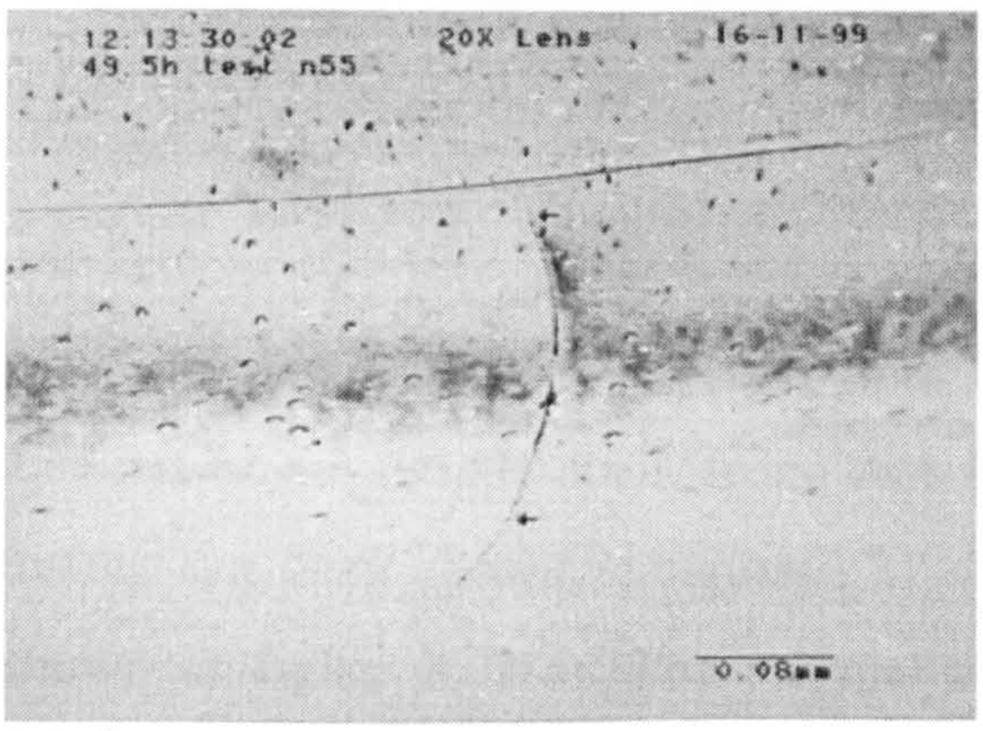

(c) Contact path and ring crack (49.5 hrs)

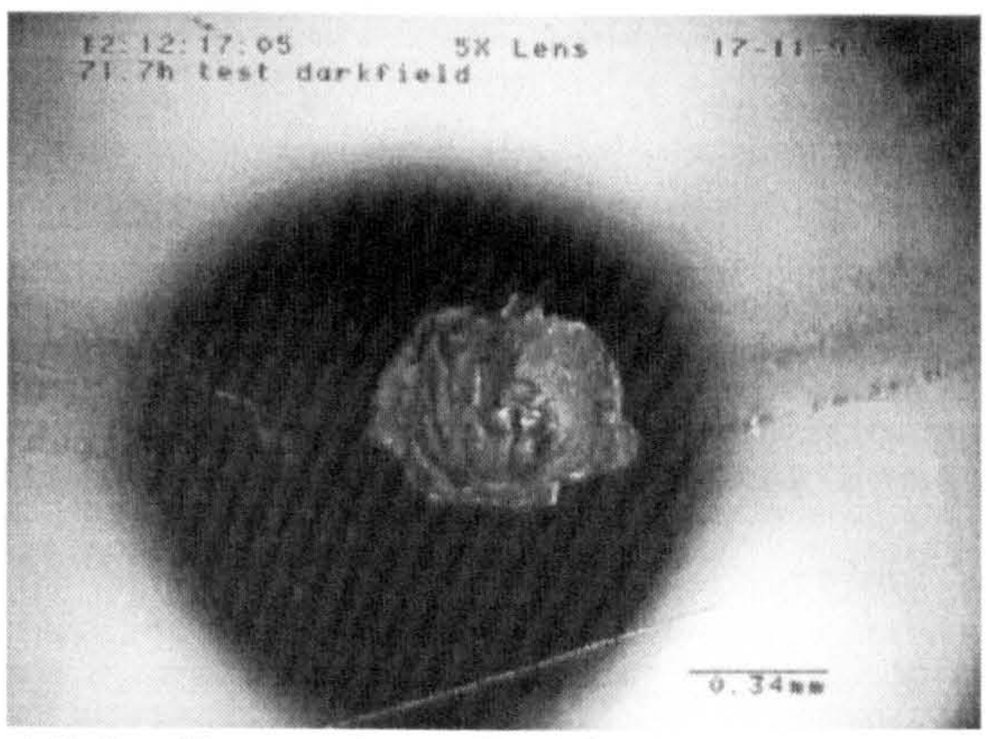

(d) Spall overview (71.1 hrs)

Figure 3.31 Optical micrographs of surface damage (Test 10).

Figure 3.31 shows the results from Test 10. Figure 3.31(a) is an optical image after 21 hours of fatigue testing, in which the original crack is clearly displayed on the contact track and indicated by the arrows. Figures 3.31(b) and 3.31(c) show the

micrographs after 32 and 49.5 hours of testing respectively. No evidence is found for crack growth along the ring crack circle. Micro-cracks are found in the contact path. The ellipse-like spall is shown in figure 3.31(d).

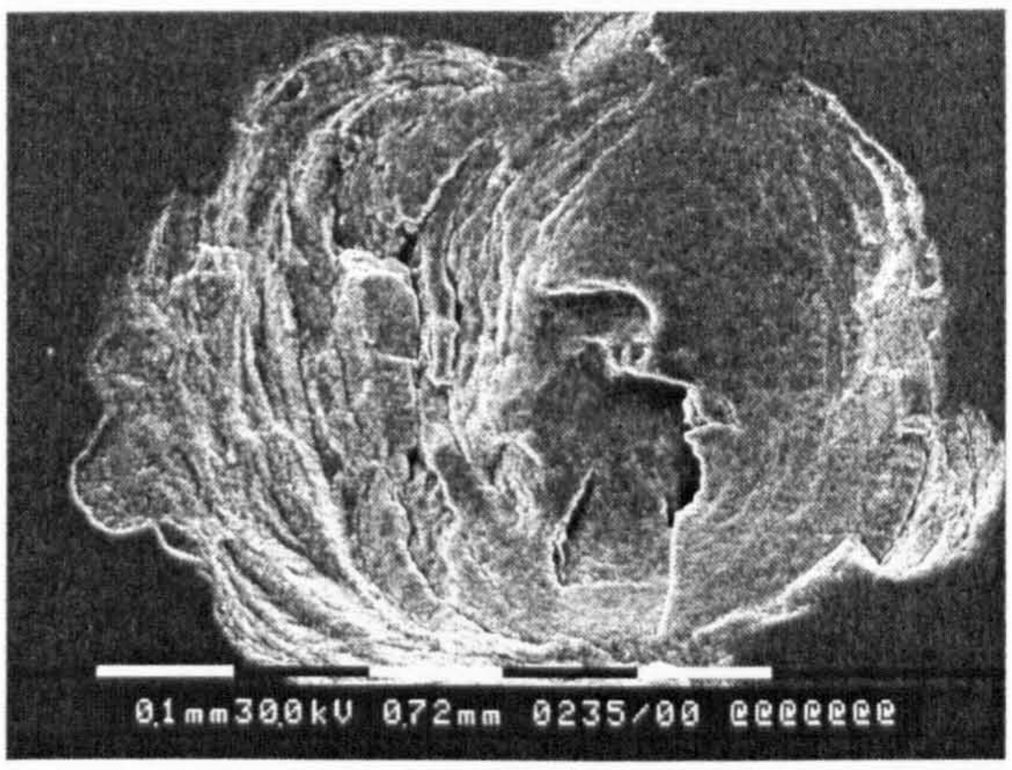

(a) Spall overview

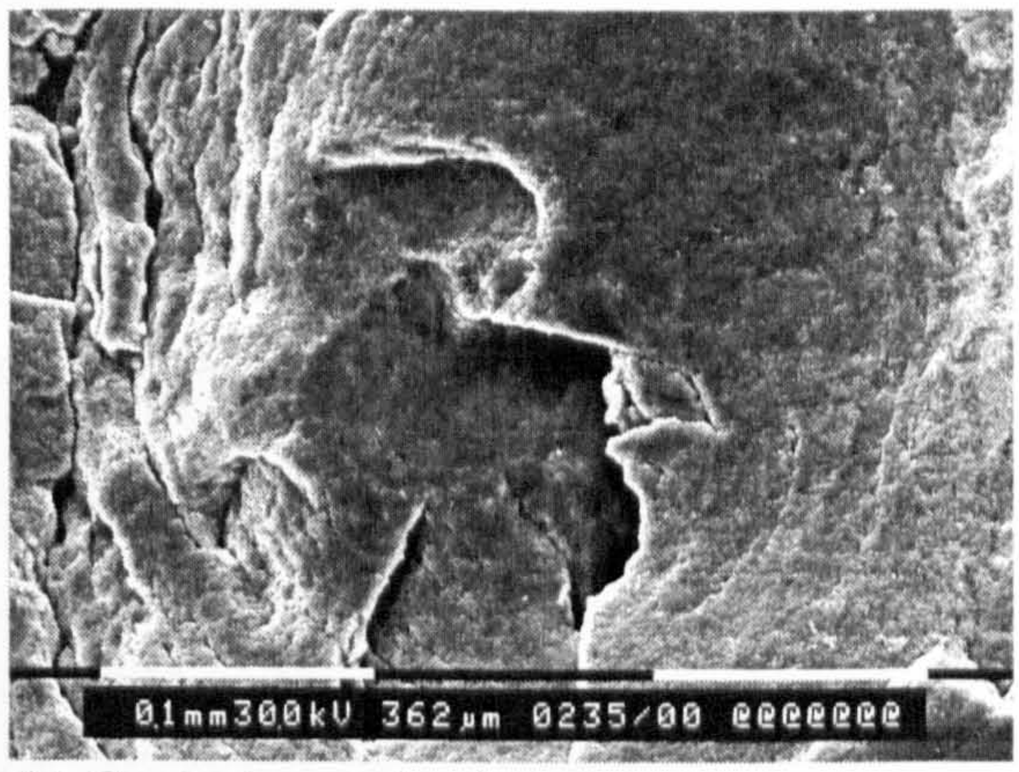

(b) Central part detail

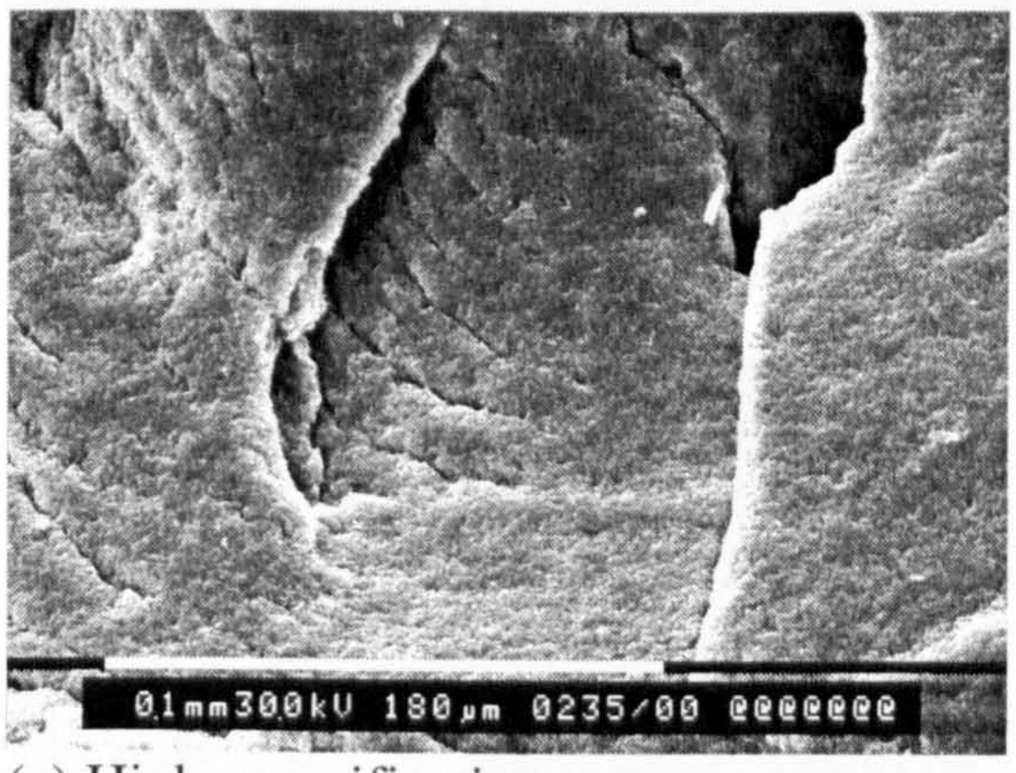

(c) High magnification

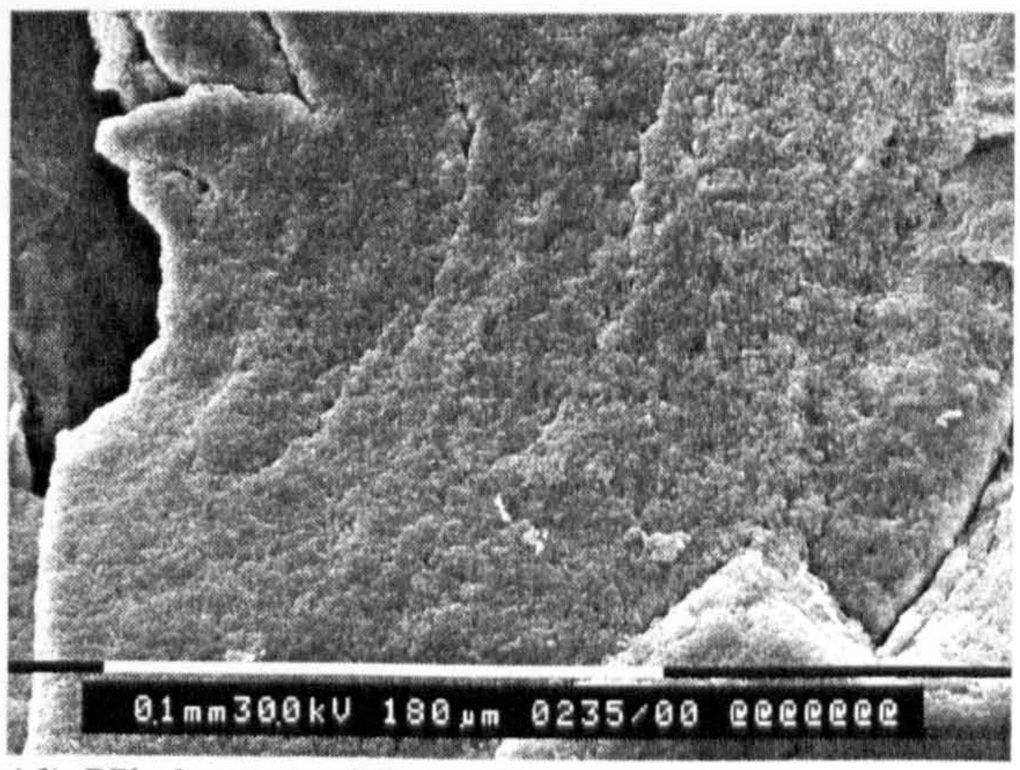

(d) High magnification

Figure 3.32 SEM micrographs of surface damage (Test 10).

Figure 3.32 shows results from the scanning electron microscope (SEM) analysis of the fatigue spall, from Test 10. The optical image of the crack during testing has been shown in figure 3.31. The SEM image of the spall overview is shown in figure 3.32(a). The original ring crack can be identified clearly. It is obvious that there are two directions of crack propagation. One is crack growth towards the right, which shows the original ring crack growth path. The other is towards the left, which shows the growth path of the subsurface branch crack formed on the lower crack face. Figure 3.32(b) enhances the magnification of the micrograph. The characteristic of fatigue fracture is apparent and subsurface branch cracks are clearly displayed on the spall surface. The geometry of the subsurface

branch cracks is influenced by the contact circle and will normally inherit the geometry of that circle. Figure 3.32(c) shows the circle-like striations formed on the left, and figure 3.32(d) those on the right. The distance between two striations is around 5-10 μm, and is close to the predicted distance in terms of crack face contact analysis. Detailed mechanics analysis of crack face contact will be discussed in Chapter 5.

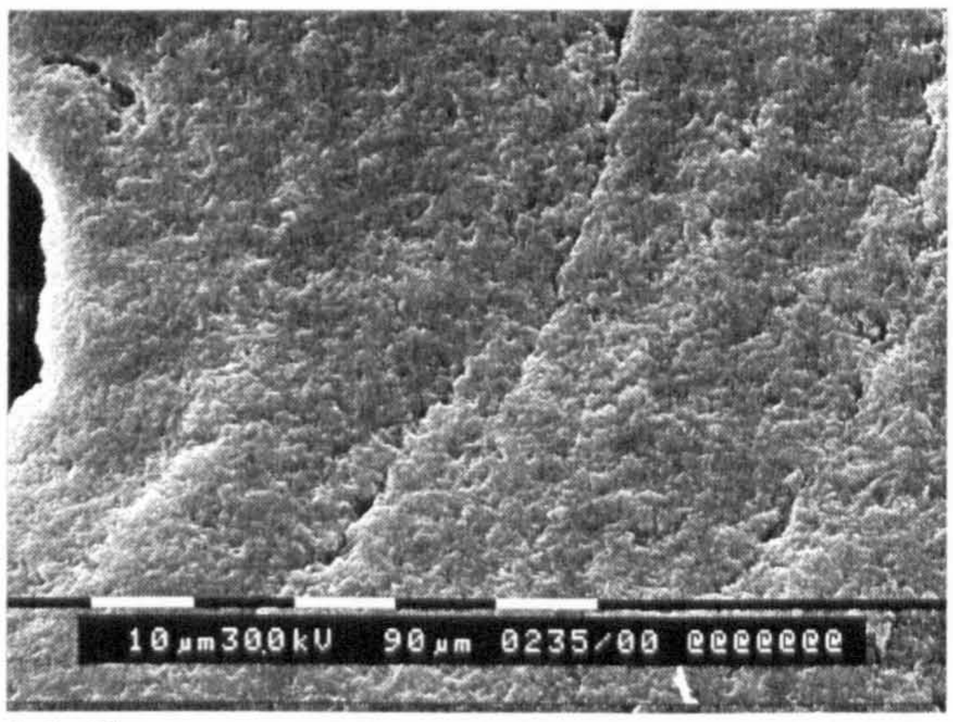

(a) Centre area

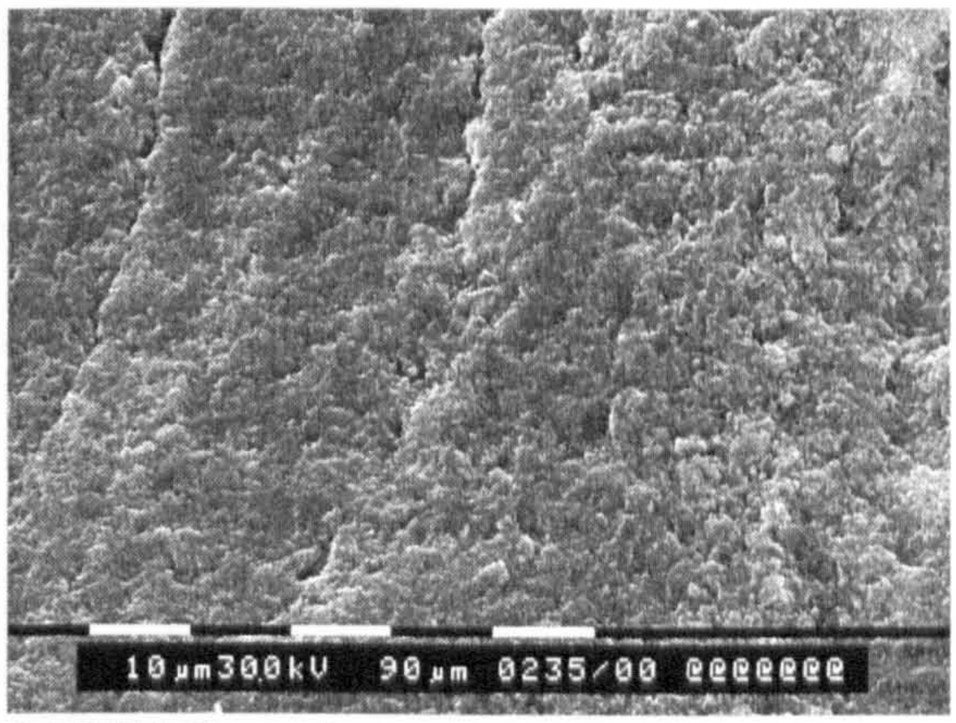

(b) Middle region

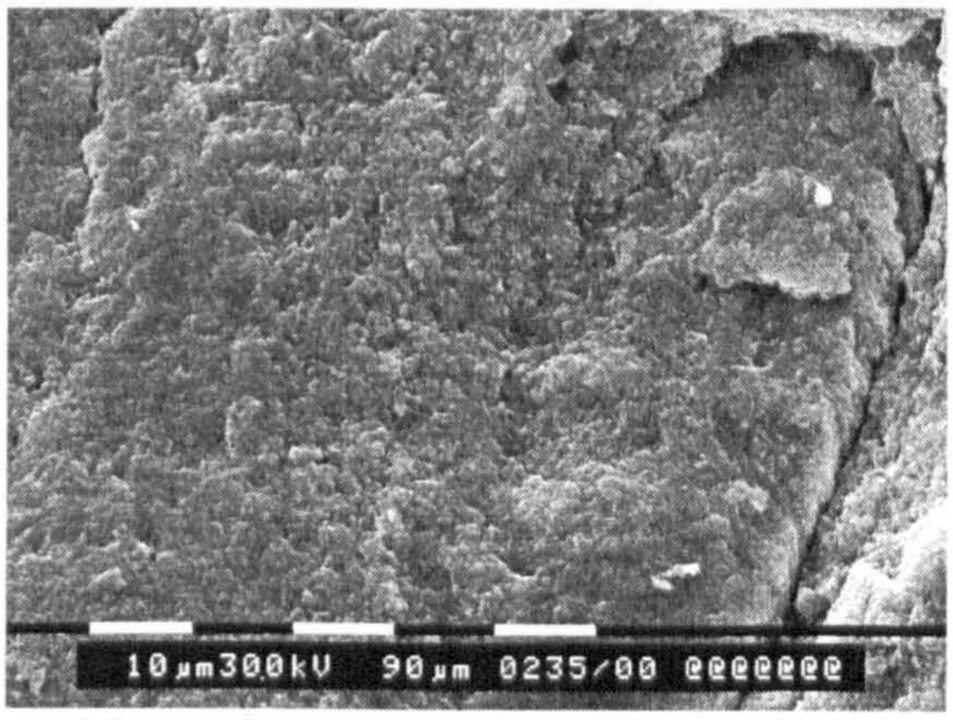

(c) Near edge area

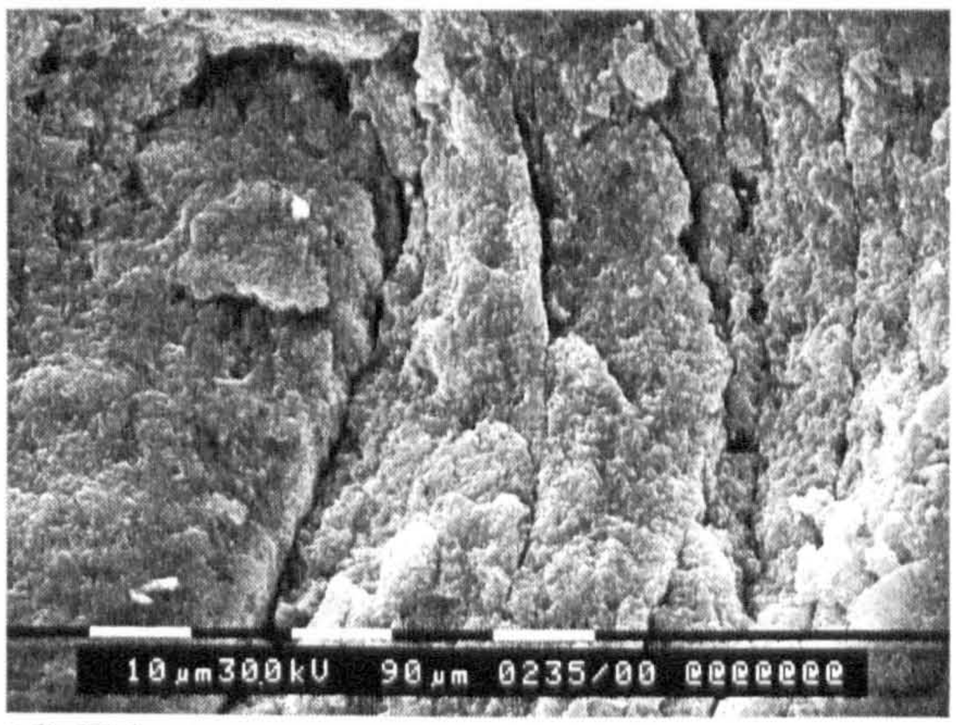

(d) Edge area

Figure 3.33 SEM micrographs from the centre to the right edge (Test 10).

The surface characteristic of the fatigue spall varies with the position of the spall surface. The result from Test 10 is shown in figure 3.33. The images are scanned from the centre (figure 3.32(a)) to the right edge. The smoothness of the surface decreases as the scanning position moves from the centre to the edge area. Figures 3.33(a) and 3.33(b) show a smooth fatigue surface, on which the subsurface

branch cracks are clearly displayed. The smoothness of the surface lessens in the edge area, see figure 3.33(c). Figure 3.33(d) shows the rough surface formed at the edge of the spall, on which secondary surface cracks are apparent.

Figure 3.34 shows the images scanned from the centre to the left edge of the spall. As discussed in figure 3.33, the smoothness of the spall surface changes as the scanned position changes. The surface is smoother in the centre area, and rougher in the edge area. Figure 3.34(a) shows the centre area image, which illustrates the circle-like striations formed at the initial stage of fatigue crack propagation. Fatigue crack growth derives from the subsurface crack generated on the lower crack face. Figures 3.34(b) and 3.34(c) show the variations of the spall surface gradually moving outwards from the centre. Figure 3.34(d) shows the peeling failure mode formed in the edge of the spall.

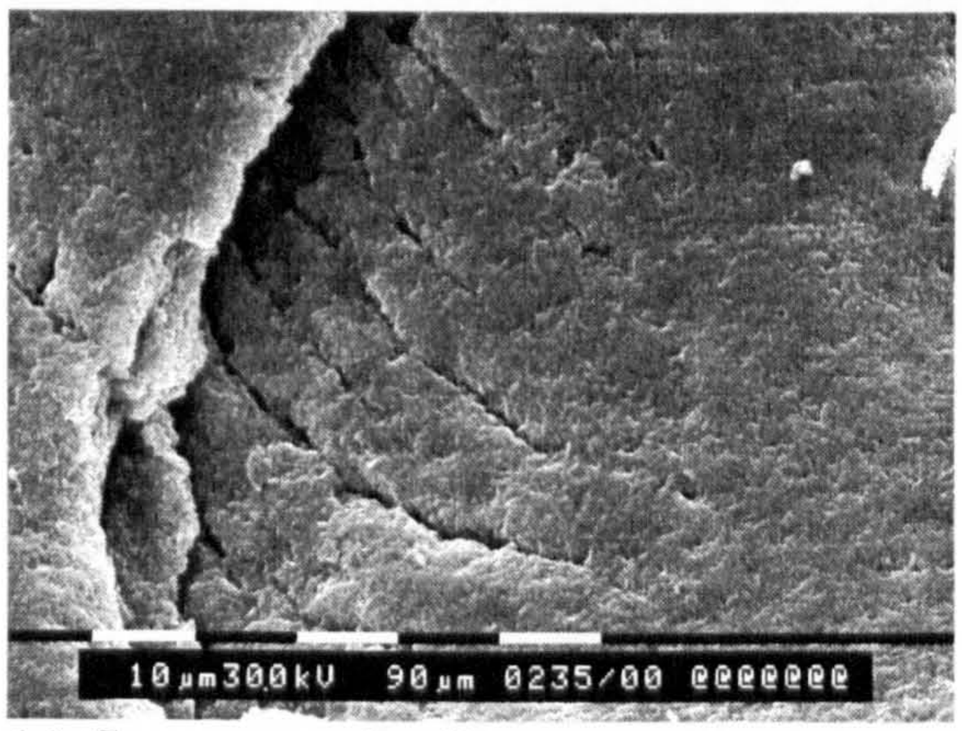

(a) Centre area detail

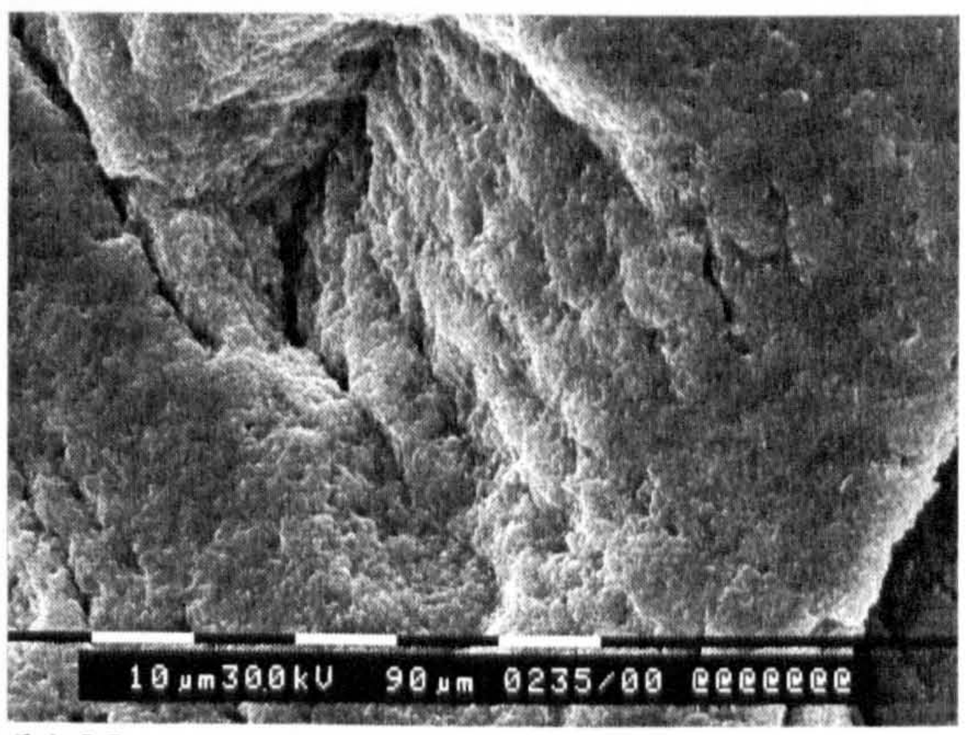

(b) Near centre part

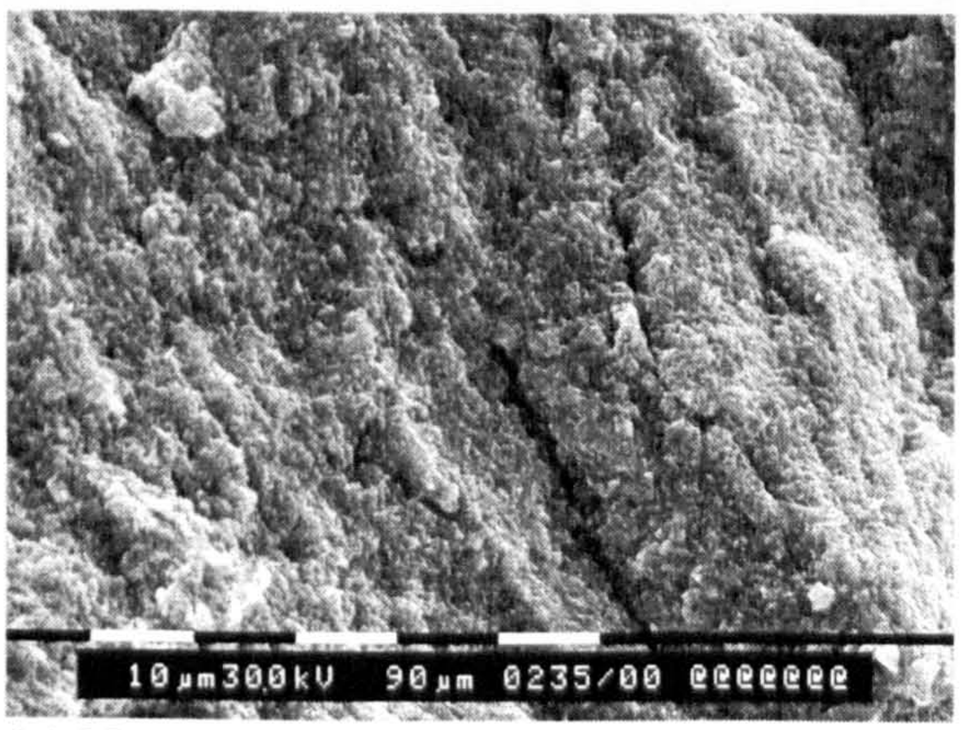

(c) Near edge area

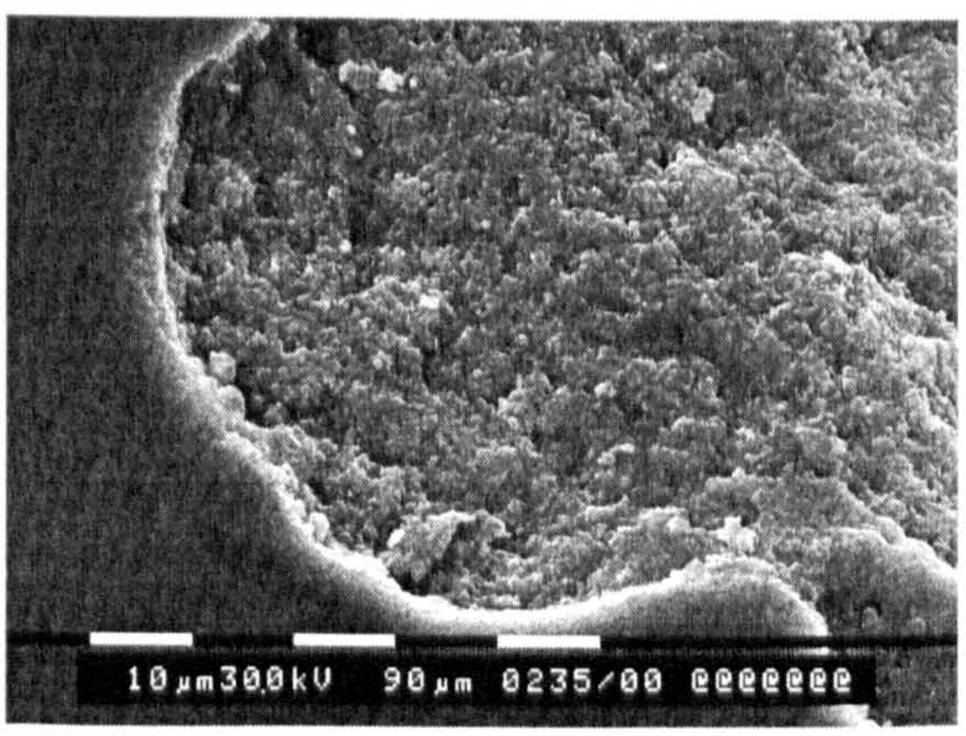

(d) Edge area

Figure 3.34 SEM micrographs from the centre to the left edge (Test 10).

Post-test analysis of the ceramic balls reveals that the fatigue spall at high contact load is similar to that at low contact load. SEM micrographs from Test 13 are shown in figure 3.35. An overview of the spall, figure 3.35(a), shows that the original ring crack is clearly displayed on the top of the micrograph. Figure 3.35(b) shows the origin of crack propagation derived from the original ring crack. Figure 3.35(c) shows the secondary surface cracks which are formed on the left edge area. Figure 3.35(d) shows the detailed view from the right edge area. The secondary surface cracks are obvious.

(a) Spall overview

(b) Further magnified image

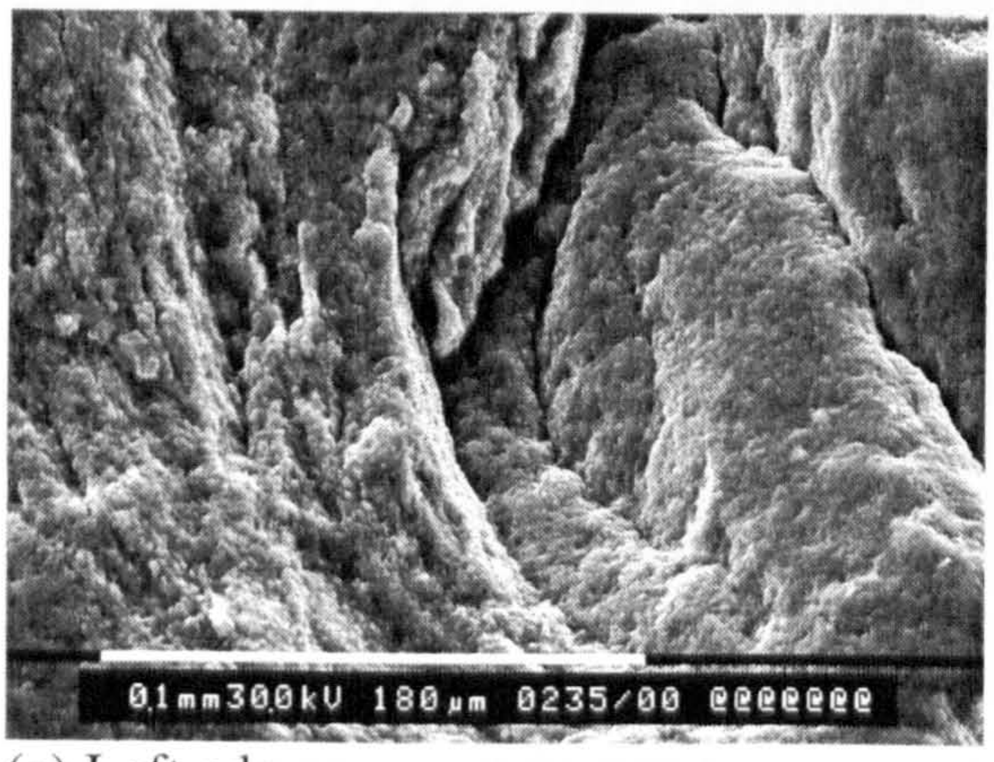

(c) Left edge area

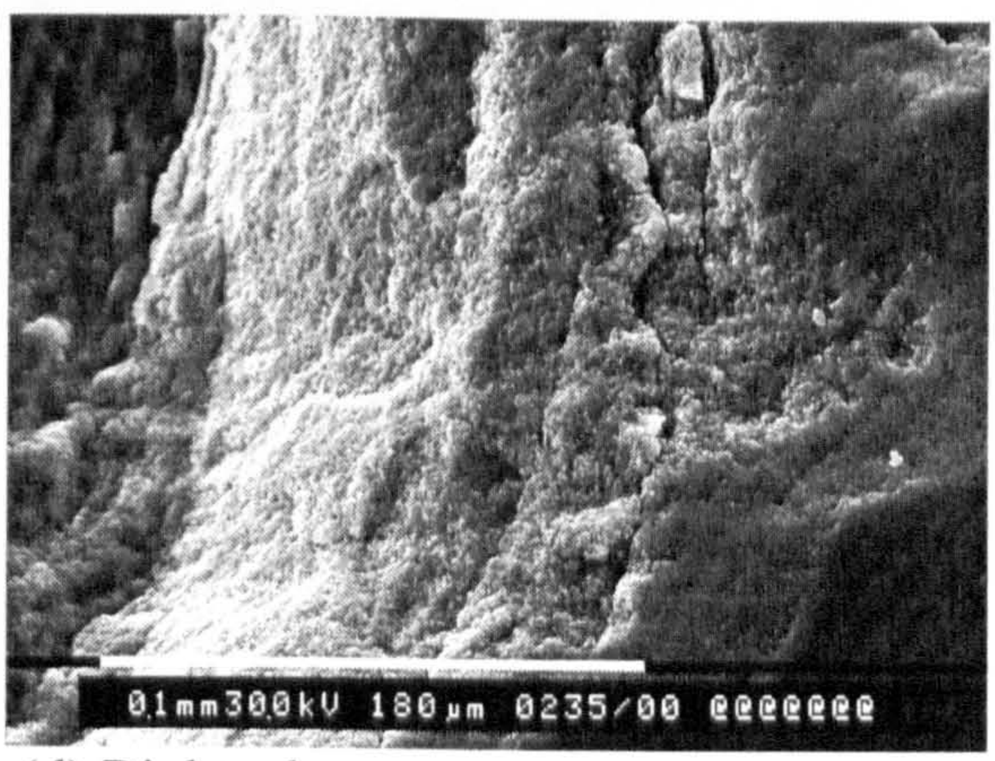

(d) Right edge area

Figure 3.35 SEM micrographs of surface damage (Test 13).

Figure 3.36 shows the SEM micrographs from Test 14. Figure 3.36(a) shows a spall overview. The contact stress is quite high in this case (7.6GPa). Unlike the fatigue spall which occurs at low contact stresses, the peeling area increases. Figure 3.36(b) shows a crack growth path. Figure 3.36(c) shows the left edge area of the spall, on which secondary surface cracks are displayed. Figure 3.36(d) shows the right edge area, on which the secondary surface cracks are shown. Again, the fracture surface in the centre area is smoother than the edge area.

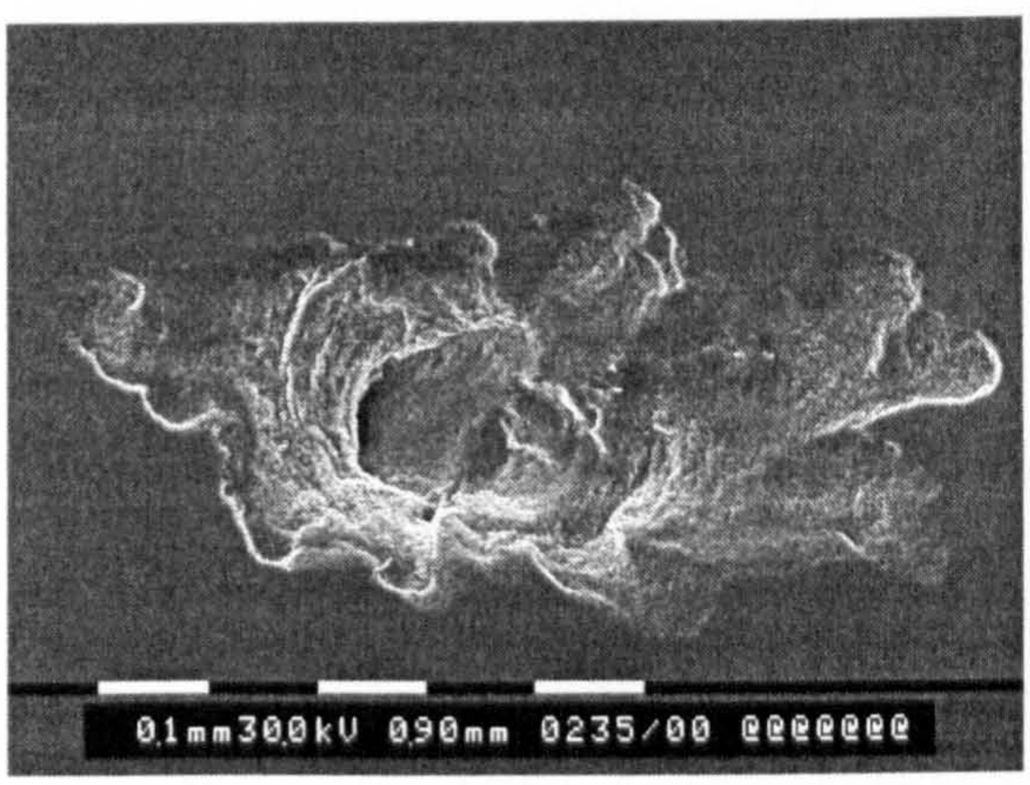

(a) Spall overview

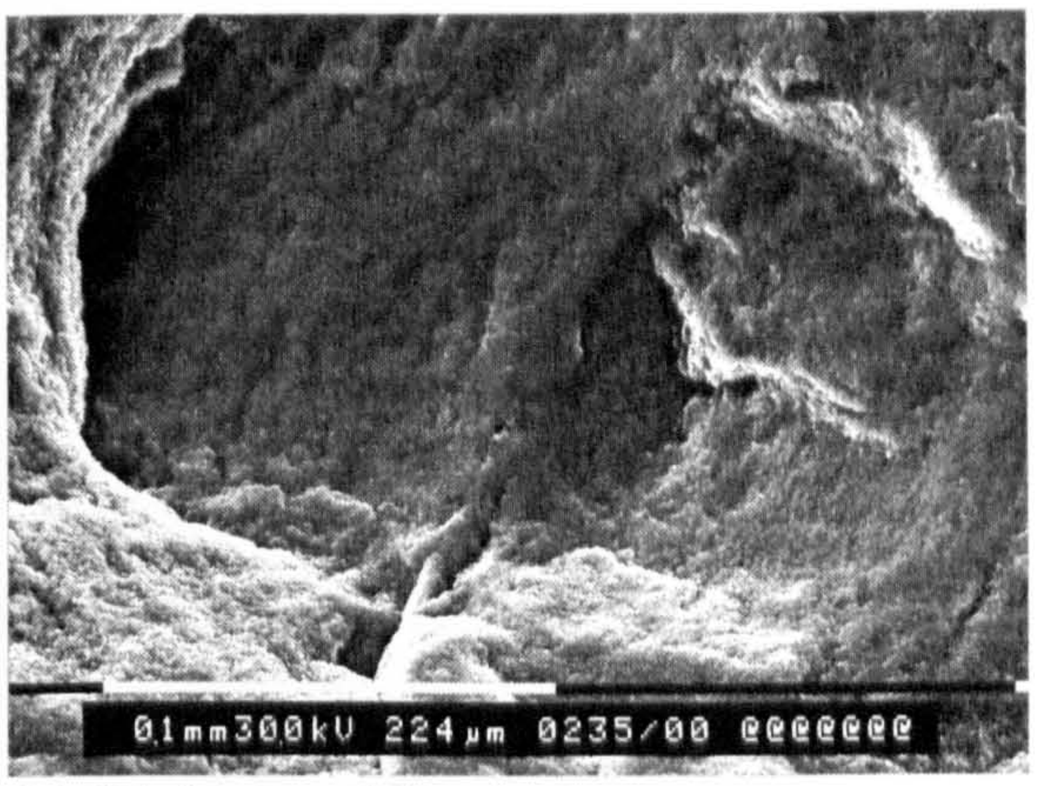

(b) High magnification

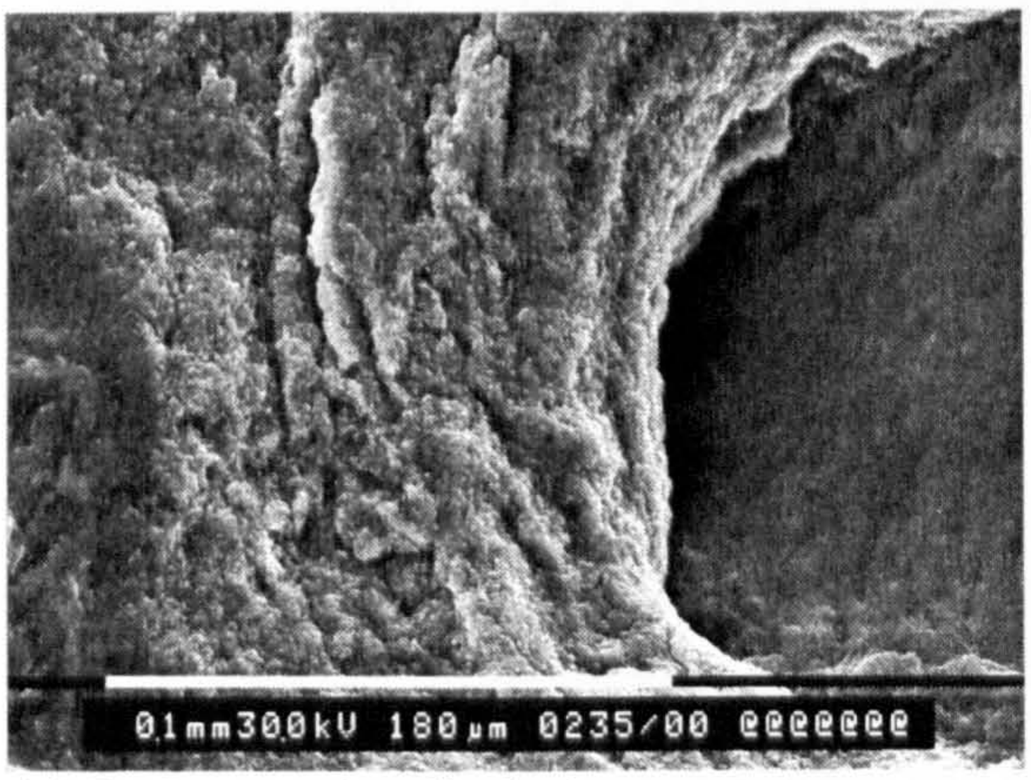

(c) Left area detailed view

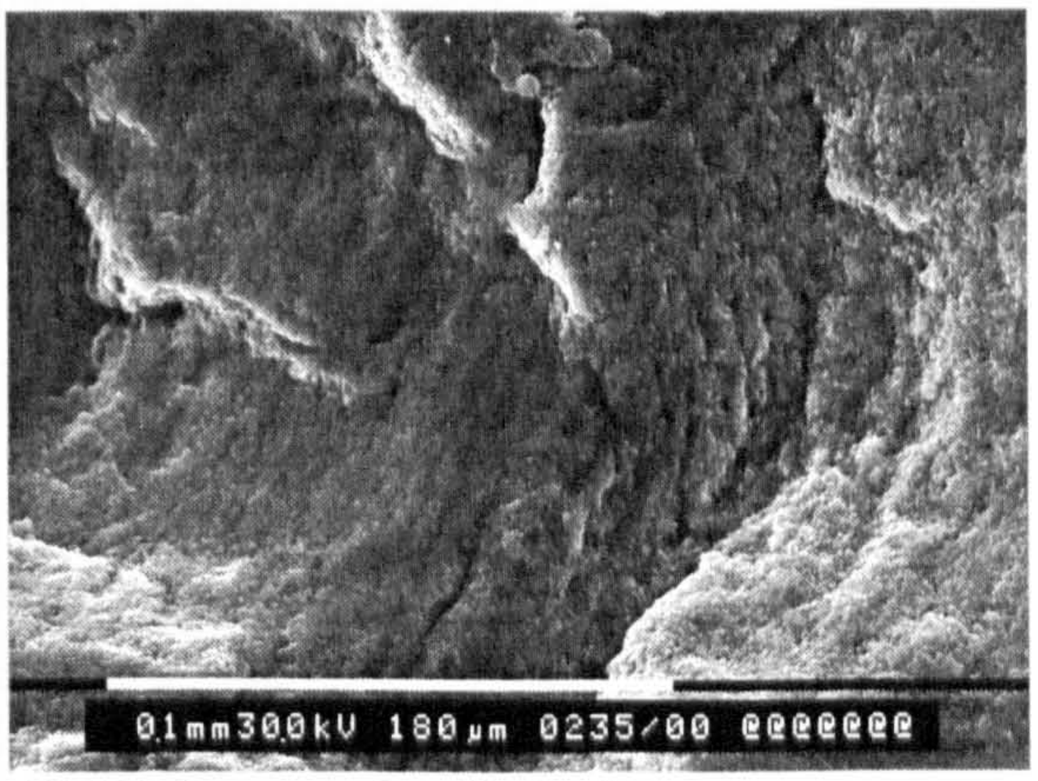

(d) Right area detailed view

Figure 3.36 SEM micrographs of surface damage (Test 14).

3.3.2 High viscosity oil lubrication

Observations of surface damage under low viscosity oil lubrication are described above. The spalling shape of rolling contact fatigue always looks like an ellipse. The longer semi-axis is always parallel to the rolling direction, and the short axis is perpendicular to the rolling direction. The short semi-axis approximates to the

magnitude of the contact radius under applied load. Results from the high viscosity oil lubrication are discussed below.

Results of surface observation from Test A are shown in figure 3.37. The contact track after 22 hours of testing is shown figure 3.37(a). The contact track is covered by lubricant deposit. The lubricant deposit tends initially towards the edge of the track. As the test proceeds the whole track will be covered. Figure 3.37(b) shows that the lubricant deposit is removed after spalling due to the effect of debris machining. The SEM image is shown in figure 3.37(c), in which the striations are displayed clearly. Crack propagation occurs in both sides of the original ring crack. Figure 3.37(d) shows the high magnification of the striations formed on the spall surface.

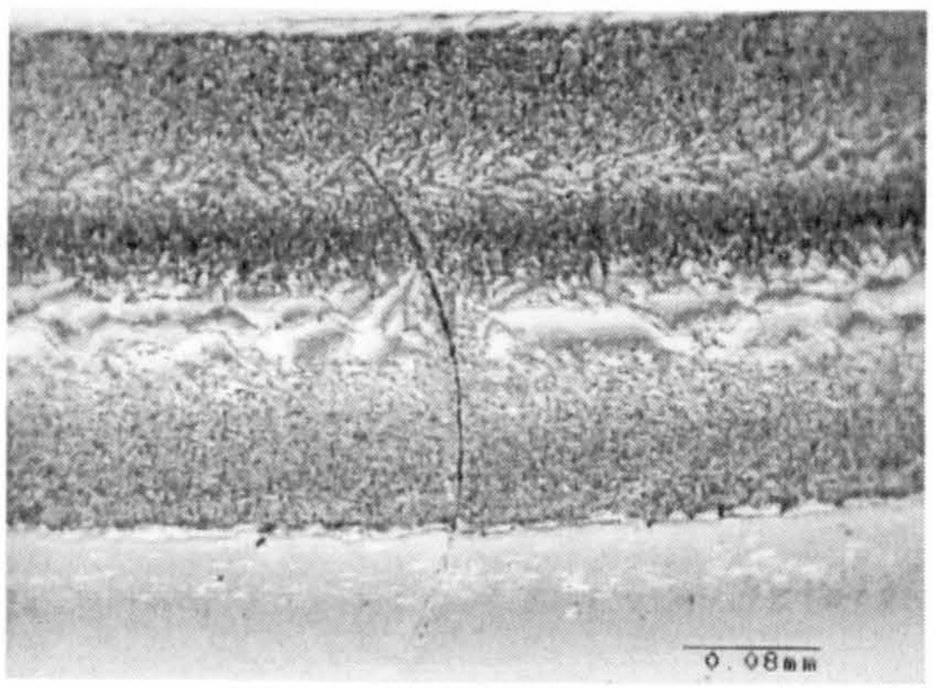

(a) Optical micrograph (22 hrs)

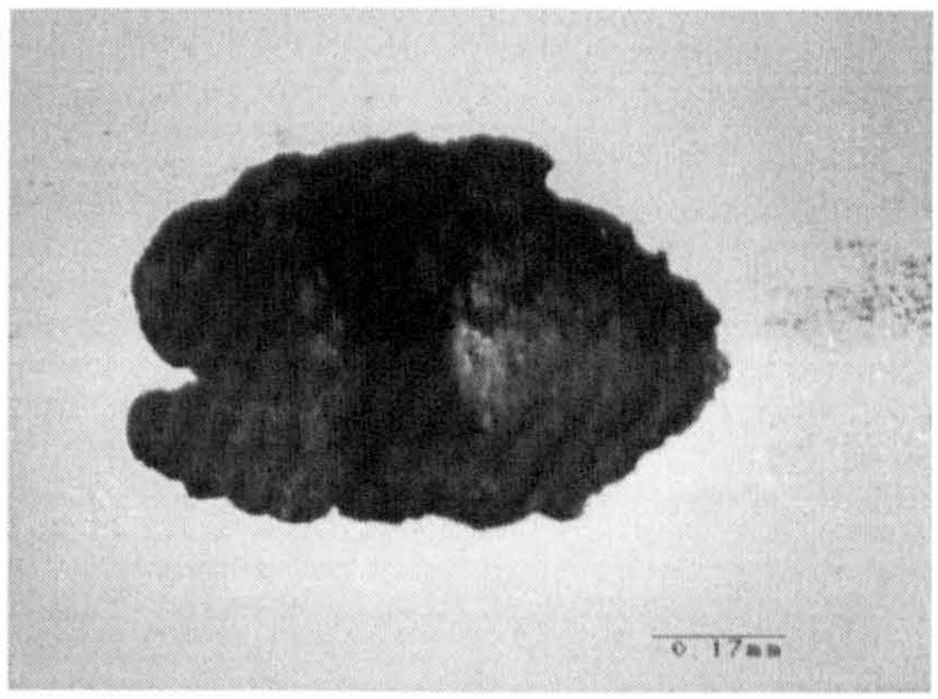

(b) Spall optical micrograph (34.6 hrs)

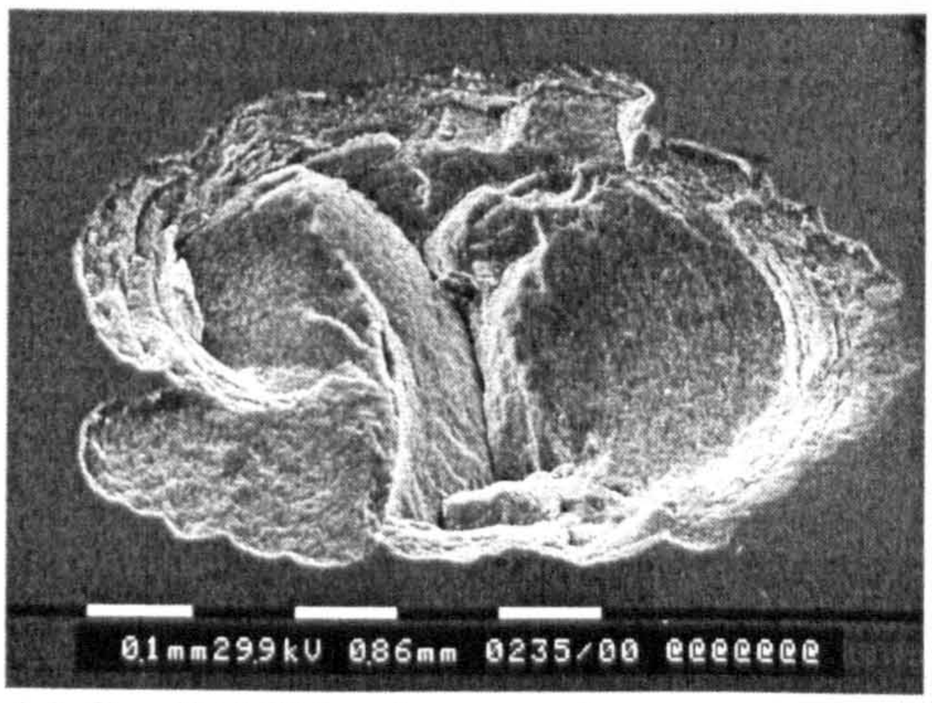

(c) Spall SEM micrograph

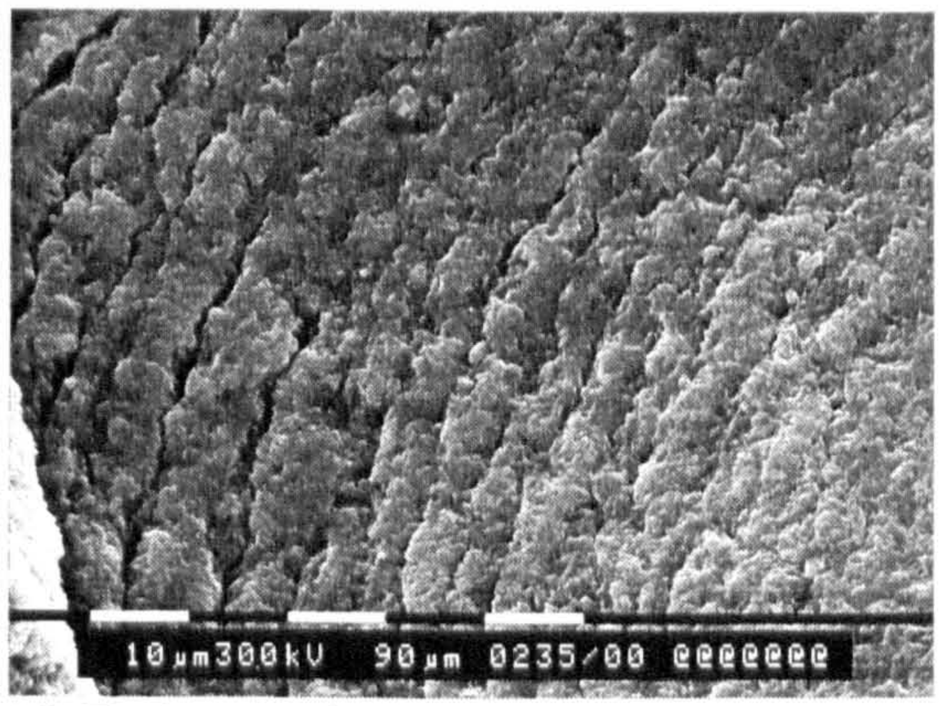

(d) Fatigue striations

Figure 3.37 Micrographs of surface damage (Test A).

Observations of surface damage from Test D are shown in figure 3.38. Figure 3.38(a) shows an optical micrograph after 28.5 hours of testing. The deposit material pattern is similar to the previous images. Figure 3.38(b) is an overview of a spall. As in figure 3.37, the deposit material is removed after the spall. Figure 3.38(c) shows a SEM micrograph of the spall. Figure 3.19(d) shows the central part in a greater detail.

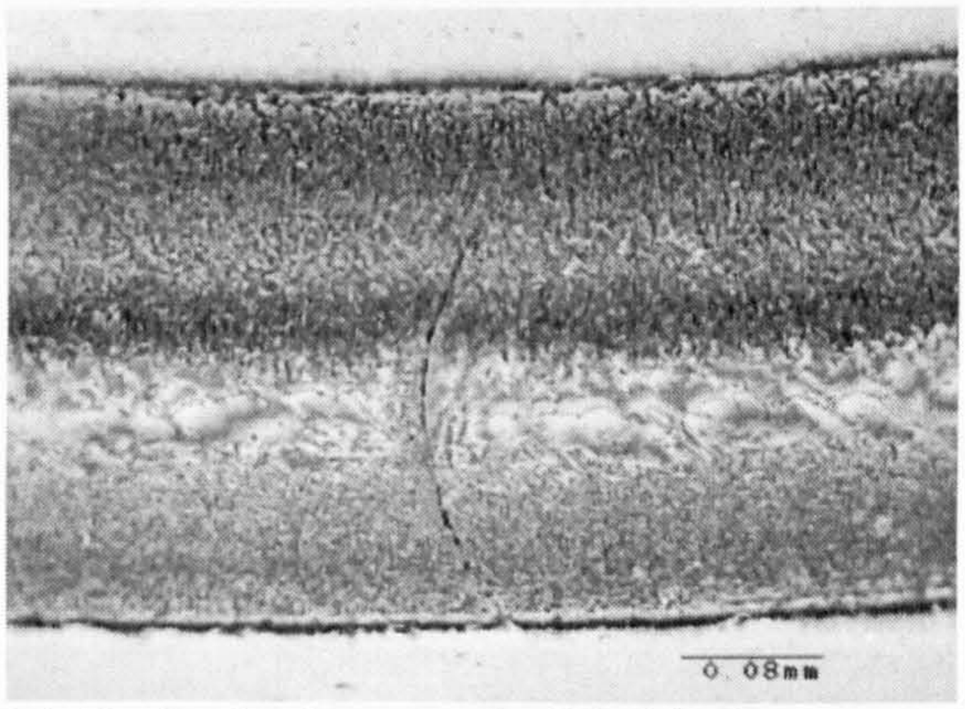

(a) Optical micrograph (28.5 hrs)

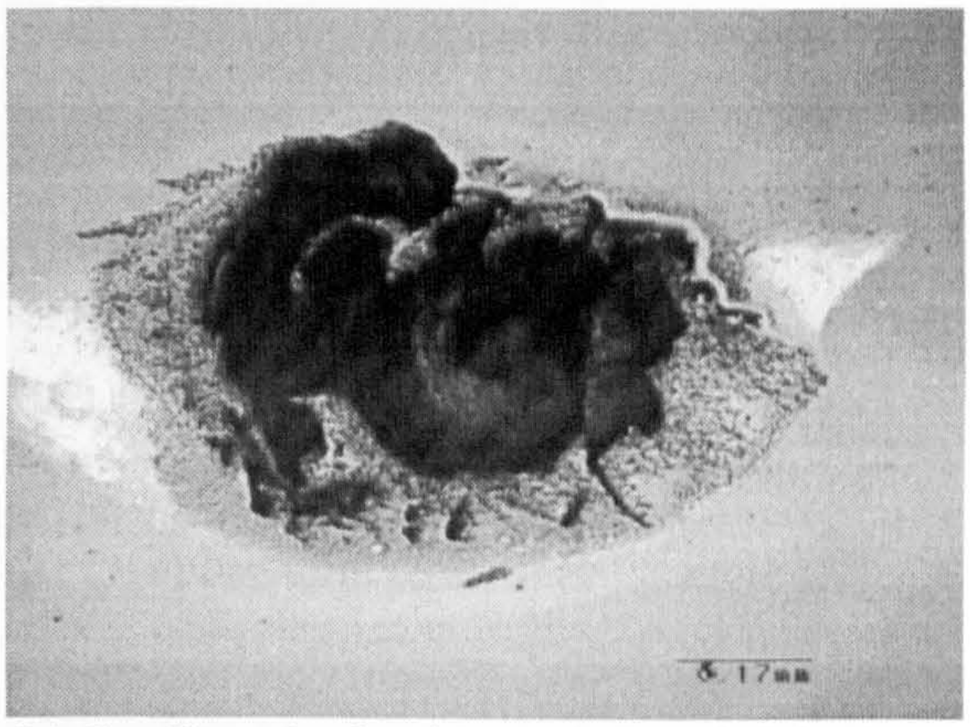

(b) Spall optical micrograph (42.7 hrs)

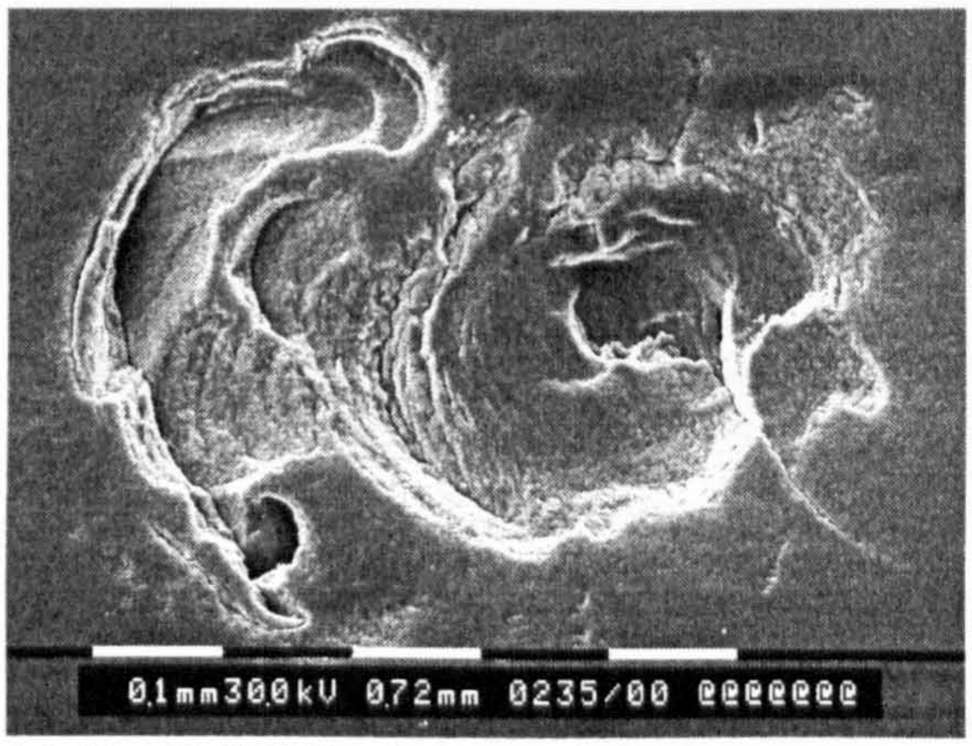

(c) Spall SEM micrograph

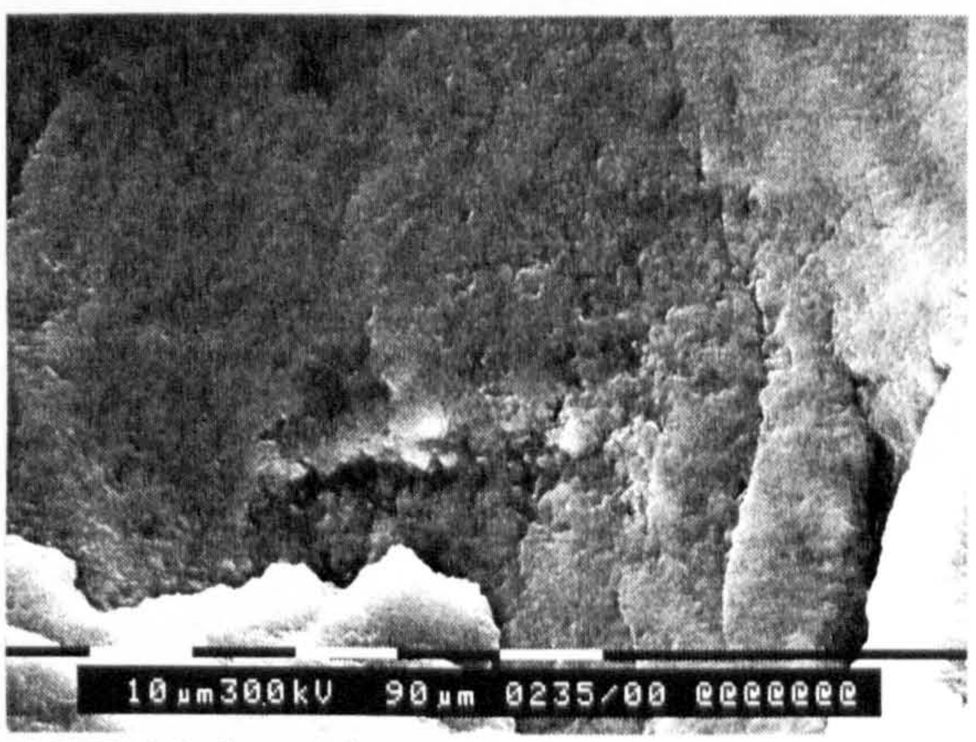

(d) Initial crack propagation

Figure 3.38 Micrographs of surface damage (Test D).

SEM micrographs of surface damage (Test F) are shown in figure 3.39. Crack propagation is initiated from the original ring crack. The striations are strongly influenced by the contact stress field (see figures 3.39(a) and 3.39(b)). As

discussed above the circle-like striations are formed due to the characteristic of the stress field. Figure 3.39(c) illustrates the detailed striations formed on the spall surface. Figure 3.39(d) shows a peeling failure which occurs on the left edge area.

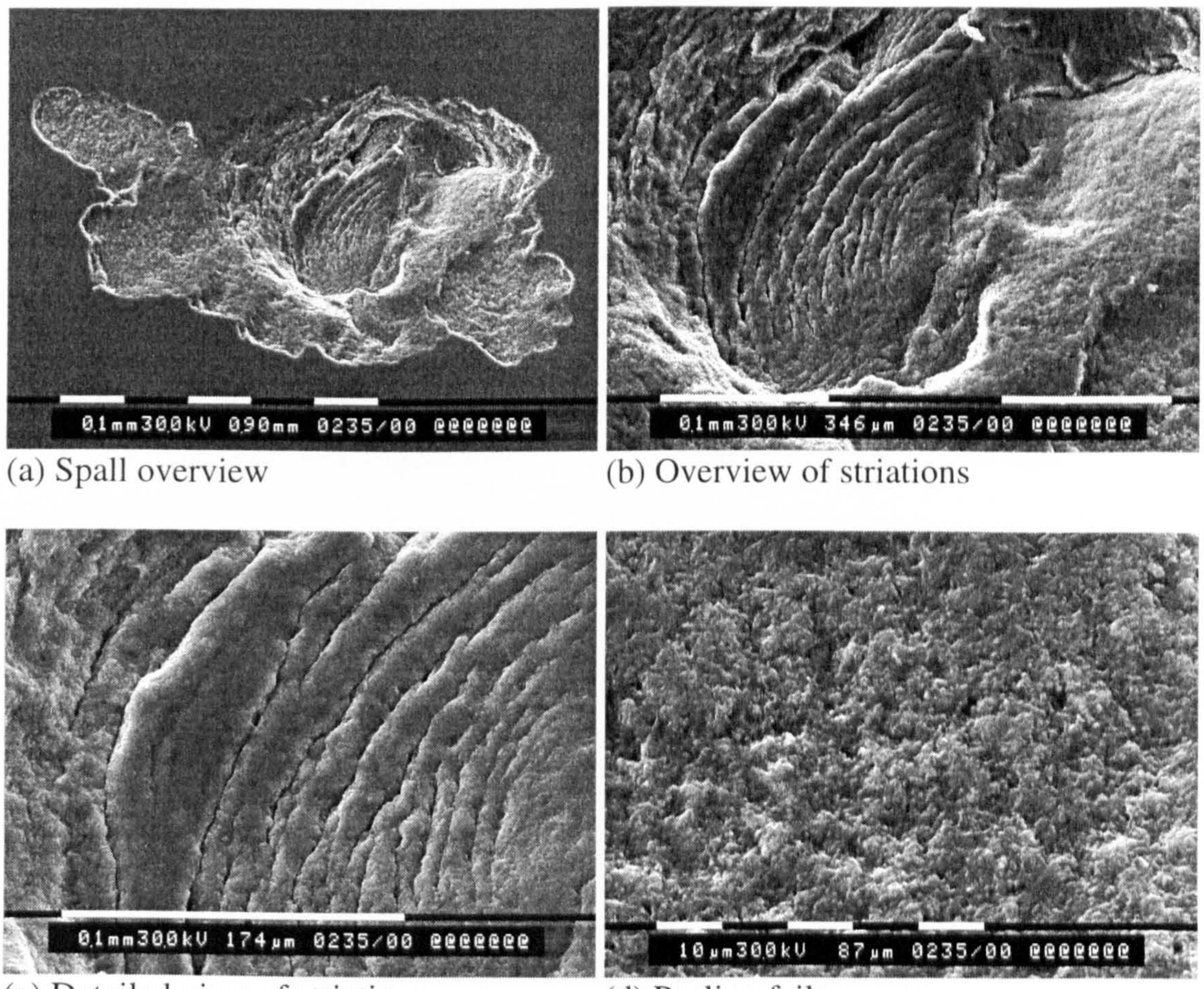

(a) Spall overview

(b) Overview of striations

(c) Detailed view of striations

(d) Peeling failure area

Figure 3.39 SEM micrographs of surface damage (Test F).

3.4 SUBSURFACE OBSERVATIONS OF CRACK PROPAGATION

To understand the mechanics process of a ring crack failure, experimental observations of the spalling processes are important. A dynamic experimental observation has been carried out to ascertain ring crack propagation behaviour. A typical transition process from normal to a spall is shown in figure 3.40. All the images in figure 3.40 are from Test 5. Figure 3.40(a) shows pre-test ring cracks (note a 'V' defect on the right side). After 27 million stress cycles, new surface cracks are found beside the original ring cracks (see figure 3.40(b), the 'V' defect is still visible). These new cracks are defined as secondary surface cracks in this study. Most of the secondary surface cracks lie to the right of the original ring crack and only a few to the left. This ball is sectioned and polished to investigate the subsurface crack propagation behaviour. Figure 3.40(c) is a surface view of the failure ball, which shows the section positions to be observed. Figure 3.40(d) is a dark field image of surface view.

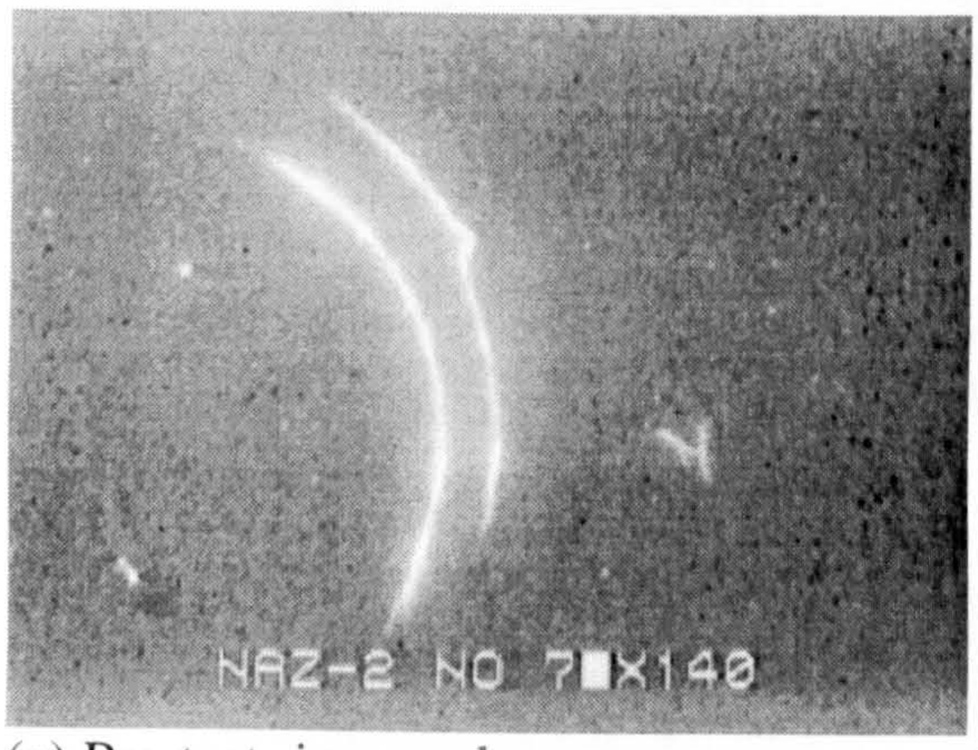

(a) Pre-test ring cracks

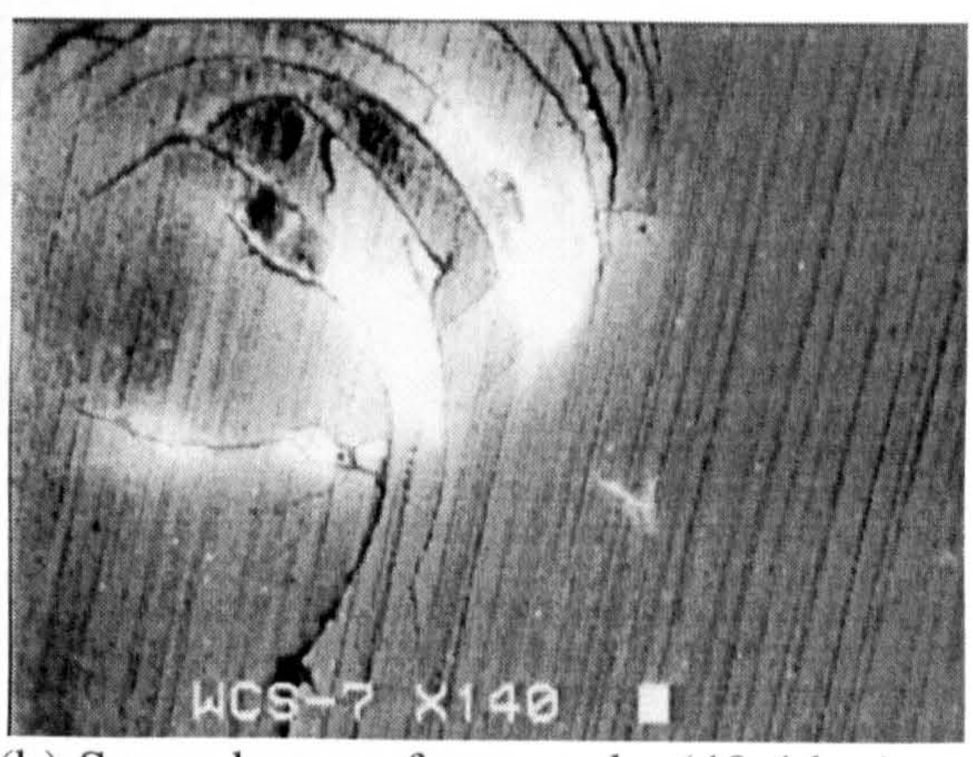

(b) Secondary surface cracks (40.4 hrs)

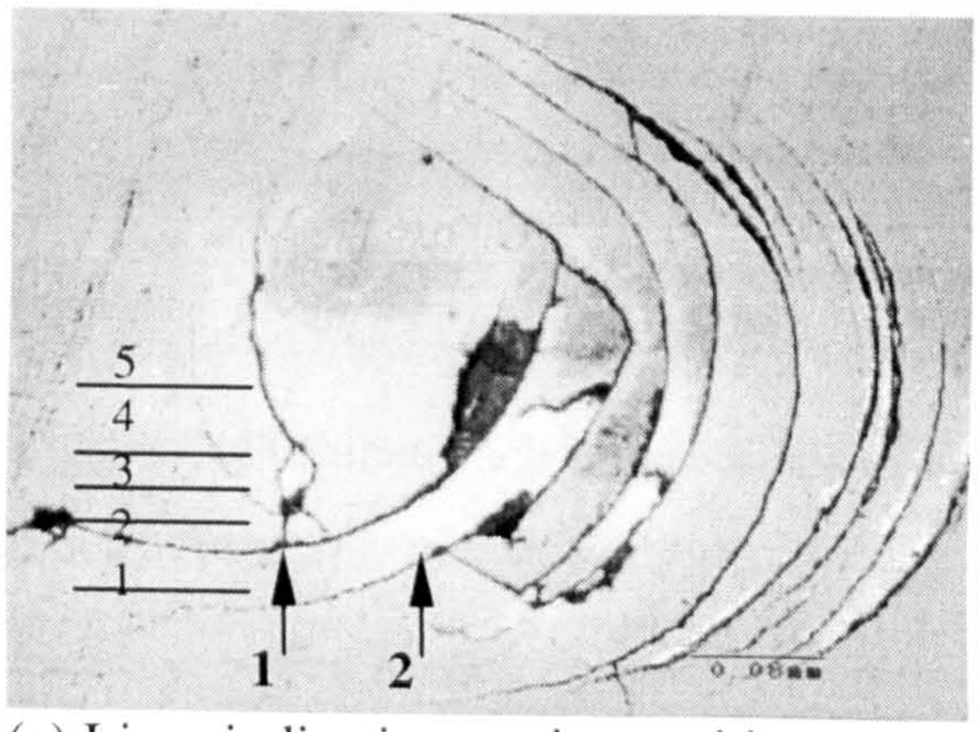

(c) Lines indicating section position

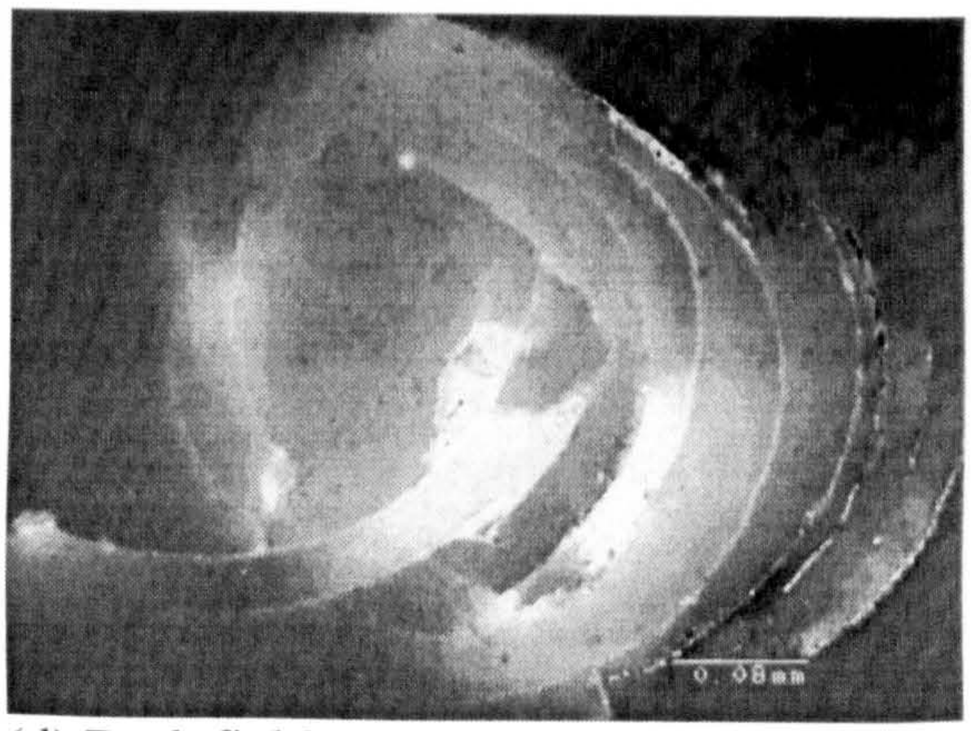

(d) Dark field

Figure 3.40 Surface observations of original ring crack incipient failure (Test 5).

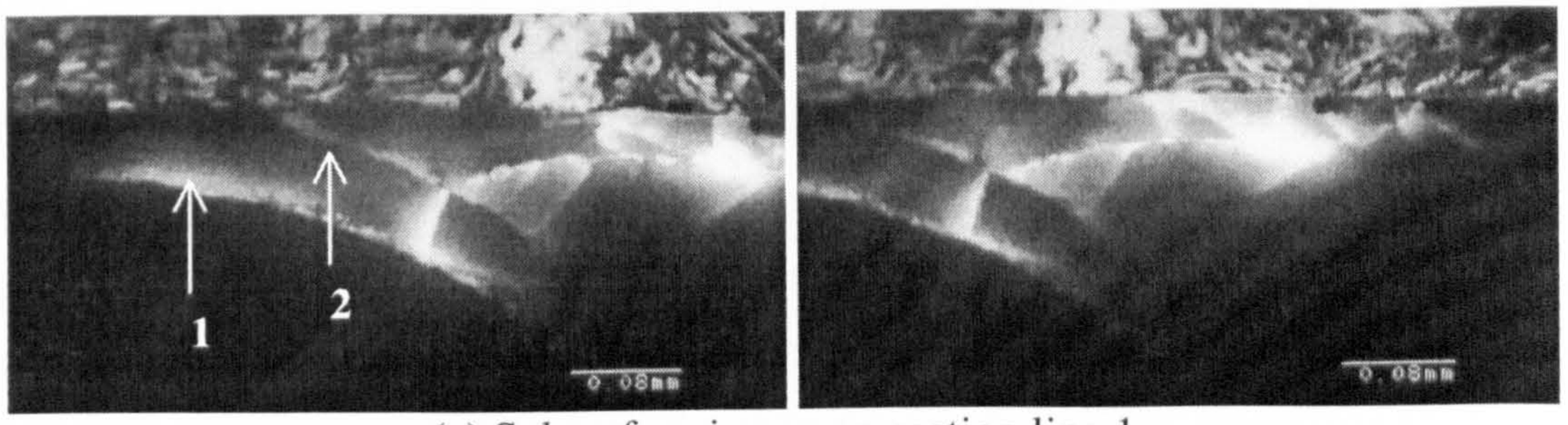

(a) Subsurface image on section line 1

(b) 15 μm from line 1

(c) 30 μm from line 1

(d) Subsurface image on section line 2

Figure 3.41 Subsurface observations of the original ring cracks and secondary surface cracks (Test 5).

The ball is sectioned near the crack and then polished gradually across the ring crack to examine the profile of crack propagation. There are five lines on figure 3.40(c), which show the sites at which the section images are taken. From the first line

to the secondary line the micrographs are taken at every 15 μm. The subsurface image from the first section (line 1) is shown in figure 3.41(a), using microscopic analysis with ultra-violet light. Figures 3.41(b) and 3.41(c) show later images taken at every 15 μm. Figure 3.41(d) shows the image taken at the second line. The number in figure 3.41(a) indicates the cracks corresponding to the cracks in figure 3.40(c). In this case the maximum crack extension is 0.21 mm for crack number 1 and 0.13 mm for crack number 2. The ring crack section indicates that the crack growth path is conical away from the surface.

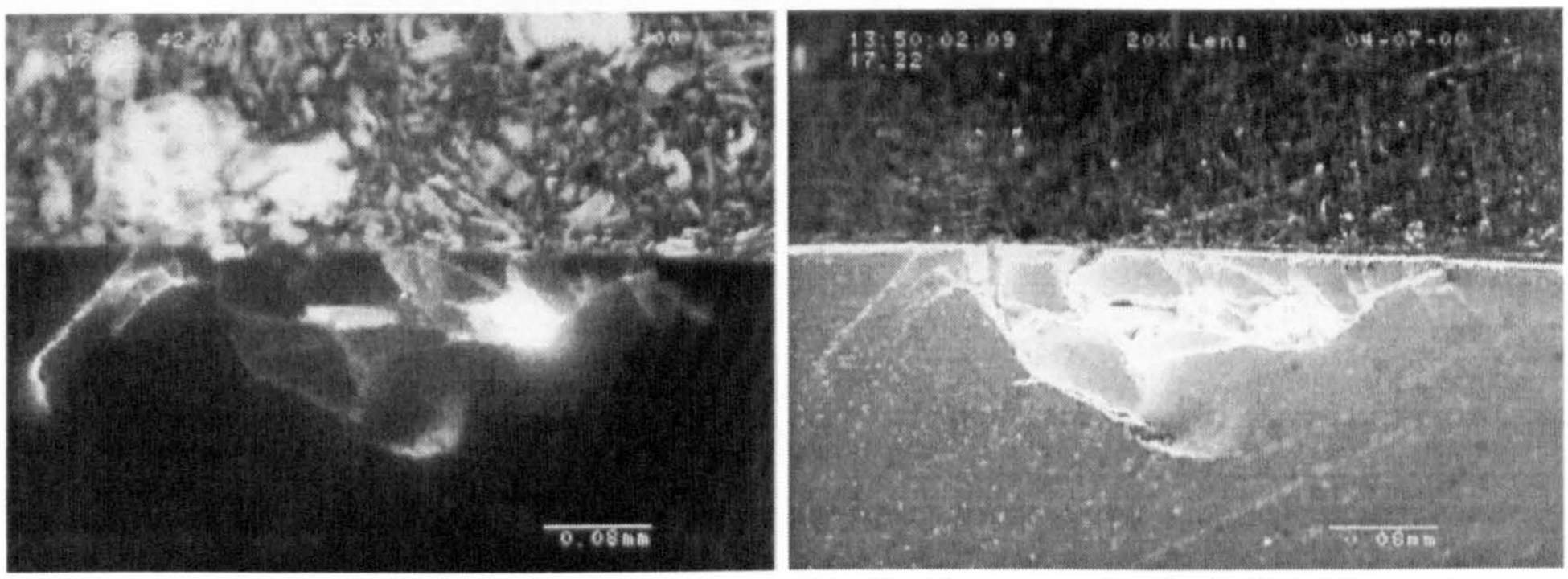

(a) Crack network (UV light image) (b) Crack network (dark field image)

Figure 3.42 Subsurface observations at line 3 (Test 5).

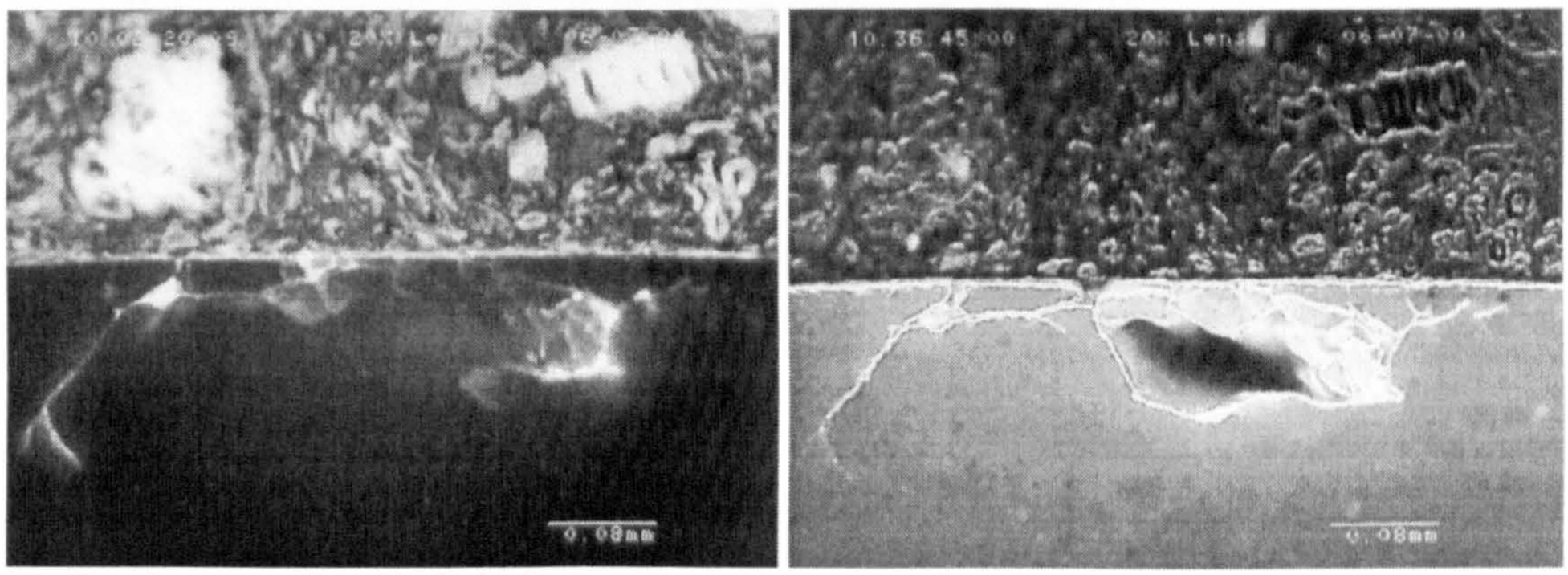

(a) Crack network (UV light image) (b) Crack network (dark field image)

Figure 3.43 Subsurface observations at line 4 (Test 5).

Figure 3.42 shows the subsurface images observed at line 3. A detailed crack network (just before spalling) is clearly exhibited. Figure 3.42 reveals that the secondary surface cracks propagate conically towards the material. Subsurface

branched cracks are formed along the crack growth path. Results indicate that the spalling may reach a depth of about 100 μm.

Figure 3.43 shows the subsurface images observed at line 4. Results reveal that the depth changes due to the section position are less than the depth observed at line 3 (figure 3.42). Some material is removed during the processes of grinding and polishing. The crack network is clearly shown in figures 3.43(a) and 3.43(b).

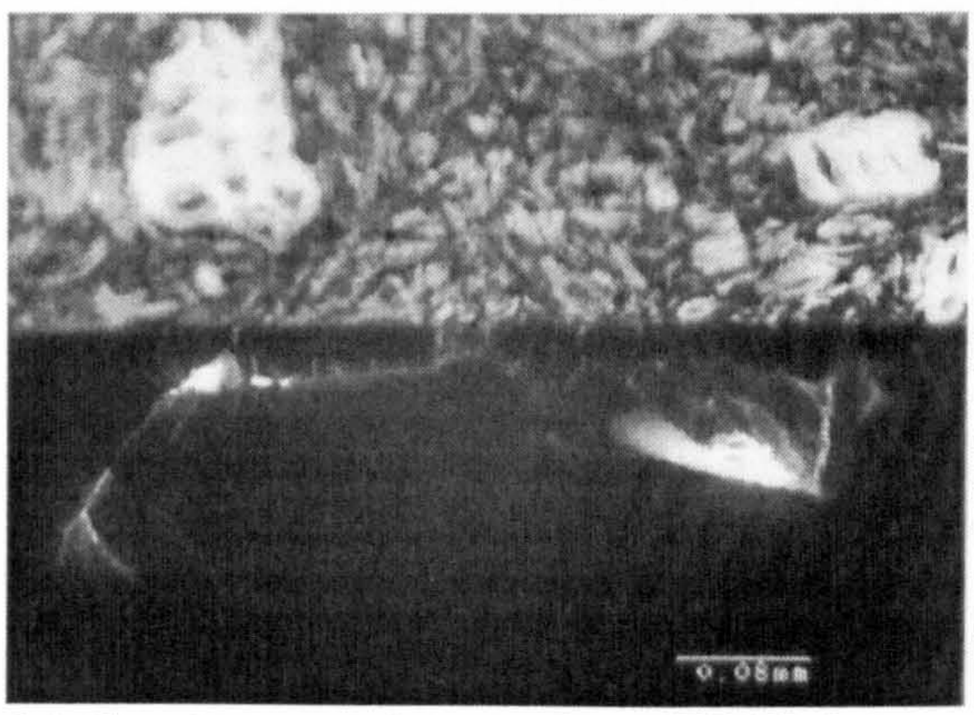

(a) Crack network overview (UV light)

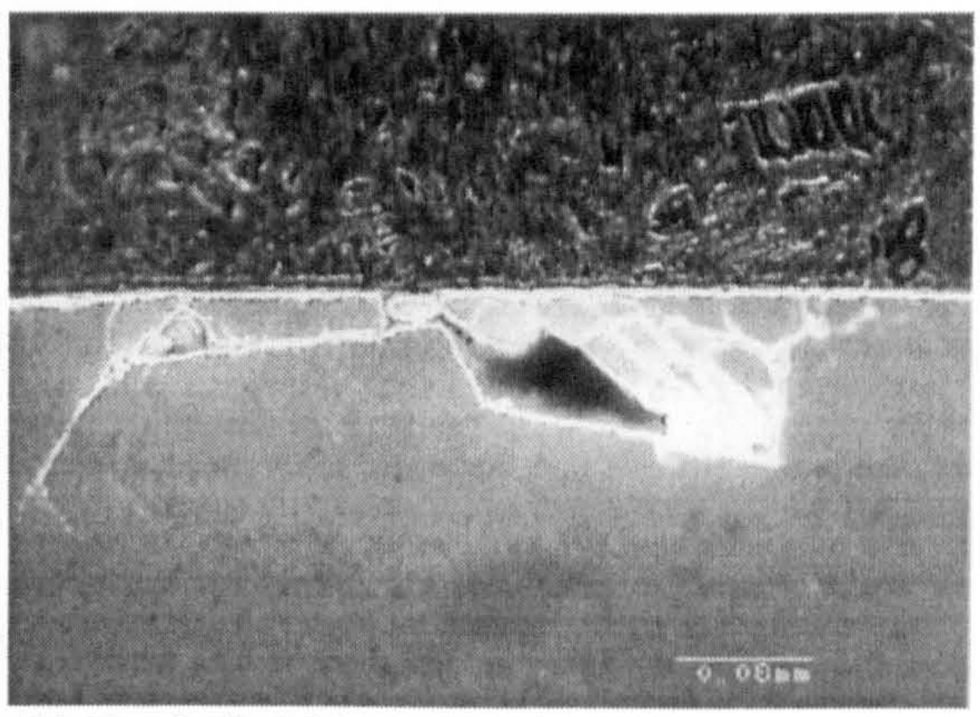

(b) Dark field image

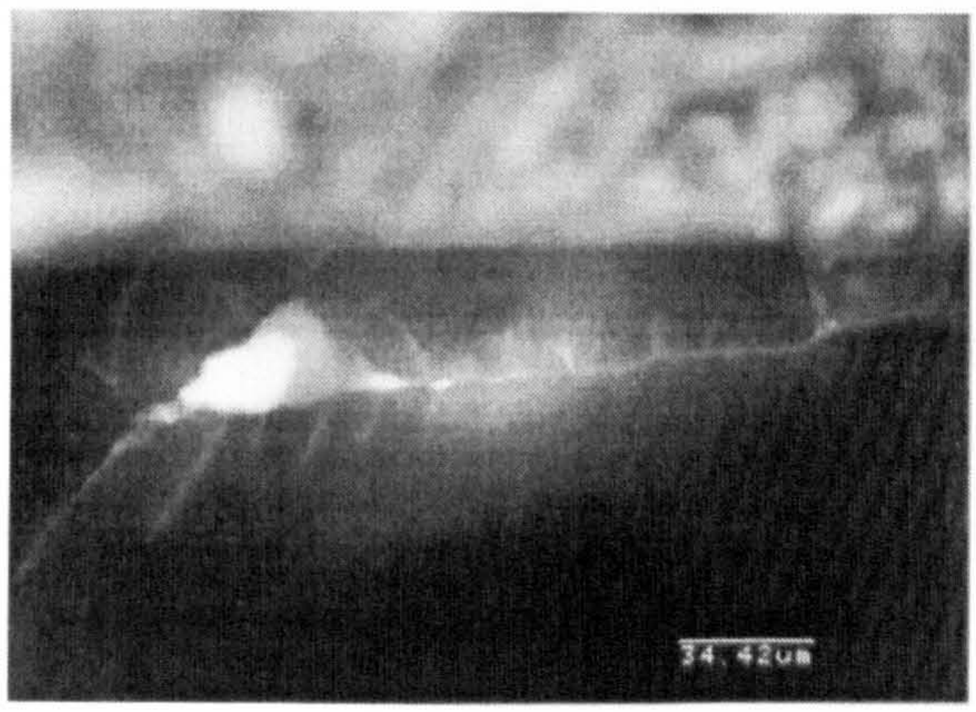

(c) Left part detailed view (UV light)

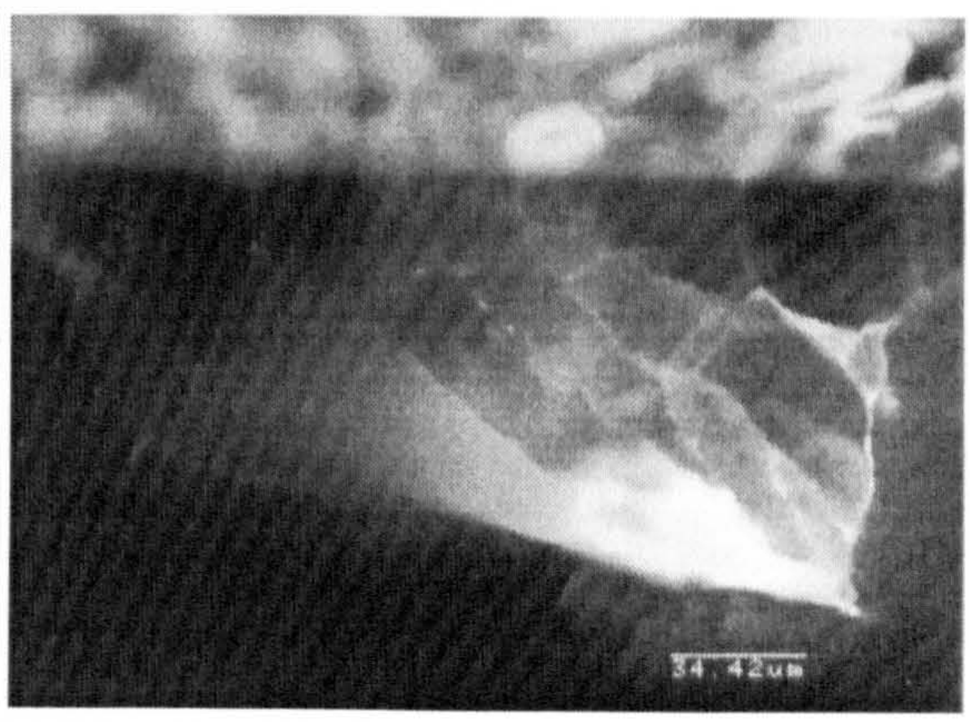

(d) Right part detailed view (UV light)

Figure 3.44 Subsurface observations at line 5 (Test 5).

Figure 3.44 shows the subsurface images observed at line 5. This location is close to the central line of the contact path. An overview of crack network is shown in

figures 3.44(a) and 3.44(b). The subsurface network is clear and the depth is less than the depth observed at line 4 (figure 3.43). Unlike figure 3.43, many branched cracks are generated on the upper and lower crack faces. A detailed view of these branched cracks is shown in figure 3.44(c). The distance between the branched cracks is on average of 8-10 μm, which is close to the predicted distance (5-10μm) (see Chapter 5). The subsurface observations provide evidence supporting the prediction that subsurface branch cracks can be generated on the crack faces from numerical analysis. Figure 3.44(d) shows a detailed view of the right part in figure 3.44(a), which shows how a spall is formed.

Subsurface observations reveal that the fatigue spall is mainly caused by two factors. One is from secondary surface crack propagation. The secondary surface cracks propagate conically away from the surface and will meet the main crack growth path from original ring cracks. Branched cracks can also be generated on the faces of each secondary crack and these cracks connect with each other to form a broken crack network. Spalling sheets eventually come away due to the broken crack network. Another contributing factor is from subsurface branch crack propagation. These branched cracks formed on the upper crack face may grow towards the ball surface acted on by the contact circle when they lie in certain positions. Aspects of crack growth mechanics will be discussed in Chapter 5.

3.5 INVESTIGATIONS OF MICRO-CRACK WEAR PATTERNS

In previous sections, spalling fatigue failure caused by pre-existing ring cracks is described. Micro-cracks on the contact path are found, which cause surface damage. Detailed observations of micro-crack wear patterns are described below.

Surface damage derived from these micro-cracks always starts at the edge of the contact path and then gradually spreads into the centre of the contact path as the test proceeds. The micro-cracks form first and develop into wear scars. The micro-cracks always take the shape of a small partial circle. These micro-cracks may be caused by Hertz contact through the asperity contacts. The contact geometry and surface traction conditions (slip or spin) influence the micro-crack distribution on the contact path. Figure 3.45 shows an example of micro-crack wear patterns in silicon nitride from Test C (high viscosity lubricant).

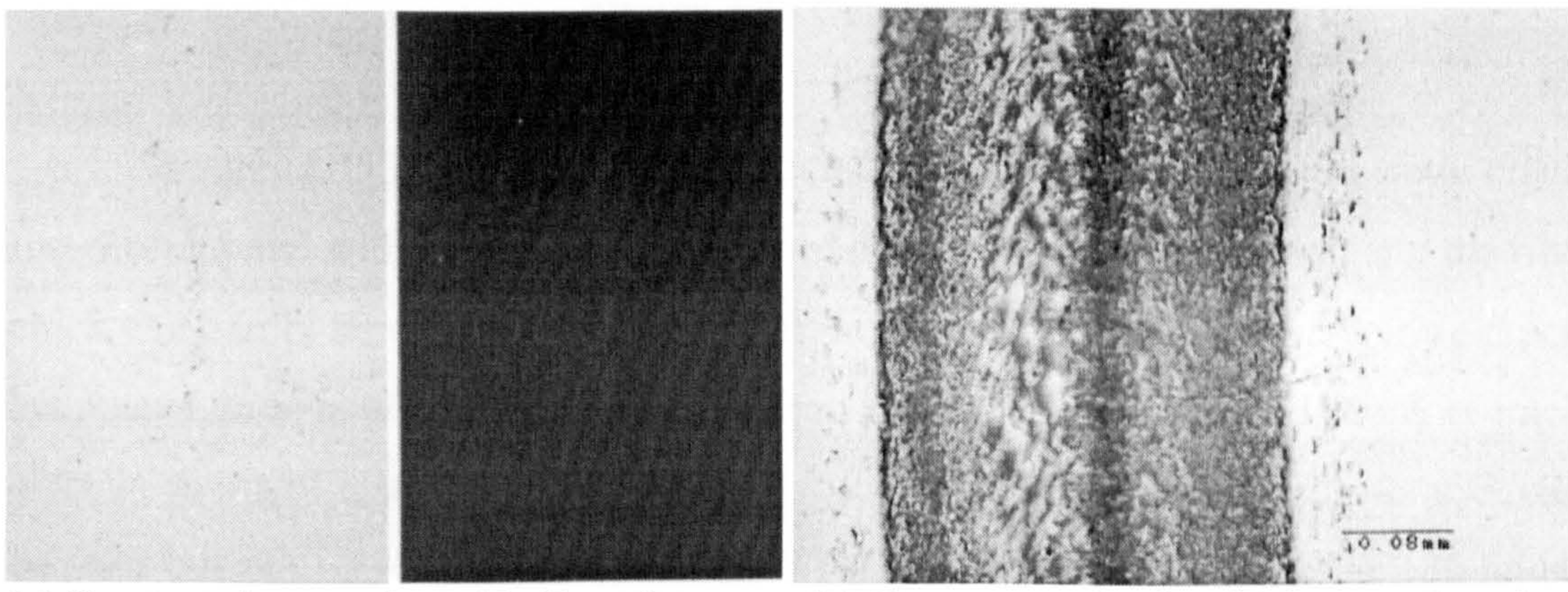

(a) Pre-test ring crack and ball surface

(b) Contact track after 21 hours of testing

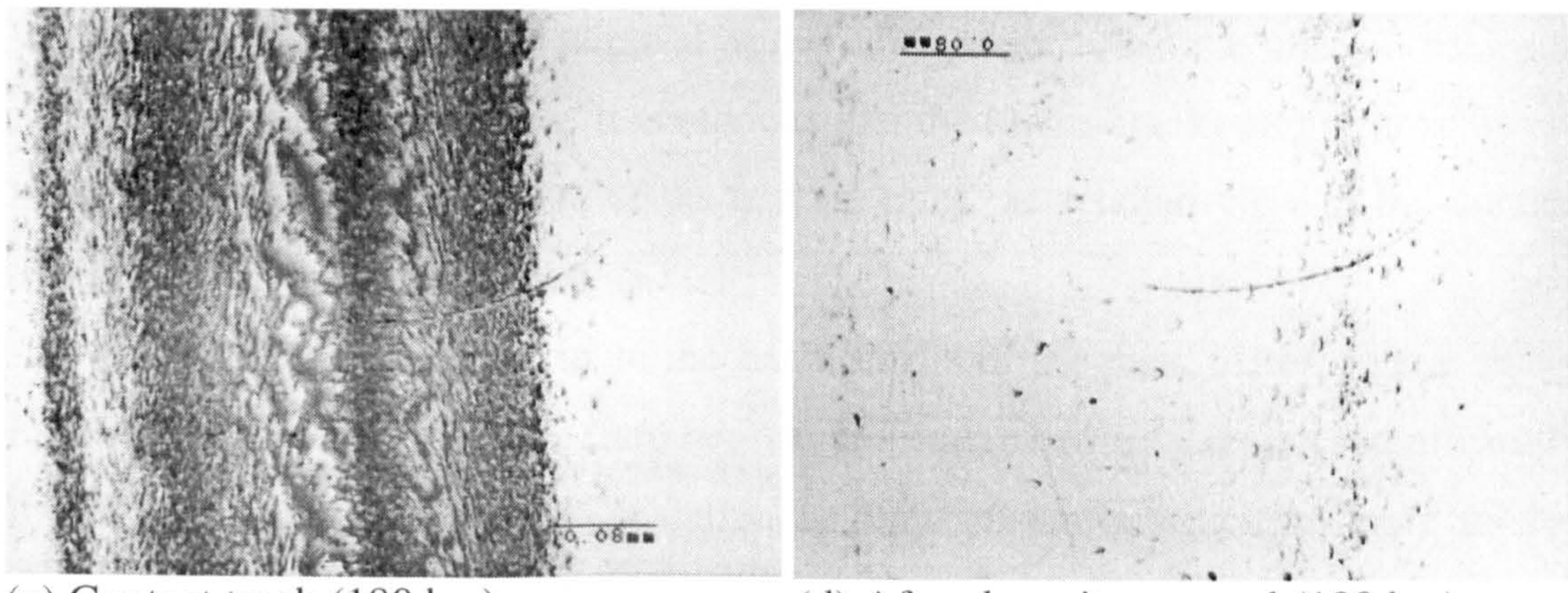

(c) Contact track (180 hrs)

(d) After deposit removed (180 hrs)

Figure 3.45 Surface observations of the contact track (Test C).

(e) Detailed views of the contact track after deposit removed

Figure 3.45 Continued.

Figure 3.45(a) illustrates ceramic ball surface with a pre-test ring crack (bright field and with UV light). The surface is in an excellent condition and the ring crack can hardly be seen without the UV light illumination. However, the ring crack becomes more visible during the fatigue test. Figure 3.45(b) shows the contact track after 21 hours of testing. Oil deposits cover the contact track. The micro-cracks can be seen but not very clearly. Figure 3.45(c) shows the contact track after 180 hours of testing. As in figure 3.45(b), oil deposits cover the contact track. Figure 3.45(d) shows the contact track after removal of the oil deposits, when the micro-cracks and wear scars can be seen clearly. It is obvious that the micro-cracks and wear scars are mainly distributed on the edge of the contact track. A detailed view of the contact track is shown in figure 3.45(e).

The micro cracks occur in the early stages of the tests. After a great many micro-cracks are formed the number of the micro-cracks are not significantly increased as the tests proceed. A stationary phase exists in which no more micro-cracks are generated. Consequently, the contact path will not significantly change in this period of time. Figure 3.46 shows this phenomenon (Test 10, low viscosity lubricant). Figure 3.46(a) is the surface after 26 hours of testing, which shows that micro-cracks have occurred at the edge. Figure 3.46(b) shows the micro-cracks

occurring at the upper edge. Figure 3.46(c) shows the micro-cracks occurring at the lower edge area. Figures 3.46(d) to 3.46(f) show the surface image of the same area but after different testing times.

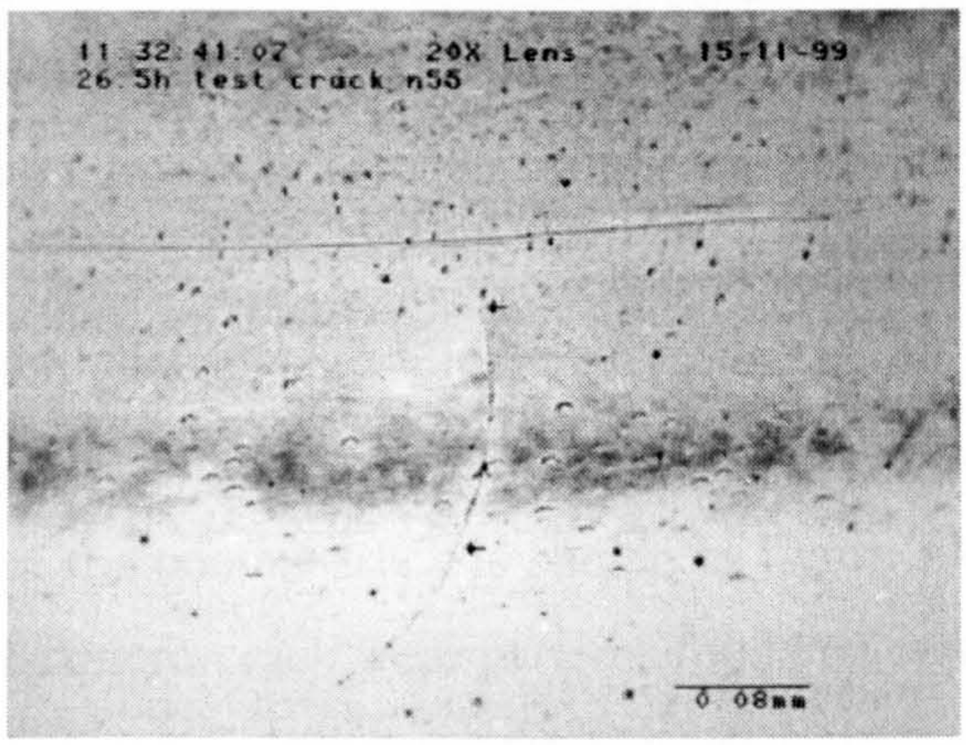

(a) Overview of contact track (26.5 hrs)

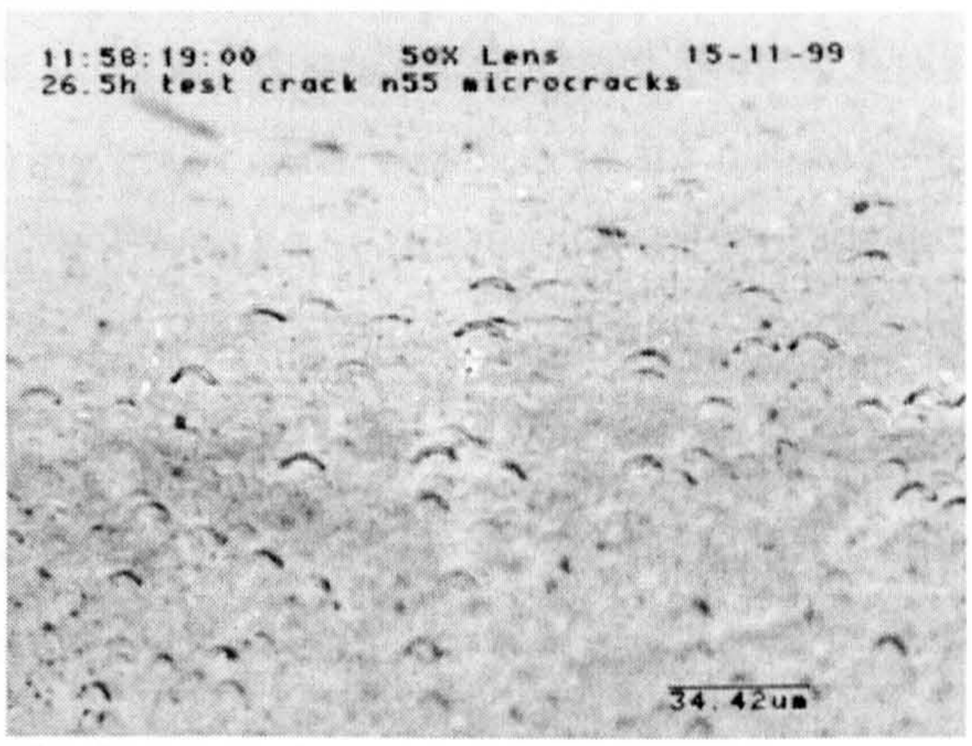

(b) Upper edge area detail (26.5 hrs)

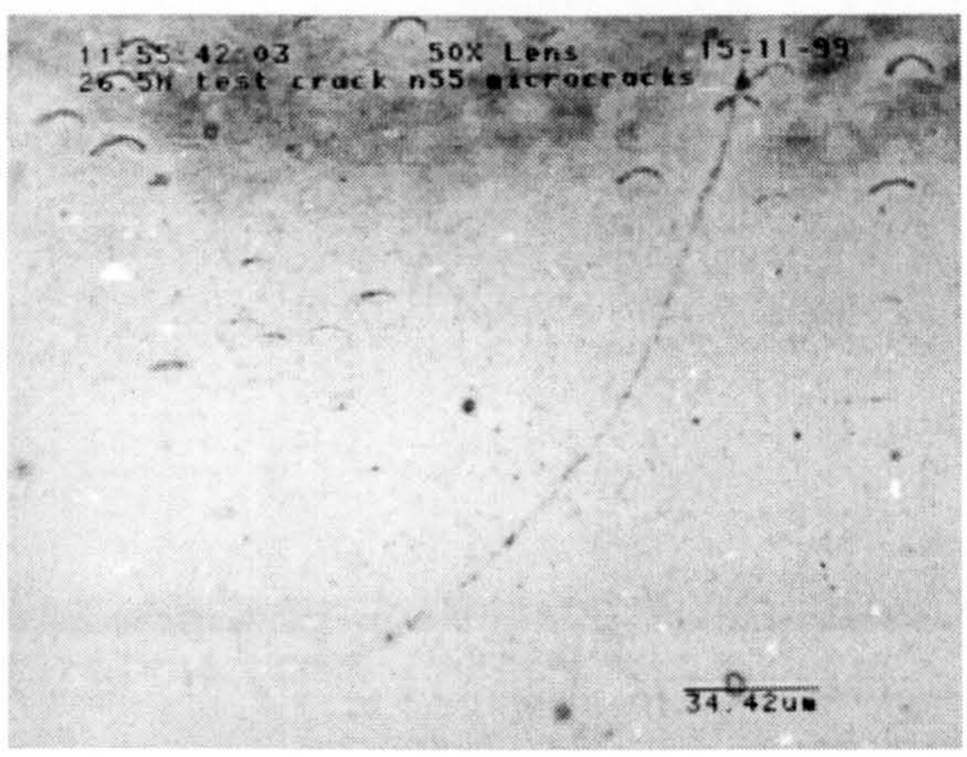

(c) Lower edge area detail (26.5 hrs)

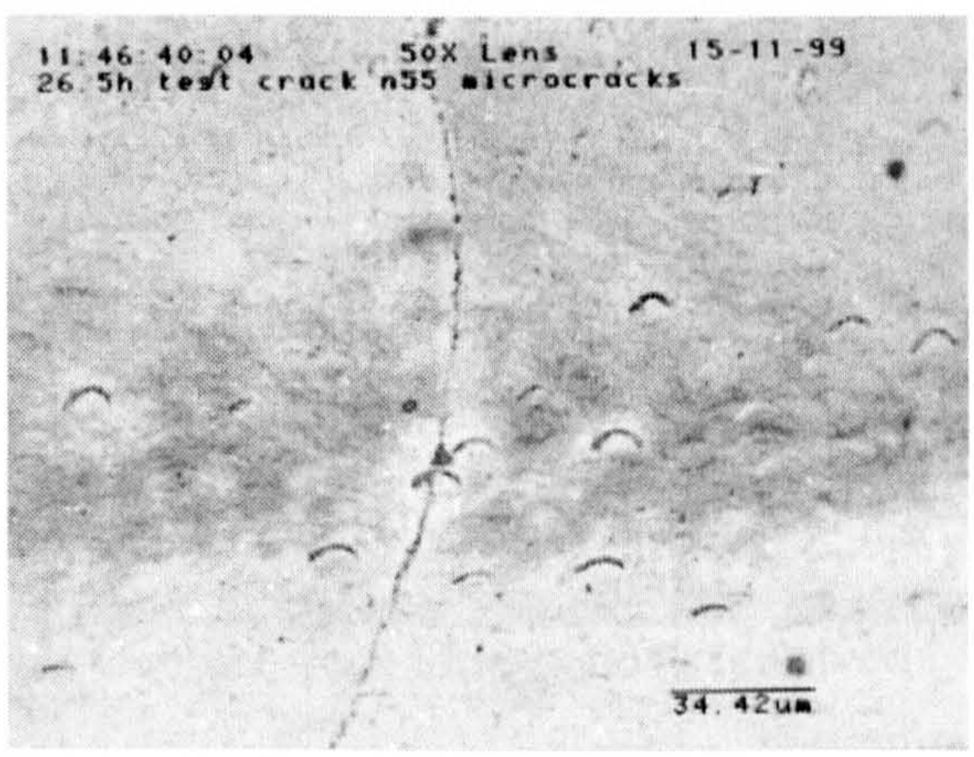

(d) Micro-crack detail (26.5 hrs)

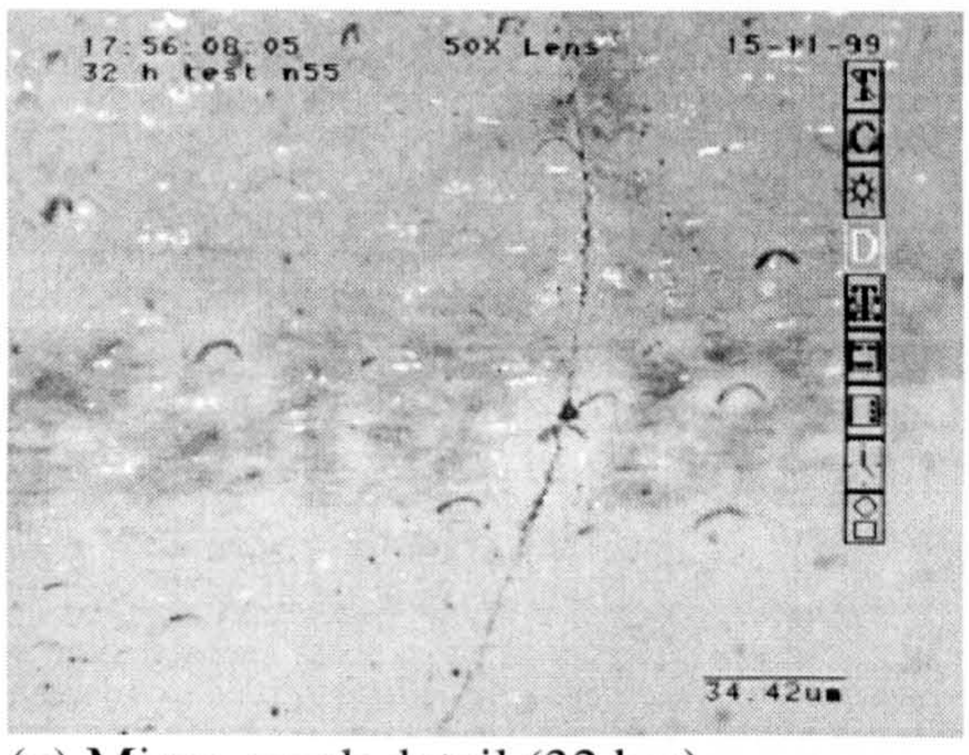

(e) Micro-crack detail (32 hrs)

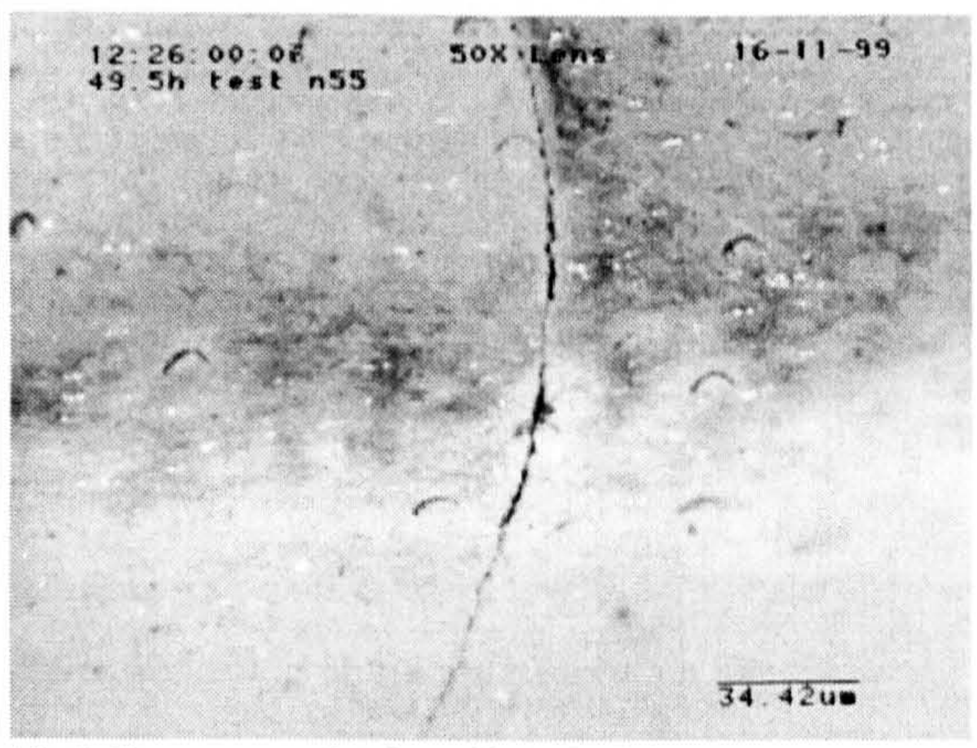

(f) Micro-crack detail (49.5 hrs)

Figure 3.46 Surface observations of the contact track (Test 10).

Contact track observations of high contact stresses (Test G) are shown in figure 3.47. The process of surface damage has been described in the previous section (see figure 3.15, Section 3.1), where the micro-crack wear did not occur before about 70 hours of testing. Figure 3.47(a) shows the contact track after 94 hours of testing. The micro-cracks and wear scars are distributed on the contact track and more wear is seen around the original ring crack. The wear scars are not easy to see clearly due to the oil deposits covering the contact path. Figure 4.47(b) shows the contact path after removal of the oil deposits. The wear distribution is clearly shown on the track. The surface damage caused by spin is apparent. A detailed view of the contact track is shown in figure 3.47(c). Figure 3.48 shows another example of micro-crack wear patterns found on ceramic balls (Test G).

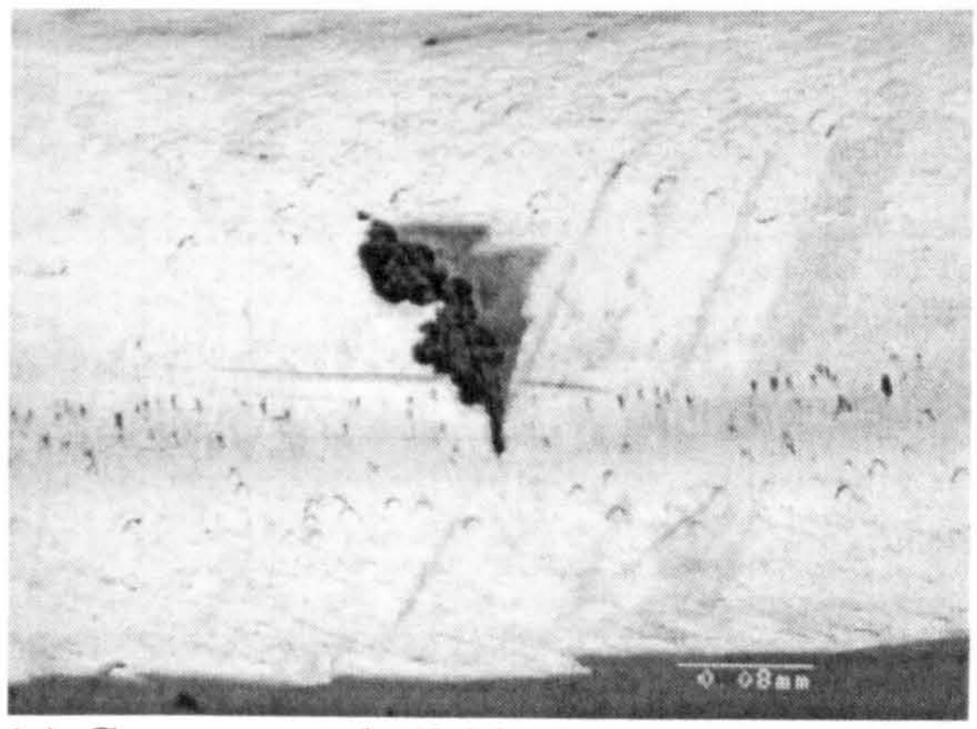

(a) Contact track (94 hrs)

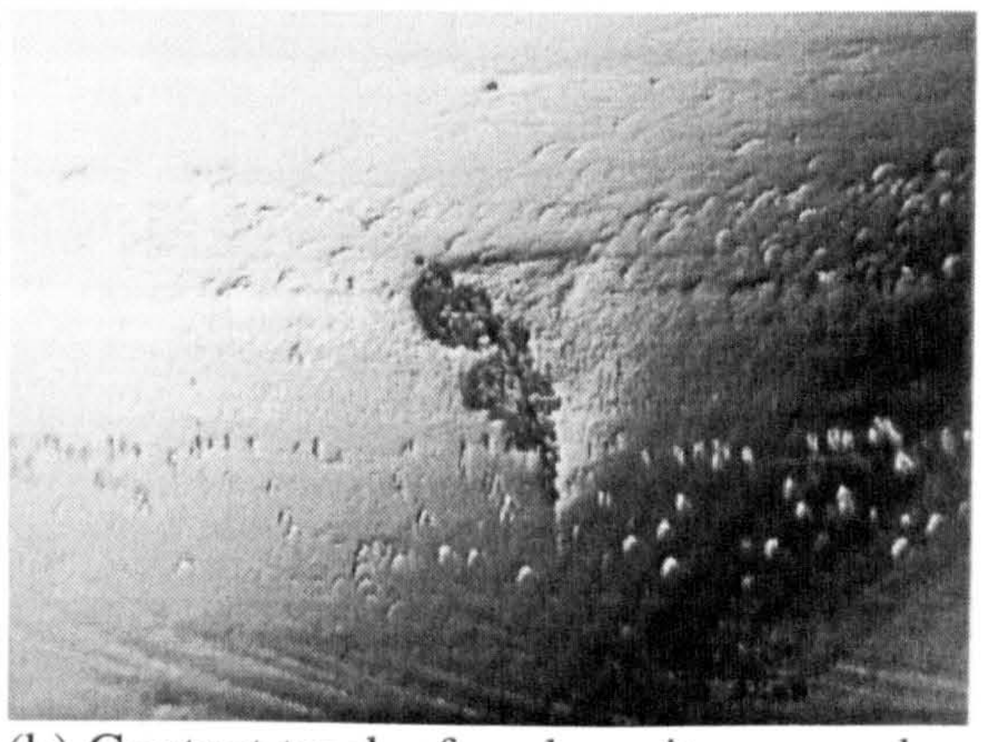

(b) Contact track after deposit removed

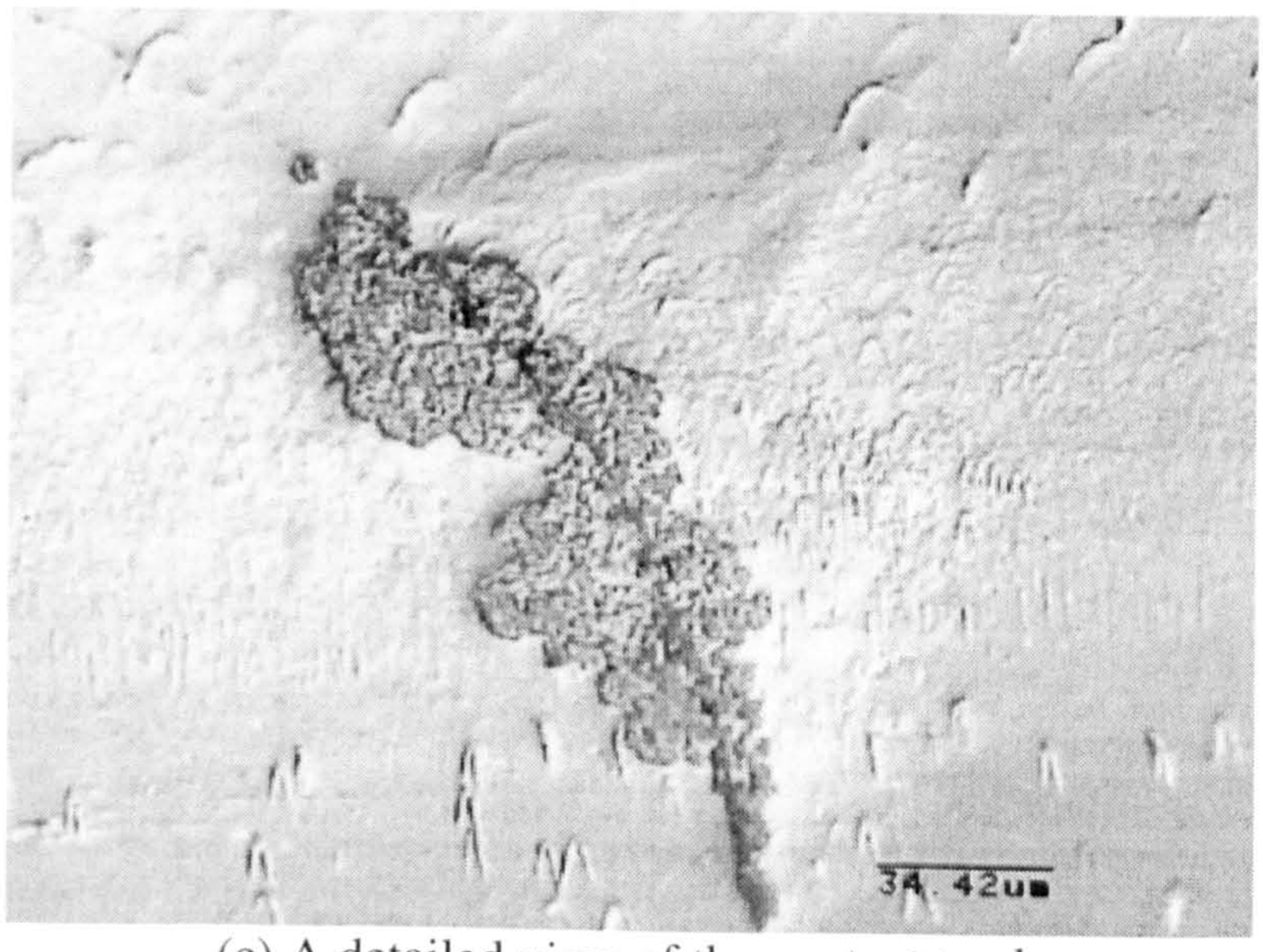

(c) A detailed view of the contact track

Figure 3.47 Surface observations around the ring crack (Test G).

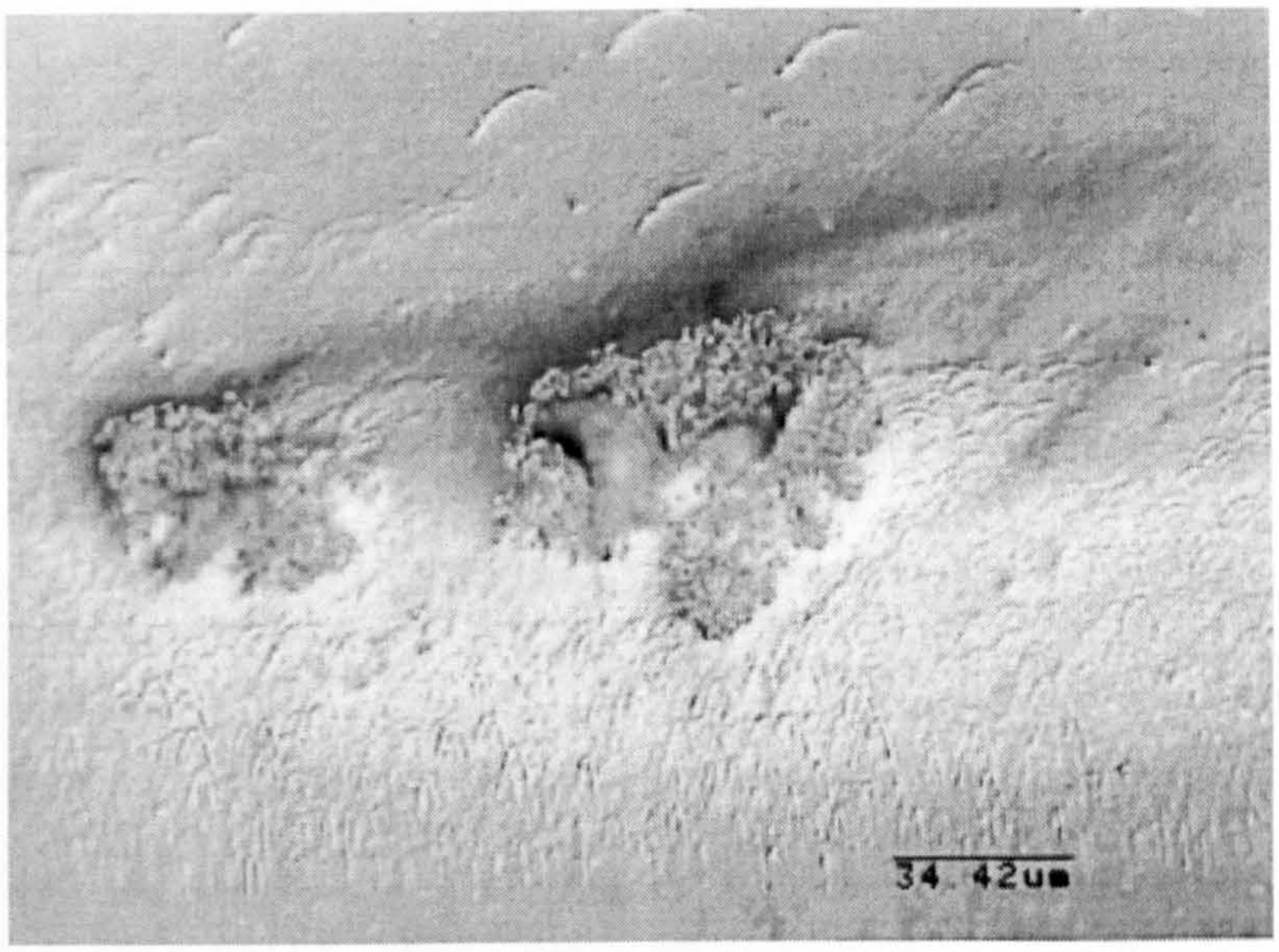

Figure 3.48 Surface observations of the contact track (Test G).

The reason for these micro-crack wear patterns can be explained using the mechanics of crack face contact (see Chapter 5) though the scale of micro-cracks is small. As discussed above, the micro-cracks are normally formed at the beginning of the tests. Wear scars derived from these micro-cracks occur after some hours of testing. According to the analysis of the crack face contact, secondary surface cracks will not be generated until the crack gap reaches a certain size. Time is required for this gap to form. When the crack gap reaches the critical size, secondary surface cracks are generated around the pre-microcracks. These new small surface cracks propagate and connect to form a very small scar.

3.6 RING CRACK CHARACTERISATION

3.6.1 Surface appearance

Light microscopy is employed to examine the silicon nitride ball surfaces and characterise ring crack defects. A dye-penetrant method is utilised to enhance the detection of ring cracks. Seventy-five silicon nitride balls are inspected, and ninety six percent are found to contain surface defects, the majority of which are surface ring cracks.

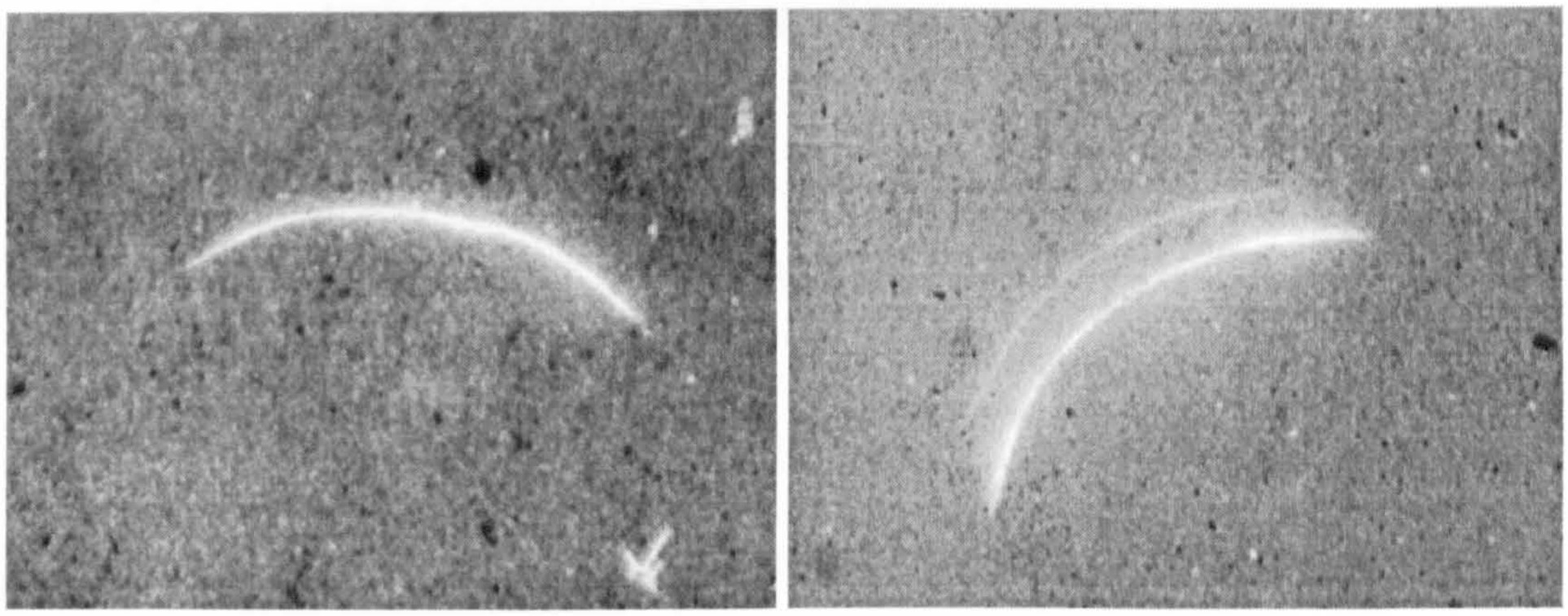

(a) Single crack on one side (× 140) (b) Double cracks on one side (× 140)

(c) Single crack on two sides (× 140) (d) Multiple cracks on two sides (× 140)

Figure 3.49 Surface ring cracks found on silicon nitride ball surfaces.

Figure 3.49 shows four examples of ring cracks found on the silicon nitride ball surfaces before testing. These ring cracks are circular, extending for the arc length, approximately one-quarter of the circumference of a circle. Most of them present in the form of a single ring crack on one side (figure 3.49(a)) or double ring

cracks on one side (figure 3.49(b)), a few are double ring cracks on two sides, or multiple cracks on two sides (figure 3.49(c) and (d)).

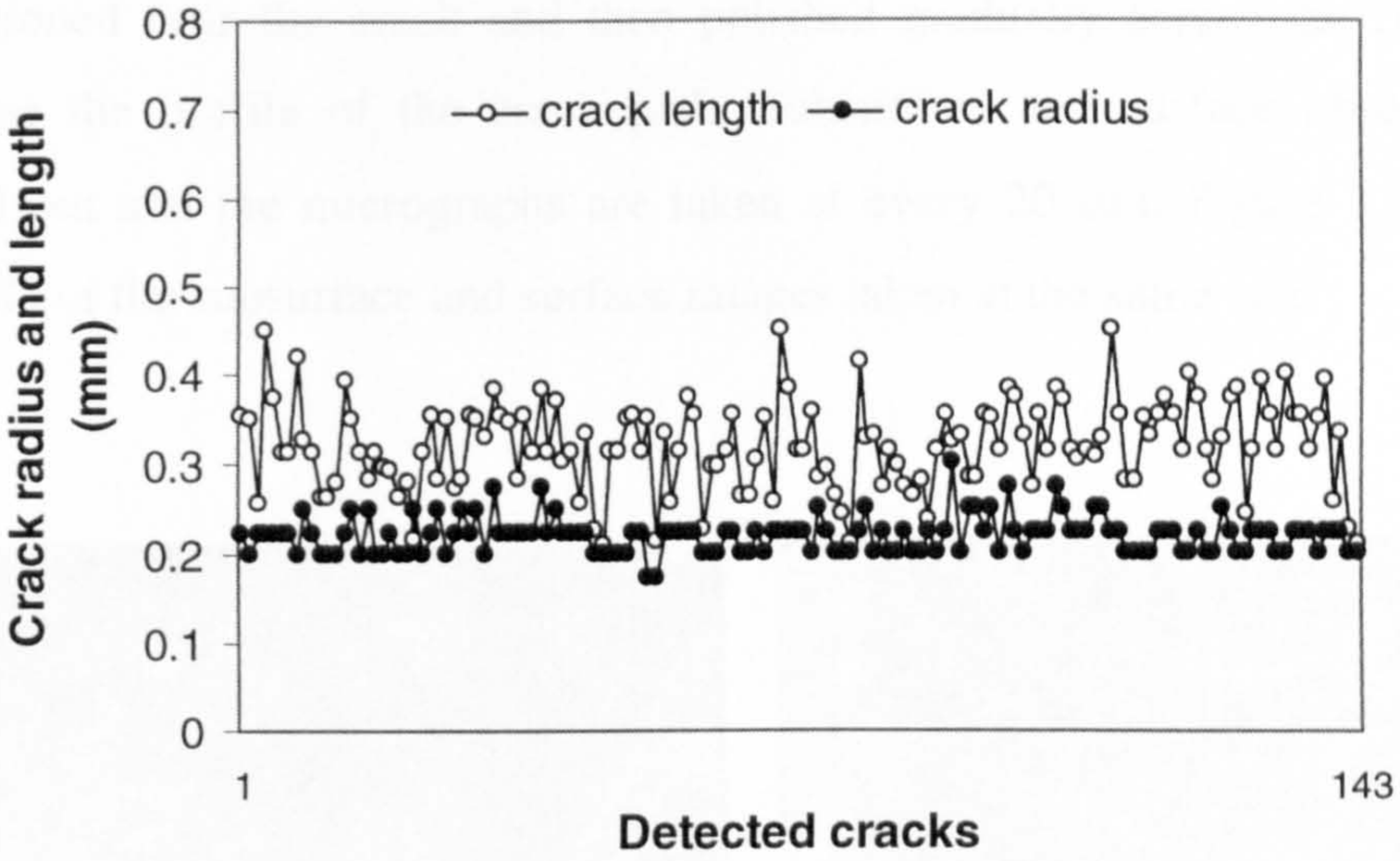

Figure 3.50 Crack radius and length versus detected cracks.

Figure 3.50 plots the radius and arc length of the detected cracks. The ring crack radius varies in the range of 0.19 mm to 0.27mm, most are around 0.22 mm and the average radius is approximately 0.224 mm. These cracks are called "natural" ring cracks here because they were present on purchased silicon nitride balls. Statistical distributions of detected surface ring cracks in silicon nitride balls are shown in figure 3.51.

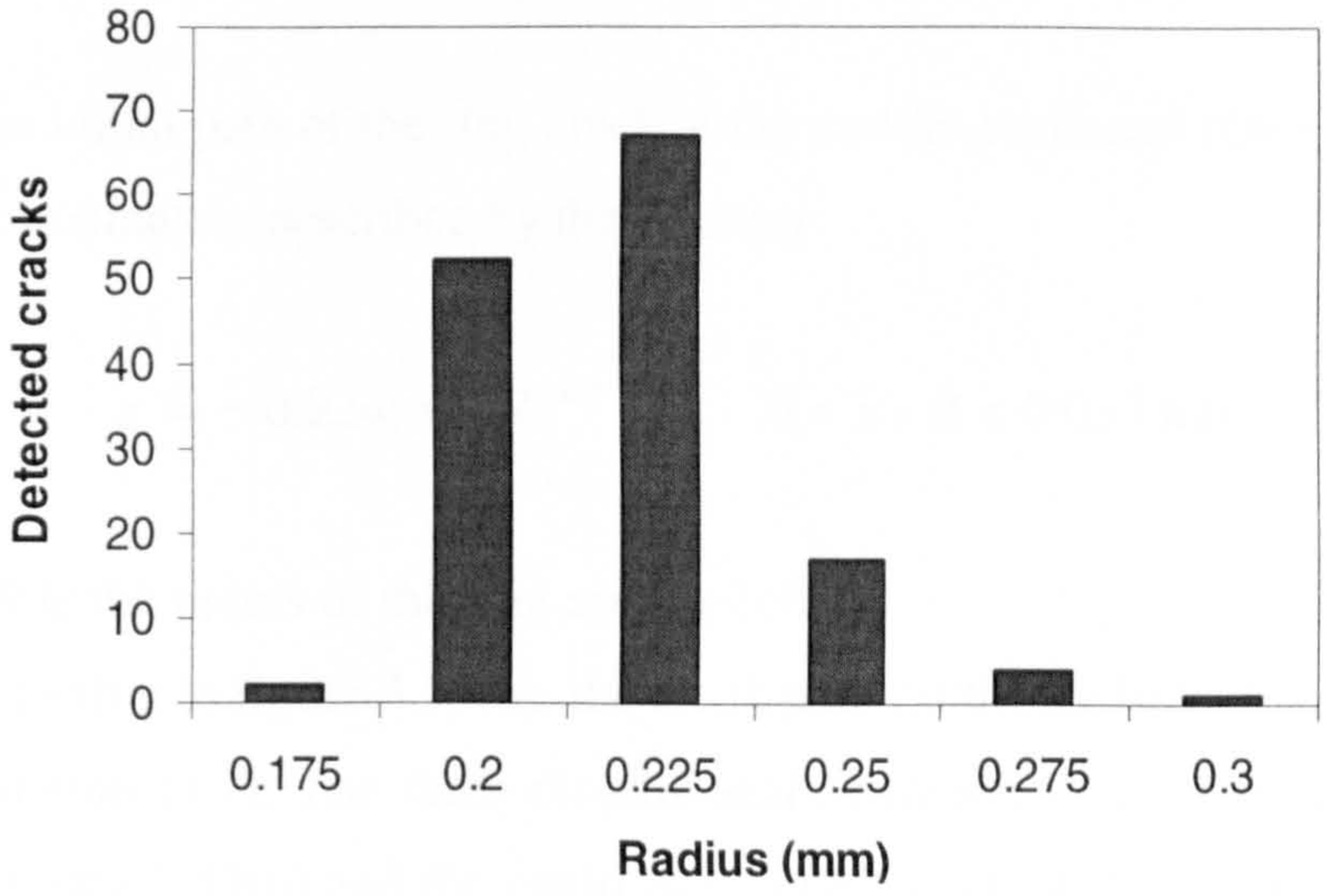

Figure 3.51 Statistical distributions of detected surface ring cracks.

3.6.2 Subsurface geometry characteristics

To study the subsurface geometry of the surface ring crack, the cracked ball is sectioned near the crack and then polished gradually across the ring crack to examine the profile of the crack path. Subsurface and surface observations are carried out and the micrographs are taken at every 20 μm. Figure 3.52 shows an example of the subsurface and surface images taken at the same site.

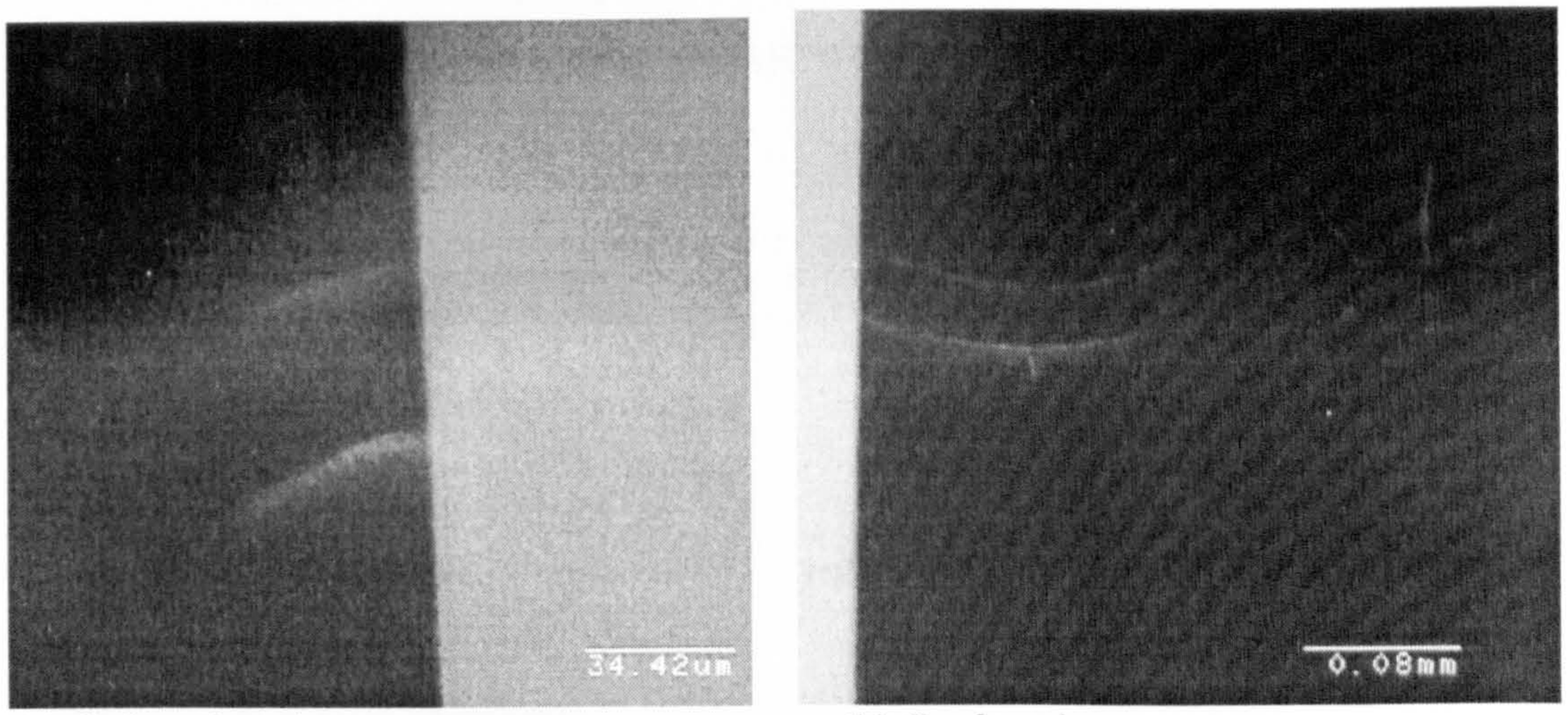

(a) Subsurface image (b) Surface image

Figure 3.52 Surface and subsurface observations of a ring crack.

The initial path of the ring crack at the middle-sectioned plane (figure 3.53(a)) can be approximately described by the equation

$$z = -0.224(x - R)^{0.5} \qquad 0 < x - R < 0.035 \text{ mm} \qquad (3.1)$$

in which R is the radius of the ring crack circle.

Referring to figure 3.53(b), the crack path on the sectioned plane is described by the equation (3.1). The three-dimensional geometry of the surface ring crack is shown in figure 3.53(b) and the position of an element on the crack face referring to the co-ordinates, (x,y,z), may be written as

$$x = (R + l\cos\alpha\sqrt{1-(\phi/\phi_0)^2})\cos\phi \tag{3.2}$$

$$y = (R + l\cos\alpha\sqrt{1-(\phi/\phi_0)^2})\sin\phi \tag{3.3}$$

$$z = -0.224(l\cos\alpha\sqrt{1-(\phi/\phi_0)^2})^{1/2} \tag{3.4}$$

where l = crack depth, $0 < l <=$ maximum depth (line P_1P_2)

α = angle of line P_1P_2 to the ball surface, $0 < \alpha < \pi/2$

ϕ = angle of an element position on the crack face, $-\phi_0 < \phi < \phi_0$

ϕ_0 = half angle of ring crack arc AB, $0 < \phi_0 < \pi/2$

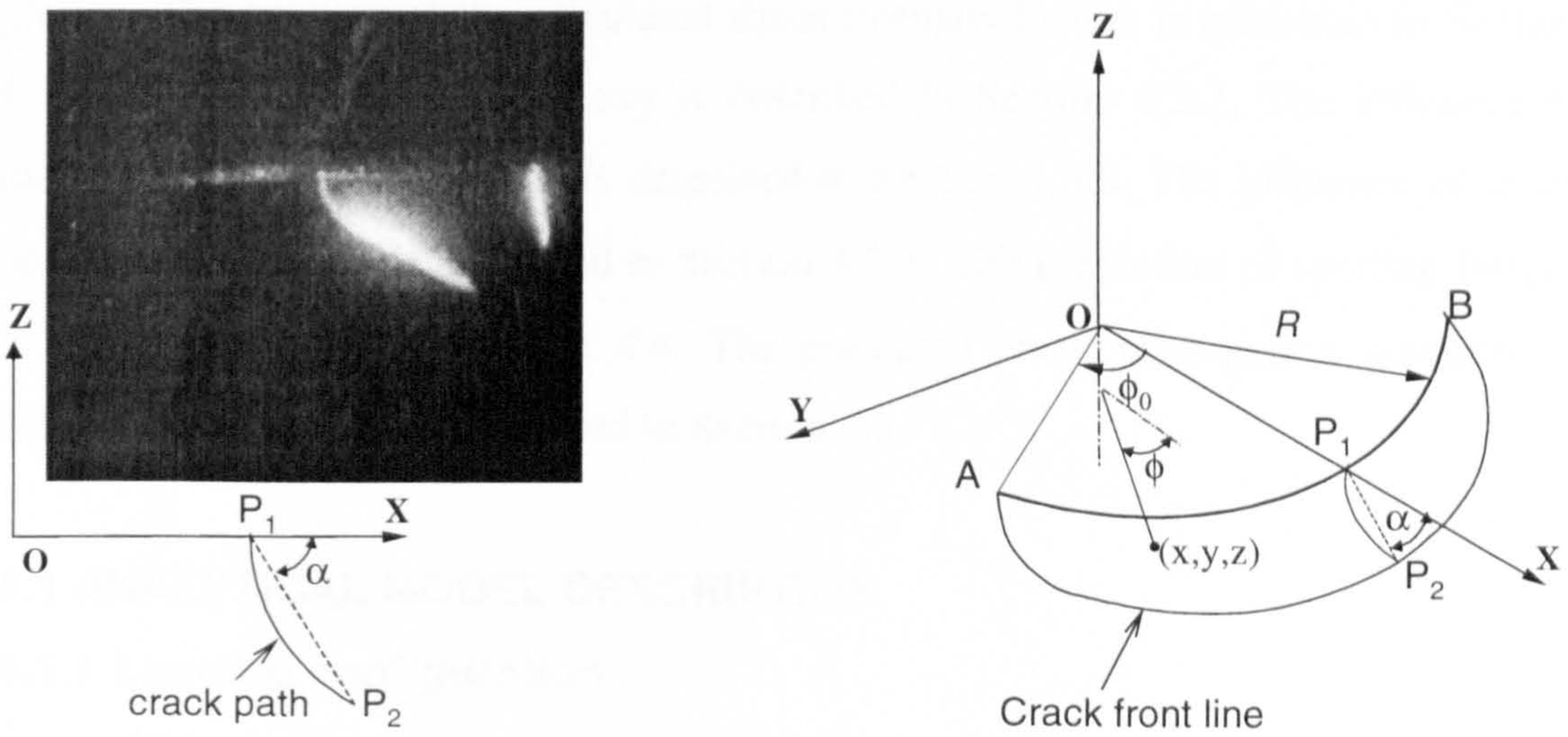

Figure 3.53 Ring crack geometry: (a) sectioned plane view, (b) 3D view.

CHAPTER 4

ANALYSIS OF RING CRACK PROPAGATION

An analytical study of surface ring crack propagation is presented in this Chapter. The purpose of the work is to accurately determine the stress intensity factor solution along the crack front loaded under both normal and tangential traction. A three-dimensional fracture model associated with surface ring crack propagation is developed and described in Section 4.1. Based on the model, stress intensity factors (SIF) are calculated using a boundary element method. The numerical fracture analysis scheme is described in Section 4.2.

The SIF solution is compared with the fracture toughness K_{IC} and threshold value ΔK_{th} of silicon nitride bearing materials to determine the possibility of crack growth. The analysis of the calculated stress intensity factors is presented in Section 4.3. The SIF with crack geometry is described in Section 4.3.1. The influence of loading conditions on the SIF is described in Section 4.3.2. The influence of crack positions on the SIF is described in Section 4.3.3. Life prediction of spalling fatigue failure is described in Section 4.4. The predicted crack propagation contours in different conditions are illustrated in Section 4.5.

4.1 ANALYTICAL MODEL DESCRIPTION

4.1.1 Loading configuration

The physical configuration of the testing environment is described in the previous discussion (Chapter 2, Section 2.3). This loading configuration is often used to simulate the service conditions of a real bearing working environment. The surface loading traverses the surface of the silicon nitride ball. This cyclic load moves across the surface ring crack, repeatedly. Figure 4.1 shows a surface ring crack subjected to this surface loading. For the purpose of the calculation, the surface loading is specified in terms of an assumed contact stress distribution. Assume that normal pressure $p(x,y)$ and tangential traction $q(x,y)$ within the contact region are expressed by the following equations:

$$p(x, y) = p_0(1 - x^2 / a^2 - y^2 / a^2)^{1/2} \qquad (4.1)$$

$$q(x, y) = fp(x, y) \qquad (4.2)$$

where p_0 is maximum normal pressure, a is the radius of the contact circle and f is the friction coefficient of Hertzian contact. It is assumed that $f < 0$ when the contact circle passes over the ring crack (arc AB) from right to left and $f > 0$ when passing from left to right. The maximum contact pressure p_0 is assigned to the various values to compare the loading effect. The co-ordinate x measures the distance from the centre of the contact circle to the centre of the ring crack circle and the stress intensity factors will be changed as the distance x changes.

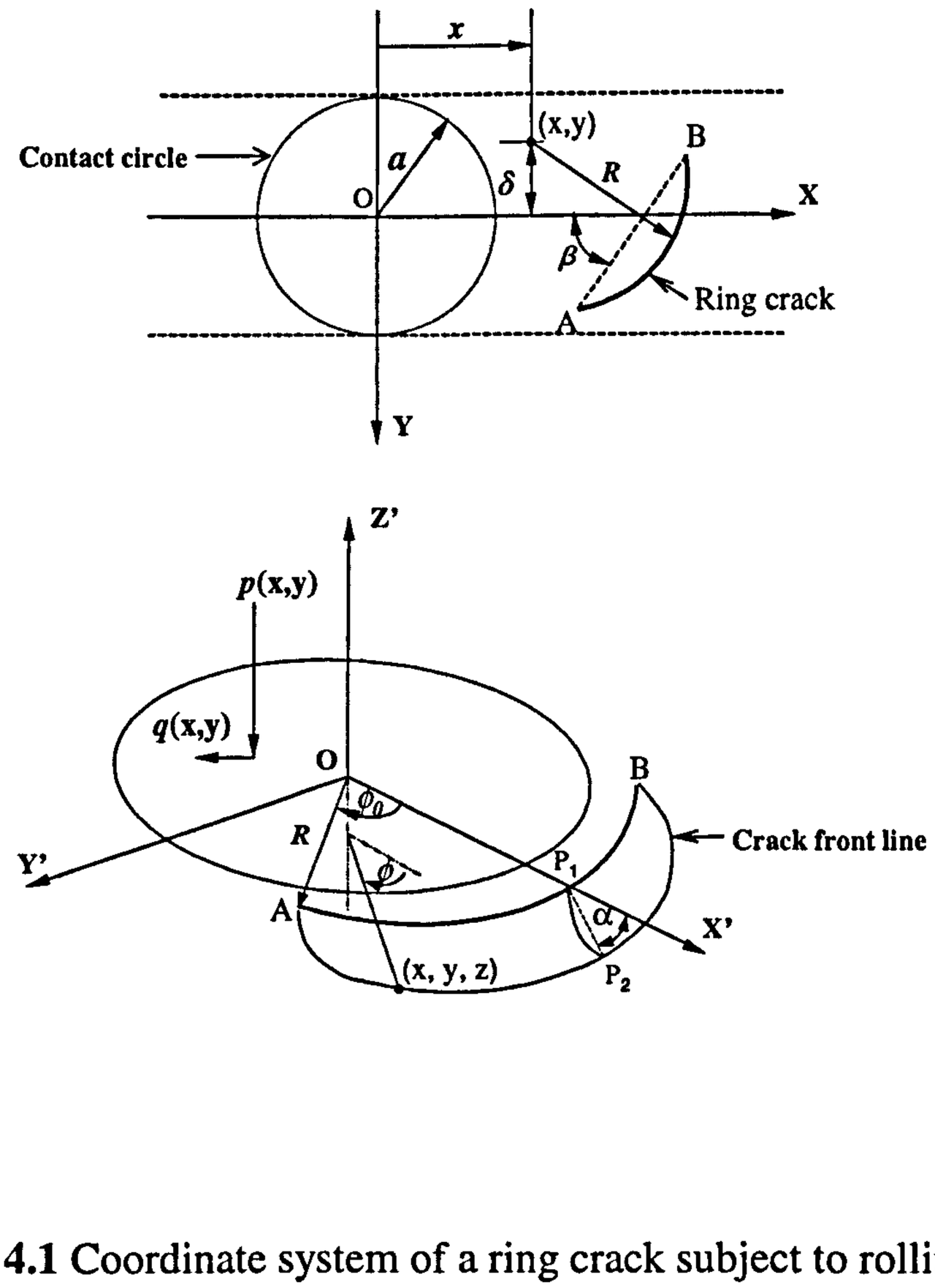

Figure 4.1 Coordinate system of a ring crack subject to rolling contacts.

As the contact circle passes over the ball surface, the crack front will pass from compressive to tensile stress continuously. When the crack lies in the compressive region ($-2a < x < 0$), the crack is suppressed ($K_I \leqslant 0$). Consequently, the crack front will not propagate along the main growth path in the compressive region. However, subsequent surface cracks may occur due to the pre-existence of ring cracks, and the branch cracks on the crack faces may also occur due to the crack face contact. The co-ordinate x affects the subsurface behaviour, which may be a rather complex process due to Hertzian loading in a cyclic fashion. This aspect will be discussed in Chapter 5.

Fluid lubricant effects are described in terms of different friction coefficients, which are determined in terms of the lubricant properties. For Hertzian contact friction coefficient f (contact between steel ball and ceramic ball), assume that f ranges from 0.005 to 0.05 due to EHL effect (Appendix 4).

4.1.2 Ring crack geometry

The geometry of a ring crack is very important to fracture mechanics analysis and will be considered carefully. Based on the experimental study, a surface ring crack is assumed to have a cone shaped crack face with a curved line as the crack front. The position of an element on the crack surface in figure 4.1 may be written as

$$x = (R + l\sqrt{1 - (\phi / \phi_0)^2}\cos\ \alpha)\cos\ \phi \qquad (4.3)$$

$$y = (R + l\sqrt{1 - (\phi / \phi_0)^2}\cos\ \alpha)\sin\ \phi \qquad (4.4)$$

$$z = -0.224\ (l\cos\ \alpha\sqrt{1 - (\phi / \phi_0)^2})^{1/2} \qquad (4.5)$$

where l denotes the crack depth, $0 < l \leq$ maximum crack depth (line P_1P_2), R is the radius of the ring crack, α is the angle of line P_1P_2 to the ball surface, $0 < \alpha < \pi/2$, ϕ represents the angle of an element position on the crack face, $-\phi_0 < \phi < \phi_0$ and ϕ_0 denotes the half angle of the ring crack arc AB, $0 < \phi_0 < \pi/2$.

This crack geometry is observed in the experimental study. According to the

experimental observations, the dimension of an original ring crack was defined as crack radius R = 0.21 mm, crack angle $\alpha = 50^{o}$, crack depth l = 0.05 mm, and half angle $\phi_0 = \pi/4$.

The influence of the crack geometry change on crack propagation is also considered and three extra crack geometrical shapes are adopted to study their effects. Figure 4.2 presents a detailed view of the selected crack geometry.

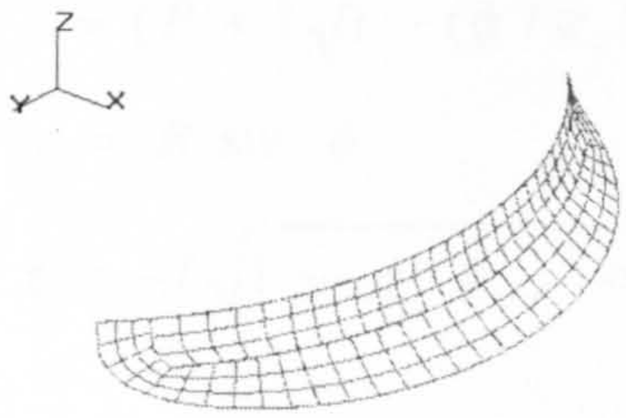

(a) Geometry I

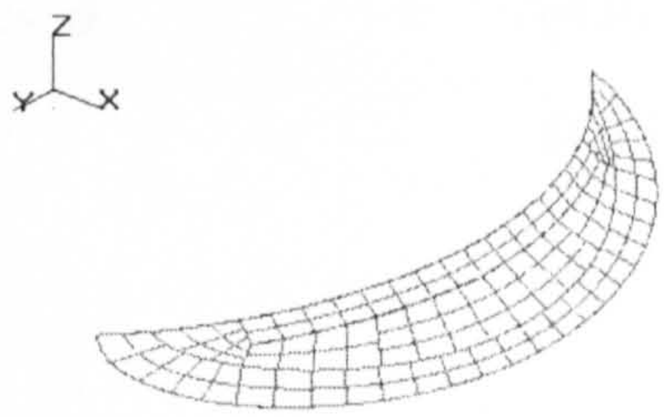

(b) Geometry II

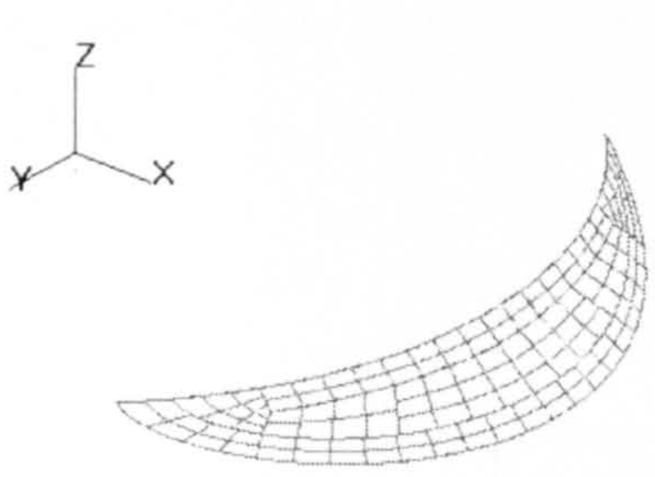

(c) Geometry III

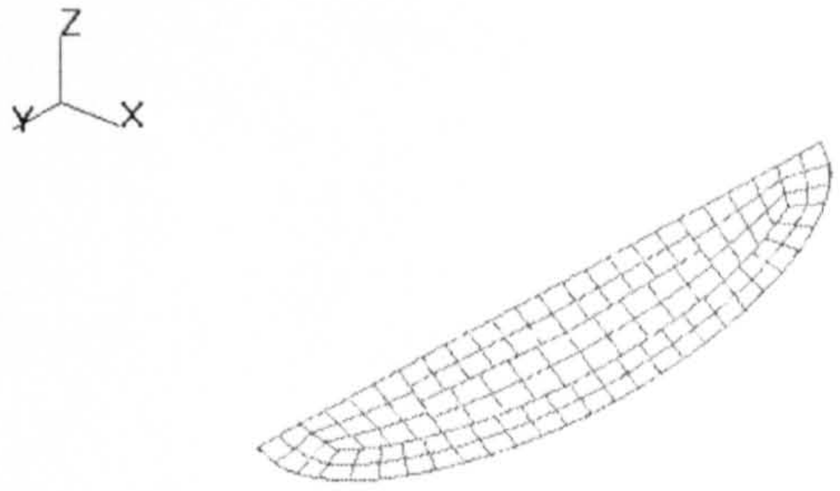

(d) Geometry IV

Figure 4.2 Detailed views of various crack shapes.

For the geometry I, the co-ordinate system has been shown in figure 4.1 and the position of an element on the crack face has been presented in the equations (4.3) to (4.5). For the geometry II, the position of an element on the crack surface can be described by the following equations:

$$x = (R + l\sqrt{1 - (\phi / \phi_0)^2}\cos\ \alpha)\cos\ \phi \qquad (4.6)$$

$$y = (R + l\sqrt{1 - (\phi / \phi_0)^2}\cos\ \alpha)\sin\ \phi \qquad (4.7)$$

$$z = -l\sqrt{1 - (\phi / \phi_0)^2}\cos\ \alpha\ \tan\ \alpha \qquad (4.8)$$

For the geometry III, the position of an element on the crack surface can be described by the following equations:

$$x = (R + l\sqrt{1 - (\phi / \phi_0)^2}\cos\ \alpha)\cos\ \phi \qquad (4.9)$$

$$y = R\ \sin\ \phi \qquad (4.10)$$

$$z = -l\sqrt{1 - (\phi / \phi_0)^2}\cos\ \alpha\ \tan\ \alpha \qquad (4.11)$$

The geometry IV is a semi-ellipse crack. This crack geometry is always employed in the stress intensity factor analysis due to the simple flat surface. The coordinate system for this crack geometry is shown in figure 4.3.

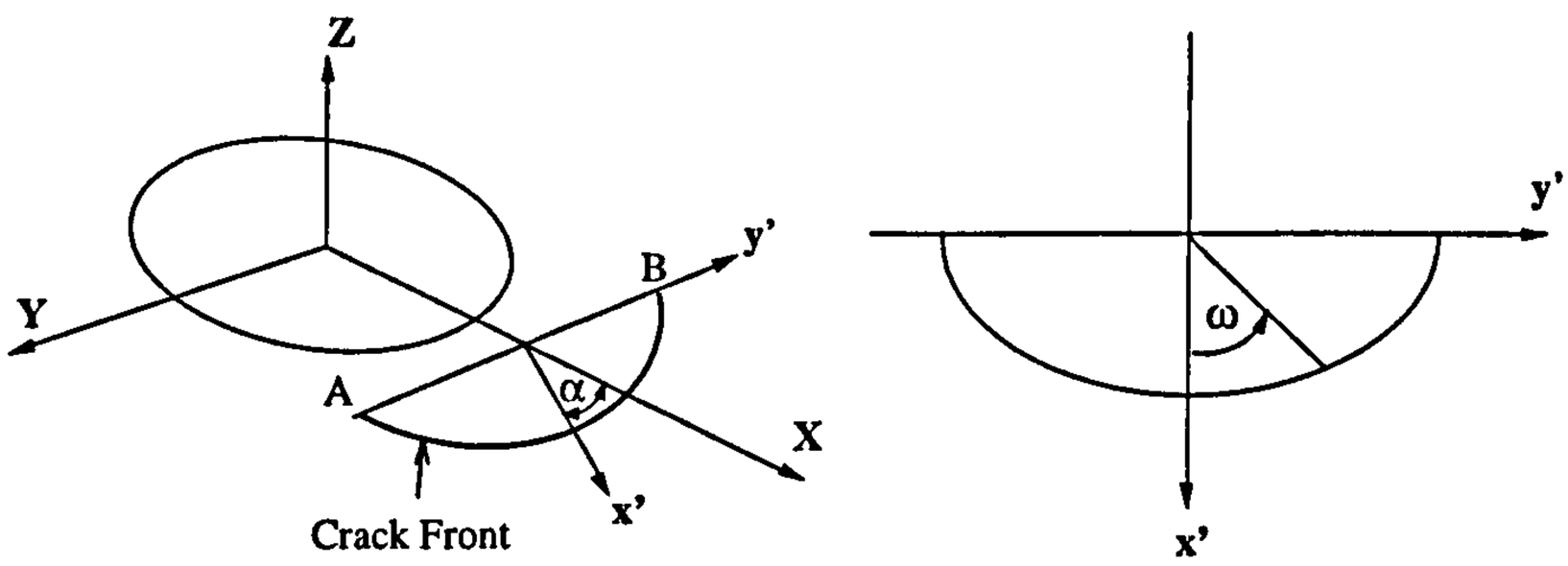

Figure 4.3 Coordinate system of geometry IV.

4.2 BOUNDARY ELEMENT MODELLING

4.2.1 The dual boundary element method

The analytical models for the three-dimensional fracture analysis have been developed in the above analysis. The computation of the stress intensity factors is now considered. In general, the geometry and loading encountered in three-dimensional crack problems is too complex for the stress intensity factors (SIF) to be solved analytically. The SIF calculation is further complicated because it is a function of the position along the crack front, the crack size and shape, type of loading and geometry of the structure. Therefore, in this study the current available numerical analysis tools are used to perform a fracture mechanics analysis.

The boundary element method based computer modelling package BEASY (Computational Mechanics BEASY 1998) is utilised in the present study. There are several ways to model a crack in boundary element modelling. The dual boundary element method (DBEM) is used for the crack growth analysis. The dual boundary element method (Portela et al. 1992, Brebbia et al. 1984) considers two independent equations: the displacement and traction boundary integral equations, with the same integration path for each pair of coincident source points (Appendix 5). The crack is represented by two elements occupying the same physical location, each element representing a face of the crack. The displacement and traction boundary integral equations are on the crack surface. The use of dual elements for 3-D crack growth means that only one surface of the crack needs to be defined.

Because of the continuity requirements of the displacements and tractions for the existence of the traction boundary integral equations and the coplanar characteristic of the crack surface, special consideration has to be given to modelling discretization. Discontinuous quadratic elements are used for the crack modelling.

A discontinuous element plays an important role in the boundary element method because the problem variables are not forced to be continuous across the elements. The major benefit of discontinuous elements is their ability to model discontinuous stress results. They are therefore very useful in fracture mechanics analysis for modelling the stress behaviour at a crack front. Figure 4.4 shows an example of a detailed view of the original crack mesh adopted in the calculation of

stress intensity factors.

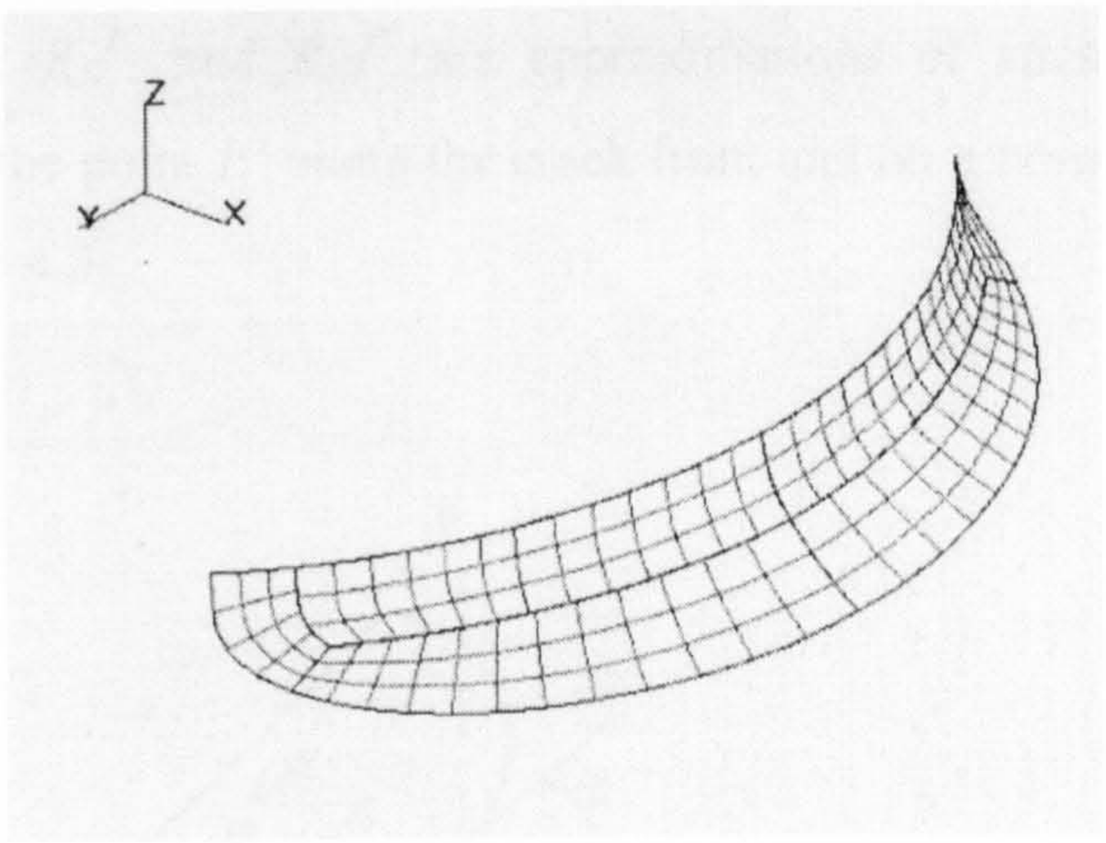

Figure 4.4 Detailed view of the crack mesh.

4.2.2 Stress intensity factors (SIF)

Since Irwin (1957) demonstrated the importance of the stress intensity factor in determining crack-tip stress fields in two-dimensional problems, many different methods have been devised for obtaining SIF (Aliabadi 1991).

In this study, the stress intensity factors are computed using crack opening displacement method. When one point formulae are employed, the Mode I, II and III stress intensity factors are evaluated using the following equations (Aliabadi 1991):

$$K_I^{P'} = \frac{E}{4(1-\nu^2)}\sqrt{\frac{\pi}{2r}}\left(u_b^P\,|_{\theta=\pi} - u_b^P\,|_{\theta=-\pi}\right) \tag{4.12}$$

$$K_{II}^{P'} = \frac{E}{4(1-\nu^2)}\sqrt{\frac{\pi}{2r}}\left(u_n^P\,|_{\theta=\pi} - u_n^P\,|_{\theta=-\pi}\right) \tag{4.13}$$

$$K_{III}^{P'} = \frac{E}{4(1-\nu^2)}\sqrt{\frac{\pi}{2r}}\left(u_t^P\,|_{\theta=\pi} - u_t^P\,|_{\theta=-\pi}\right) \tag{4.14}$$

where the displacement u^P is evaluated at point P as shown in figure 4.3; u_b^P u_n^P and

u_i^P are projections of u^P on the co-ordinate directions of the local crack front co-ordinate system and $\theta = \pi$ and $\theta = -\pi$ denote upper and lower crack surfaces respectively. $K_I^{P'}$, $K_{II}^{P'}$ *and* $K_{III}^{P'}$ are approximations of stress intensity factors corresponding to the point P' along the crack front and on a normal line to the front as shown in figure 4.5.

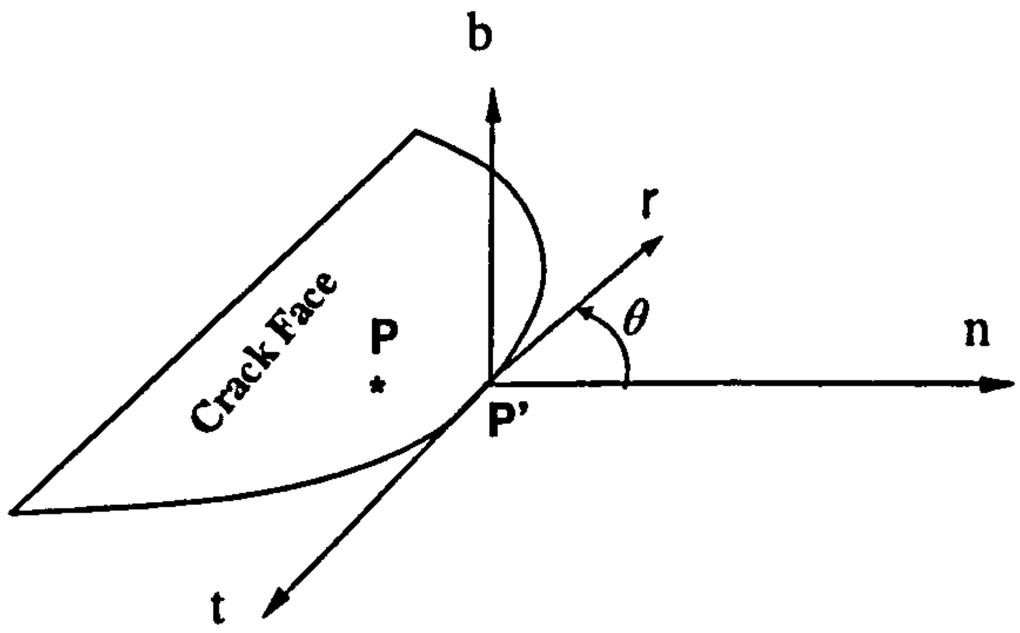

Figure 4.5 Calculations of SIF using crack opening displacement.

4.2.3 The propagation direction

The crack growth direction is computed by the minimum strain energy density criterion. This criterion for three-dimensional problems is proposed by Sih and Cha (1974), Sih(1991). The theory is based on the following hypotheses.

Hypothesis (1): the direction of crack propagation at any point along the crack front is toward the region with the minimum value of strain energy density factors S as compared with other regions on the same spherical surface surrounding the point

Hypothesis (2): crack extension occurs when the strain energy density factor in the region determined by hypothesis (1), $S = S_{min}$, reaches a critical value, say S_{cr}.

Hypothesis (3): the length of r_0, of the initial crack extension is assumed to be proportional to S_{min}, such that S_{min} / r_0 remains constant along the new crack front.

The strain energy density factor S is given by

$$S = a_{11}K_I^2 + a_{12}K_IK_{II} + a_{22}K_{II}^2 + a_{33}K_{III}^2 \qquad (4.15)$$

where

$$a_{11} = \frac{1}{16\pi\mu}[(3-4\nu-\cos\theta)(1+\cos\theta)] \qquad (4.16)$$

$$a_{12} = \frac{1}{8\pi\mu}\sin\theta(\cos\theta-1+2\nu) \qquad (4.17)$$

$$a_{22} = \frac{1}{16\pi\mu}[4(1-\nu)(1-\cos\theta)+(3\cos\theta-1)(1+\cos\theta)] \qquad (4.18)$$

$$a_{33} = \frac{1}{4\pi\mu} \qquad (4.19)$$

in which μ stands for the shear modulus of elasticity, ν is the Poisson's ratio, and θ is the angle in the crack front co-ordinate system as shown in figure 4.5.

The crack growth direction (angle θ_0) is obtained by minimising the strain energy density factor $S(\theta)$ of equation (4.15) with respect to θ. The minimum strain density factor $S(\theta_0)$ is denoted by S_{min}.

The equivalent stress intensity factor, K_{eq}, can be calculated from the minimum strain density factor as:

$$K_{eq} = \sqrt{\frac{4\mu}{2\nu-1}S_{min}} \qquad (4.20)$$

4.2.4 The propagation size

Determination of the incremental size poses two problems: the first is the determination of the amount of each increment in terms of a reference size, the second is the relationship between the maximum incremental size and other incremental sizes along the crack front. The maximum incremental distance that a crack would be expected to propagate can be determined using the strain energy density criterion or empirical methods.

For the strain energy density criterion, since the strain energy factor S_{min} is proportional to the squared power of the equivalent stress intensity factor K_{eq} (Hypothesis (3) in Section 4.2.3), the incremental size at the crack front point under consideration is given by:

$$\Delta a = \Delta a_{\max}\left(\frac{K_{eq}}{\max\{K_{eq}\}}\right)^2 \tag{4.21}$$

where $\max\{K_{eq}\}$ is the maximum strain energy factor evaluated at a set of discrete points along the front, and Δa_{max} is the incremental size at the point to the $\max\{K_{eq}\}$ which is chosen beforehand as being the maximum distance from the crack front to the opposite side of the element containing the crack front.

The empirical method is based on the Paris equation (Paris and Erdogan 1963), which is expressed as follows:

$$da/dn = c(\Delta K)^m \tag{4.22}$$

where

$$\Delta K = K_{\max} - K_{\min} = K_{\max}(1 - R_\sigma) \tag{4.23}$$

$$R_\sigma = K_{\min} / K_{\max} \tag{4.24}$$

The *da/dn* is the rate of change of crack length with respect to the loading cycles, the c and m are the material constants. For the mixed-mode problem the stress intensity

factor K_{max} is replaced by the effective stress intensity factor K_{eff} (Gerstle 1986), which is expressed as follows:

$$K_{eff} = [(K_I + |K_{III}|)^2 + 2K_{II}^2]^{1/2} \qquad (4.25)$$

Since linear elasticity is considered, R_σ in equation (4.24) can be written as

$$R_\sigma = K_{eff}^{min} / K_{eff}^{max} = \sigma_{min} / \sigma_{max} \qquad (4.26)$$

The σ_{min} is set at zero (when loading moves away from the crack) and σ_{max} is considered as the maximum affecting stress resulting from the loading circle. Hence,

if $\Delta K = K_{eff} > \Delta K_{th}$, $da/dn > 0$ crack growth,

if $\Delta K = K_{eff} < \Delta K_{th}$, $da/dn = 0$ no crack growth.

The maximum incremental distance (Δa_{max}) is a fixed value based on initial crack front element dimensions (Δa_{max}) taken where ΔK_{eff} is a maximum and is equal to the length of the element side oriented perpendicular to the crack front. From equation (4.23)

$$\Delta a = c(\Delta K_{eff})^m \Delta N \qquad (4.27)$$

and

$$\Delta a_{max} = c(\Delta K_{eff}^{max})^m \Delta N \qquad (4.28)$$

Therefore, the incremental size at the crack front point is given by

$$\Delta a = \Delta a_{max} (\Delta K_{eff} / \Delta K_{eff}^{max})^m \qquad (4.29)$$

4.3 ANALYSIS OF THE CALCULATED STRESS INTENSITY FACTORS

4.3.1 SIF with crack geometry

4.3.1.1 Crack surface shape

Four types of crack shapes (figure 4.2) are adopted to study the influence of the crack surface shape on the stress intensity factors. For the purpose of the calculation comparison, assume that these cracks have the same crack angle (α = 50°), crack length (one-fourth of ring crack circle) and crack depth (l = 0.05 mm). The crack location for the calculation is $\beta = 90°$, $\delta = 0$, and $x = 0$. The maximum contact stress is assigned a value of 5.58 GPa, and friction coefficient f = -0.05.

Figures 4.6 to 4.9 show the calculated results of the stress intensity factors. As can be seen from the plots, the SIF solutions change as the crack geometry changes. Mode I stress intensity K_I is always higher than mode II and III stress intensities. It is reasonable to assume that the mode I stress intensity will dominate the crack growth behaviour. For a certain geometry, the K value is a function of ϕ. For the geometry I, K_I value at $\phi = 0°$ (lower point) is about 3.5 MPa $m^{1/2}$ and gradually decreases as ϕ changes almost until $\phi = \pm 44°$, and rises quickly to 5.5 MPa $m^{1/2}$ as ϕ approaches $\pm 45°$ (surface point). K_{II} and K_{III} vary slightly with ϕ except where $\phi = \pm 45°$ (surface point), when the values of K_{II} and K_{III} drop sharply.

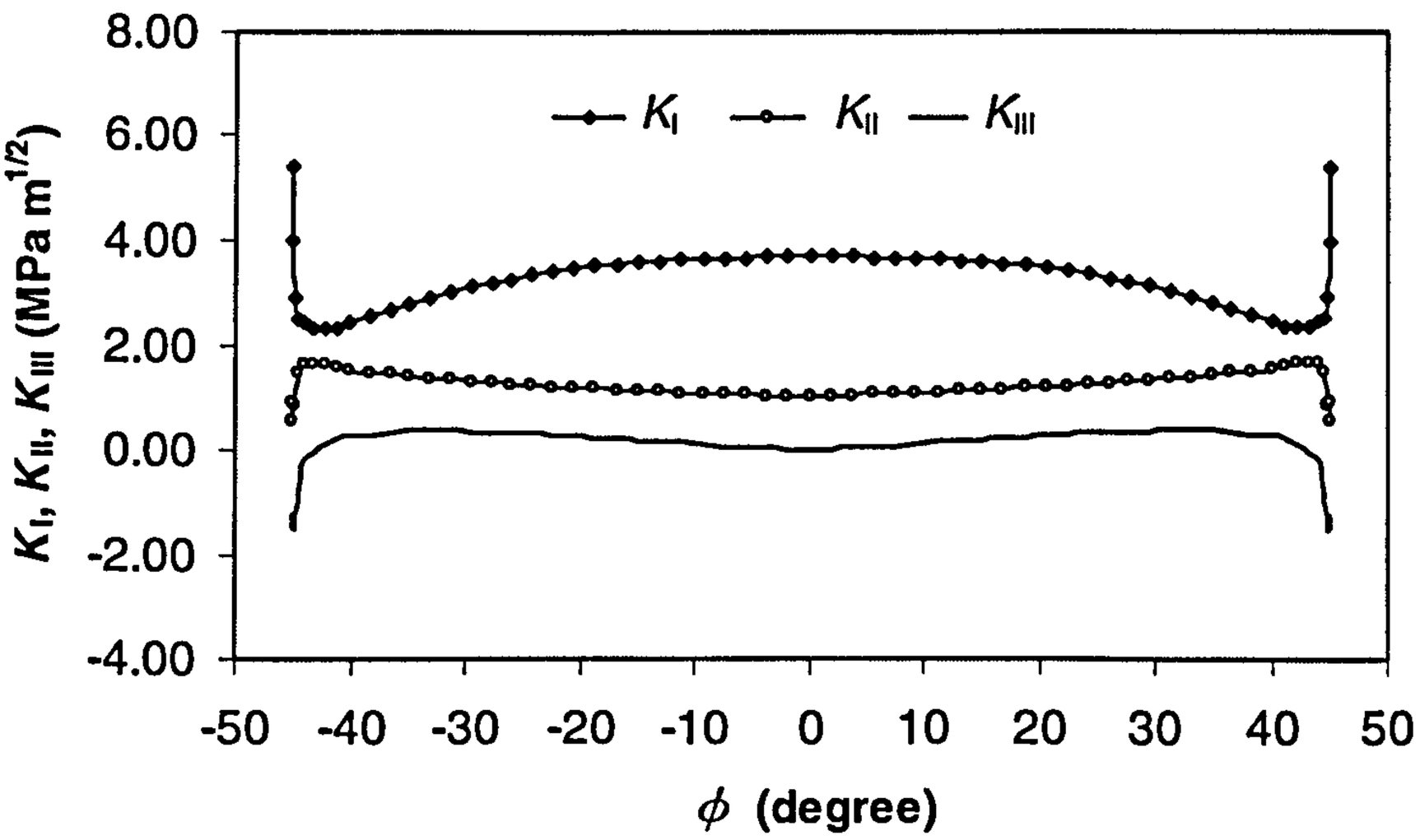

Figure 4.6 Stress intensity factors versus ϕ (Geometry I).

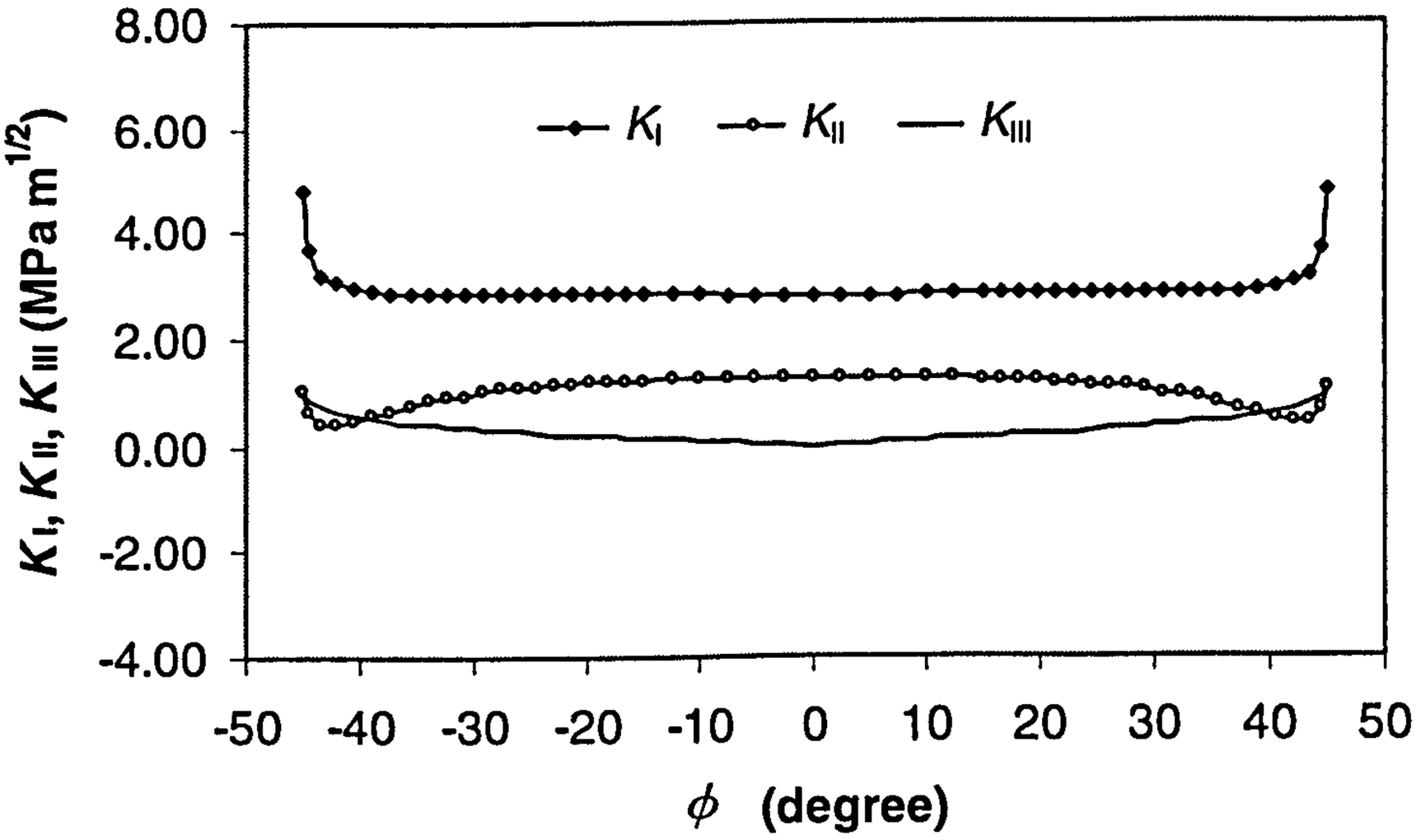

Figure 4.7 Stress intensity factors versus ϕ (Geometry II).

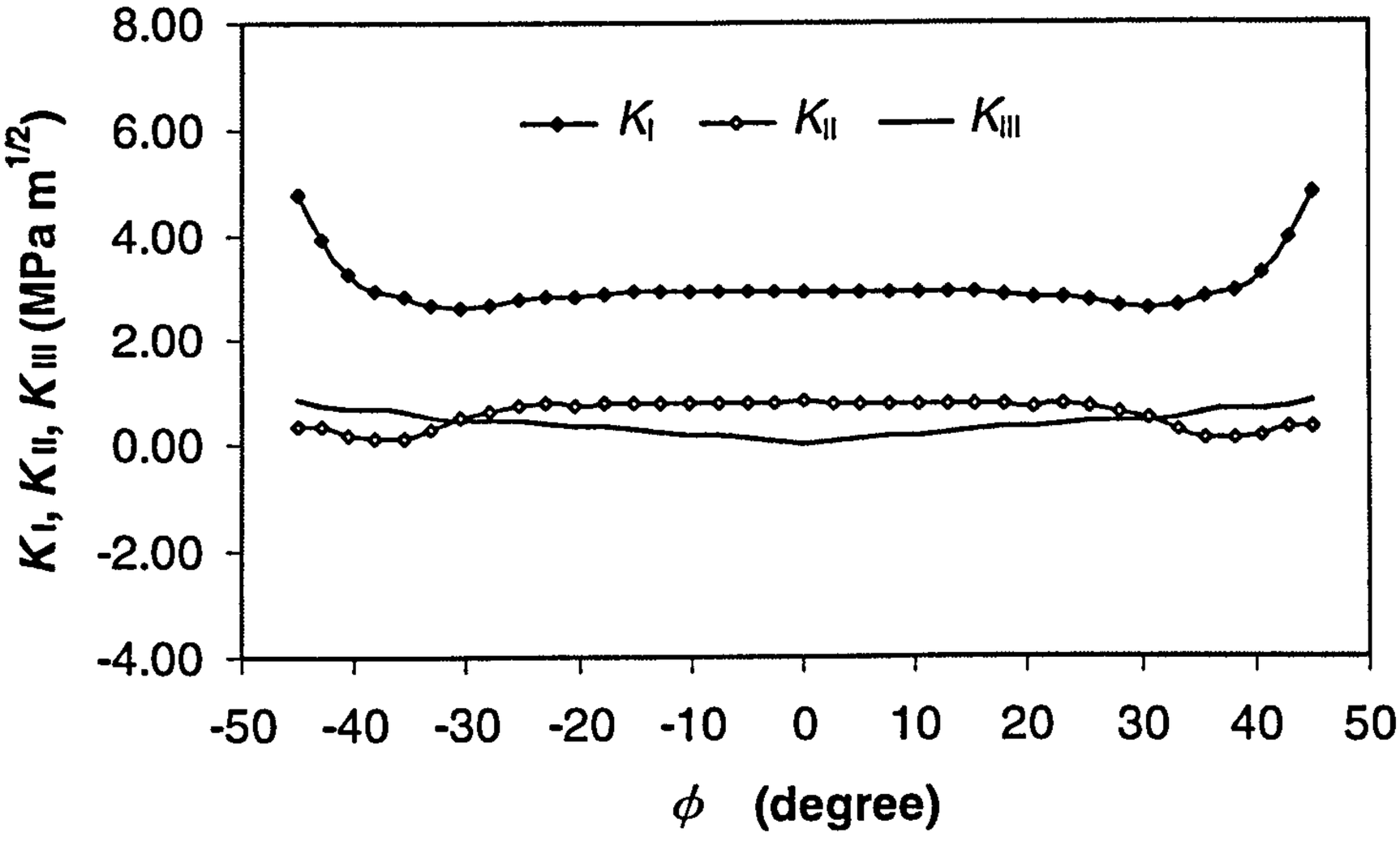

Figure 4.8 Stress intensity factors versus ϕ (Geometry III).

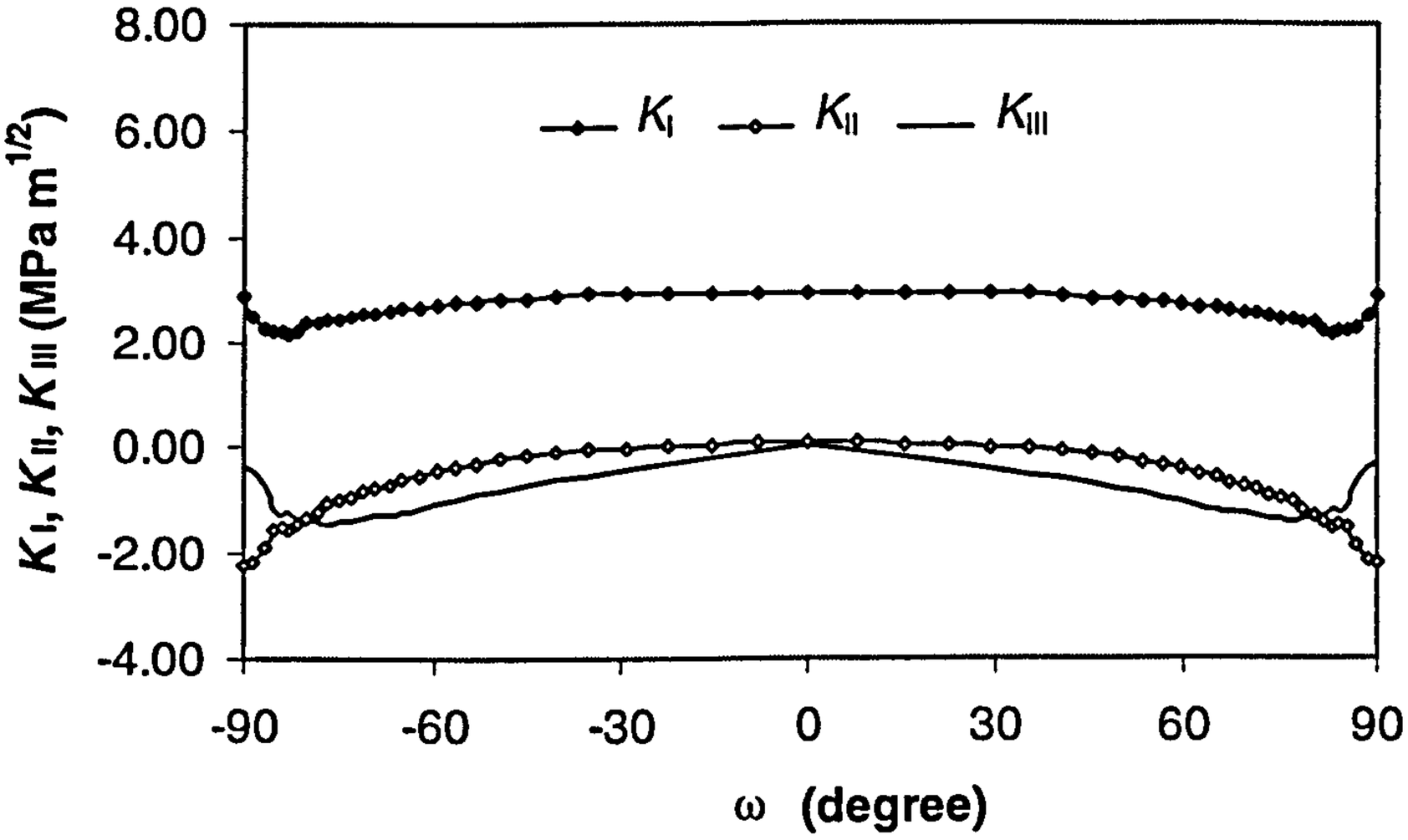

Figure 4.9 Stress intensity factors versus ω (Geometry IV).

The calculation result for geometry II is shown in figure 4.7. At $\phi = 0^o$ (lower point) the mode I stress intensity K_I is about 3.0 MPa m$^{1/2}$ and stays at the same value almost until $\phi = \pm 40^o$, and rises quickly to 5.0 MPa m$^{1/2}$ as ϕ approaches $\pm 45^o$ (surface point). There are slight variations in the K_{II} and K_{III} values.

The calculation results from geometry III are shown in figure 4.8. The mode I stress intensity K_I is about 3.0 MPa m$^{1/2}$ when $\phi = 0^o$ and hardly changes until almost the point where $\phi = \pm 30^o$. It rises gradually to 4.7 MPa m$^{1/2}$ as ϕ approaches $\pm 45^o$. The K_{II} and K_{III} vary slightly with ϕ.

The SIF value along the crack front is changed when the crack shape changes from a ring crack to a semi-ellipse crack (geometry IV). Figure 4.9 shows the variations of stress intensity factors for the geometry IV. In contrast with the cone shape crack face (geometry I to III), the mode I stress intensity K_I has a maximum value of about 3 MPa m$^{1/2}$ at $\omega = 0^o$, and decreases gradually to 2.2 MPa m$^{1/2}$ at about $\omega = 80^o$. After this point, K_I returns to a value of about 3 MPa m$^{1/2}$ at $\omega = 90^o$ (ball surface). Mode II stress intensity K_{II} decreases gradually in line with ω. The trend in the K_{III} variation is similar to that in the K_I variation.

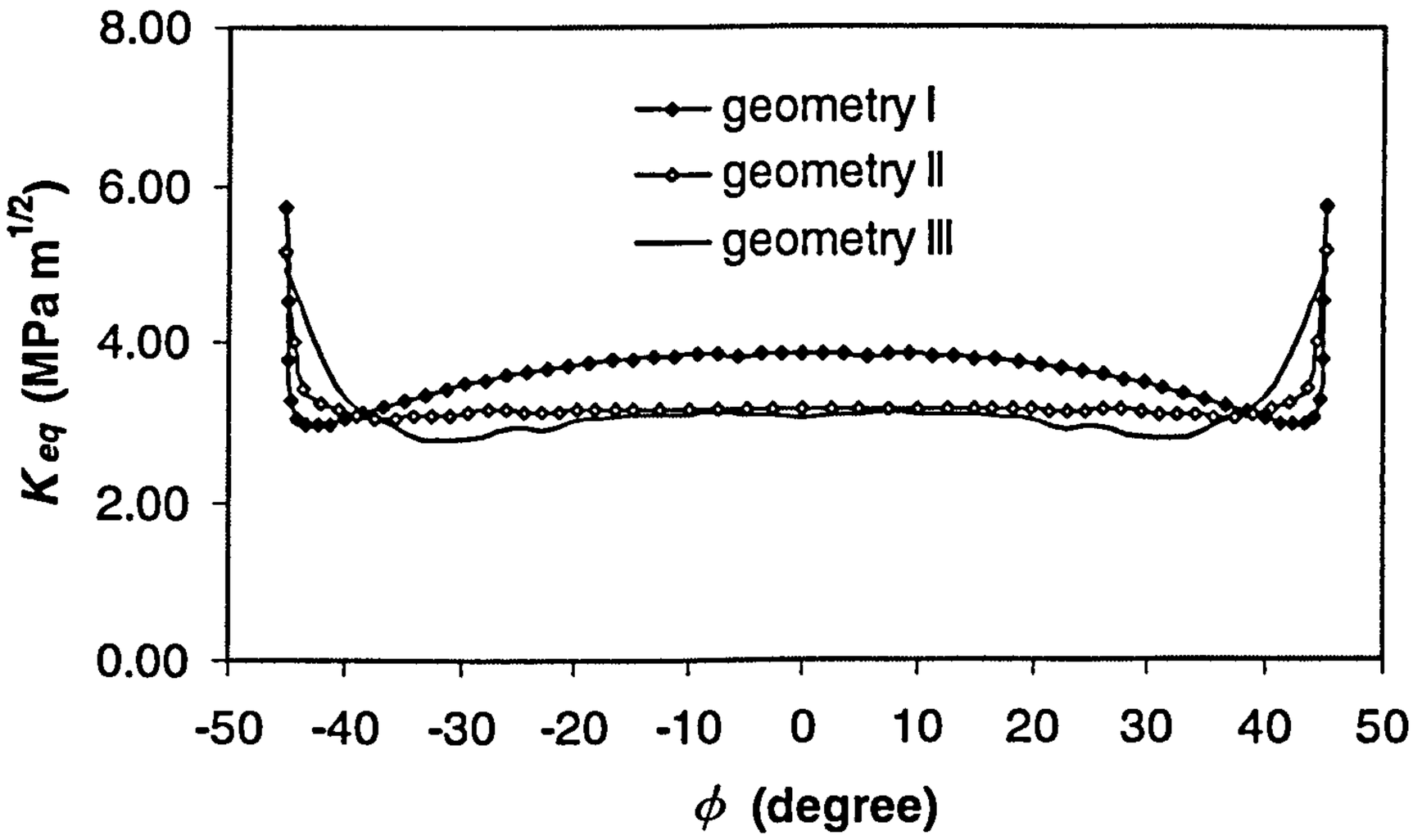

Figure 4.10 Influence of crack geometry on equivalent stress intensity factor K_{eq}.

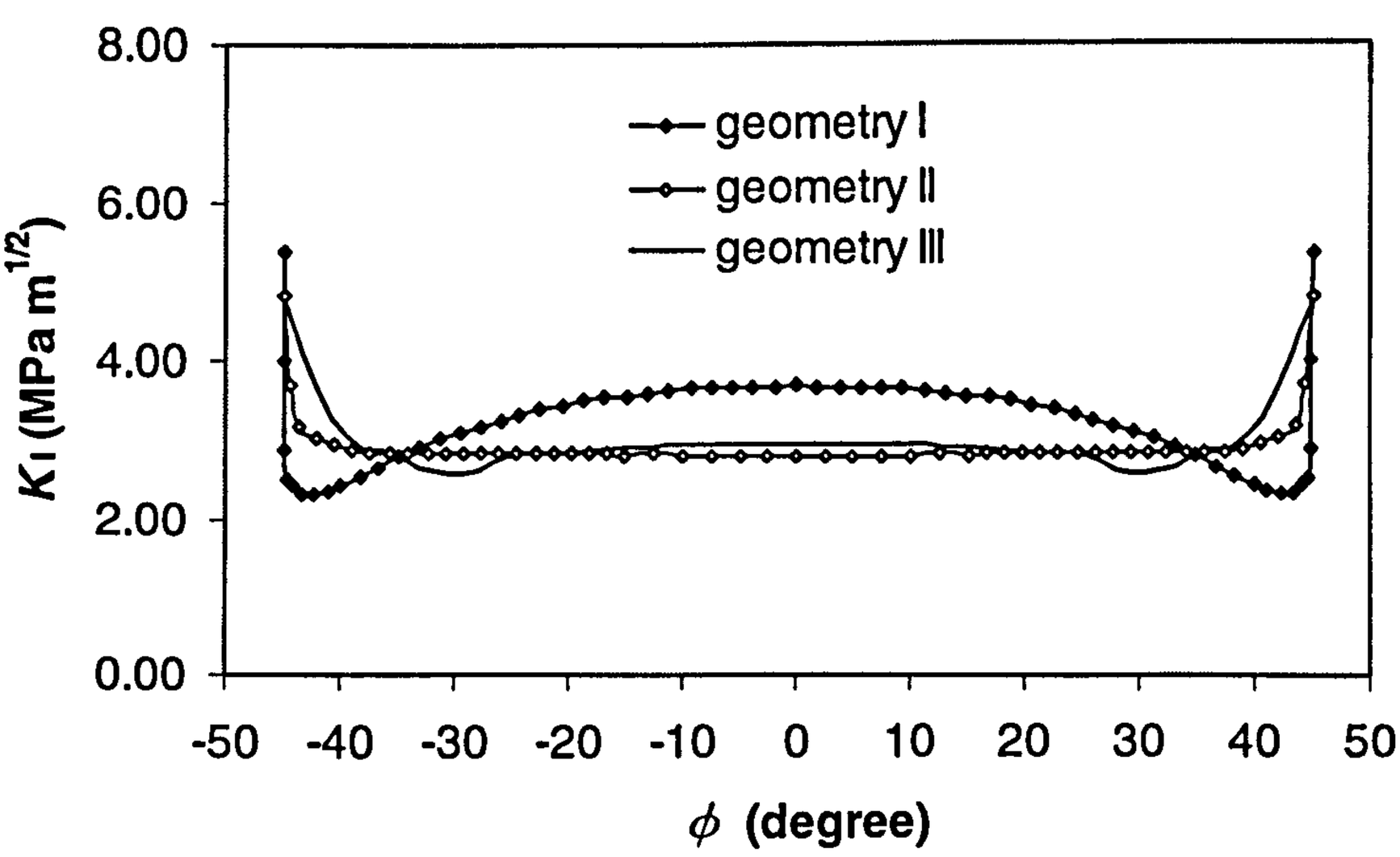

Figure 4.11 Influence of crack geometry on stress intensity factor K_I.

For the mixed-mode problem, the equivalent stress intensity factor or effective intensity factor is often adopted to assess the possibility of crack growth. Figure 4.10 shows plots of K_{eq} for the geometry I, II and III. The equivalent stress intensity for the geometry I is higher than that of geometry II and III. There is no big difference between geometry I and II. Figure 4.11 shows the plots of K_I. As

described in figure 4.10, the K_I for the geometry I is higher than that of geometry II and III. There is little difference between geometry I and II. The difference between K_I and K_{eq} is small. The results indicate that the mode I stress intensity K_I plays an important role in surface ring crack propagation. Consequently, K_I may be a main concern in determining crack propagation behaviour. For HIP silicon nitride bearing material, the fracture toughness K_{IC} is around 6.0 MPa $m^{1/2}$. The threshold ΔK_{th} of crack propagation ranges from 2 to 3 MPa $m^{1/2}$. The calculation results indicate that there is no possibility of an unstable fracture. However, the crack front will propagate in the calculated geometry. The crack growth behaviour will be changed slightly due to the crack geometry effect.

4.3.1.2 Crack angle

Firstly, let us consider a simple case: a semi-ellipse crack inclining at an angle α to the surface (Geometry IV). Assume $\beta = 90^o$, $\delta = 0$, and $x = 0$. The maximum contact stress and friction coefficient are assigned to the values of 5.58 GPa and f = -0.05, respectively. This semi-ellipse crack can be considered to be a special case when the ring crack radius R approaches ∞. Figures 4.12 to 4.14 show the influence of the crack angle on the stress intensity factors (K_I, K_{II}, K_{III}).

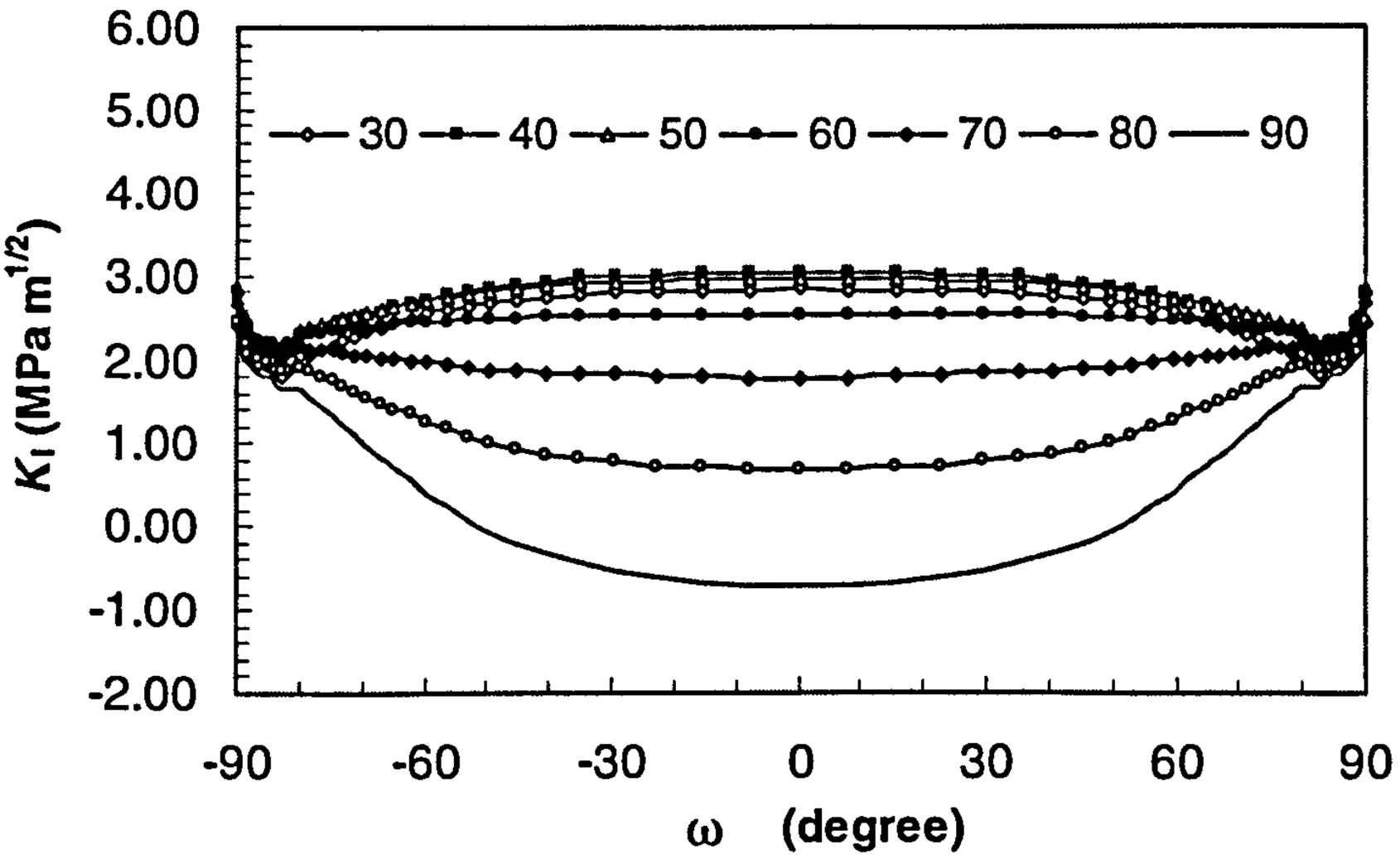

Figure 4.12 K_I versus ω for various crack angles (Geometry IV).

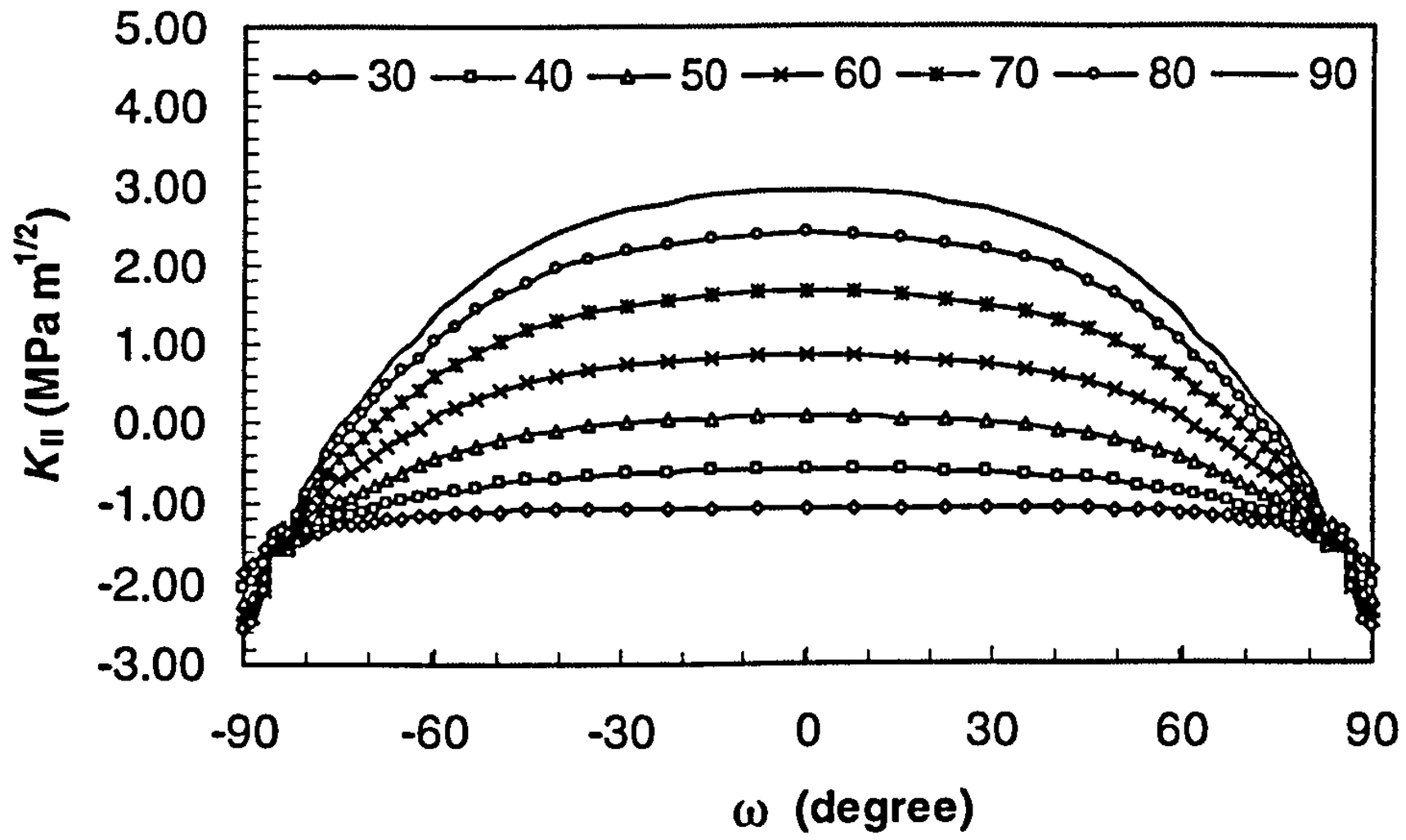

Figure 4.13 K_{II} versus ω for various crack angles (Geometry IV).

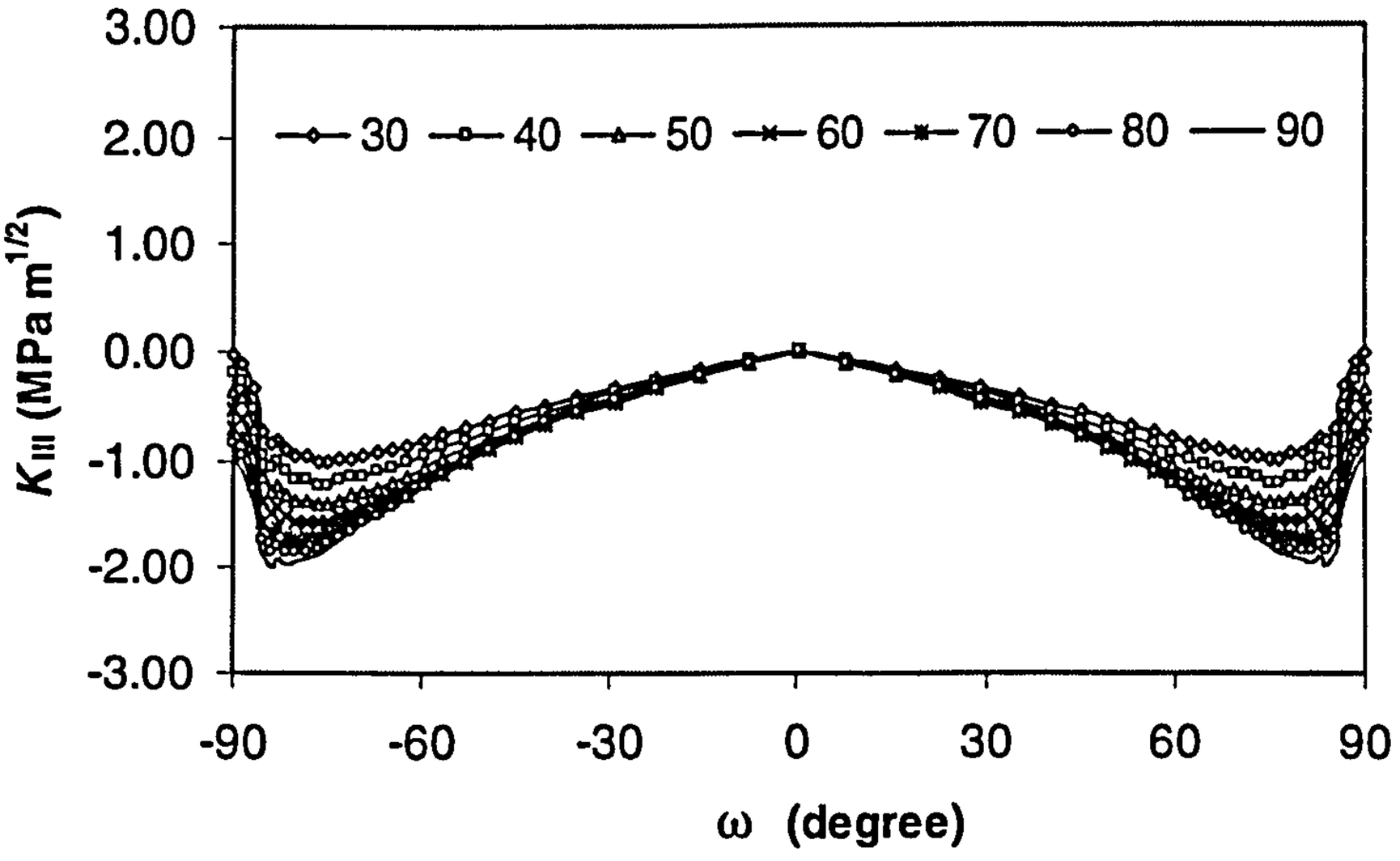

Figure 4.14 K_{III} versus ω for various crack angles (Geometry IV).

Mode I stress intensity factor, K_I, changes slightly from the crack angle 30° to 50°, and after 50°, decreases as the crack angle increases. The stress intensity factors on the crack front are a function of ω. In contrast with K_I, the mode II stress intensity, K_{II}, increases as the crack angle increases. The K_I and K_{II} values have a significant change at ω = 0° and little change at ω = 90°. However, the mode III

stress intensity, K_{III}, is different from K_I and K_{II}. No change occurs at $\omega = 0^o$ and little change at $\omega = 90^o$.

To compare the K_I, K_{II}, and K_{III} variation clearly, we concentrate on $\omega = 0^o$ and $\omega = 90^o$ to investigate the crack angle effect. Figure 4.15 illustrates the relationship between K value and crack angle α when $\omega = 0^o$. As can be seen from the plot, the K_I value increases very slightly as the crack angle increases, and reaches the maximum value of about 3.1 MPa $m^{1/2}$ at the crack angle = 40^o, and decreases with the increase of the crack angle. The K_{II} value increases as the crack angle increases. There is no change in K_{III}. Figure 4.15 also reveals that the mode II stress intensity, K_{II}, will dominate crack propagation when the crack angle > 70^o.

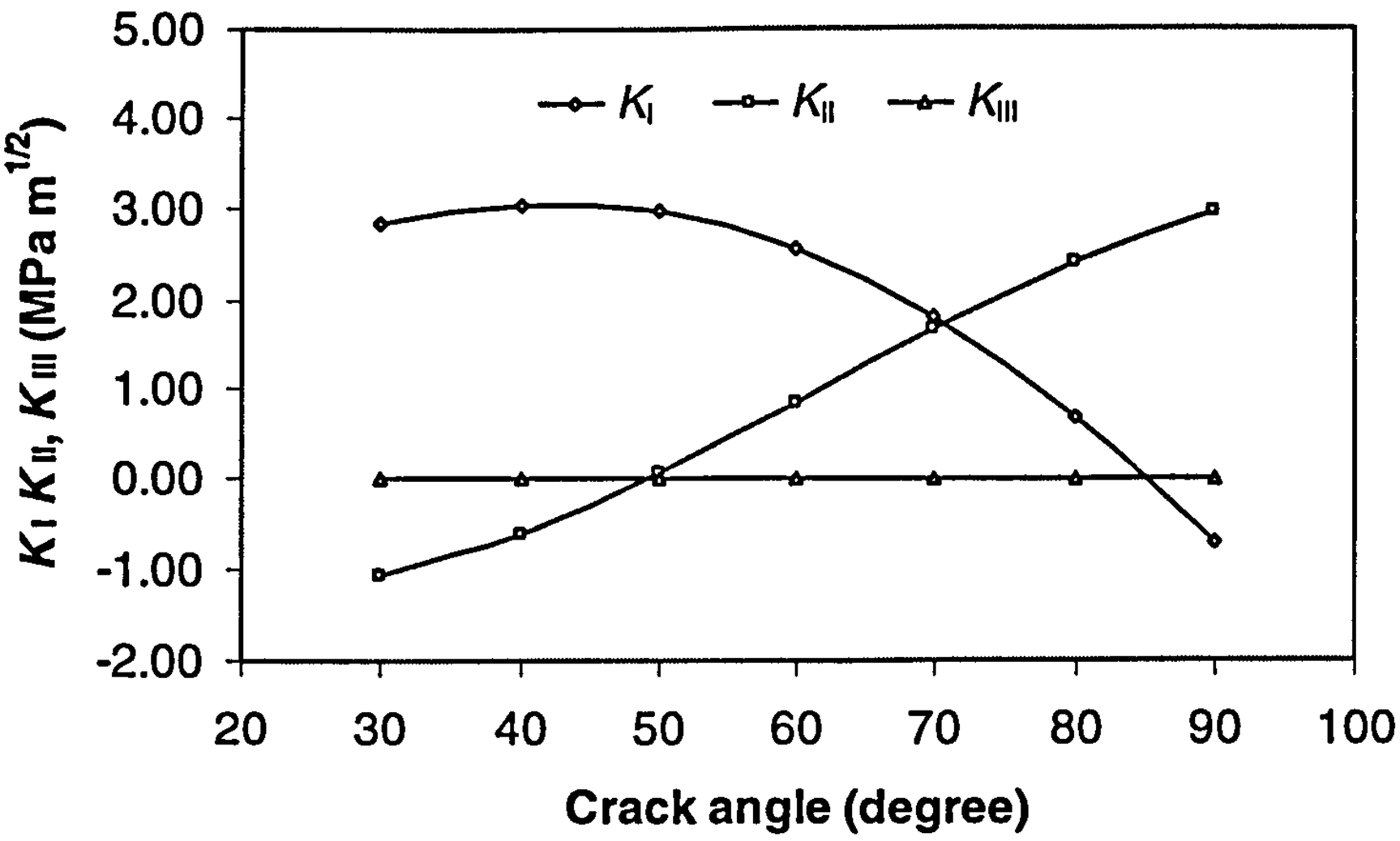

Figure 4.15 Stress intensity factors versus crack angle at $\omega = 0^o$ (Geometry IV).

Figure 4.16 shows the variations of stress intensity factors at $\omega = 90^o$. Unlike at $\omega = 0^o$, stress intensity factors (K_I, K_{II}, and K_{III}) decrease slightly as the crack angle increases. The results indicate that there is no significant effect on the surface and the stress intensities at $\omega = 0^o$ may be considered to be the main contributing factors in determining whether or not the crack grows.

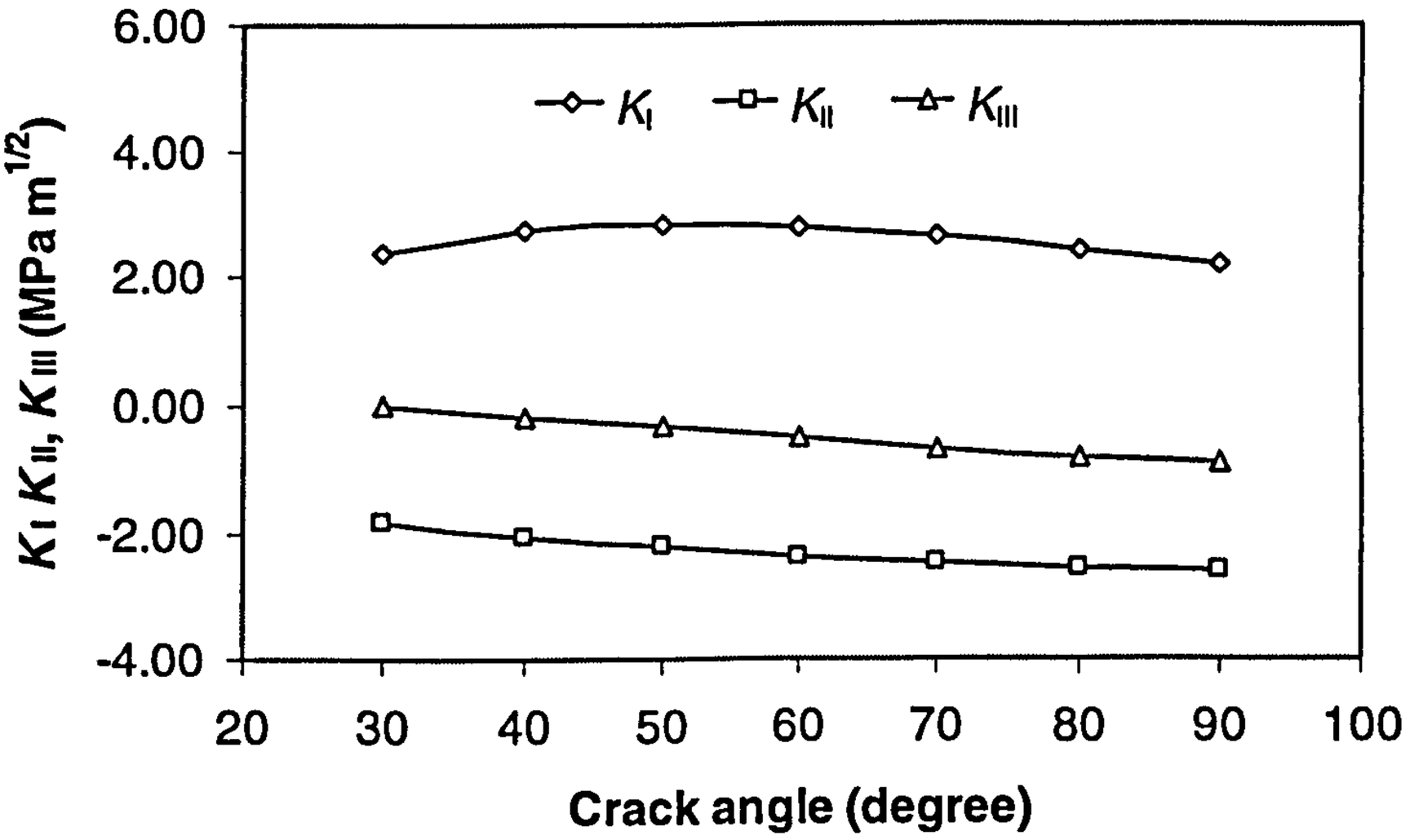

Figure 4.16 Stress intensity factors versus crack angle at $\omega = 90^{o}$ (Geometry IV).

The effect of crack angles on the stress intensity factors is now considered as the crack geometry changes. For the ring cracks, the crack angle ranges normally from 30^{o} to 50^{o} and, as discussed above, the mode I stress intensity K_I dominates the crack propagation behaviour in this range. Therefore, we concentrate on mode I stress intensity factor, K_I.

Figure 4.17 shows plots of K_I for the geometry I. It is found that the K_I decreases as the crack angle increases. The SIF distribution profile is similar for each crack angle. Figure 4.18 contains the plots of K_I for the geometry II. As with the geometry I, the stress intensity K_I decreases slightly as the crack angles increase. The K_I values are very close if they have the same crack angle. Therefore, the fatigue crack propagation will be similar for the geometry I and II.

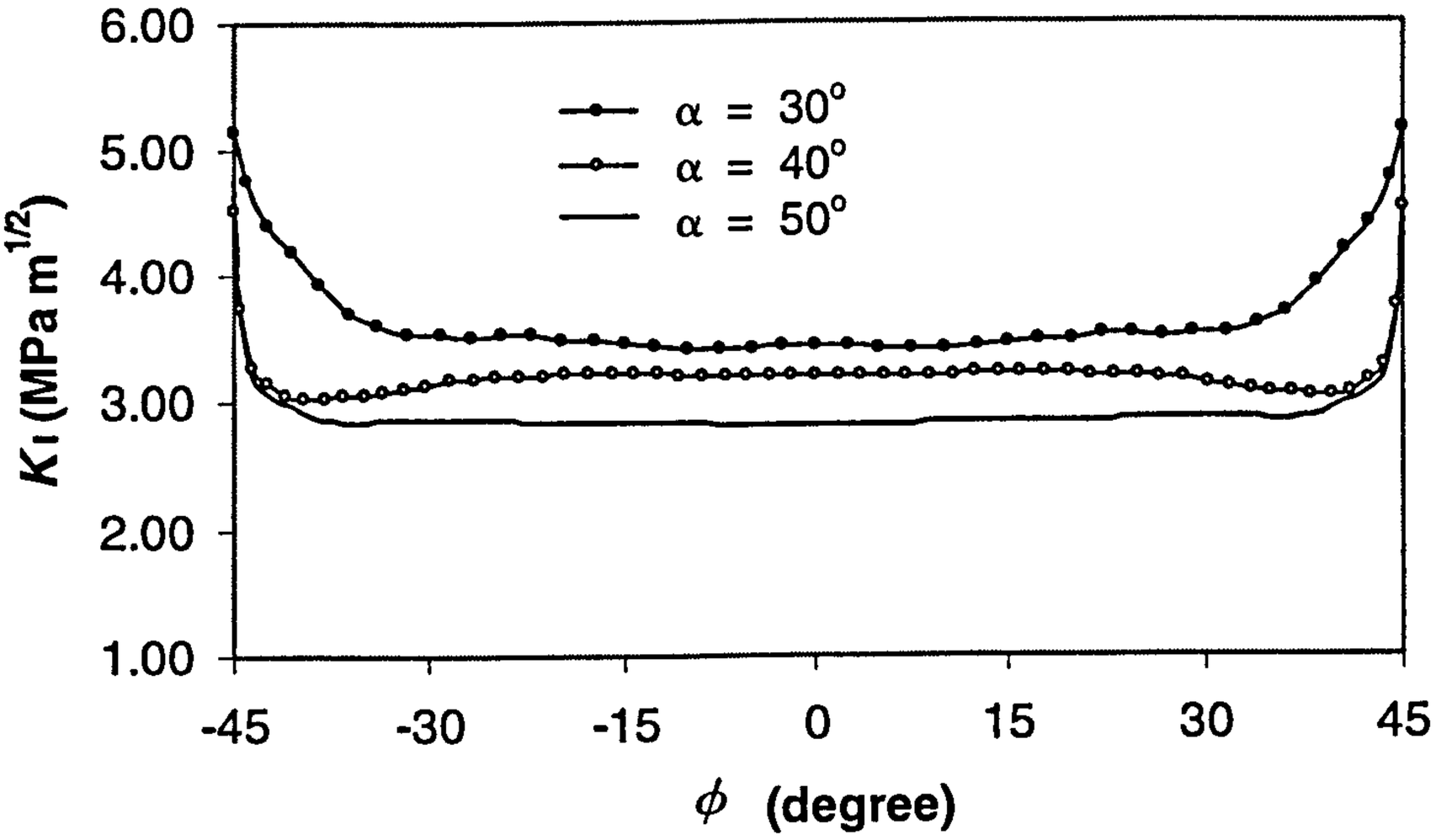

Figure 4.17 Influence of crack angle on K_I (Geometry II).

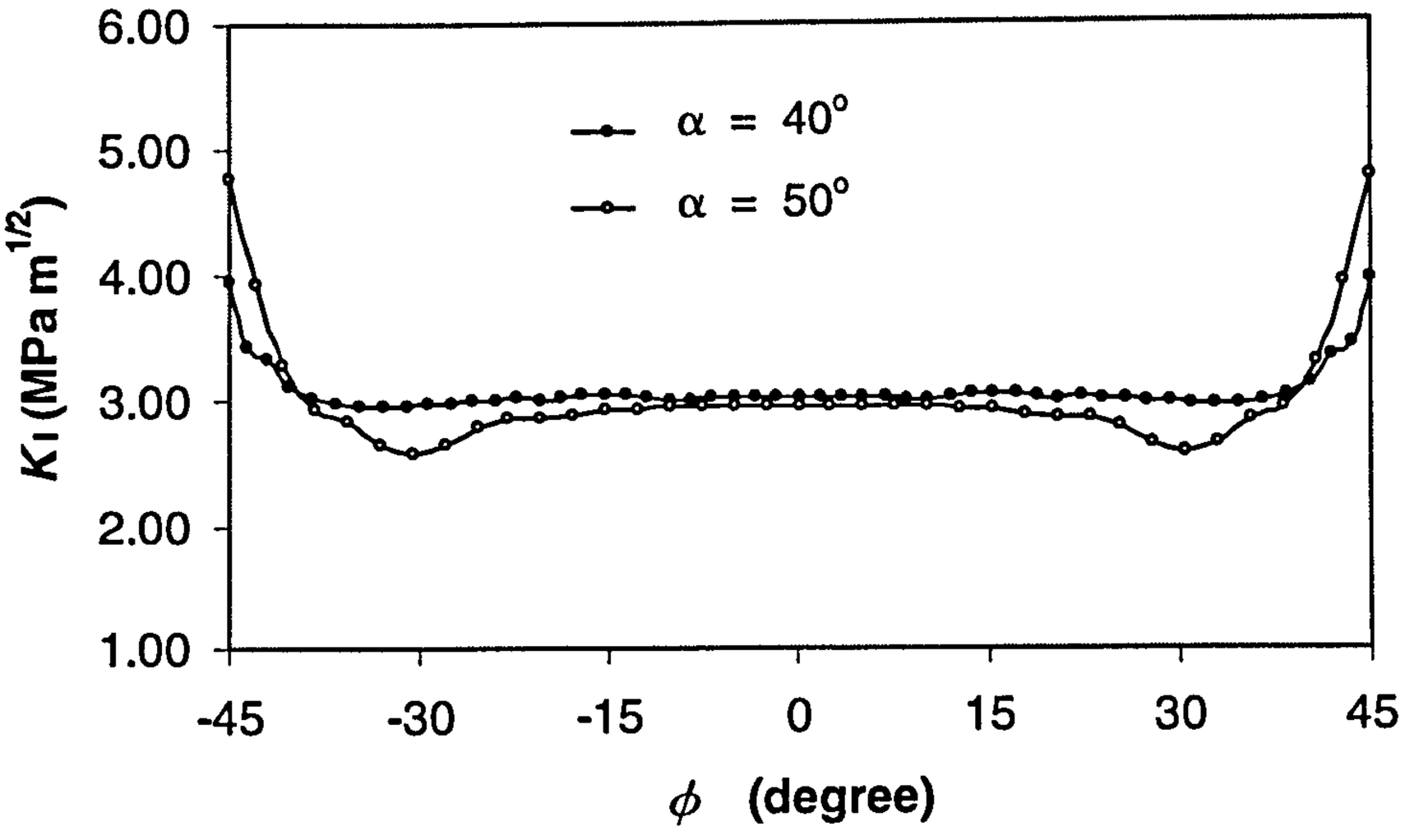

Figure 4.18 Influence of crack angle on K_I (Geometry III).

4.3.1.3 Crack length

Figures 4.19 and 4.20 depict the variation of stress intensity factors when the crack length increases to one-third of the ring crack circle ($\phi_0 = 60^o$). The geometry I (figure 4.2(a)) is employed for the comparison study. The results for $\phi_0 = 45^o$ has

been shown previously (see figure 4.6). The results show that the K values vary very slightly when the crack length is between one-quarter to one-third of the ring crack circle. The K_I increases little at $\phi = 0^\circ$ and decreases little at $\phi = \pm 45^\circ$. The SIF distribution profile is very similar. The results imply that the rolling contact fatigue life must be close if the crack length is close. For the surface ring crack defects, the length is normally between one-quarter and one-third of the ring crack circle.

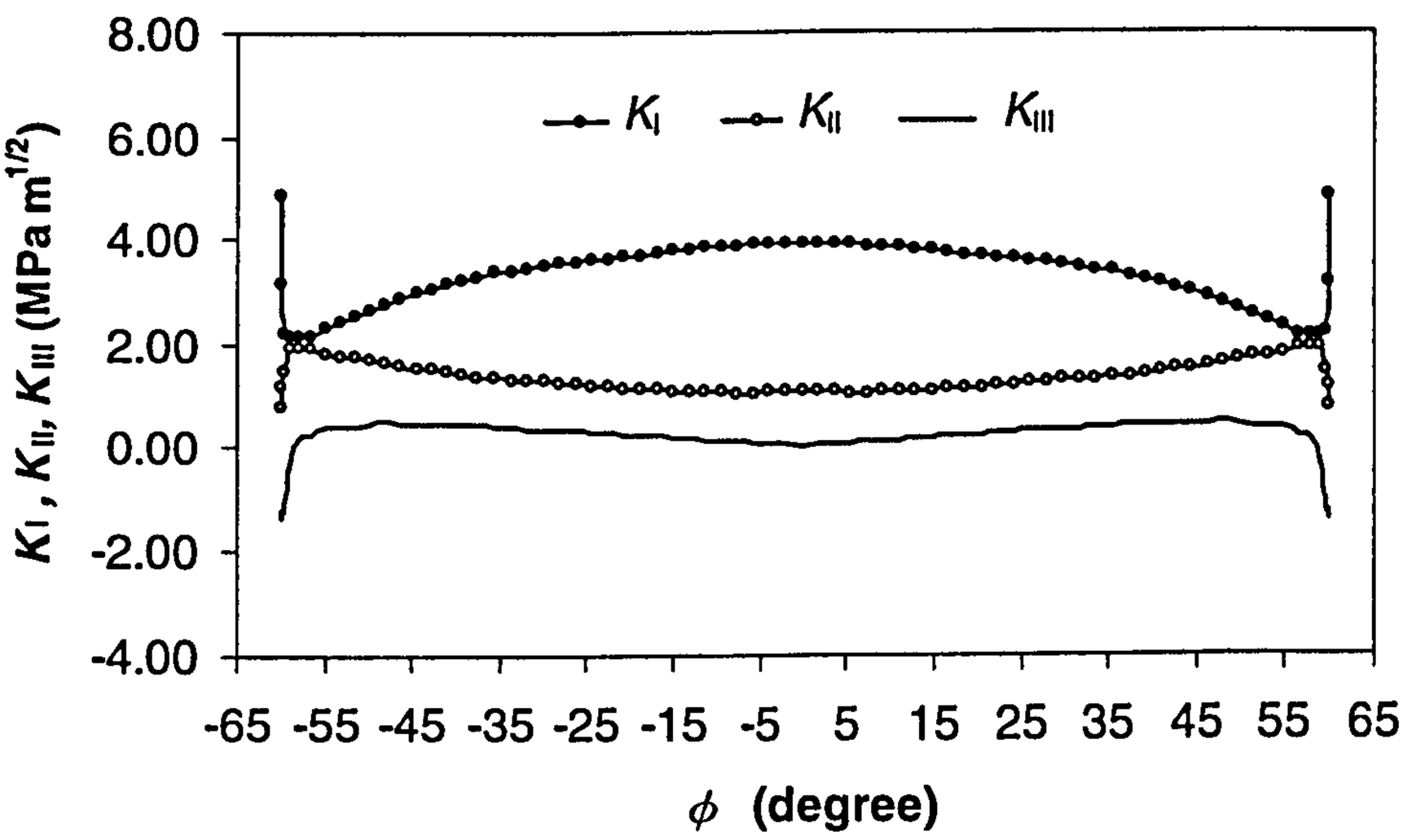

Figure 4.19 Plots of stress intensity factors at $\phi_0 = 60^\circ$ (Geometry I).

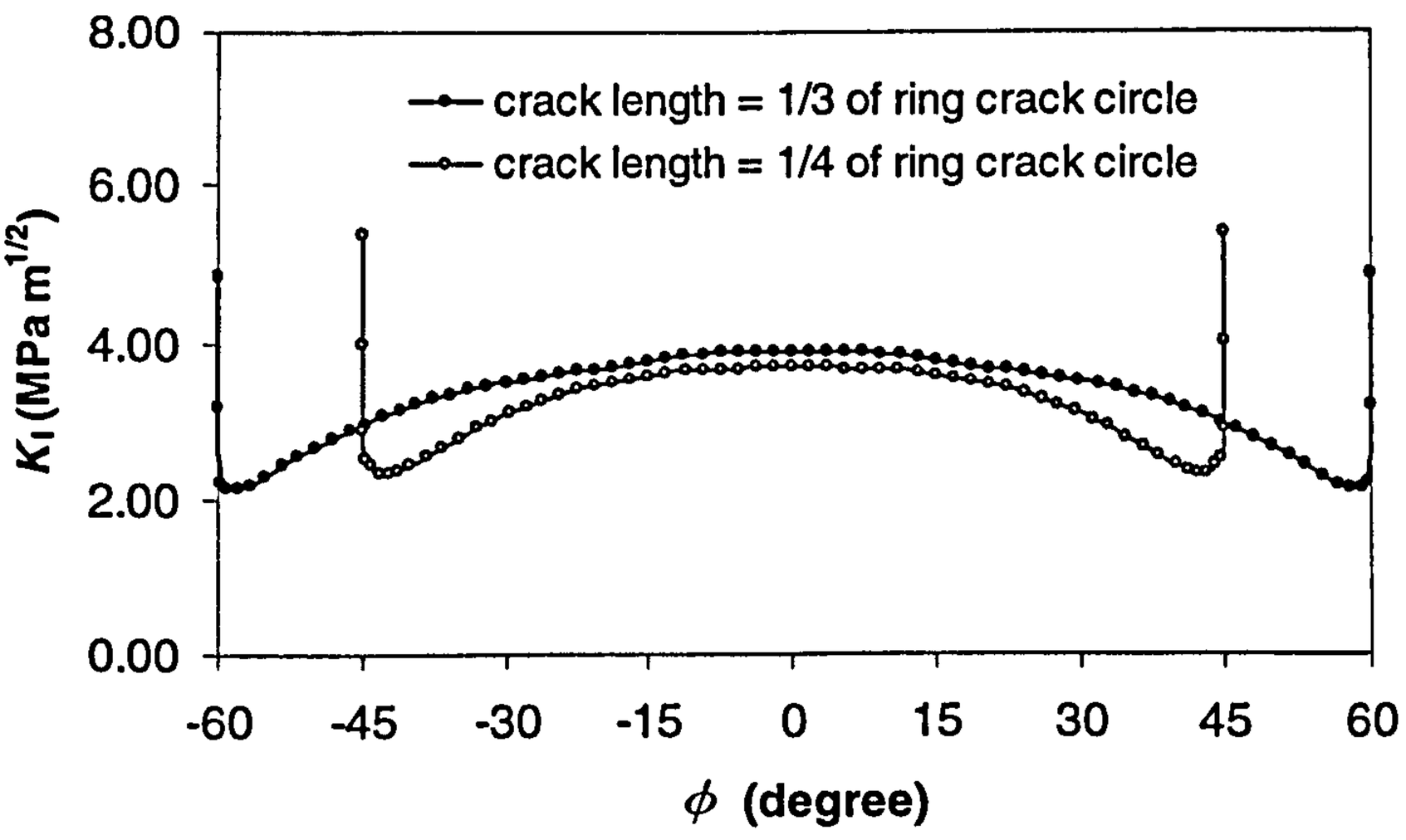

Figure 4.20 Plots of stress intensity factor K_I at different crack lengths (Geometry I).

4.3.1.4 Crack depth

Figures 4.21 and 4.22 depict the variations of the stress intensity factors for geometry III. Figure 4.21 is the calculated results when crack depth = 0.05 mm and crack angle = 40°, and figure 4.22 is when crack depth = 0.08 mm and crack angle = 40°. Comparison of figures 4.21 and 4.22 reveals that K_I decreases as the crack depth increases except when $\phi = \pm 45°$. There is little increase in K_I when $\phi = \pm 45°$. The K_I value is always higher than K_{II} and K_{III} in all positions along the crack front. The K_{II} and K_{III} also vary with ϕ but are less when compared with K_I.

Figure 4.23 illustrates the variations of stress intensity factors when the crack depth is assigned to the value of 0.083 mm for geometry I. The stress intensity factors for the crack depth = 0.05 mm has been shown previously (see figure 4.6). The comparison of these plots shows that the SIF distribution profile is very similar. The calculated results indicate that K_I decreases as the crack depth increases.

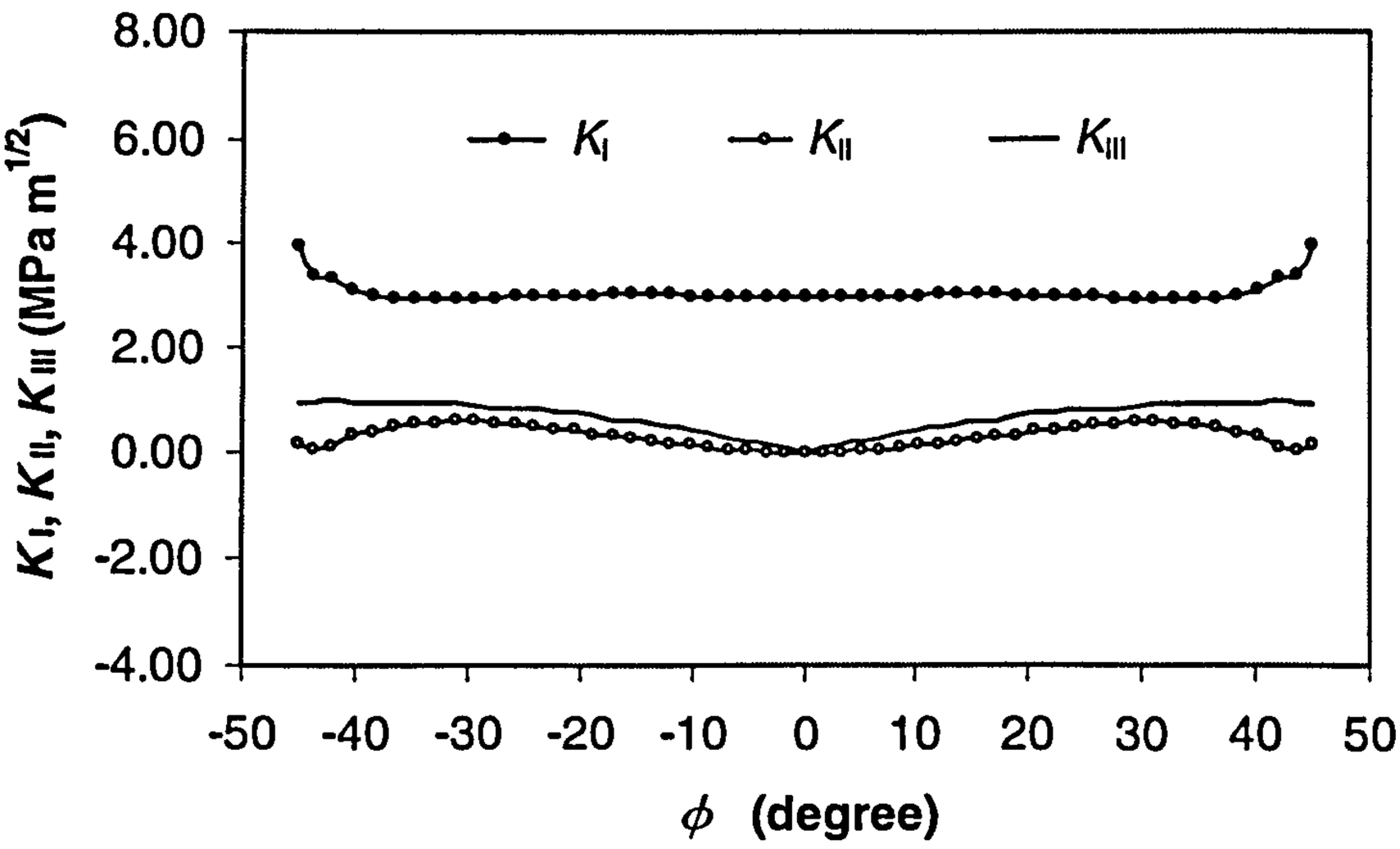

Figure 4.21 Plots of stress intensity factors at crack depth = 0.05 mm (Geometry III).

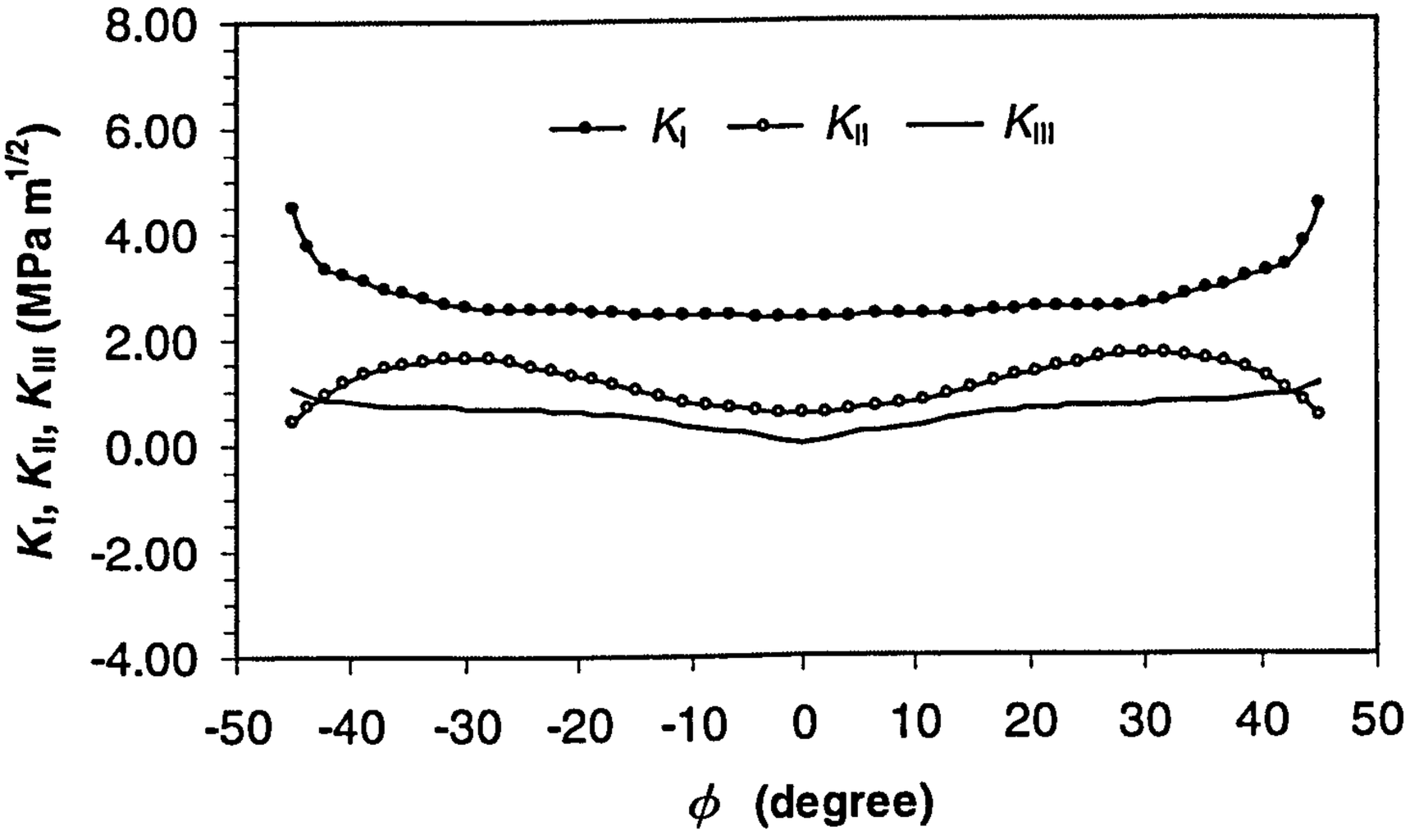

Figure 4.22 Plots of stress intensity factors at crack depth = 0.08 mm (Geometry III).

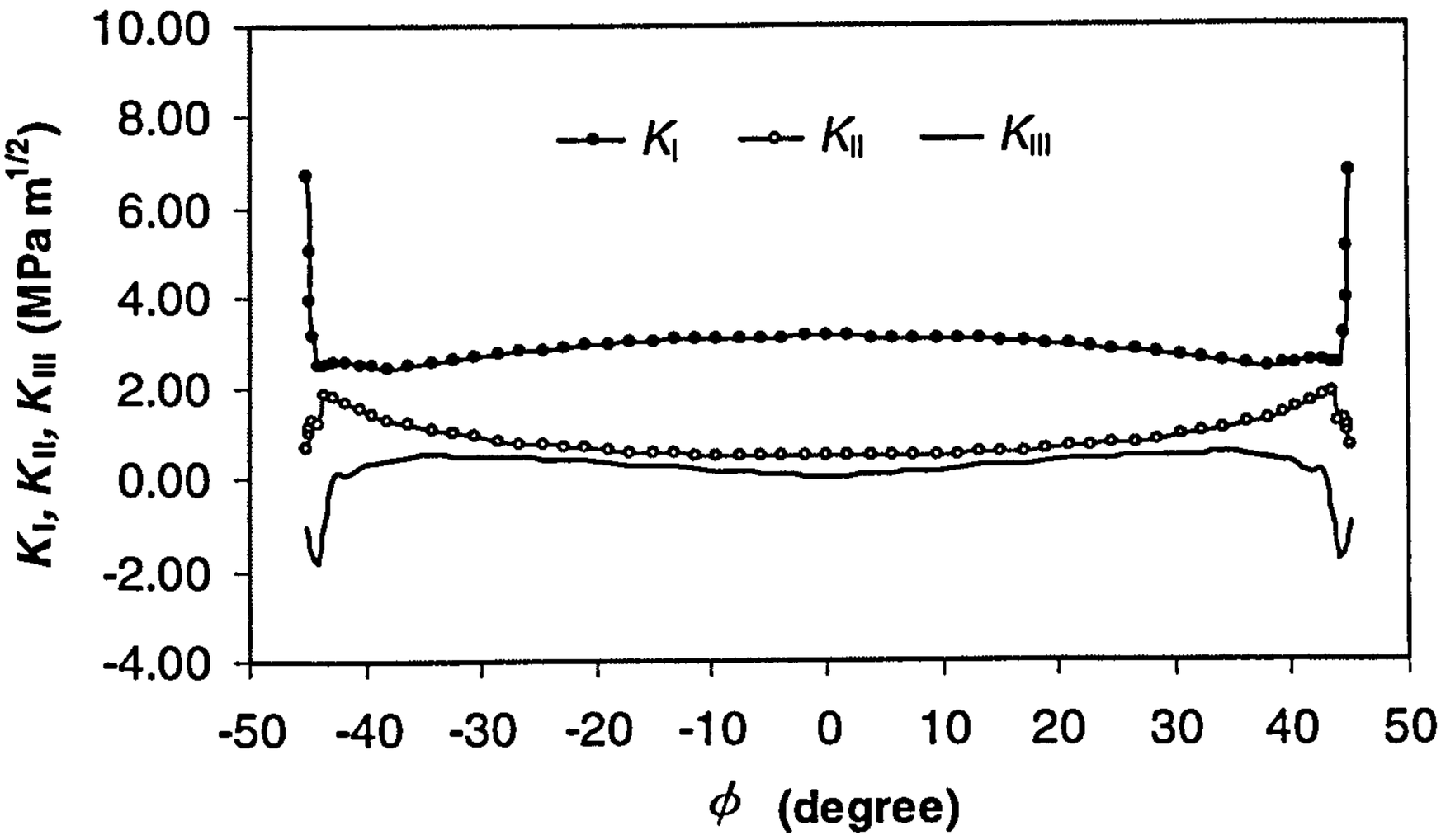

Figure 4.23 Plots of stress intensity factors at crack depth = 0.083 mm (Geometry I).

4.3.2 Influence of Loading conditions

4.3.2.1 Normal pressure

Figure 4.24 shows plots of the K_I variations caused by normal contact pressure. The geometry III is employed. Phenomena of contact radius varying with contact pressure bring some difficulties into the calculation. To compare precisely, the ring crack is placed at the same distance (0.03 mm) away from the contact circle. As can be seen from the plots, K_I increases with increasing contact stress, and reaches a maximum value at $\phi = \pm 45^{o}$. The result reveals that there is no possibility of unstable fracture due to the calculated K_I being less than K_{IC} (6.0 MPa $m^{1/2}$). Crack propagation may happen if contact stress is more than 5.0 GPa due to the threshold value ΔK_{th} = 2 to 3 MPa $m^{1/2}$. If contact stress is less than 4.0 GPa, the spalling fatigue will not happen. These predictions are consistent with the experimental observations.

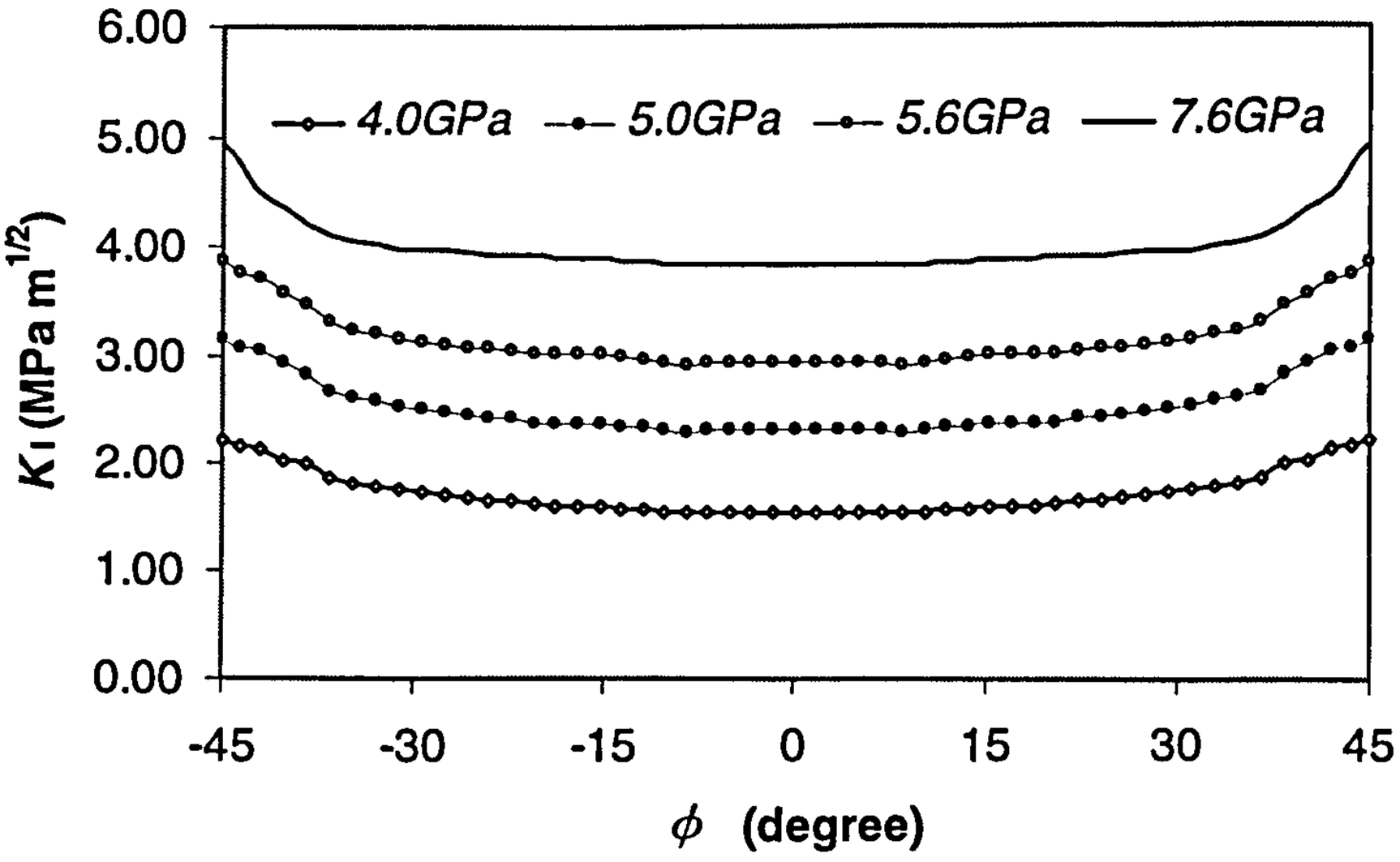

Figure 4.24 Influence of contact stresses on stress intensity factor K_I.

4.3.2.2 Tangential traction

The influence of tangential traction on stress intensity factors is investigated. The magnitude and direction of tangential traction are determined in terms of friction coefficients. The results are shown in figures 4.25 and 4.26. As can be seen from the plots, the K_I and K_{eq} stress intensity factors are influenced by tangential

traction.

Comparison of figure 4.25 and 4.26 reveals that the variations of K_I and K_{eq} are the same when the friction coefficient $f < 0.05$ and the variation profile of K_{eq} basically takes the shape of the K_I variation profile and has the same variation trend. It is concluded that K_I stress intensity factors play an important role in crack growth.

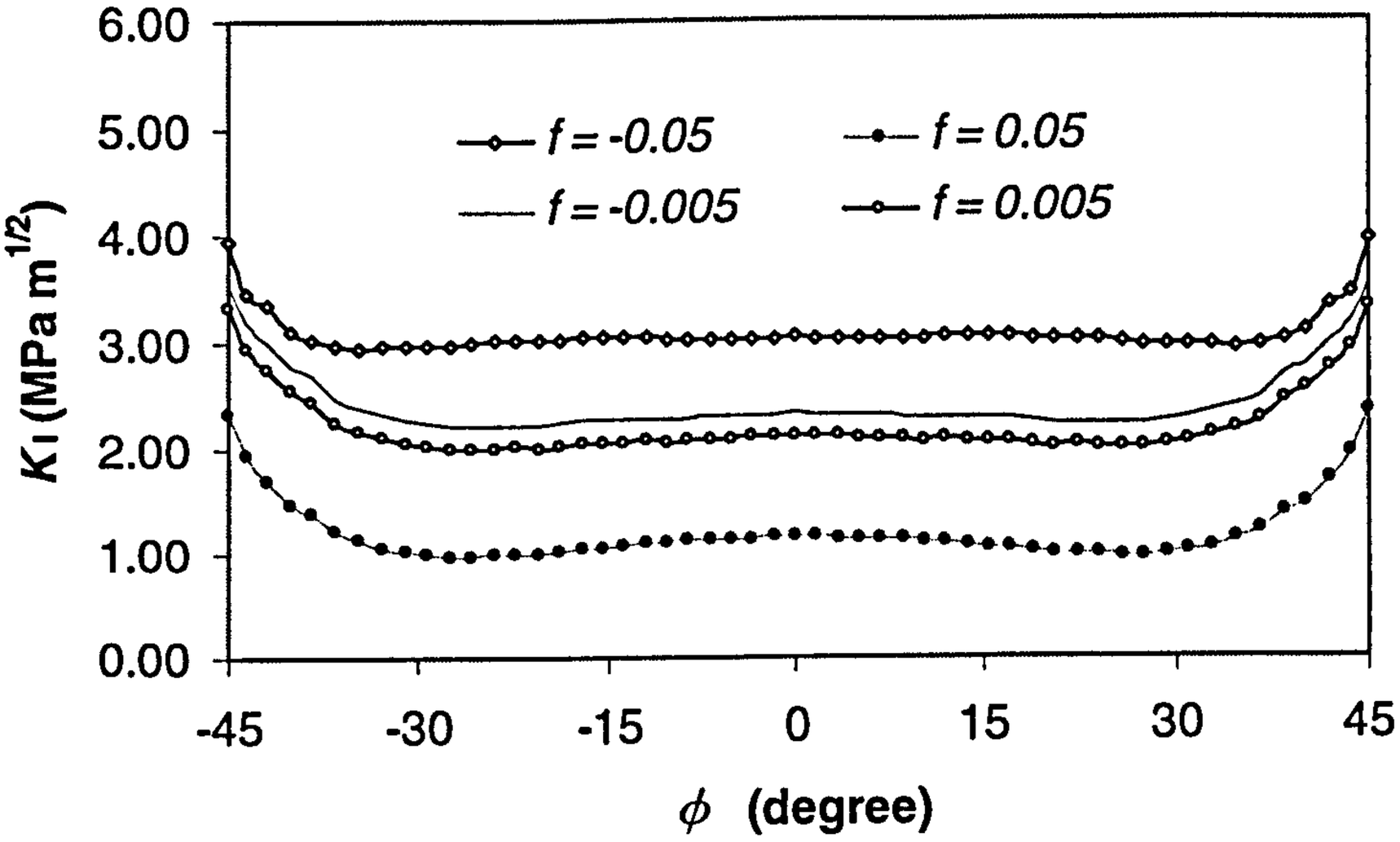

Figure 4.25 Influence of friction coefficients on stress intensity factor K_I.

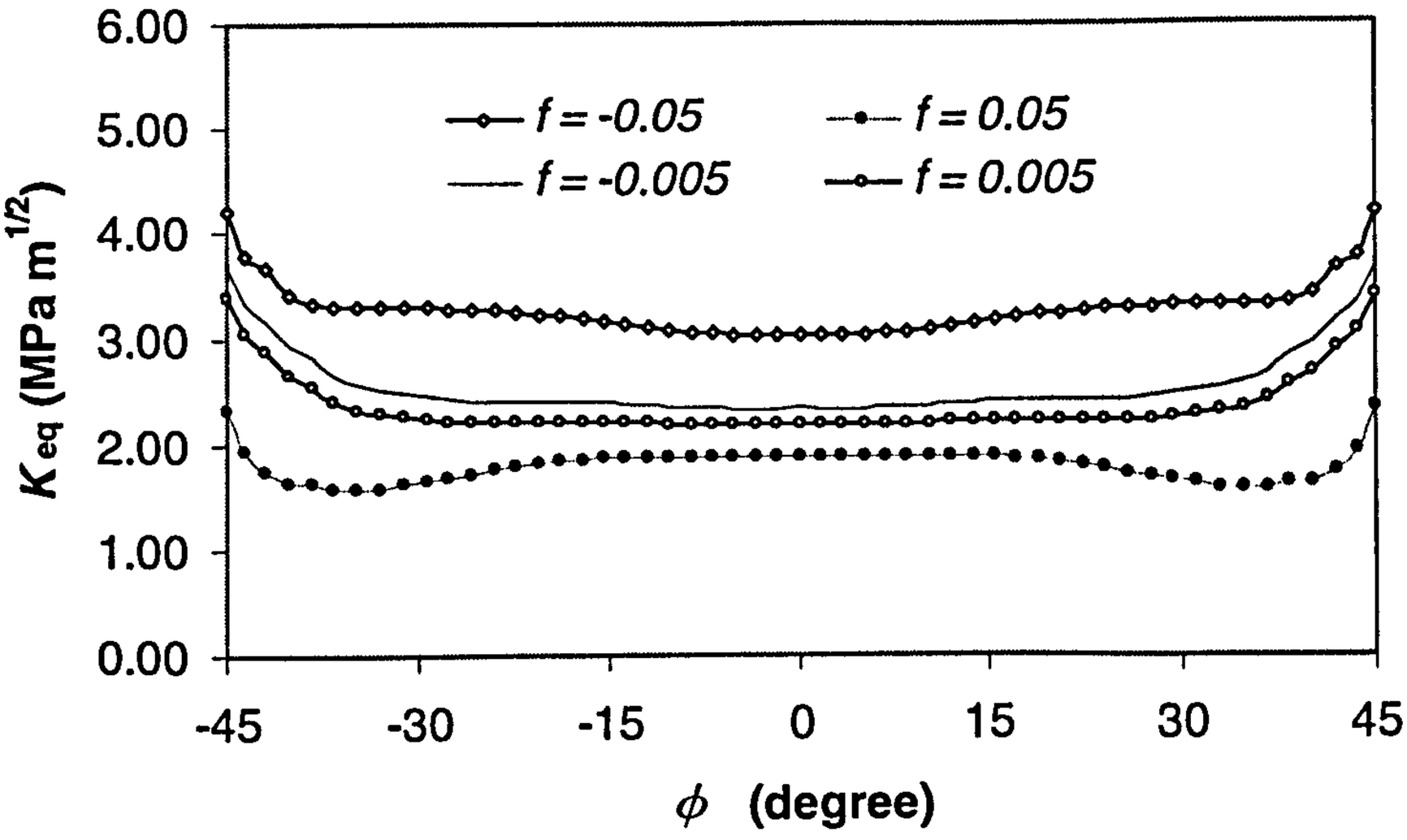

Figure 4.26 Influence of friction coefficients on equivalent stress intensity factor.

4.3.3 Influence of crack positions

4.3.3.1 Co-ordinate x

Figure 4.27 is a plot of K_I stress intensity factors as a function of the co-ordinate x. K_I stress intensity decreases slightly as co-ordinate x increases, and the variation is not significant except near the $\phi = \pm 45^o$. The results indicate that the contact circle can still cause the crack front to propagate although the distance between the contact circle centre and ring circle centre may be significantly increased.

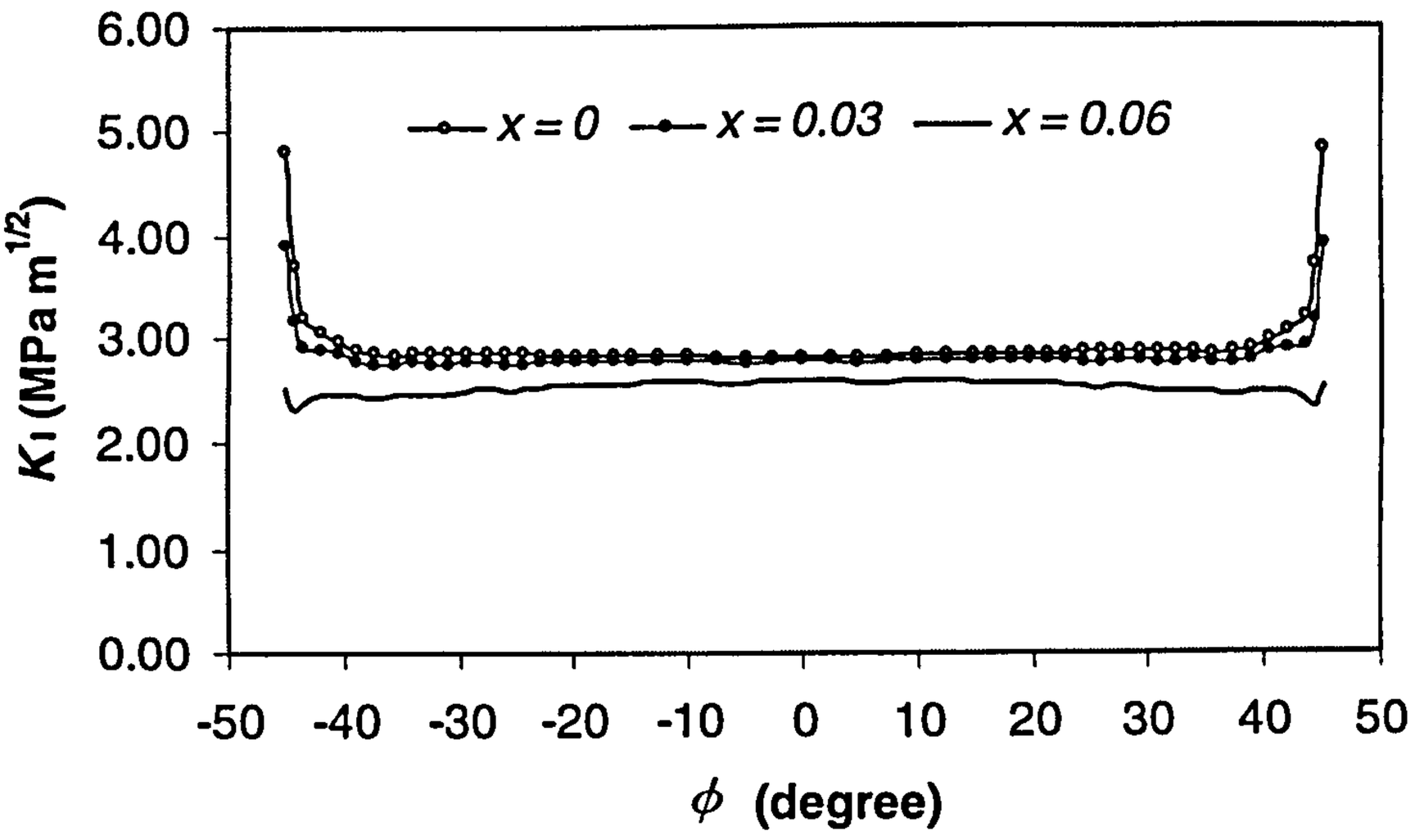

Figure 4.27 Influence of coordinate x on stress intensity factor K_I.

4.3.3.2 The parameter β

The influence of the parameter β on K_{eq} and K_I is shown in figure 4.28 and 4.29. The K_{eq} and K_I stress intensity factors are sensitive to the variations of β value. The K_{eq} and K_I for $\beta = 90^o$ are always higher than those of the $\beta = 45^o$ and $\beta = 0^o$. The results indicate that the fatigue life will be different due to the different stress intensity factors, which govern the crack propagation behaviour. The fatigue life for $\beta = 90^o$ must be shorter than others. It can be concluded that rolling contact fatigue life performance increases with the increase of β. This prediction has been verified by the experimental results.

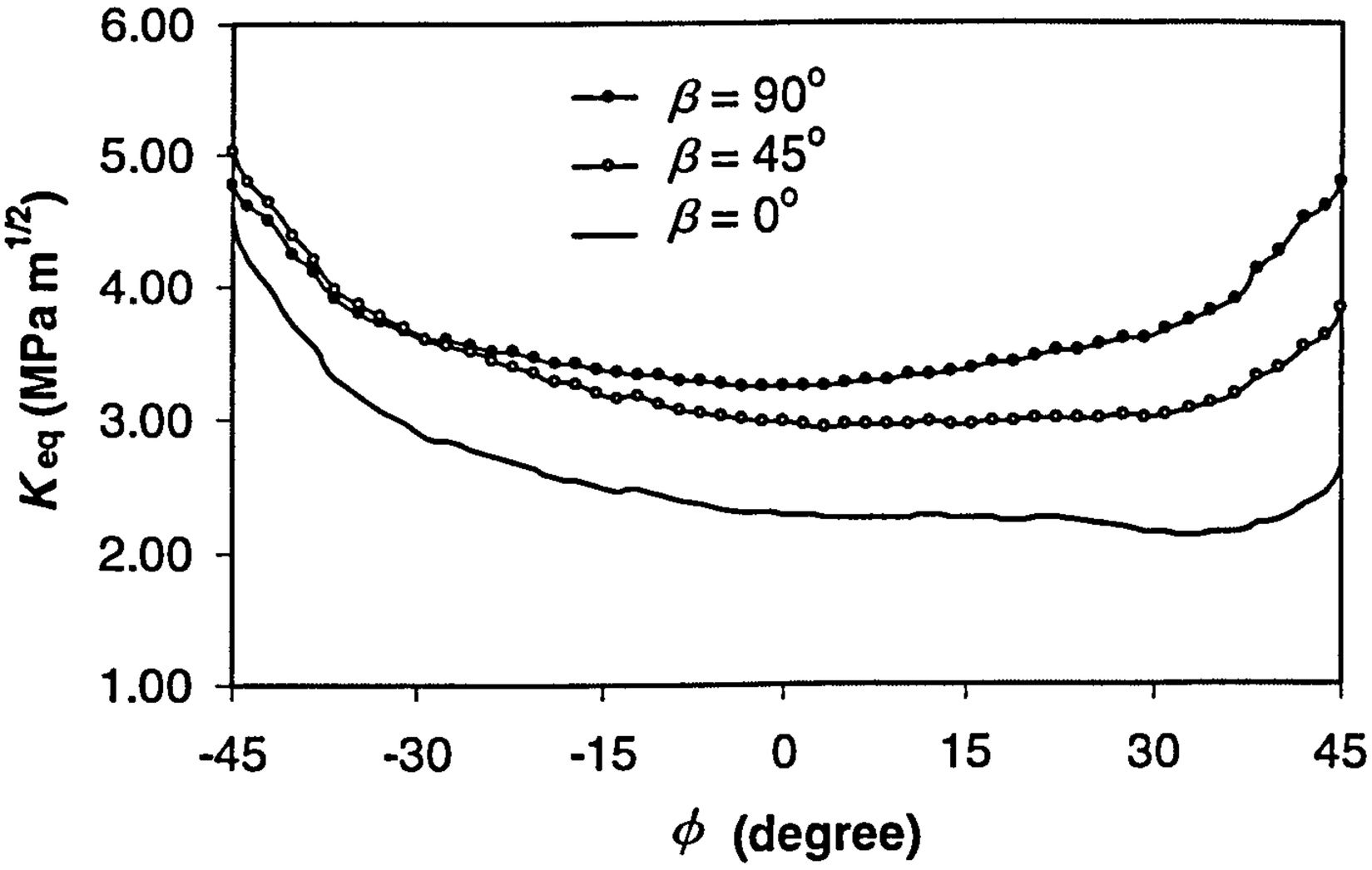

Figure 4.28 Influence of β on equivalent stress intensity factor K_{eq}.

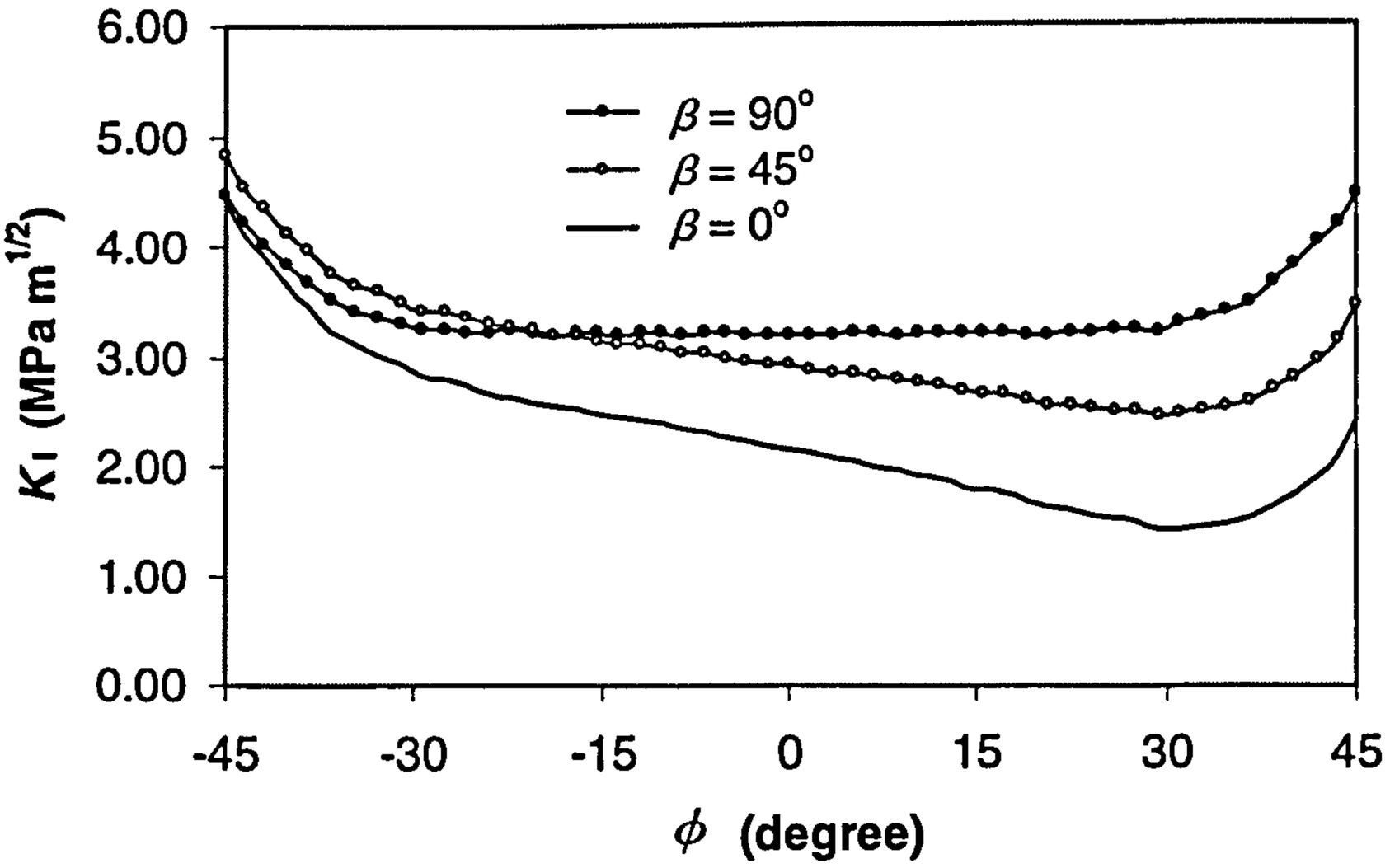

Figure 4.29 Influence of β on stress intensity factor K_I.

4.3.3.3 The parameter δ

Figure 4.30 shows the effect of δ on K_I stress intensity. The K_I values along the crack front for $\delta = 0$ are always larger than those of the $\delta = 0.5a$ and $\delta = a$. This result indicates that the possibility of crack propagation increases as the parameter δ decreases. The present prediction is consistent with the experimental observations.

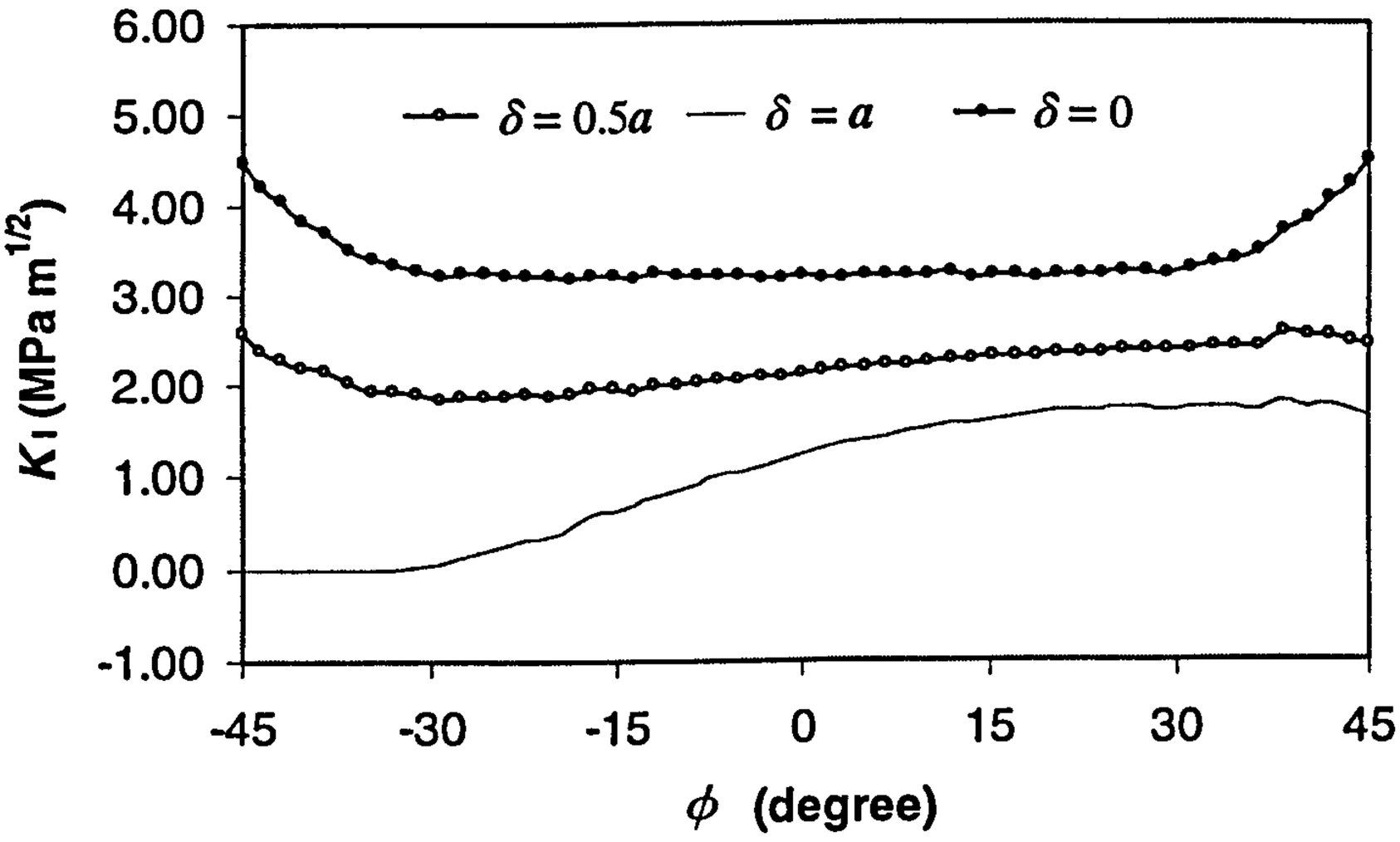

Figure 4.30 Influence of δ on stress intensity factor K_I.

4.4 LIFE PREDICTION OF SPALLING FATIGUE FAILURE

Figure 4.31 is a plot of the stress intensity factor K_I as a function of crack extension which shows that stress intensity factors decrease with crack front propagation. There are two lines in figure 4.31. The upper line is the result of crack length = one-third of ring crack circle, and the lower line is for the crack length = one-fourth of ring crack circle. The results indicate that crack propagation will be arrested when a certain extension size is reached. This may explain why the rolling contact failure mode of silicon nitride is non-catastrophic. The computations are based on an assumed crack path derived from the equations (4.3) to (4.5). The aim is to relate the stress intensity factors to crack propagation. The calculation of stress intensity factors presented here, while approximately in the plane of $\phi = 0^o$, may be useful in fatigue life prediction.

To demonstrate what spall size may be expected to be reached in the spalling failure, we will use the Paris equation (Paris and Erdogan 1963)

$$da/dn = c(\Delta K)^m \tag{4.30}$$

by substituting $K_I = -19.181x + 4.5475$ from figure 4.31 to solve fatigue cycles requested for a certain crack size. Fatigue cycles can be obtained by the integrating equation (4.30), which is expressed as follows:

$$n = \int_{a_0}^{a_c} \frac{da}{c(\Delta K)^m} = \int_{a_0}^{a_c} \frac{da}{c(4.5475 - 19181a)^m} \tag{4.31}$$

Integration of equation (4.31), then

$$n = \frac{1}{19181c(m-1)}\left[(4.5475 - 19181a_c)^{-m+1} - (4.5475 - 19181a_0)^{-m+1}\right] \tag{4.32}$$

The constants in the Paris law of equation (4.31) are obtained from the fatigue crack propagation studies. The value for c is 1.01×10^{-21} and the exponent m for HIP material is 18 (Bar-On and Beals 1990).

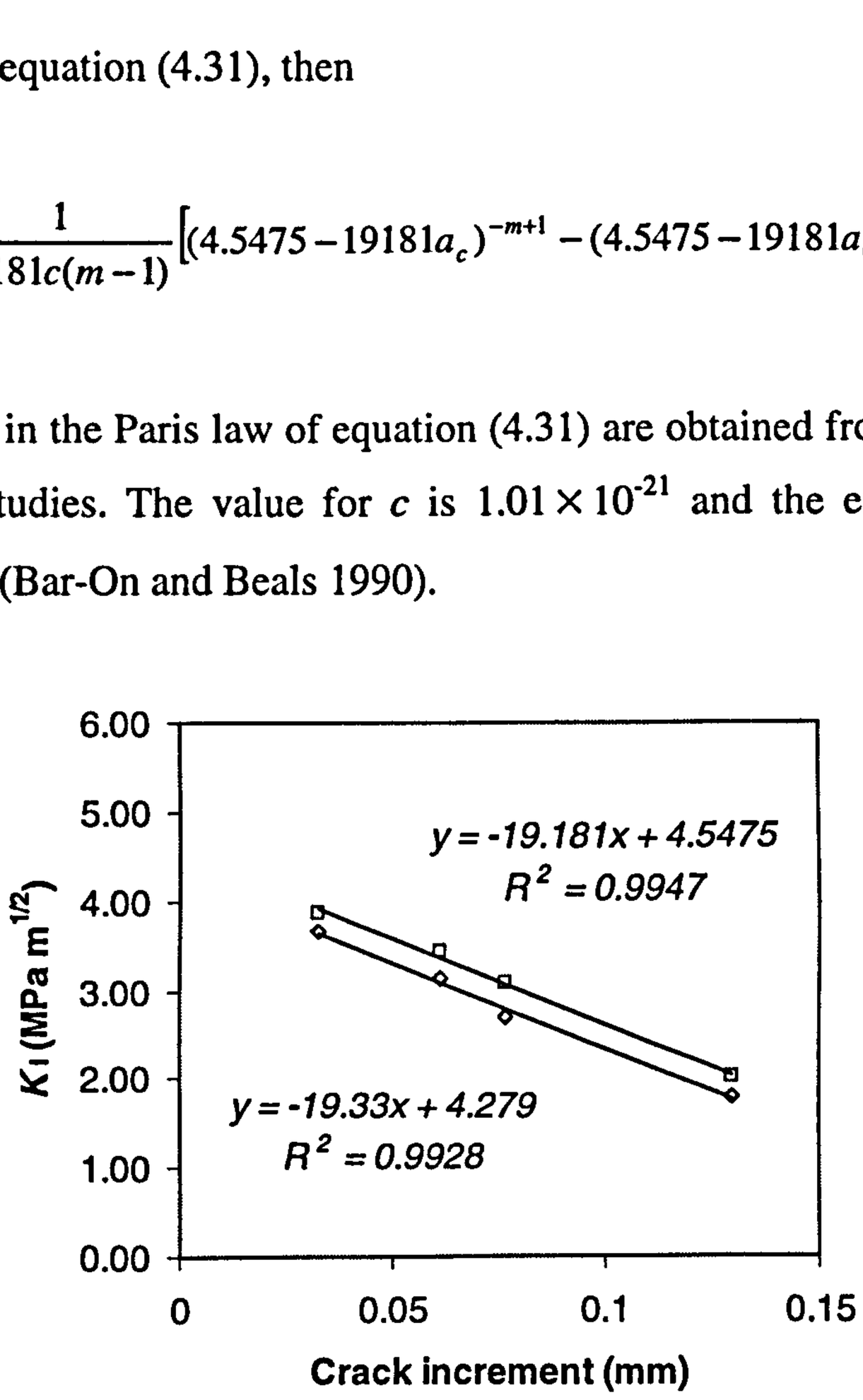

Figure 4.31 Plots of K_I versus crack increment.

Fatigue cycles for the different crack extensions are shown in figure 4.32. The calculated fatigue cycles indicate that the original ring crack propagation may be able to reach the lower boundary of a spall size normally observed (0.3 to 0.4 mm in

diameter). It should be emphasised that it is still hard to describe the spall sheet separation although the crack may be able to propagate to the spall size.

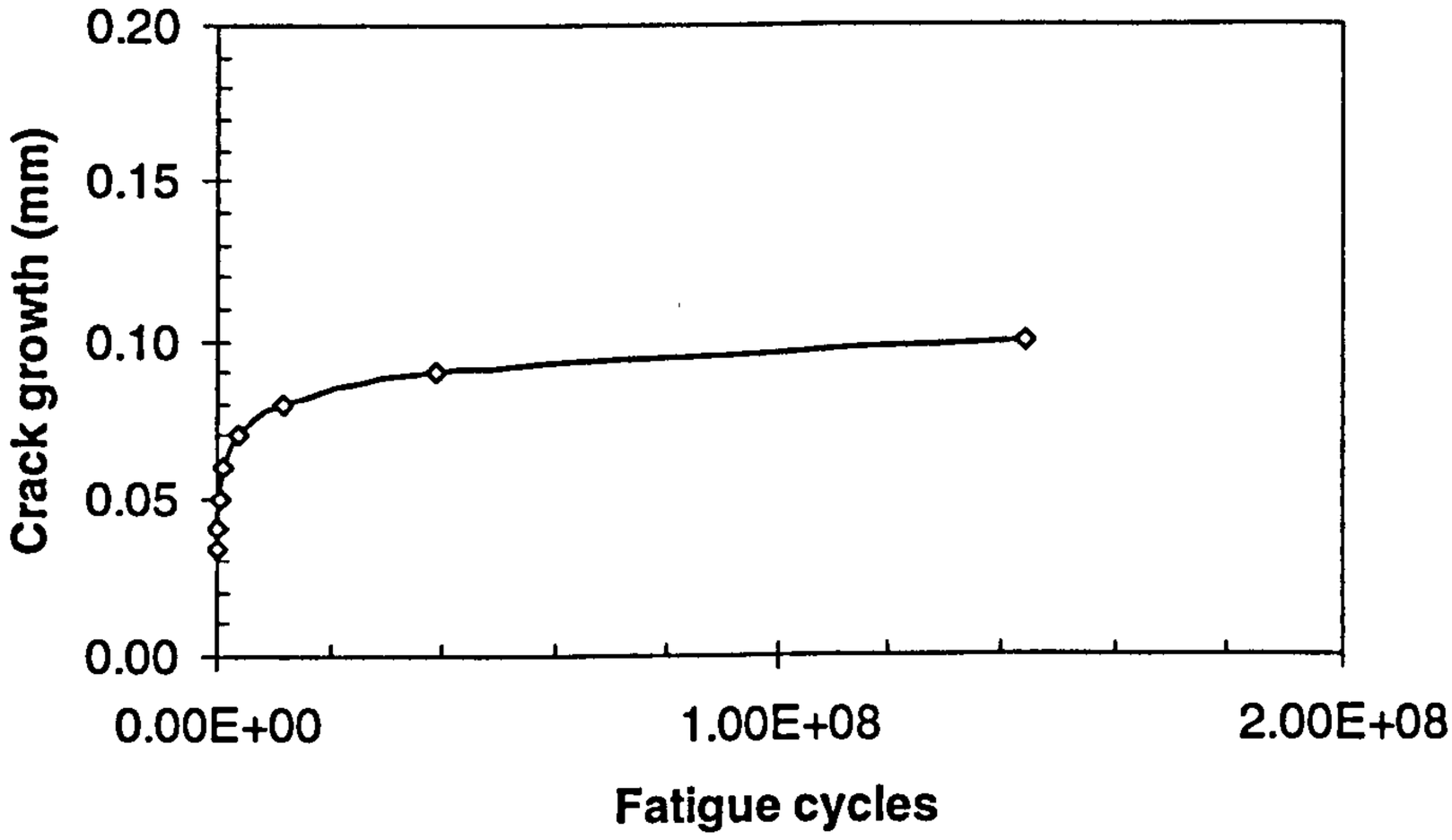

Figure 4.32 Plots of crack growth versus fatigue cycles.

Inspection of figure 4.32 reveals that the crack front is hard to propagate when it grows to 0.09 mm (5×10^7 fatigue cycles). Experimental observations show that the fatigue cycles are between 1.5×10^7 and 5×10^7. The contour radius is on an average of 0.2 to 0.25 mm. The predicated spall size is smaller than the observed size. There may exist other crack growth to enlarge the spall size.

Figure 4.33 depicts the variations in stress intensity factors for different stages of crack extensions. Computations are based on a predicted crack growth path and the crack is re-meshing again after having propagated. As can be seen from the stress intensity factor plots, stress intensities on the crack front are a function of the angle ϕ. K_I values at $\phi = \pm 45^o$ (ball surface) reach a maximum for the initial crack front and decrease as the crack front grows. It is found that the crack front propagation will take different increment sizes depending on ϕ. In the middle plane ($\phi = 0$), crack front growth reaches a maximum extension compared with other locations. This is why a fatigue spall contour always takes an ellipse shape. The corresponding crack propagation contour is shown in figure 4.34 (Section 4.5).

For ball bearing elements, crack propagation happens within inhomogeneous stress fields. The stress intensity factor calculation shows that K decreases as the crack grows. The results indicate that crack growth will be arrested at a certain size.

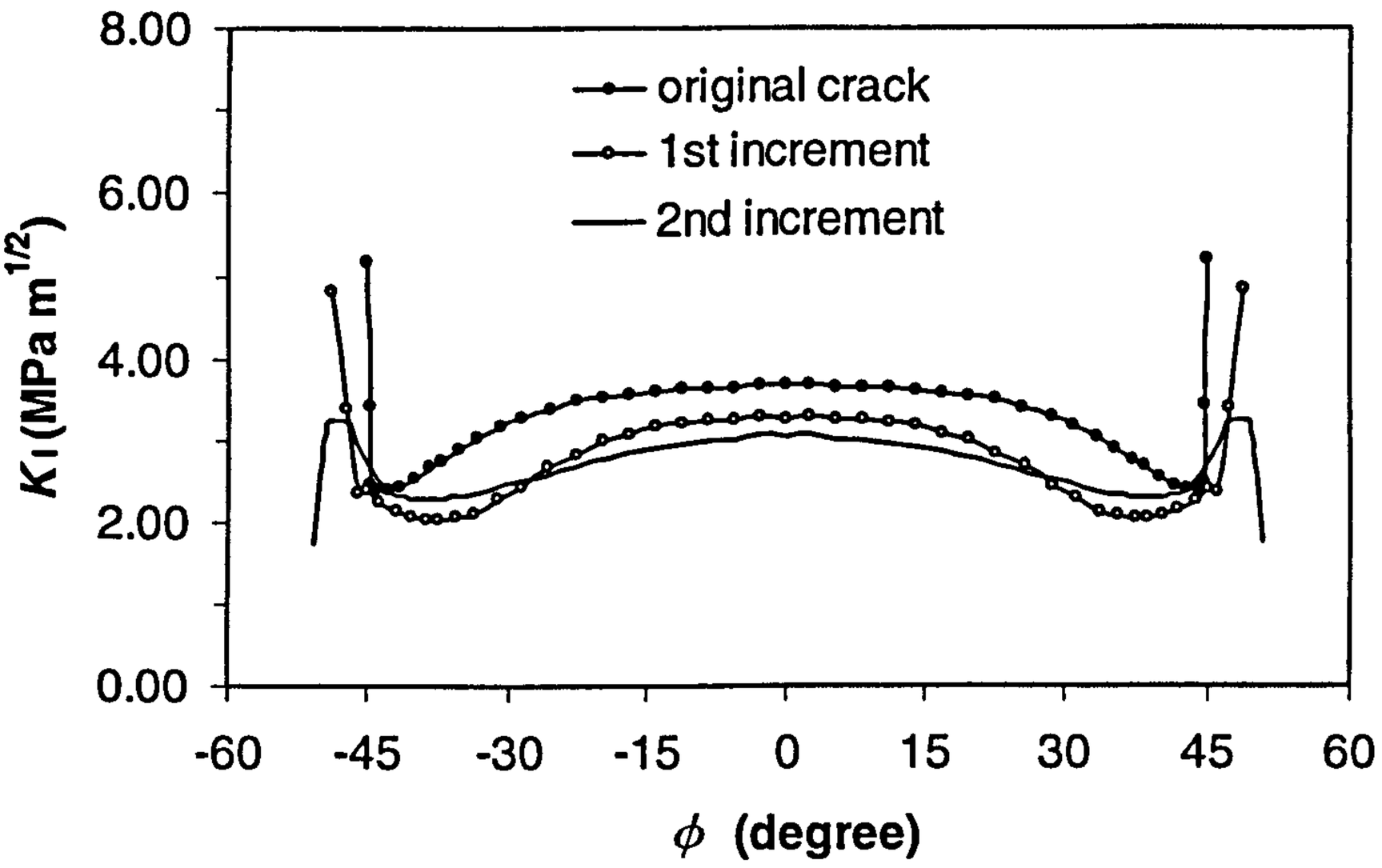

Figure 4.33 Plots of K_I variations in crack propagation.

The spalling surface is now studied in detail. The radius of the spall is approximately 0.2 mm (see Chapter 3, figures 3.30 and 3.32). The crack front propagates about 0.15 mm to reach the spall size (in the plane of $\phi = 0^o$) and the fatigue cycles are 1.6 to 4.8 $\times$ 10^7 for these two tests. Average cyclic crack growth rate ($\Delta a/\Delta N$) is approximately 0.3 to 0.9 $\times$ 10^{-11} m / cycle, which is much less than the so-called threshold value (10^{-10} m / cycle). The result indicates that the crack front will not grow if it grows at that crack growth rate. This implies that the fatigue life is not simply described by the da/dn-ΔK relation. The fatigue spall life for a cracked ball involves two parts: crack propagation life for the formation of a certain size crack and fatigue cycles required for the spall sheet separation. There must be a period in which the crack stays at the same size. During this period, the crack face is suppressed under repeated rolling contact and the crack gap will increase due to the wear of the crack surfaces. The secondary surface cracks will be formed if the crack

gap reaches a critical size. These surface cracks will then propagate downwards to join the main crack propagation path and a spall is eventually generated. This aspect will be discussed in Chapter 5.

4.5 THE PREDICTED CRACK PROPAGATION PATH

4.5.1 The path in continuous propagation

The predicted crack growth path is shown in figure 4.34. According to this contour the crack grows slightly in width at the initial crack propagation and then it propagates into the inside of the material. Look at the case $\phi = 0^{o}$, crack growth is almost parallel to the surface in the first crack increment. In the second and third extension, the crack grows in the direction of 10^{o} to 15^{o} with the surface, depending on the loading condition. Will the crack grow in the same way as the predicted contour above? The correct answer for crack propagation can only be determined by the experimental investigations, and it is found that the present prediction is consistent with the experimental observations. The experimental observations have been described in Chapter 3 (Section 3.3).

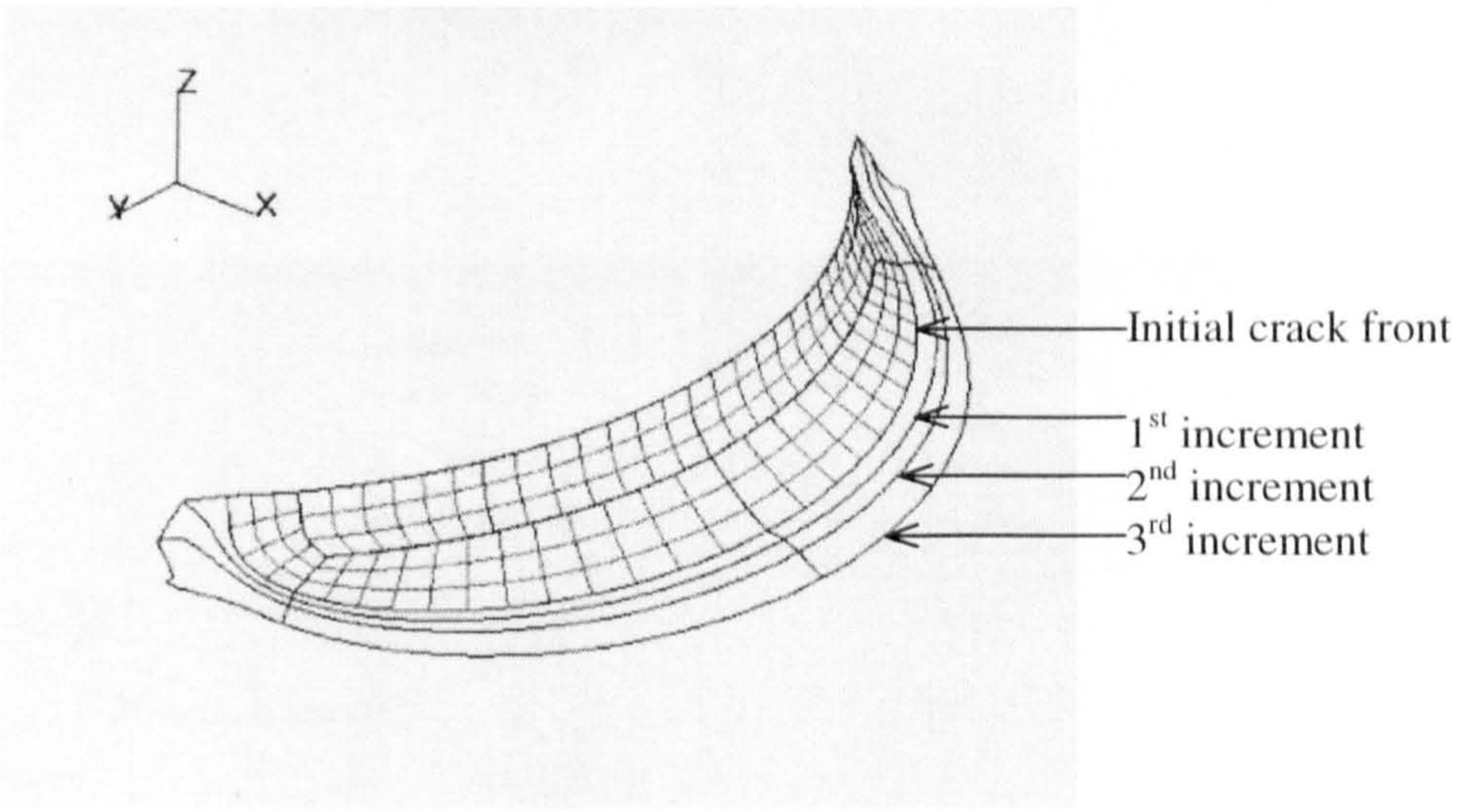

Figure 4.34 Crack growth contours in continuous propagation (Geometry I).

4.5.2 Influence of crack locations

Figure 4.35 shows the crack growth direction for the $\beta = 90^{o}$ and $\delta = 0$. It can be seen that the crack will grow towards the materials, which is roughly at 30^{o} (in the middle section plane) to the surface. At point A and B, the crack extending size has a maximum of about one-third of crack depth, and the increment size along the crack front is determined in terms of the stress intensity factors corresponding to point locations.

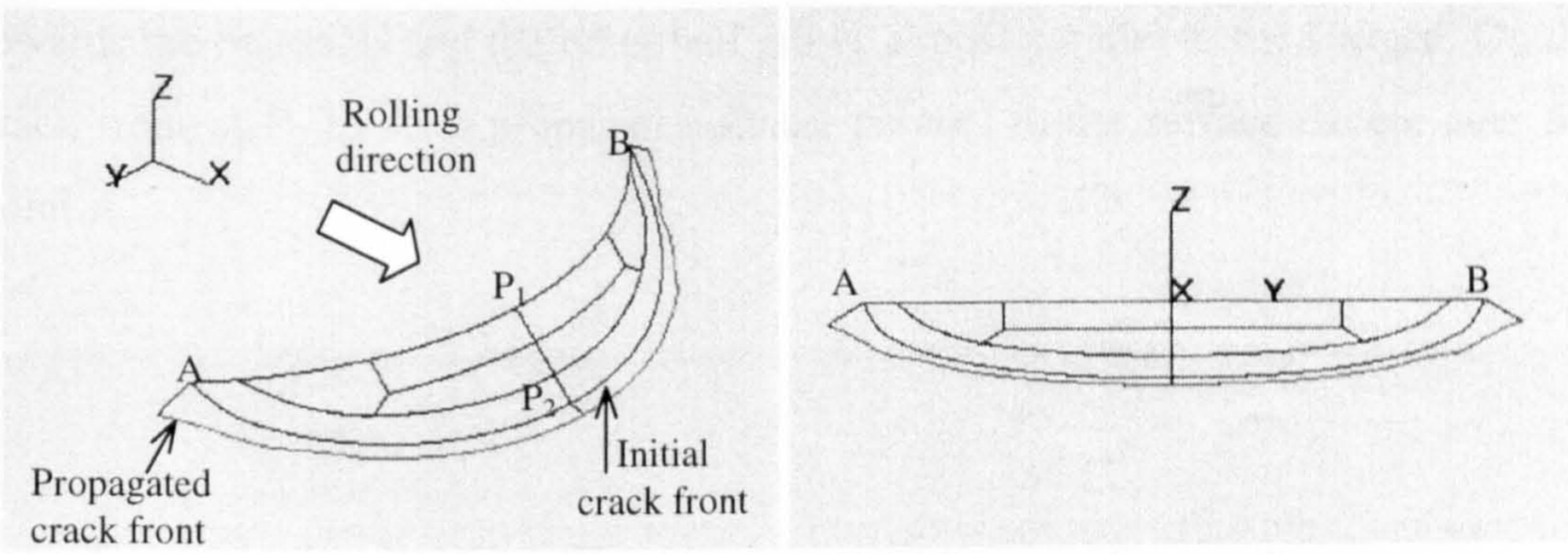

Figure 4.35 Views of crack propagation (geometry III, $\beta = 90^{o}$, $\delta = 0$ and $\alpha = 50^{o}$).

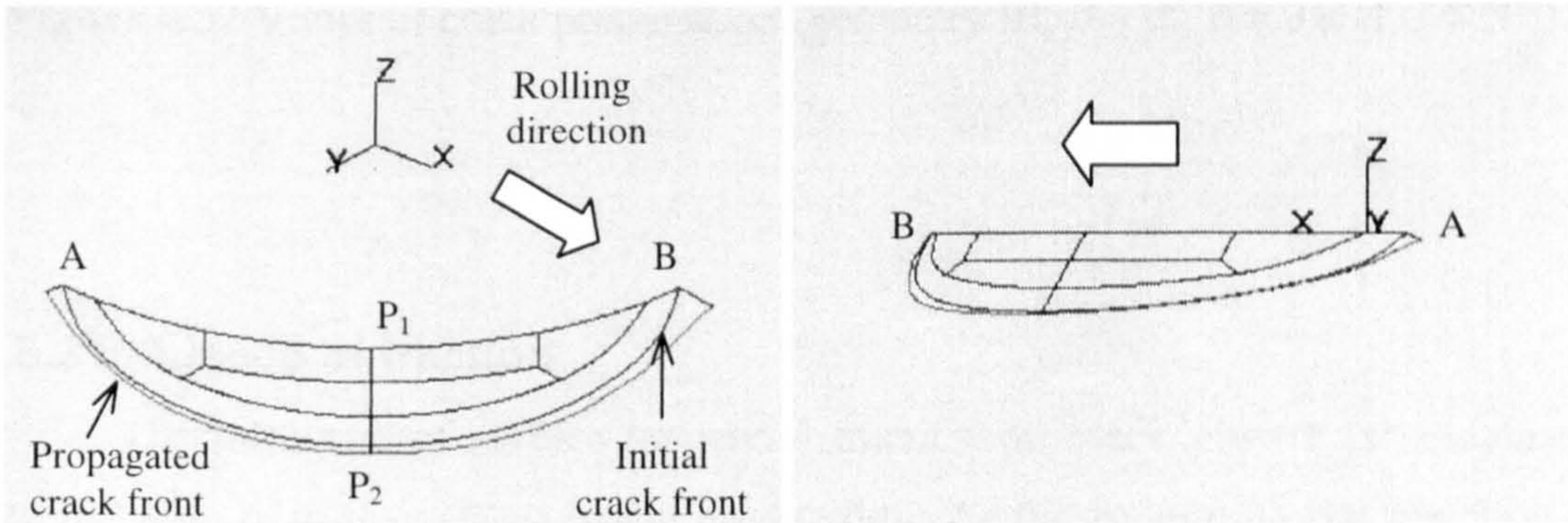

Figure 4.36 Views of crack propagation (geometry III, $\beta = 45^{o}$, $\delta = 0$ and $\alpha = 50^{o}$).

Figure 4.36 shows the crack growth direction for the $\beta = 45^{o}$ and $\delta = 0$. The crack growth direction changes with the change of point location along the crack front. On the front of B to P_2, the crack propagates towards the materials and on the front of P_2 to A, the crack propagates almost parallel to the surface except near the point A.

Figure 4.37 shows the crack growth direction for the $\beta = 0^{o}$, $\delta = 0$. As in Figure 4.36, the crack growth direction changes with the change of the point location along the crack front. On the crack front of B to P_2, the first half will propagate towards the materials and the other half grows almost parallel to the surface. On the crack front of P_2 to A, it propagates almost parallel to the surface except near the point A.

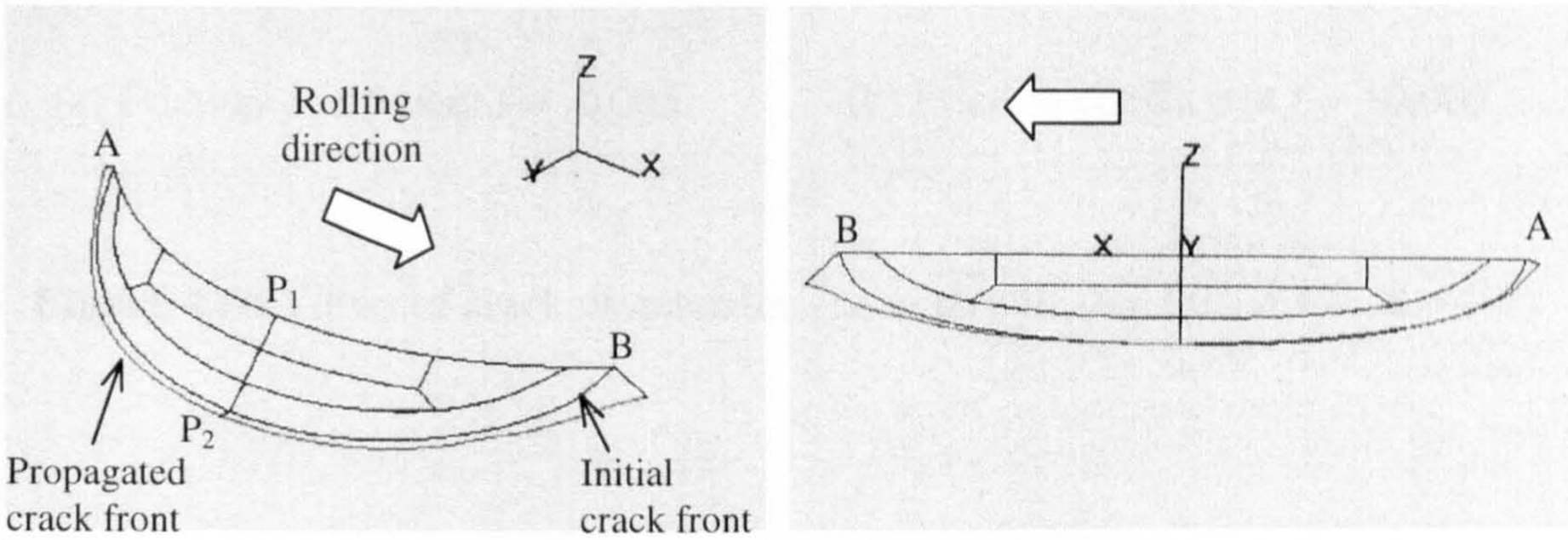

Figure 4.37 Views of crack propagation (geometry III, $\beta = 0^{o}$, $\delta = 0$ and $\alpha = 50^{o}$).

4.5.3 Influence of traction

The influence of surface tangential traction on crack growth is calculated. The different friction coefficients are used to describe the magnitude and direction of the tangential traction. As described in numerical analysis, the incremental size along the crack front is determined in terms of the equivalent stress intensity factor corresponding to point locations. The calculation result is shown in figure 4.38. As can be seen from the plots, the crack front will grow towards the materials. The extending size of the crack front reaches its maximum at points A and B. The crack

growth direction and incremental size change in line with ϕ. The comparison of figures 4.38(a) and (b) reveals that the crack growth direction is slightly influenced by the change of rolling direction.

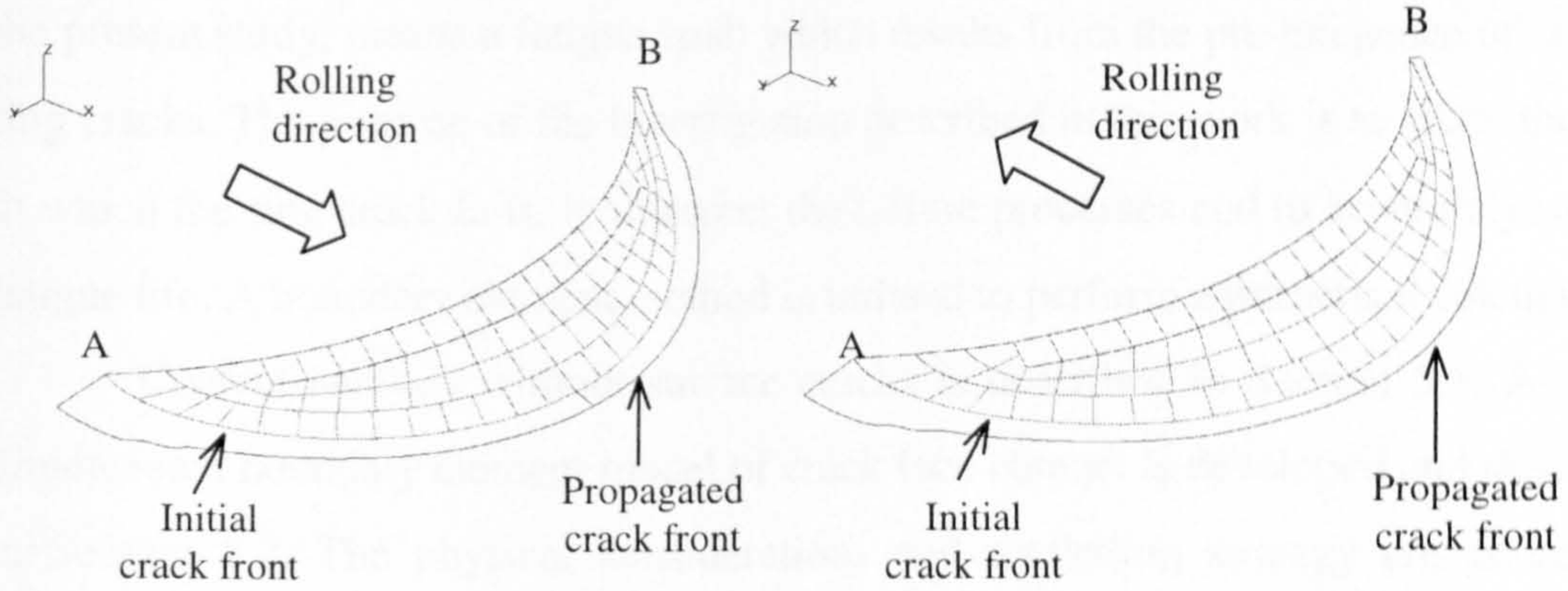

(a) Friction coefficient f = -0.005 (b) Friction coefficient f = +0.005

Figure 4.38 Views of crack propagation (geometry III, $\beta = 90^{o}$, $\delta = 0$, $\alpha = 40^{o}$).

CHAPTER 5

CONTACT ANALYSIS OF CRACK FACES

Analytical models of ball stress fields are presented to increase understanding of ring crack fatigue failure processes. Ring crack fatigue failure, as the term is used in the present study, means a fatigue spall which results from the pre-existence of surface ring cracks. The purpose of the investigation described in this work is to study the way in which the ring crack fails, to interpret the failure processes and to accurately predict fatigue life. A boundary element method is utilised to perform a numerical calculation.

Contact analysis without surface cracks is described in Section 5.1. A three-dimensional boundary element model of crack face contact is developed and described in Section 5.2. The physical considerations and modelling strategy are addressed. Based on the model, the analysis of stresses on the ball surface is presented in Section 5.3. The influence of crack gap and traction direction on the surface stress distribution is discussed in Section 5.3.1 and Section 5.3.2 respectively. The influence of crack dimension on the surface stress distribution is described in Section 5.3.3. The influence of crack face friction coefficients on the surface stress distribution is described in Section 5.3.4. Stress distributions on crack faces are discussed in the final section. The stress distribution on the lower crack face is described in Section 5.4.1 and the stress distribution on the upper crack face is described in Section 5.4.2.

5.1 CONTACT ANALYSIS WITHOUT SURFACE CRACKS

5.1.1 Model description

The boundary element method based computer modelling package BEASY (Computational Mechanics BEASY 1998) is employed to perform contact analysis. The boundary element method, quite apart from its ease of use and accuracy, is very suitable for contact analysis because contact is essentially a boundary phenomenon. It is the surface of components which come into contact with each other and, since boundary elements make all their computations on the surface, it seems natural that they should be useful for this type of analysis.

The use of the boundary element method to analyse contact problems was first described by Andersson et al. (1980), and has been addressed by numerous authors (Niku et al. 1991, Aliabadi and Brebbia 1993, Man 1994) since then. The basic problem they address is that the contact area is not known in advance and, since the boundary conditions which are used in the solution depend on the condition of contact or non/contact for each node, this type of problem cannot be solved in a direct way. Instead, we require an iterative solution scheme.

An iterative scheme is one in which a guess is made for the solution. Using this guess we can arrive at a better estimate of the solution, and from that estimate the procedure provides an estimate which is better still. After a certain number of these iterations the estimate of the solution stays the same as the previous estimate, and the iteration has converged.

The incremental load approach is adopted in the calculation. This approach is particularly important for cases involving frictional contact, as the load path becomes substantially more important.

The purpose of contact analysis is to understand completely stress field and strain distributions around the contact zone. The results will provide the specific contact volume analysis with the boundary conditions.

The model of a ceramic upper ball contacting with a steel lower ball is shown in figure 5.1. The detailed view of the contact zone is shown in figure 5.2. This model is axisymmetric, which simplifies the geometric requirements to a plane model, rotated about the load axis. The reason for this consideration is that the friction coefficient is extremely low in lubricated rolling contact and hence its influence on the stress field is limited. Lubrication regime is studied (Appendix 4) using elasto-hydrodynamic theory. The results show that a full film exists, which implies that a frictionless model is valid.

Contact is modelled in BEASY using the software's 'initial gap' boundary condition. This boundary condition defines a gap between two components. Initial gap values can be defined over an entire surface containing elements when the contact is conforming, or on an element-by-element/node-by-node basis when the contact is non-conforming.

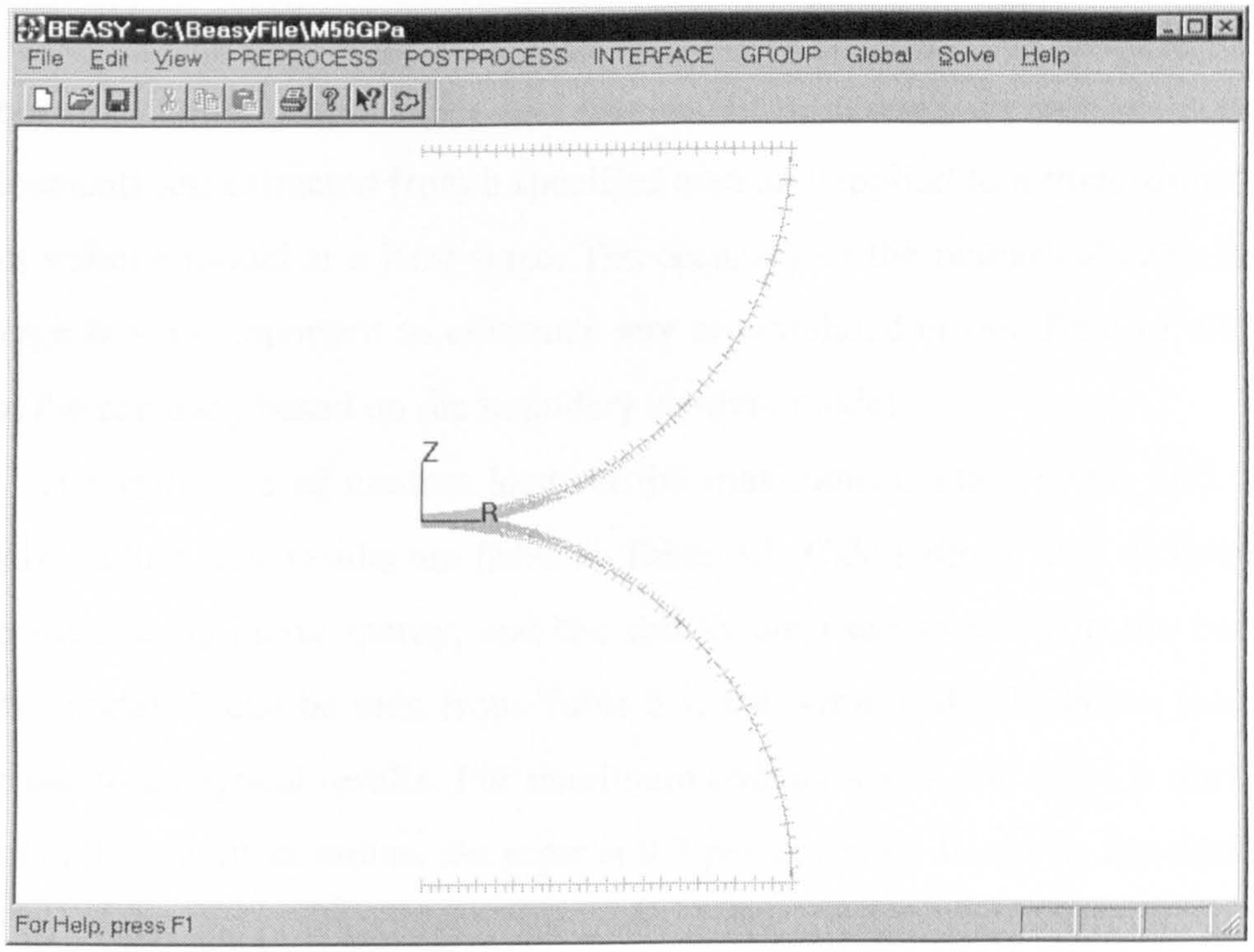

Figure 5.1 Axisymmetric boundary element model.

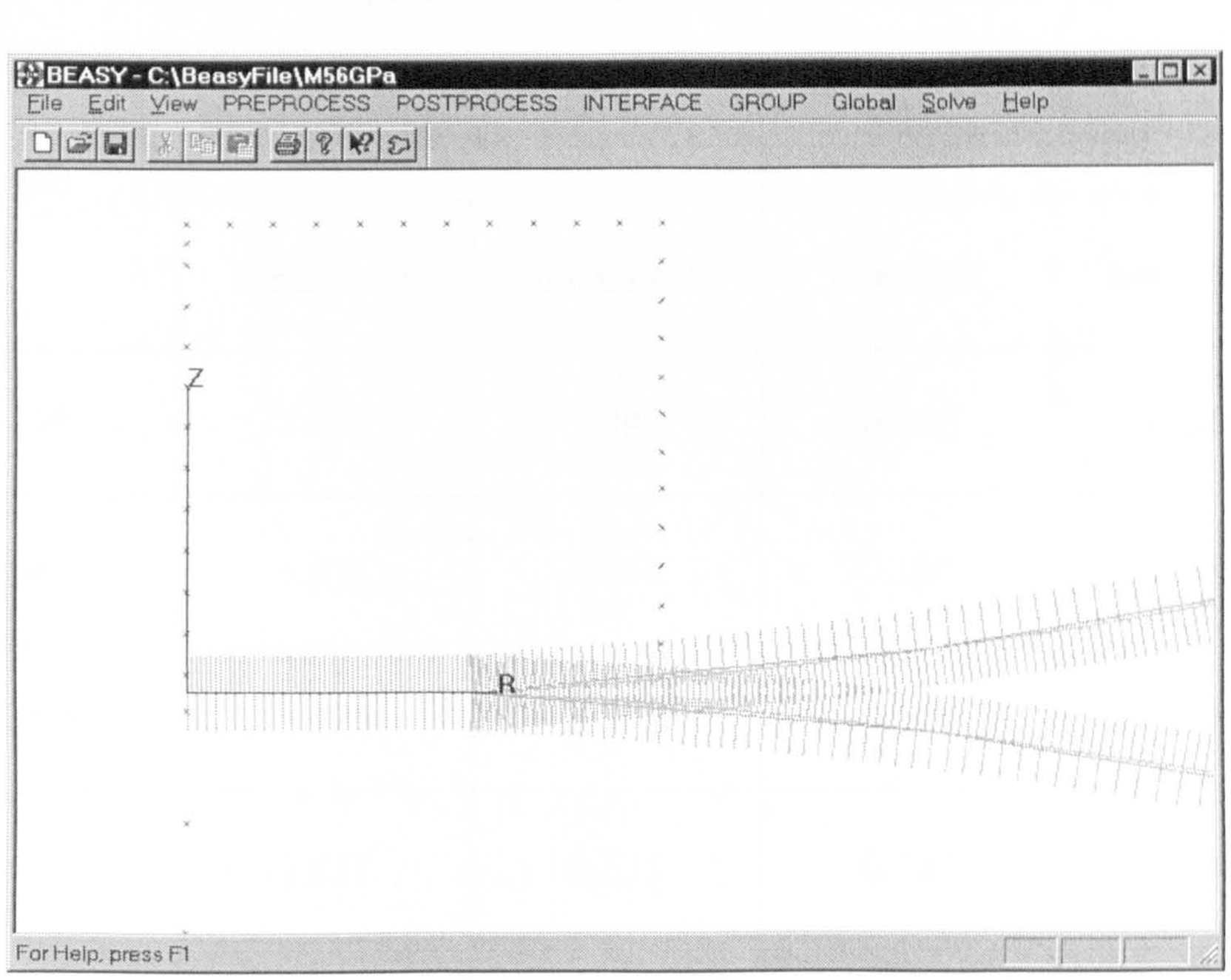

Figure 5.2 Detailed view of contact zone.

5.1.2 Result analysis

The main objective for development by the analytical models of the contact problem is to obtain stress fields and displacements around the contact zone. The displacements are extracted from a specified area and applied to a three-dimensional contact volume model at a later stage. The accuracy of the numerical calculation at this stage is very important to eliminate any accumulated errors. First of all, let us look at the accuracy based on the boundary element model.

The influence of contact load on the maximum contact stress and contact radius is studied. The results are listed in Table 5.1. Calculations with different load are verified using Hertz theory, and the results are used to validate the boundary element model. It can be seen from Table 5.1, the numerical calculation results are very close to analytical results. For maximum contact stress, the error is about 0.15 percent and for contact radius, the error is 0.3 percent only. It can be concluded that the BEM model can provide highly accurate results.

Table 5.1 Comparison of theoretical and numerical solutions

Contact load (N)	Maximum contact stress (GPa)		Contact radius (mm)	
	Analytical	numerical	analytical	numerical
179	4.000	3.998	0.146	0.145
367	5.078	5.081	0.185	0.185
490	5.589	5.592	0.204	0.205
816	6.627	6.633	0.242	0.240
1225	7.586	7.598	0.277	0.280

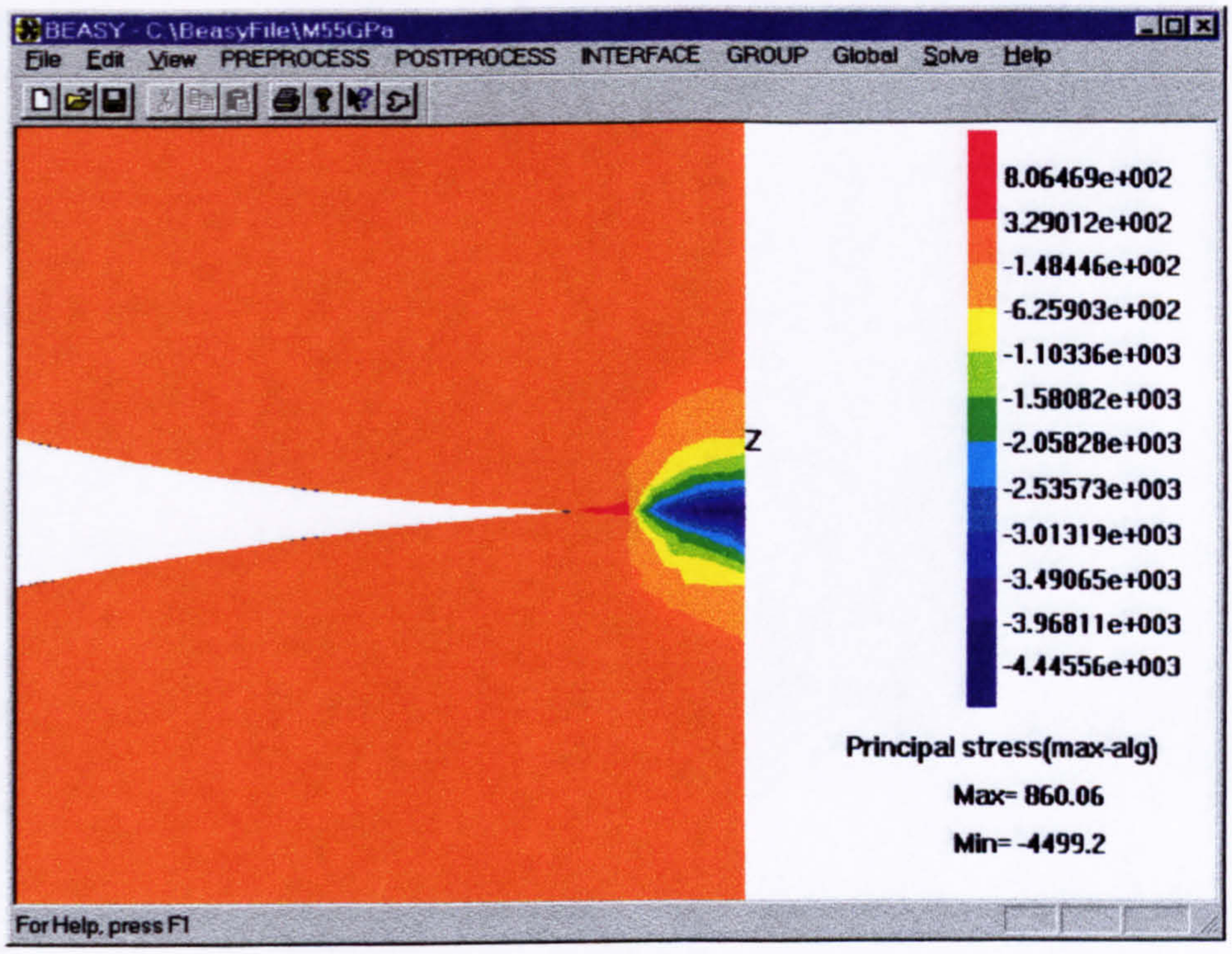

Figure 5.3 Maximum principal stress contours around the contact area.

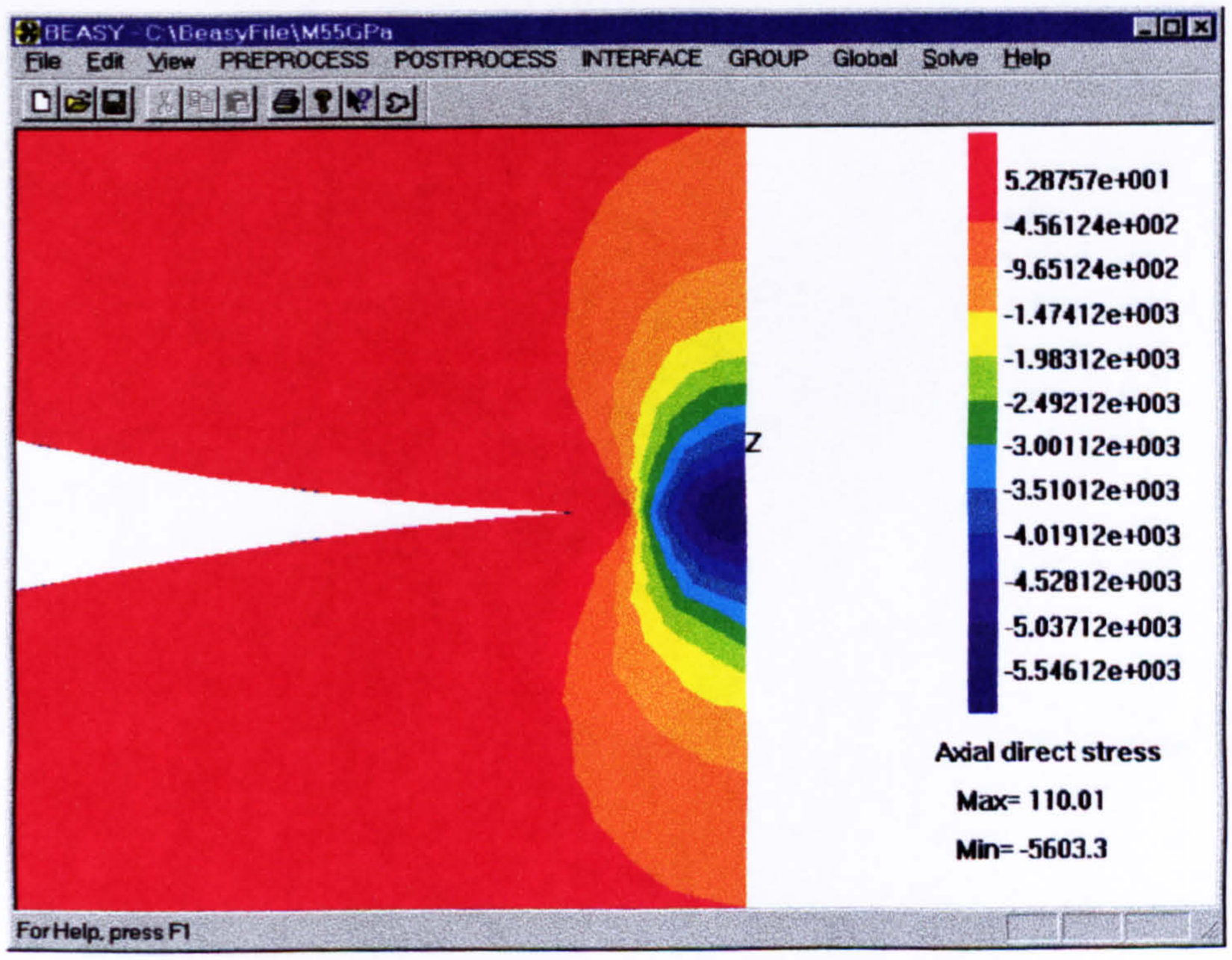

Figure 5.4 Axial direct stress contours around the contact area.

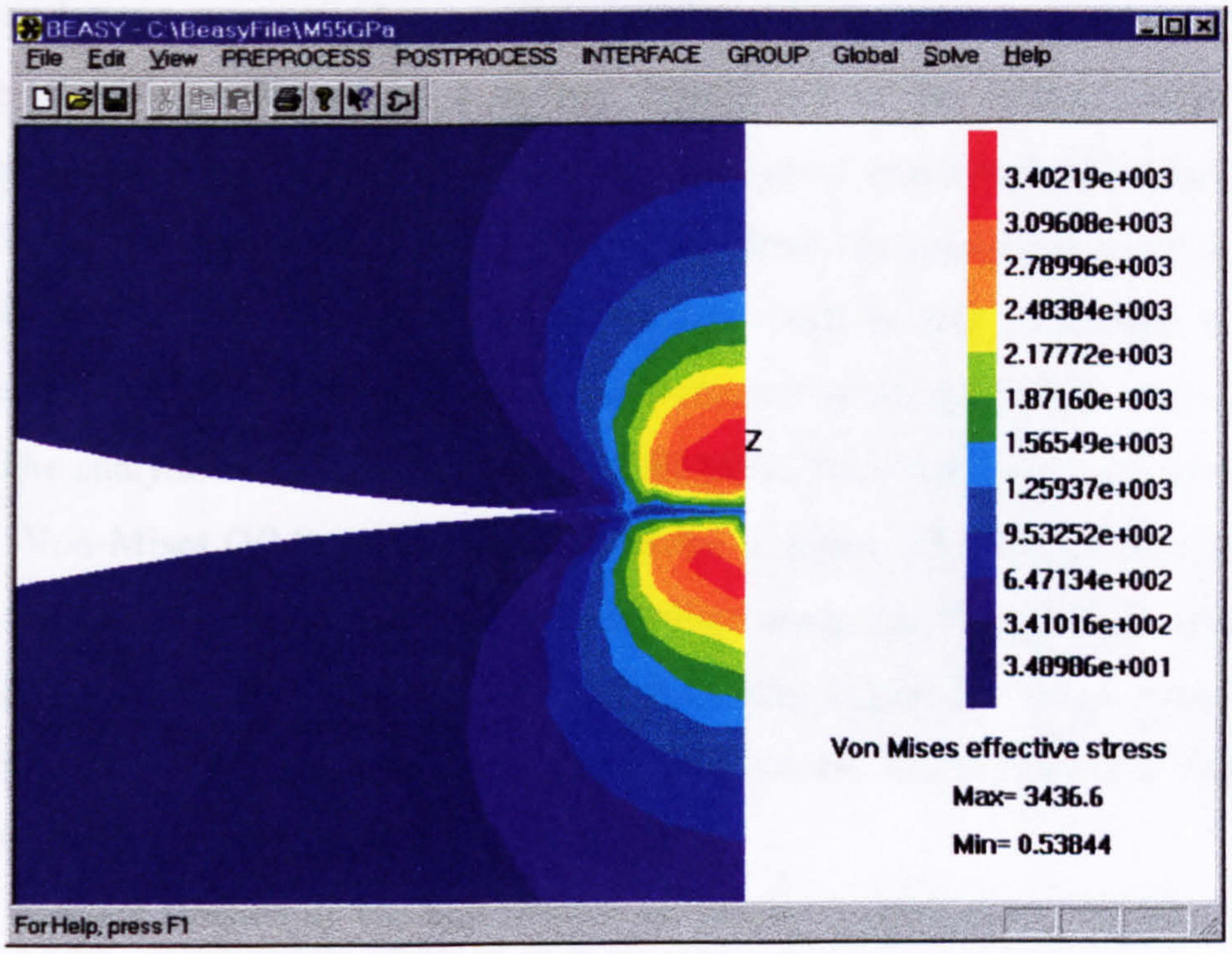

Figure 5.5 Von Mises stress contours around the contact area.

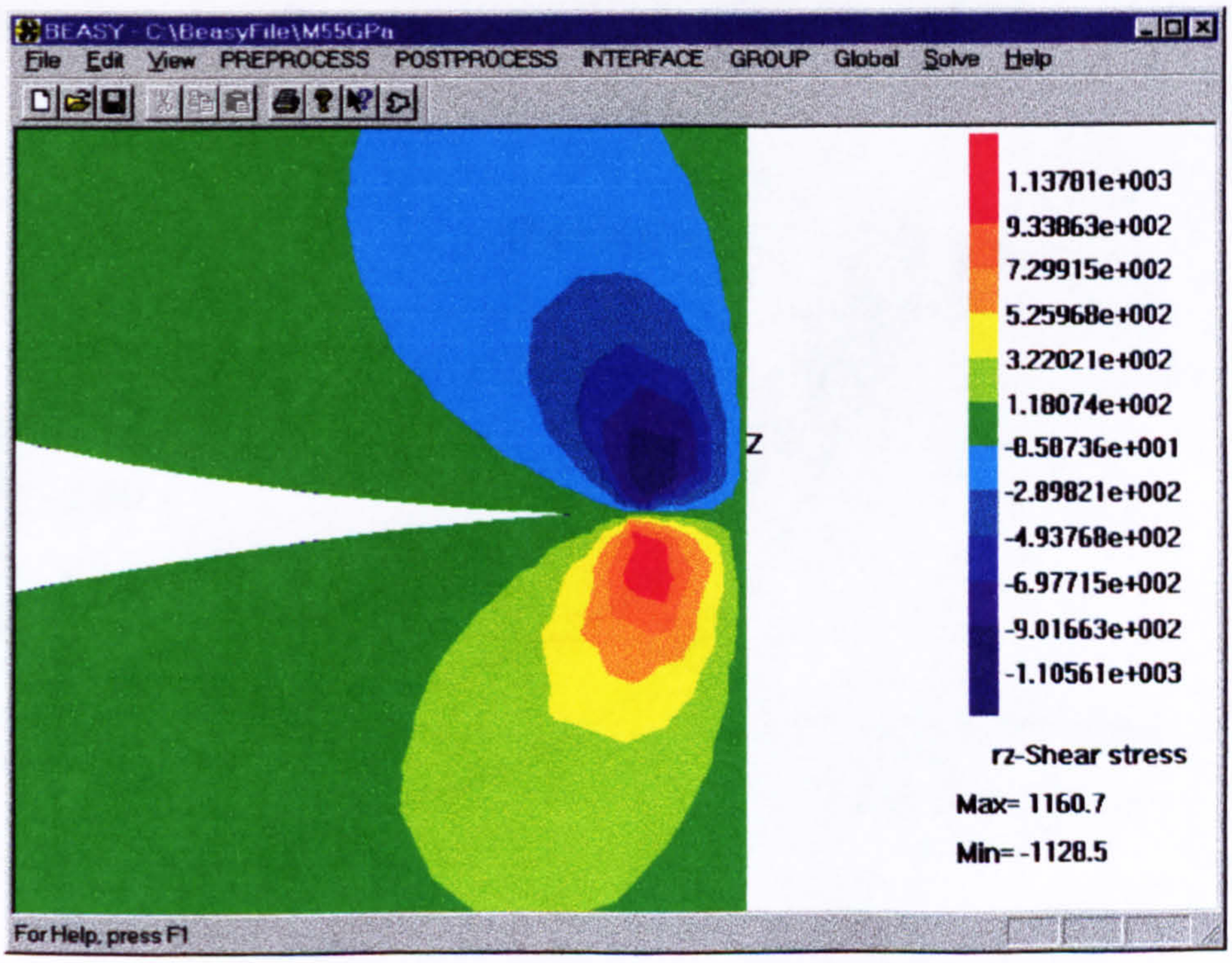

Figure 5.6 Shear stress contours around the contact area.

The load case studied presents a contact force of 490 N. Maximum principal stress and direct stress are shown in figures 5.3 and 5.4, respectively. The maximum tensile stress is positioned on a surface slightly out of the contact circle and it reaches a maximum value of 860 MPa. The analytical result with this load is 857 MPa. Hertz contact radius is 0.205 mm for this load; the analytical result is 0.204 mm. As can be seen, the numerical calculation result is very consistent with the analytical result. The maximum compressive stress is at the centre; the value is 5992 MPa. The analytical result for this load is 5589 MPa. The error is 0.05 percent only.

Von-Mises (VM) stress contour is shown in figure 5.5. As expected, the VM stress maximum is positioned on the subsurface along the load axis; it reaches a maximum value of 3.44 GPa at a depth of 0.12 mm. Figure 5.6 shows plane shear stresses. The maximum shear stress is expected to be at 45° from the centre of contact, which is consistent with the BEM model.

Surface stresses on the ball surface are plotted graphically in figure 5.7. The normal pressure (axial direct stress) distribution on the contact surface is completely consistent with the analytical result. The radial stress distribution also agrees well with the analytical result.

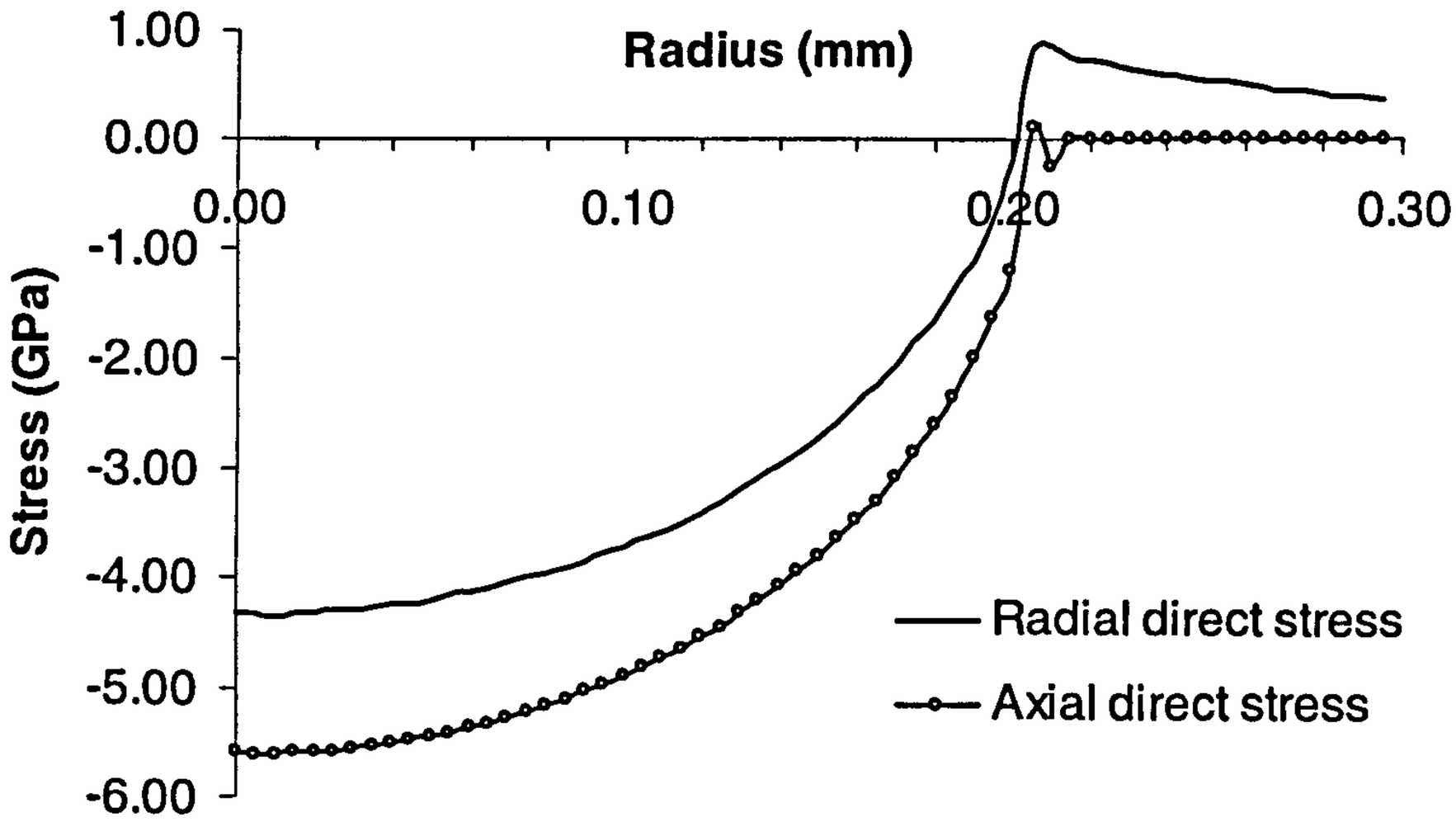

Figure 5.7 Stress distribution on contact surfaces for contact load = 490 N.

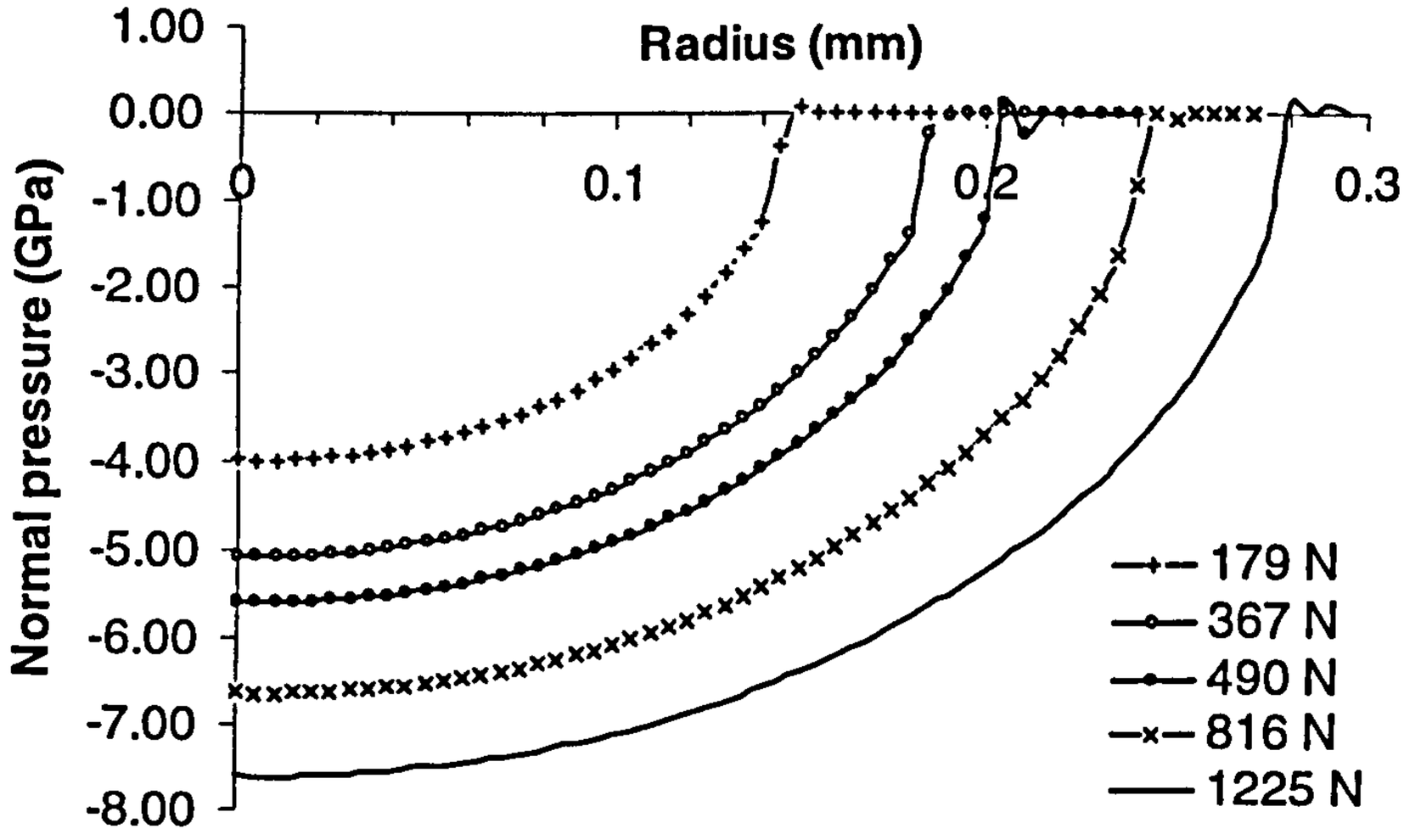

Figure 5.8 Pressure distribution on contact surfaces with different contact loads.

Figure 5.8 shows surface pressure on the ball surfaces at different contact loads. The results indicate that the pressure distributions on contact surfaces are very consistent with the analytical results.

The influence of contact load on Von Mises stress is plotted graphically in figure 5.9. The VM stress maximum is positioned on the subsurface along the load axis. The depth for the VM stress maximum increases as the contact load increases. The numerical results show a good consistency with the analytical results.

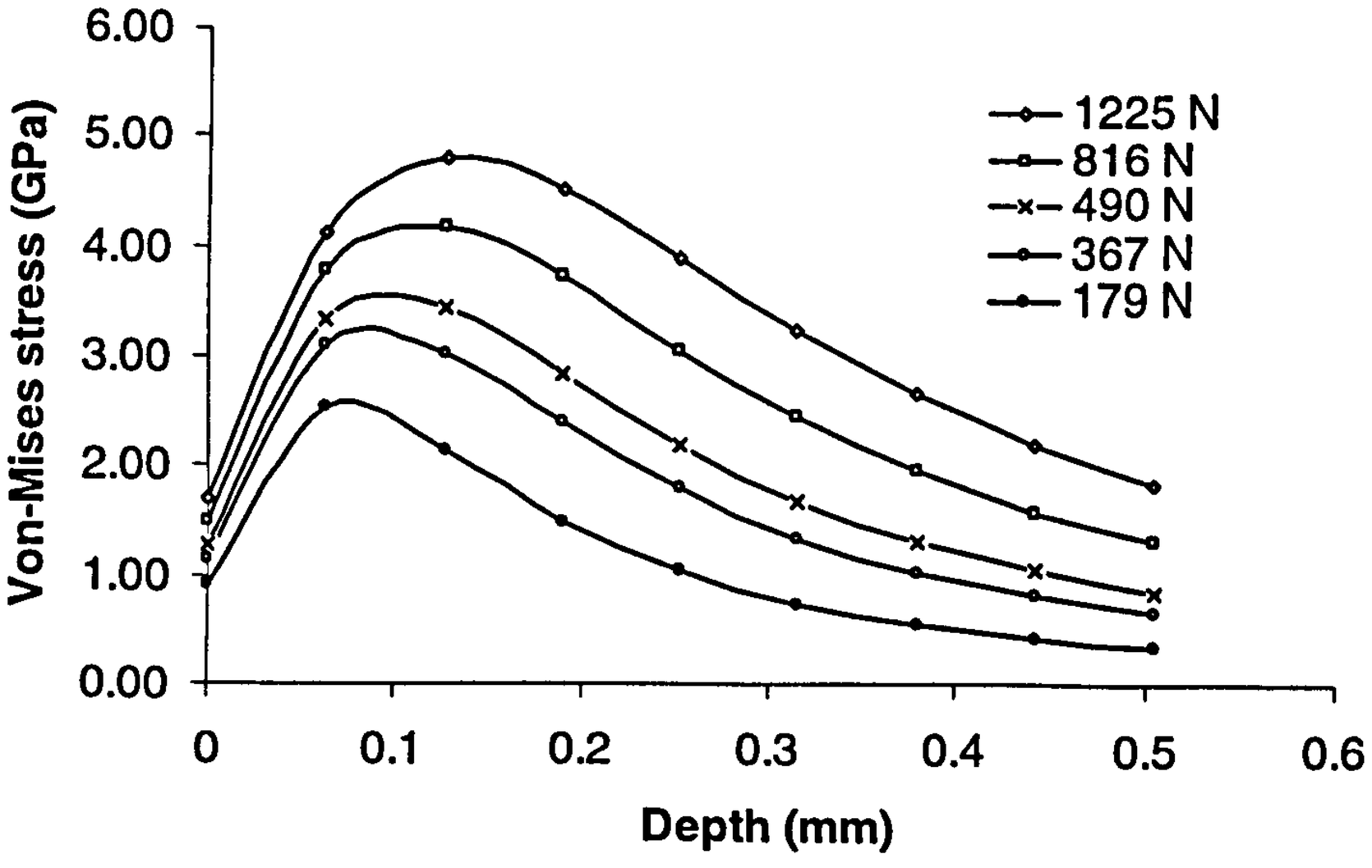

Figure 5.9 Von Mises distribution with different contact loads along load axis.

5.2 THREE-DIMENSIONAL BEM ANALYSIS OF CRACK FACE CONTACT

5.2.1 Description of loading system

Figure 5.10 shows the loading system in the three-dimensional boundary element method (BEM) analysis of crack face contact. The influence of parameters β and δ on the stress intensity factors has been studied in Chapter 4. The present analysis will focus on $\beta = 90^{\circ}$ and $\delta = 0$ to gain an insight into the mechanics processes of ring crack fatigue failure. For the purpose of the calculations presented here, it is possible to specify the surface loading in terms of an assumed stress distribution with the normal pressure and tangential traction as shown in figure 5.10. The normal pressure $p(x,y)$ and tangential traction $q(x,y)$ are expressed by the following equations:

$$p(x, y) = p_0 (1 - x^2 / a^2 - y^2 / a^2)^{1/2} \qquad (5.1)$$

$$q(x, y) = fp(x, y) \qquad (5.2)$$

where p_0 is maximum normal pressure, a is the radius of the contact circle and f is the friction coefficient of Hertzian contact. It is assumed that $f < 0$ when the contact circle passes over the ring crack (arc AB) from right to left and $f > 0$ when passing from left to right (see figure 5.10). The co-ordinate x measures the distance from the centre of the contact circle to the centre of the ring crack circle.

As the contact circle passes over the surface (from right to left in figure 5.10) the crack front will pass from compressive to tensile stress continuously. Assume that the contact radius a equals the ring crack radius R. The maximum crack extension will occur at the co-ordinate of $x = 0$ (see Chapter 4), in which stress intensity factors are computed. When the crack lies in the compressive region ($0 < x < 2R$), the crack is suppressed ($K_I \leqslant 0$). Consequently, the crack front will not propagate along the main growth path in the compressive region. However, surface breaking may occur due to the pre-existence of the ring cracks and subsurface damage may also occur due to the crack face contact. Subsurface damage is affected by the change of co-ordinate x and it can be a rather complex process due to Hertzian loading in a cyclic fashion.

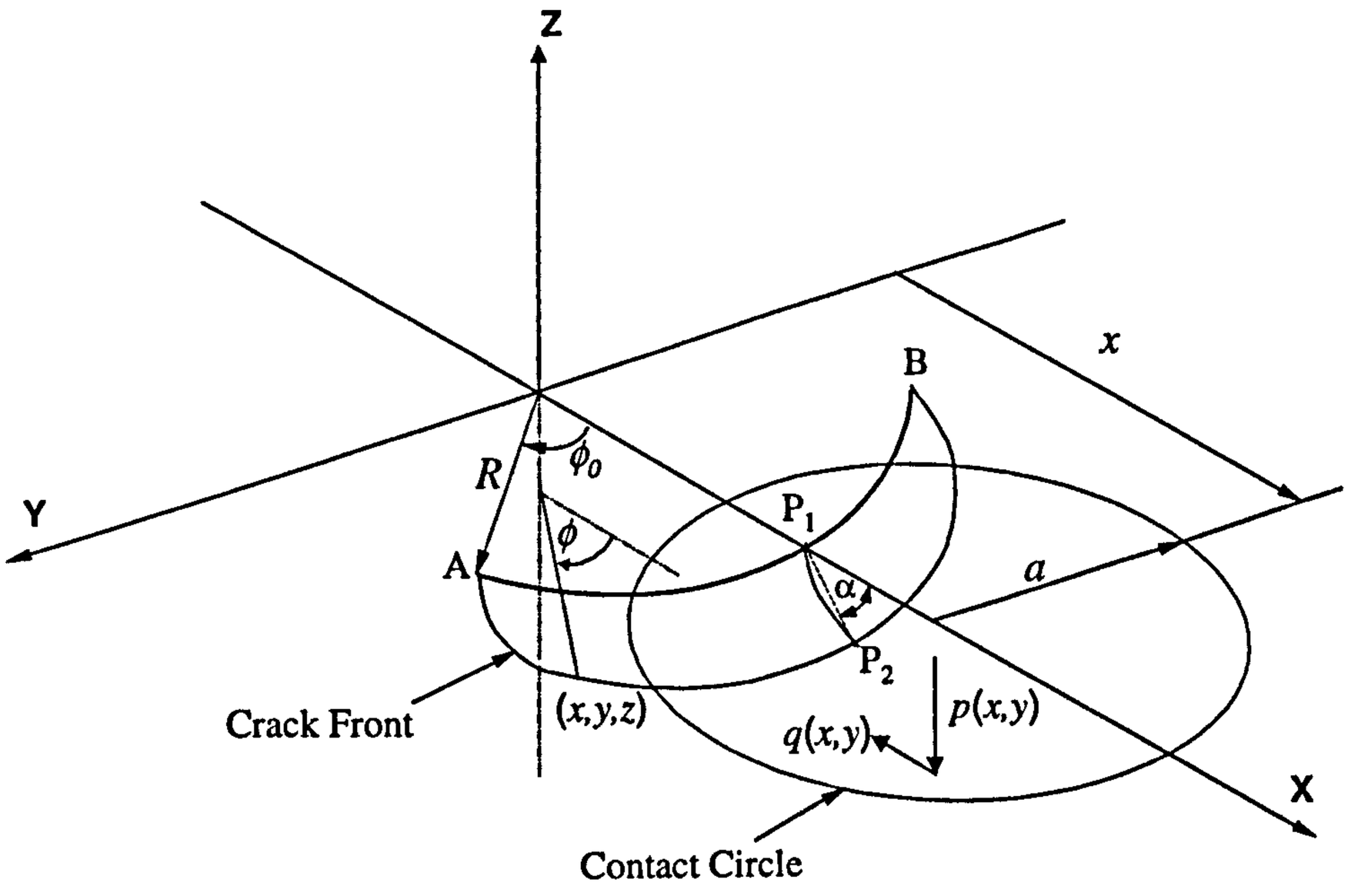

Figure 5.10 Loading system of crack face contact analysis.

5.2.2 Physical considerations

Fluid lubricant effects are represented by different friction coefficients, which are determined in terms of the lubricant properties. For Hertzian contact friction coefficient f (contact between steel ball and ceramic ball), assume that f ranges from 0.01 to 0.05 due to EHL effect. For crack faces friction coefficient f_c (contact between crack faces), assume that f_c ranges from 0.1 to 0.5 to investigate lubricant property effects.

From a physical point of view, a crack means there is a gap between two solid surfaces. This gap may increase due to the loss of materials arising from the wear of the rough crack surfaces. It is reasonable to assume that the crack gap increases with the increase of running time and will reach the maximum gap of 0.5μm. To analyse how the gap affects the contact behaviour, different gaps are adopted for numerical analysis.

Crack geometry I (see Chapter 4) is selected as this is most frequently found on ceramic balls. Based on the experimental study, the position of an element on the crack face in figure 5.10 may be written as

$$x = (R + l\sqrt{1 - (\phi / \phi_0)^2}\cos\ \alpha)\cos\ \phi \qquad (5.3)$$

$$y = (R + l\sqrt{1 - (\phi / \phi_0)^2}\cos\ \alpha)\sin\ \phi \qquad (5.4)$$

$$z = -0.224\ (l\cos\ \alpha\sqrt{1 - (\phi / \phi_0)^2})^{1/2} \qquad (5.5)$$

where l denotes the crack depth, $0 < l \leq$ maximum crack depth (line P_1P_2), R is the radius of the ring crack, α is the angle of line P_1P_2 to the ball surface, $0 < \alpha < \pi/2$, ϕ represents the angle of an element position on the crack face, $-\phi_0 < \phi < \phi_0$ and ϕ_0 denotes a half angle of the ring crack arc AB, $0 < \phi_0 < \pi/2$.

For the purpose of the calculations in the present study, assume that the propagated crack can be described by equations (5.3) to (5.5). The crack face contact analysis is performed at various co-ordinates x in which the contact circle lies. The understanding of the stresses on both the crack faces and the ball surface is the key to revealing the nature of ring crack failure in rolling contact. Two crack sizes are adopted to perform the contact analysis of crack faces. Their dimensions are described as follows:

(1) Case 1: $R = 0.21$ mm, $l = 0.051$ mm, $\phi_0 = 45°$, $\alpha = 50°$; and

(2) Case 2: $R = 0.21$ mm, $l = 0.082$ mm, $\phi_0 = 45°$, $\alpha = 42°$.

5.2.3 Modelling strategy

The BEM based computer modelling package BEASY is employed to perform contact analysis of crack faces. The BEM model that is created incorporates a vertical symmetry plane through the middle of the ball to reduce the number of elements used in the model. Elements do not need to be placed on the symmetry plane and this further reduces the size of the model.

Contact is modelled in the BEM model using the software's 'initial gap' boundary condition. This boundary condition defines a gap between two crack faces.

Initial gap values are defined over an entire crack surface containing elements.

The maximum contact pressure p_0 is assigned to a value of 5.58 GPa (equivalent to experimental studies) and applied to the numerical calculations throughout in this study. Displacements in the specified zone are extracted from the axisymmetric boundary element model discussed in Section 5.1. This method leads to a significant reduction in the computer time necessary for solution.

5.3 ANALYSIS OF STRESSES ON THE BALL SURFACES

5.3.1 Influence of crack gap

Figure 5.11 and figure 5.12 show the stress distributions on the ball surface at various crack gaps. Figure 5.11 illustrates the maximum principal stress variations in the plane of $\phi = 0^o$. Figure 5.12 is a plot of the maximum principal stress as a function of ϕ (from 0^o to 90^o) along the circle of $R = 0.21$ mm. The crack studied is the case I. The directions of principal stresses are displayed by the stress trajectories and are determined in terms of the analysis of Eigen vectors. Maximum principal trajectories at any points along the circle are approximately orthogonal to that circle and parallel to the surface. The results reveal that the tensile stress increases significantly with the increase of the crack gap. The calculated results predict that surface breaking will happen if the crack gap reaches a certain value (gap > 0.2 μm). It is evident that for brittle materials secondary surface ring cracks may control the final spall sheet separation. The secondary surface cracks are circular and are of a similar radius to the original ring crack circle. These secondary surface cracks grow downward as soon as they are formed, join and connect with the trajectory of the main crack path. Consequently, a spall is eventually formed. This may explain why the spall contours always took the ellipse shape.

In principle, the ring crack initiation of silicon nitride material can be predicted from its tensile strength. However, measurement of the tensile strength of ceramic materials is extremely difficult since test results are strongly influenced both by the stressed volume and the surface condition of the machined specimens. Ceramic tensile specimens are also extremely susceptible to even the smallest misalignments. Consequently, there is little reliable information on the tensile

strength of silicon nitride materials. Therefore, it is more convenient and effective to use the critical Hertzian maximum compressive stress to assess ring crack resistance. According to experimental studies (Hadfield 1992 and Cundill 1997), the ring crack will occur when the maximum contact pressure reaches about 15 GPa for HIP silicon nitride balls with 12.7 mm diameter. This compressive stress corresponds to the maximum tensile stress of 2.25 GPa occurring at the edge of the contact circle.

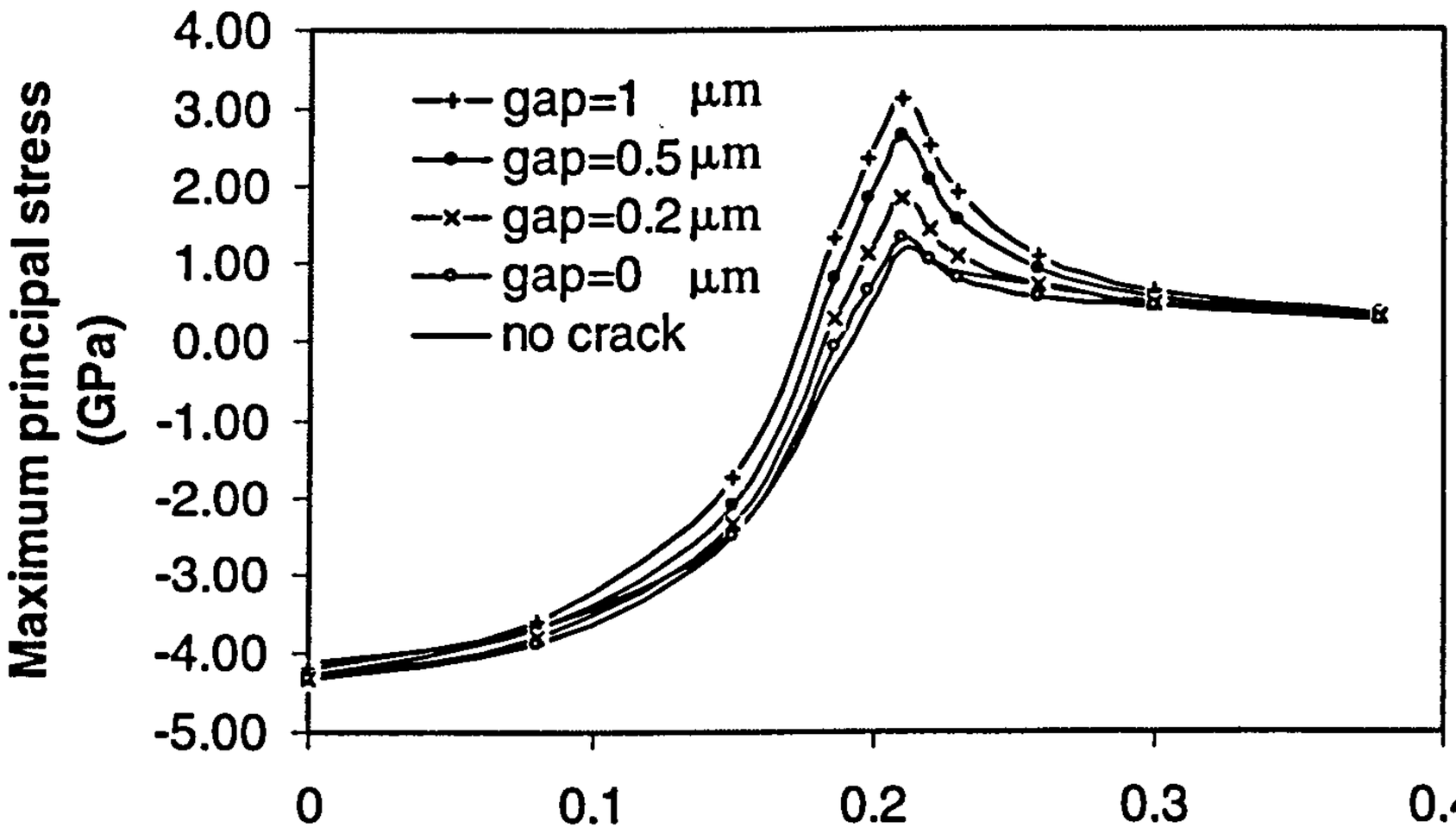

Figure 5.11 Stress distribution on the ball surface at the plane of $\phi = 0^{o}$ (Case 1, $x = 0.047$ mm, $f_c = 0$, $f = -0.05$).

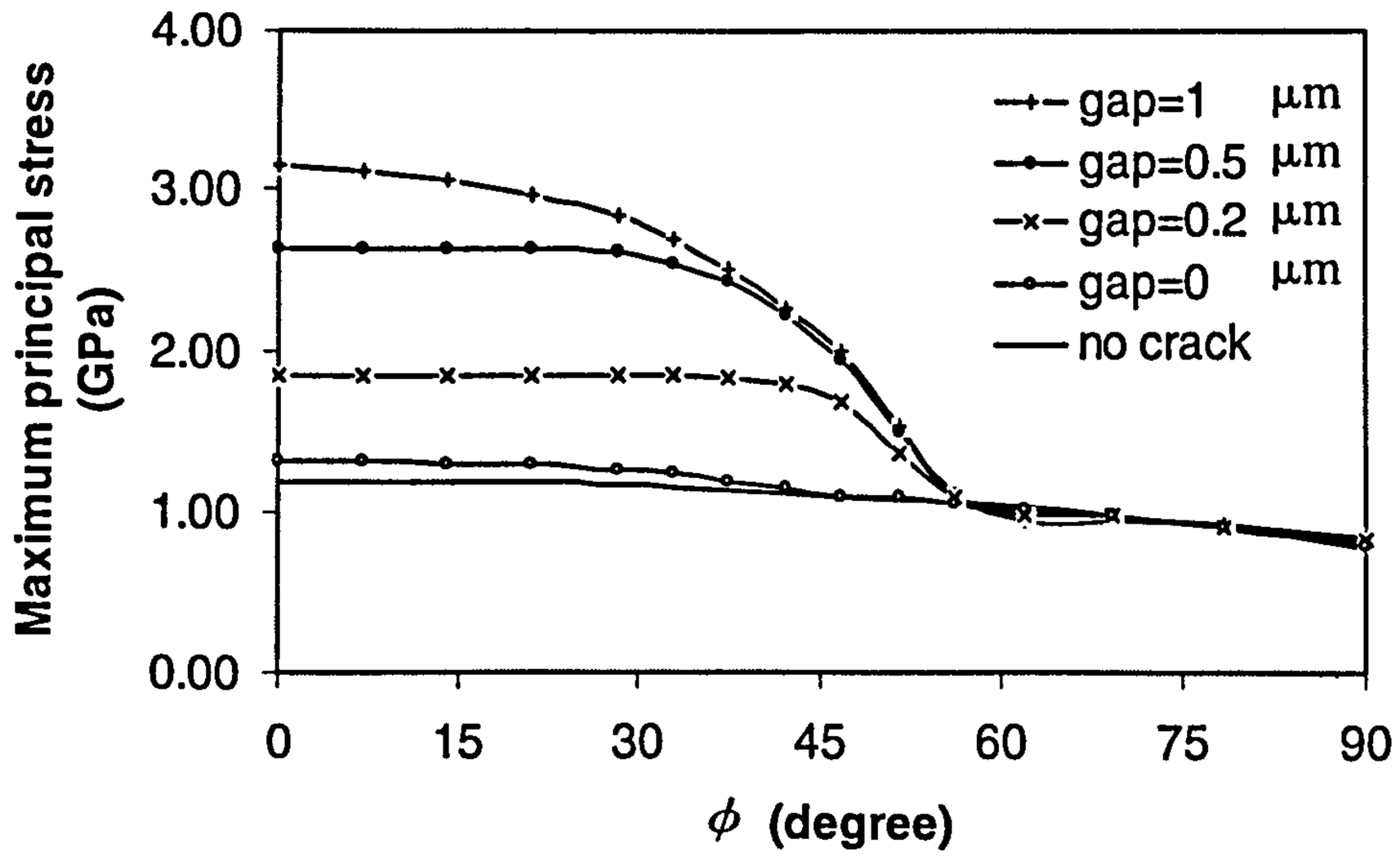

Figure 5.12 Stress distribution on the ball surface at the circle of radius = 0.21 mm (Case 1, $x = 0.047$ mm, $f_c = 0$, $f = -0.05$).

The calculated results are now studied in detail. There are hardly any changes in the stress distributions for all the gaps (0, 0.2, 0.5 and 1μm) from $\phi = 60^{\circ}$ to $\phi = 90^{\circ}$ (non-crack area). Compare the case of no crack with the case of crack gap = 0, there is very slight variation from $\phi = 0^{\circ}$ to $\phi = 60^{\circ}$ (crack area). However, the surface stresses will increase significantly when the crack gap exceeds 0.2 μm, which approximates 1.8 GPa. When the gap is 0.5 μm the tensile strength will reach 2.7 GPa. This tensile stress is large enough to initiate new surface cracks. It can be concluded that the secondary surface cracks must be formed on the surface if the crack gap exceeds 0.2 μm (0.2 at crack mouth decreases linearly to 0 at crack tip). The crack, from a physical point of view, means there is a gap between two solid faces. Therefore, it is reasonable to assume that the gap (or crack opening) will reach 0.2 μm due to the loss of materials caused by the wear of the rough crack face contact. The crack gap increasing with the increase of fatigue cycles has been observed experimentally (Chapter 3, Sections 3.3 and 3.4). Figures 5.13 to 5.15 show some examples of the stress contours. Deformation contours around the contact zone are shown in Appendix 6.

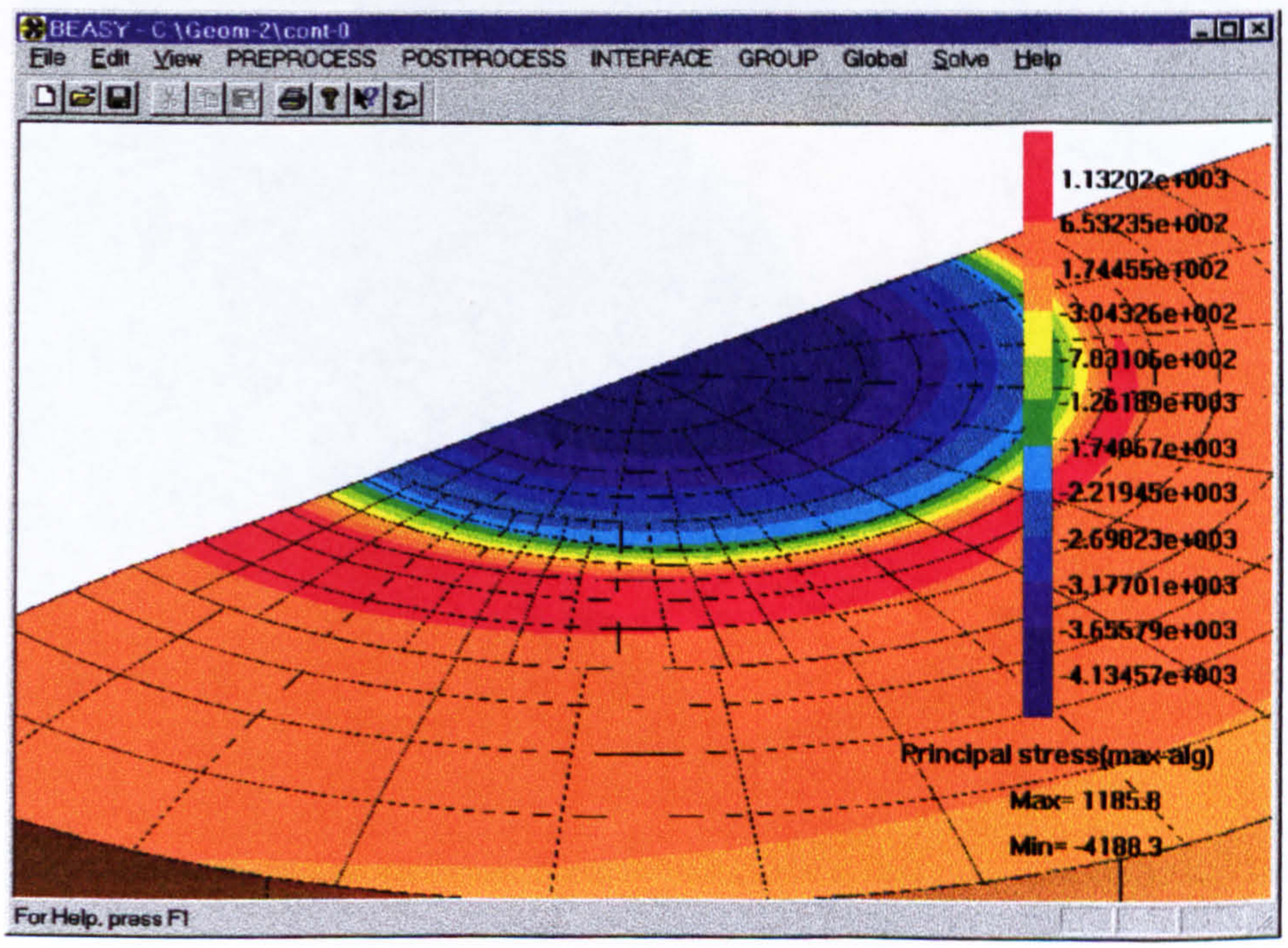

Figure 5.13 Stress contours on the ball surface for the case of no crack (Case 1, $x = 0.047$ mm, $f = -0.05$).

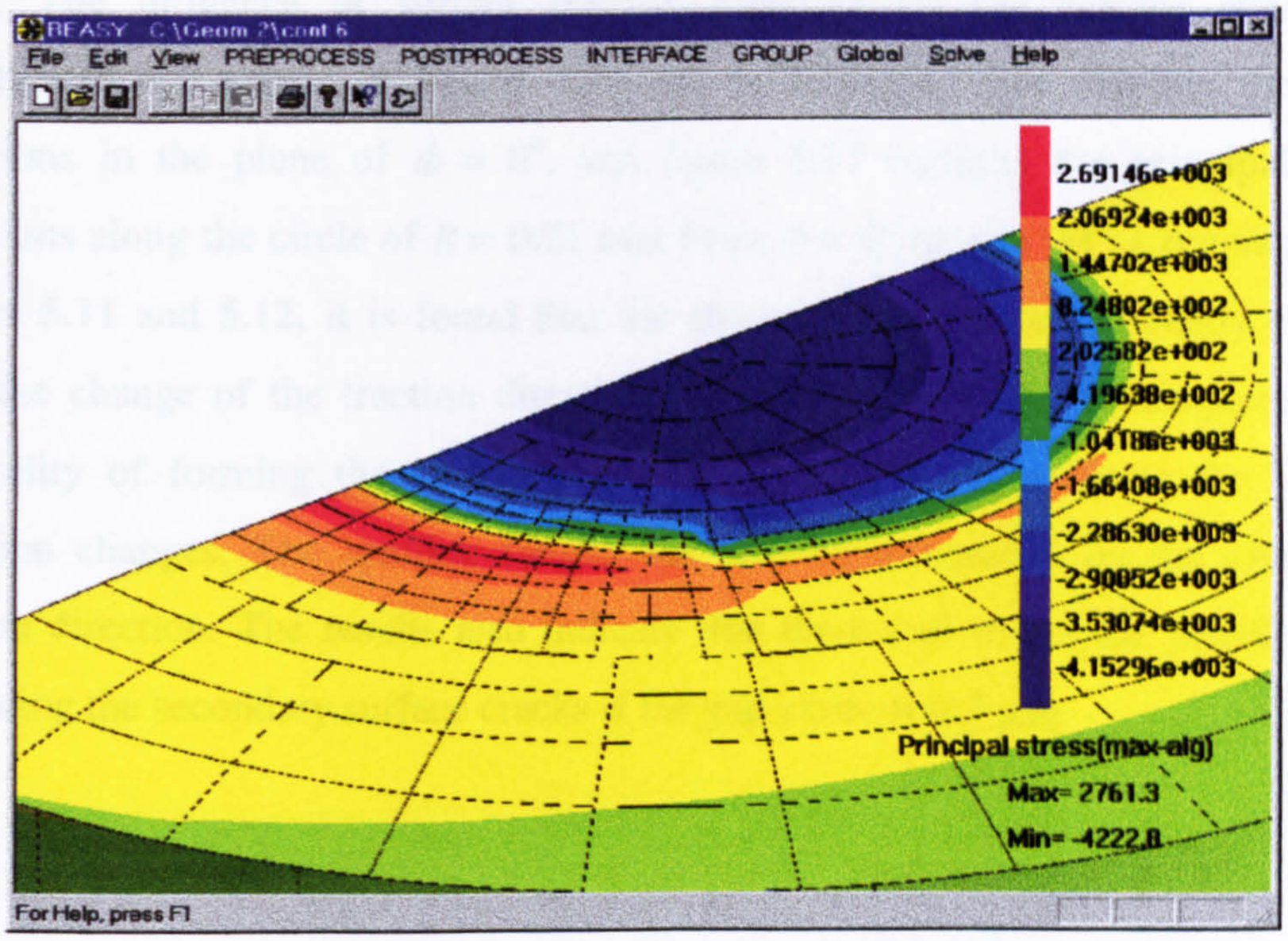

Figure 5.14 Stress contours on the ball surface for the case of crack gap = 0.5 μm (Case 1, x = 0.047 mm, f_c = 0, f = -0.05).

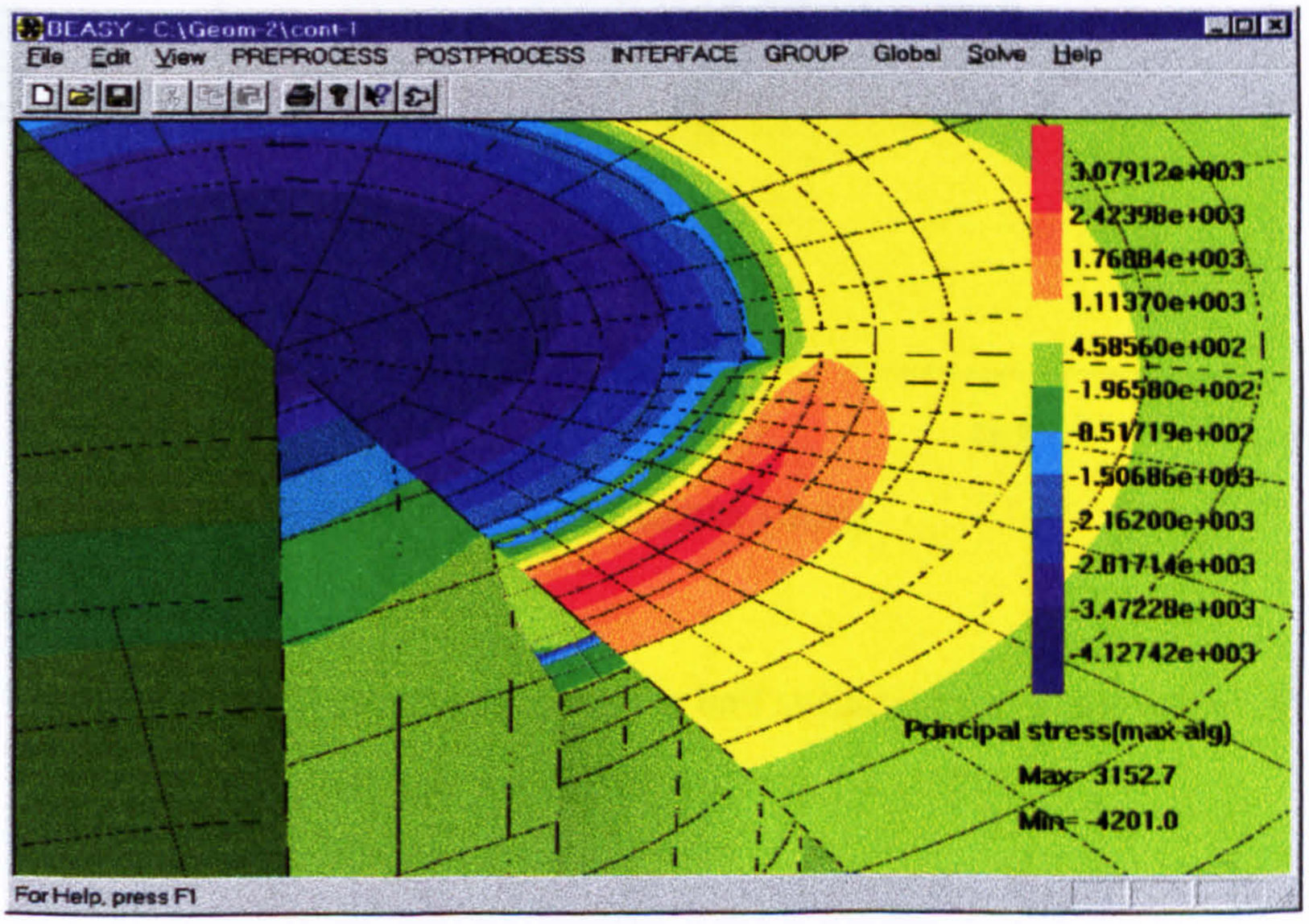

Figure 5.15 Stress contours on the ball surface for the case of crack gap = 1 μm. (Case 1, x = 0.047 mm, f_c = 0, f = -0.05).

5.3.2 Influence of traction direction

The influence of surface traction direction on the surface stresses is investigated and shown in figures 5.16 and 5.17. Figure 5.16 displays the stress variations in the plane of $\phi = 0^{\circ}$, and figure 5.17 exhibits the principal stress variations along the circle of $R = 0.21$ mm from $\phi = 0^{\circ}$ to $\phi = 90^{\circ}$. Compared with figures 5.11 and 5.12, it is found that the stress distribution significantly changes with the change of the traction direction (or rolling direction). Consequently, the possibility of forming the secondary surface cracks is different as the traction direction changes. The spalling fatigue life will be influenced by the change of traction direction. The results also indicate that there still exists the possibility of producing the secondary surface cracks if the gap exceeds 0.5 μm.

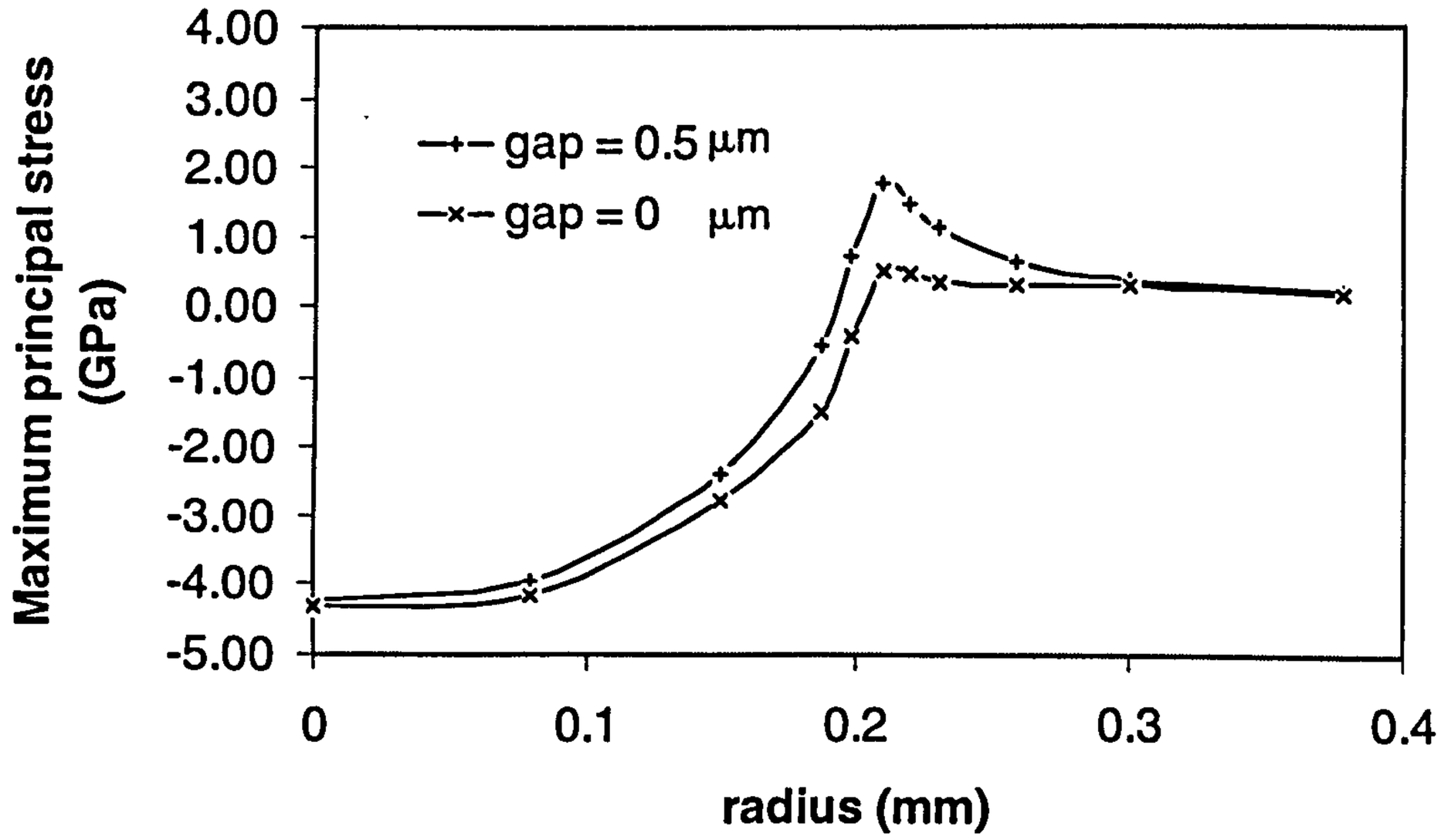

Figure 5.16 Stress distribution on the ball surface at the plane of $\phi = 0^{\circ}$ (Case 1, $x = 0.047$ mm, $f_c = 0$, $f = +0.05$).

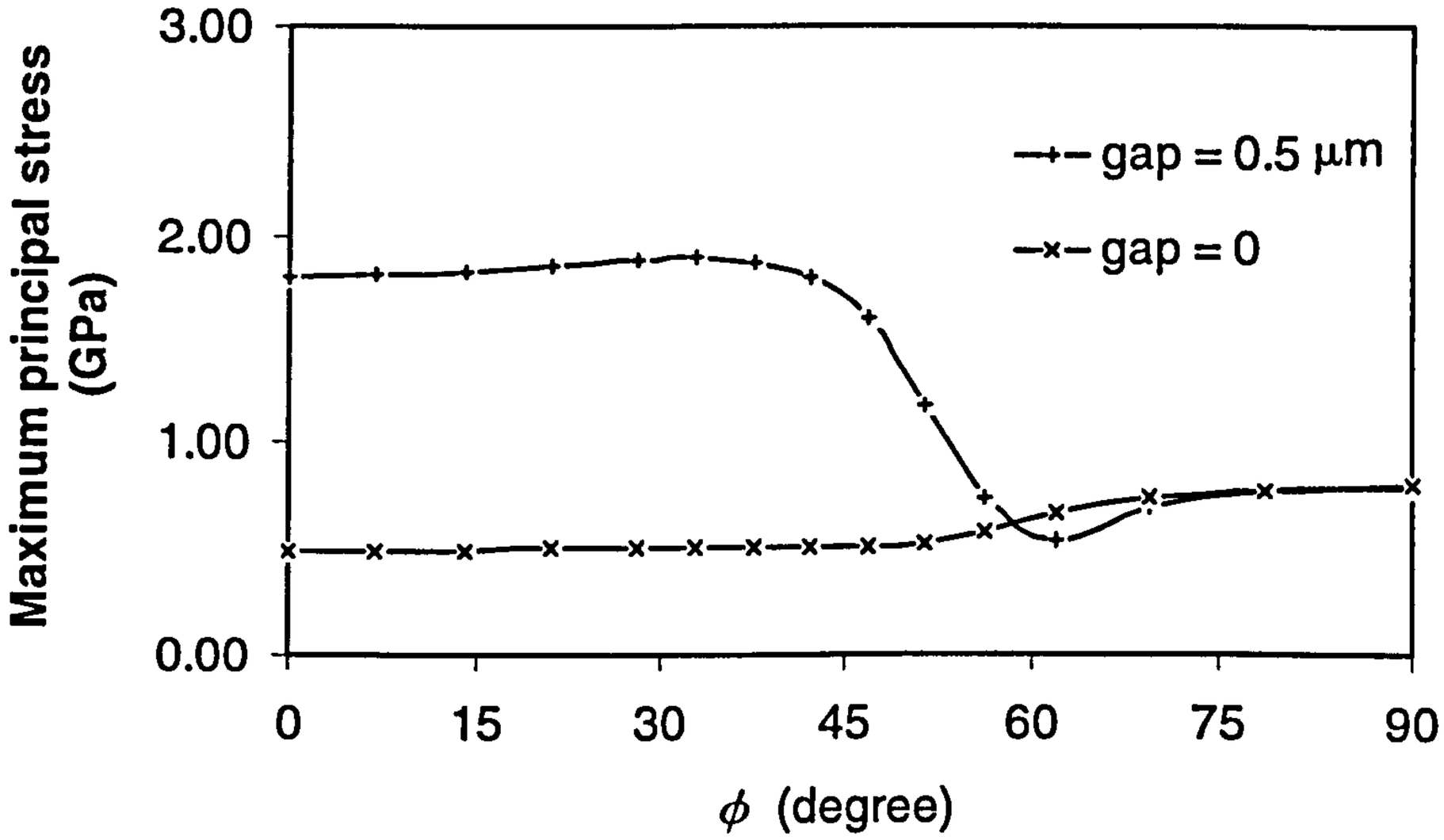

Figure 5.17 Stress distribution on the ball surface at the circle of radius = 0.21 mm (Case 1, $x = 0.047$ mm, $f_c = 0$, $f = +0.05$).

5.3.3 Influence of crack dimension

Critical crack size is an important quantity parameter in fracture mechanics analysis and for rolling element bearing quality control. The durability of the cracked product can be predicted in terms of the crack size. Hence, it is also important to understand the influences of crack dimensions on the surface stresses. The crack studied here is case 2. Figures 5.18 and 5.19 show how surface stresses vary when the crack depth increases. As can be seen from figure 5.19, there are no differences in the non-crack area from $\phi = 60^\circ$ to $\phi = 90^\circ$, but significant changes in the crack area from $\phi = 0^\circ$ to $\phi = 60^\circ$. Comparison of figures 5.11, 5.12 and figures 5.18, 5.19 reveals that the tensile stresses on the surface increase as the crack depth increases. The radius of the area affected also increases. The calculated results predict that the larger the crack size, the shorter the fatigue life. The reason for this is that a large crack has a high potential to form secondary surface cracks.

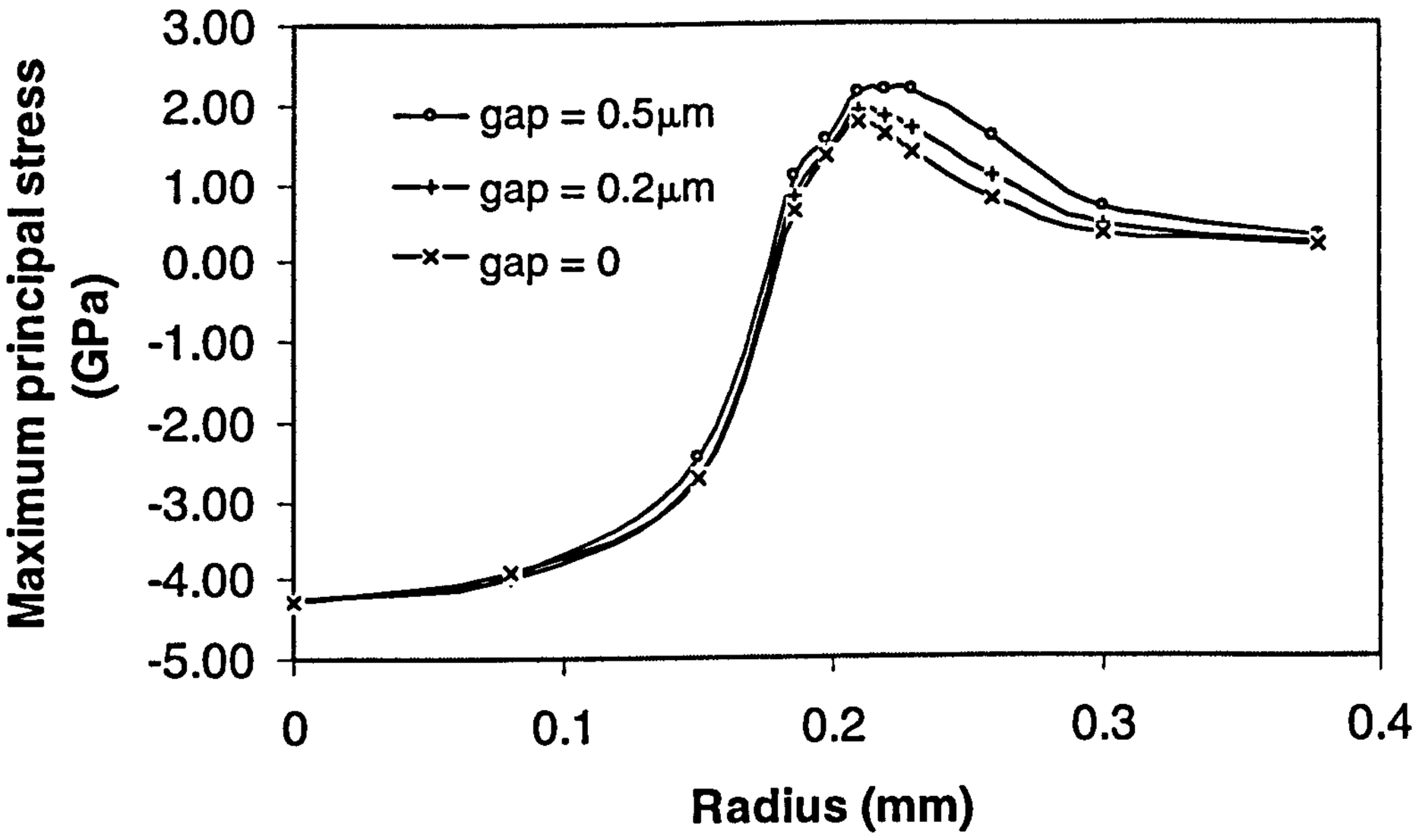

Figure 5.18 Stress distribution on the ball surface at the plane of $\phi = 0^{o}$ (Case 2, $x = 0.047$ mm, $f_c = 0$, $f = -0.05$).

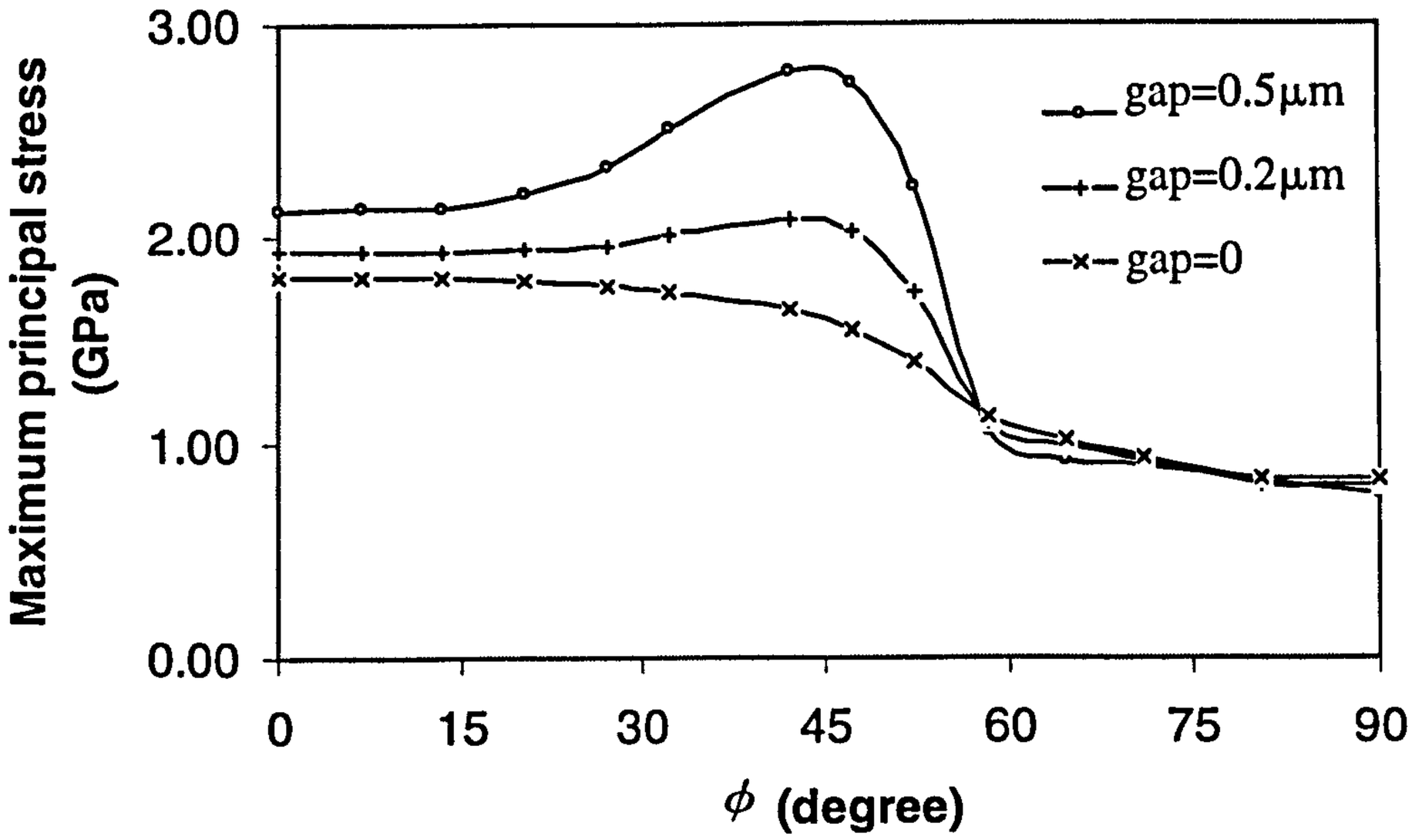

Figure 5.19 Stress distribution on the ball surface at the circle of radius = 0.21 mm (Case 2, $x = 0.047$ mm, $f_c = 0$, $f = -0.05$).

5.3.4 Influence of crack face friction coefficients

Figures 5.20 and 5.21 show the influence of the crack face friction coefficient on the stresses arising from the crack face contact. As discussed above, there are influences in the crack area (from $\phi = 0^o$ to $\phi = 60^o$) but no influences in the non-crack area (from $\phi = 60^o$ to $\phi = 90^o$). The results indicate that the stress value increases as the crack face friction coefficient decreases and approaches the value of no crack if the crack face friction coefficient exceeds 0.5.

It is found that the surface stress distribution is not sensitive to the variation of the crack face friction coefficient when the crack gap exceeds 0.2 μm.

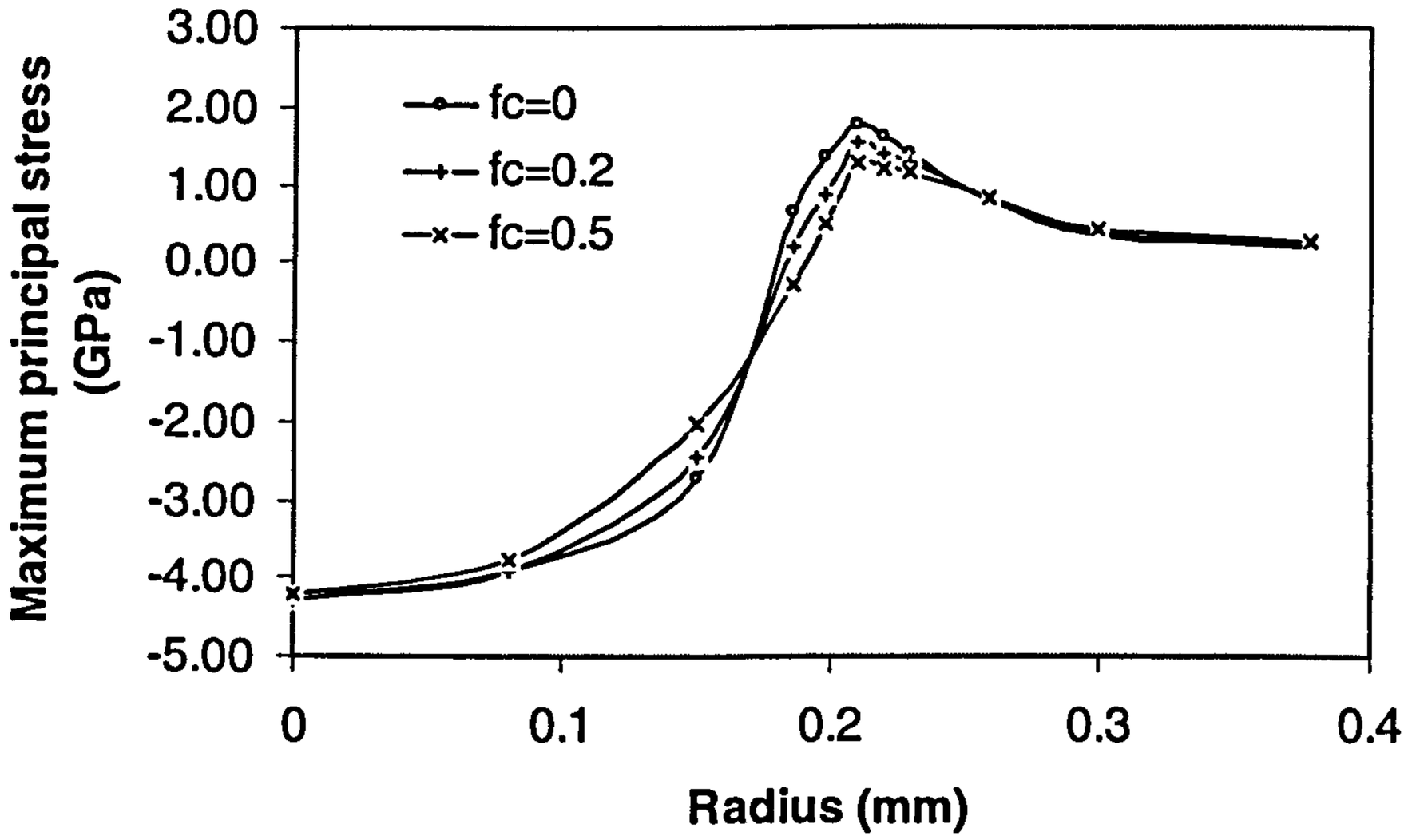

Figure 5.20 Stress distribution on the ball surface at the plane of $\phi = 0^o$ (Case 2, $x = 0.047$ mm, $f = -0.05$).

Figures 5.22 to 5.24 show the contours of the stress distributions at a different co-ordinate x. Figure 5.22 shows the stress contour on the surface (Case 2: $x = 0.047$ mm, $f_c = 0.2$, $f = -0.05$, gap = 0). Figure 5.23 shows an example of the stress contour in the contact area (Case 2: $x = 0.347$ mm, $f_c = 0$, $f = -0.05$, gap = 0). Figure 5.24 is another example of the stress distribution contours (Case 2: $x = 0.467$ mm, $f_c = 0.1$, $f = -0.05$, gap = 0). It can be seen that the stress distribution contours change as the co-ordinate x changes, resulting in changes in subsurface damage. Deformation contours around the contact zone are shown in Appendix 6. The stress distributions on the subsurface will be discussed in the following sections.

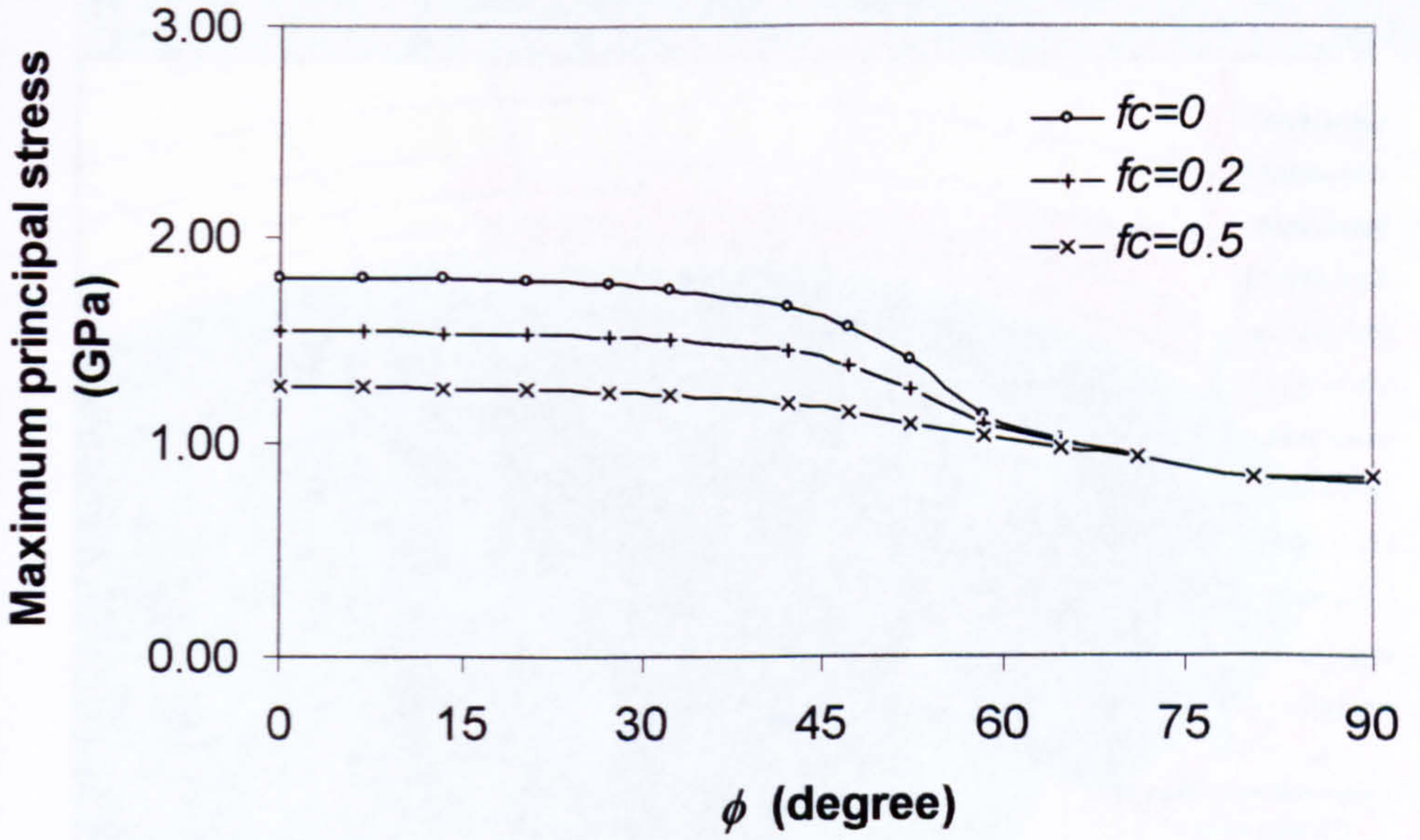

Figure 5.21 Stress distribution on the ball surface at the circle of radius = 0.21 mm (Case 2, x = 0.047 mm, f = -0.05).

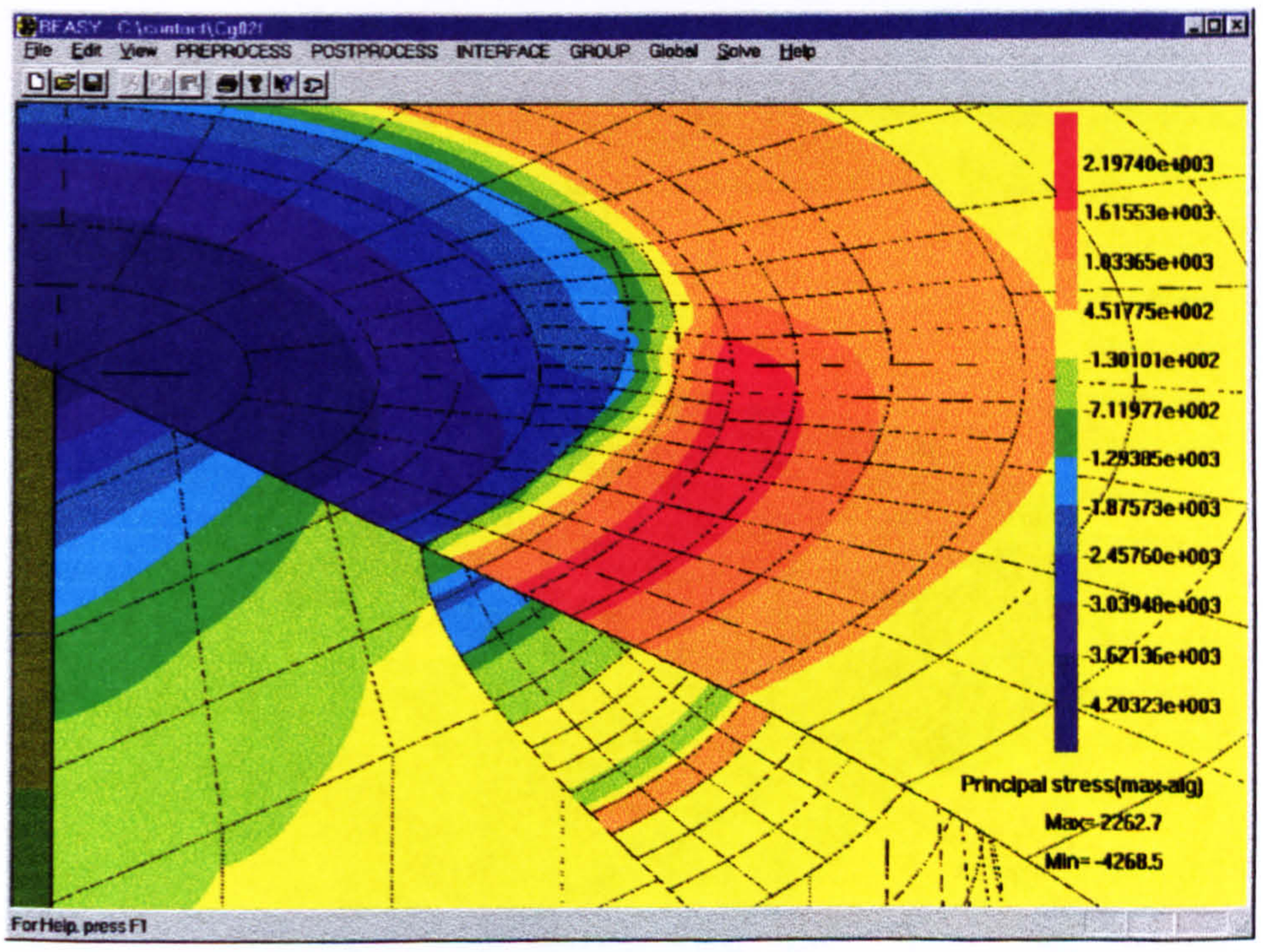

Figure 5.22 Stress distribution contours around contact region (Case 2, x = 0.047 mm, f_c = 0.2, f = -0.05).

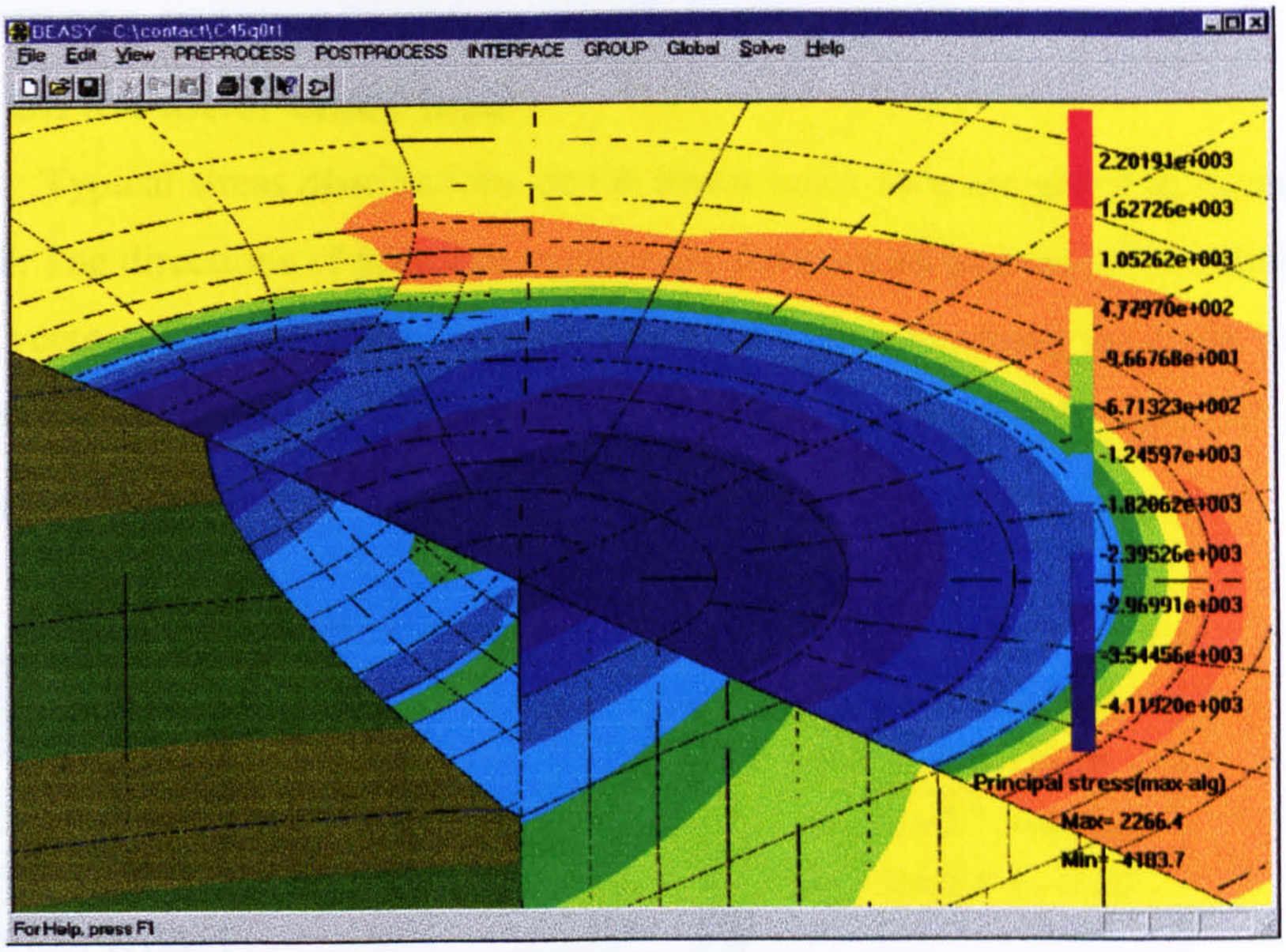

Figure 5.23 Stress distribution contours around contact region (Case 2, $x = 0.347$ mm, $f_c = 0$, $f = -0.05$).

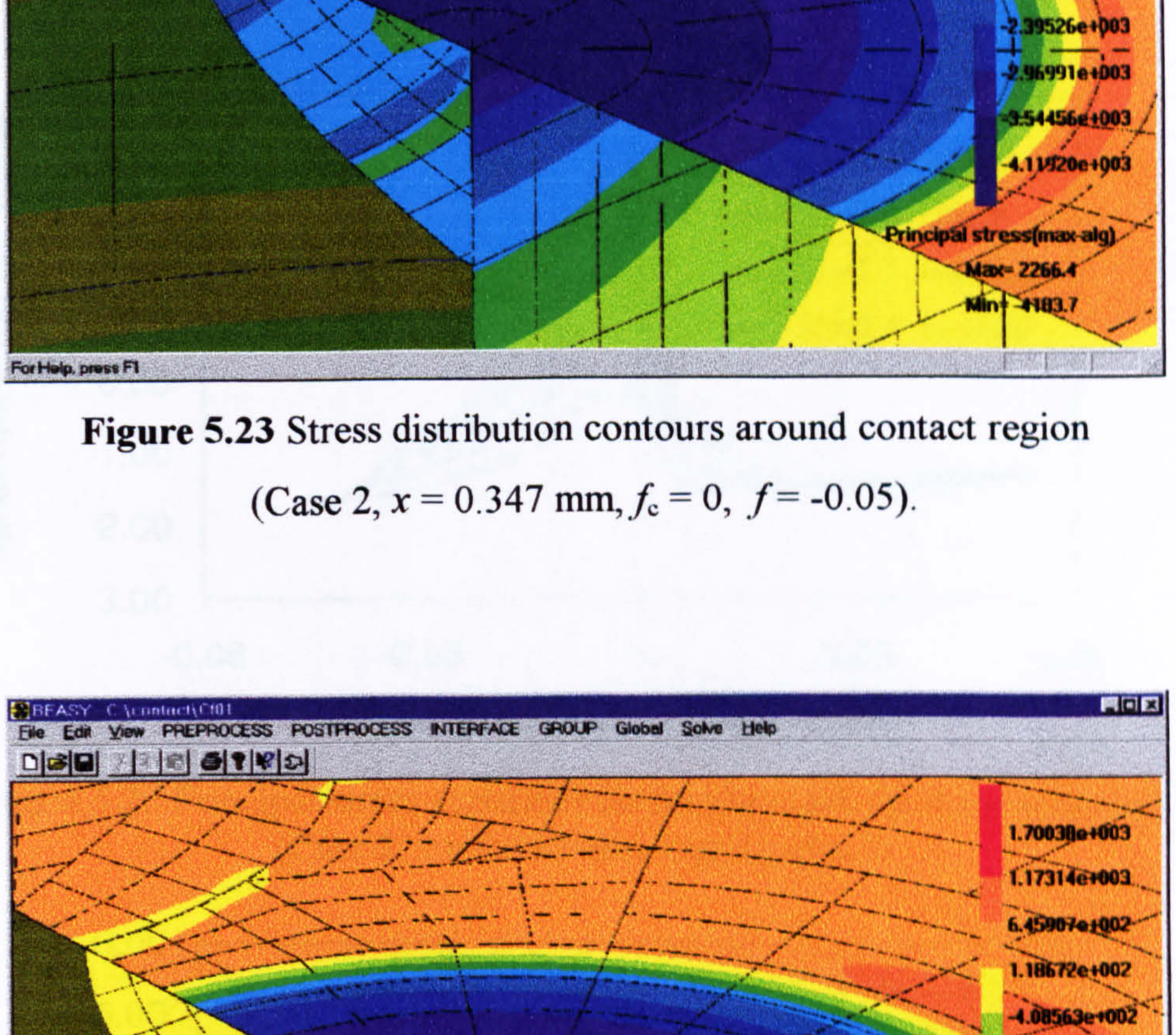

Figure 5.24 Stress distribution contours around contact region (Case 2, $x = 0.467$ mm, $f_c = 0.1$, $f = -0.05$).

5.4 STRESS DISTRIBUTION ON CRACK FACES

5.4.1 On the lower crack face

Typical stress distributions on the lower crack face are given in figures 5.25 to 5.28. The directions of principal stresses are determined in terms of the analysis of Eigen vectors. Maximum principal trajectories at any points along the crack front are approximately orthogonal to the first and second tangential direction at the corresponding point.

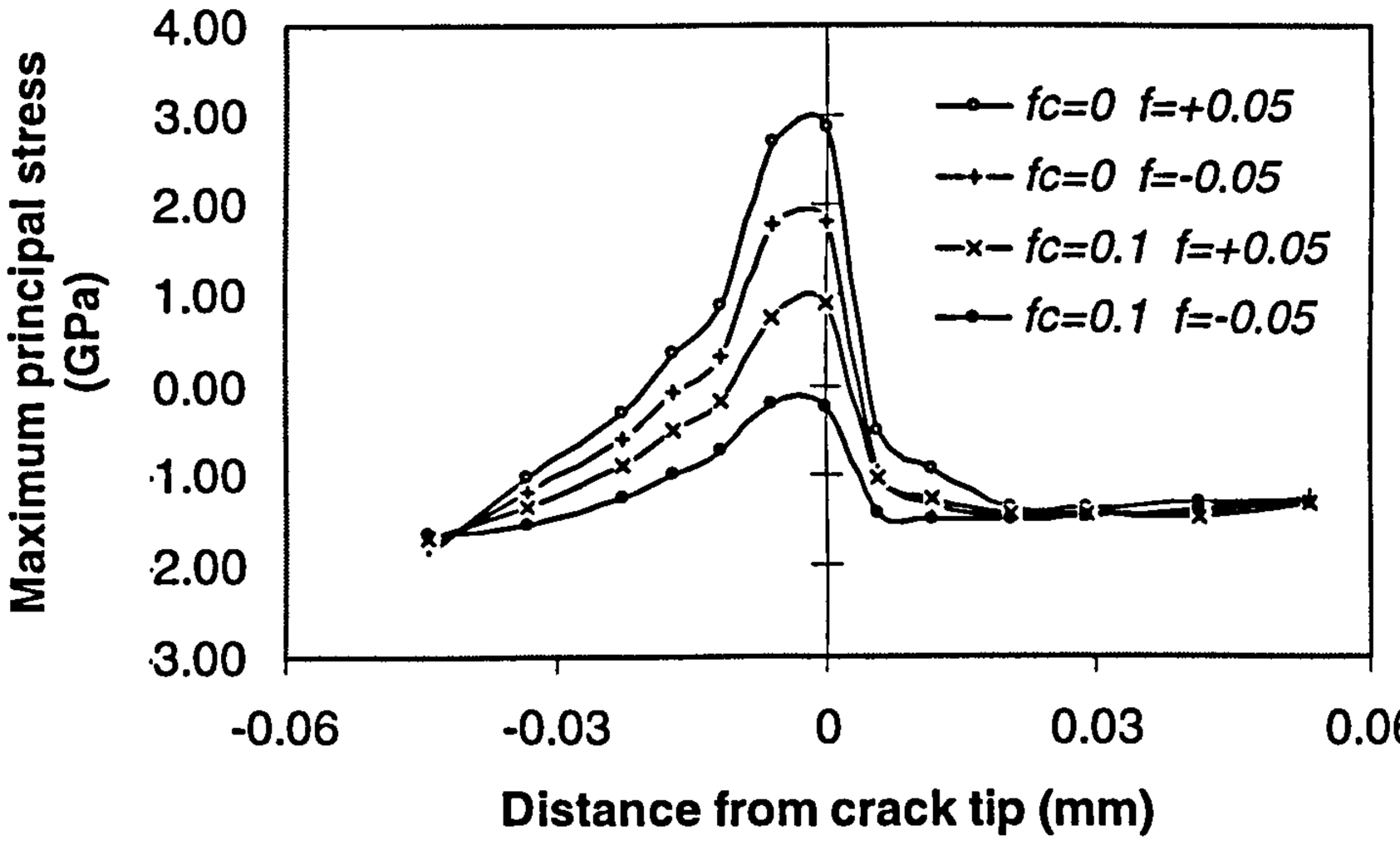

Figure 5.25 Principal stress variations across the crack tip at the plane $\phi = 0^{o}$ (Case 2, $x = 0.347$ mm, crack gap = 0).

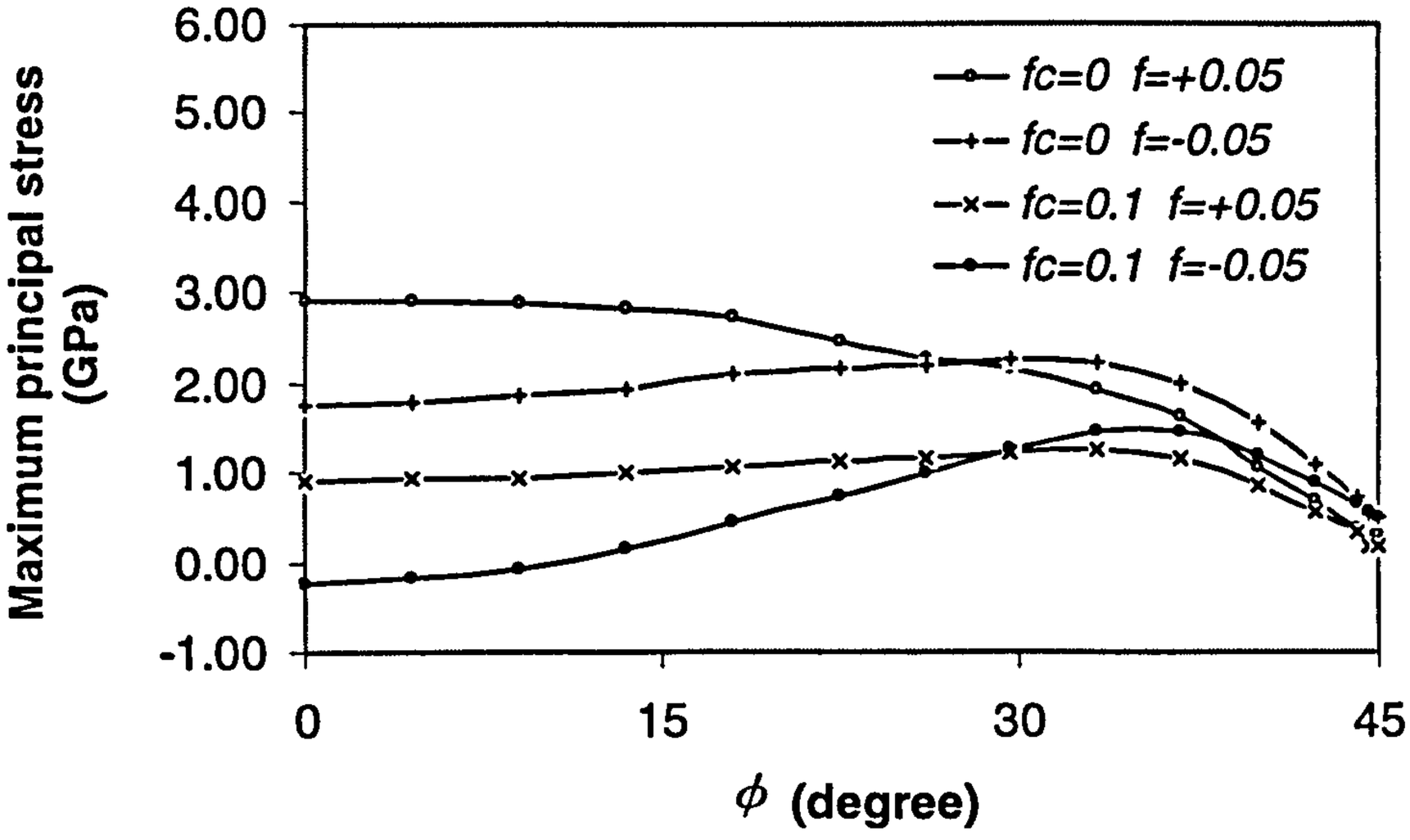

Figure 5.26 Principal stress against ϕ along the crack front (Case 2, $x = 0.347$ mm, crack gap = 0).

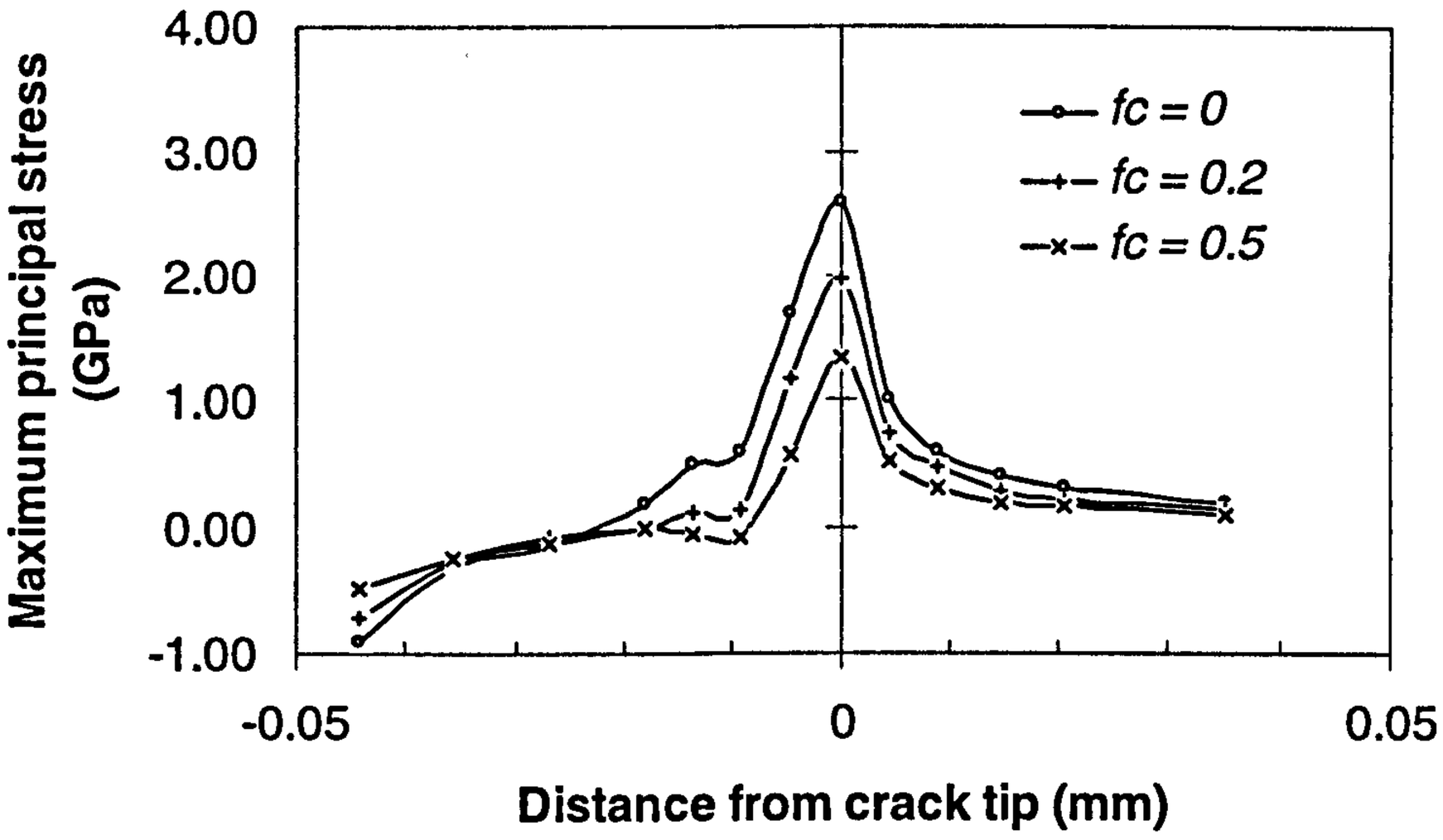

Figure 5.27 Principal stress variations across the crack tip at the plane $\phi = 0^{o}$ (Case 2, $x = 0.047$ mm, crack gap = 0).

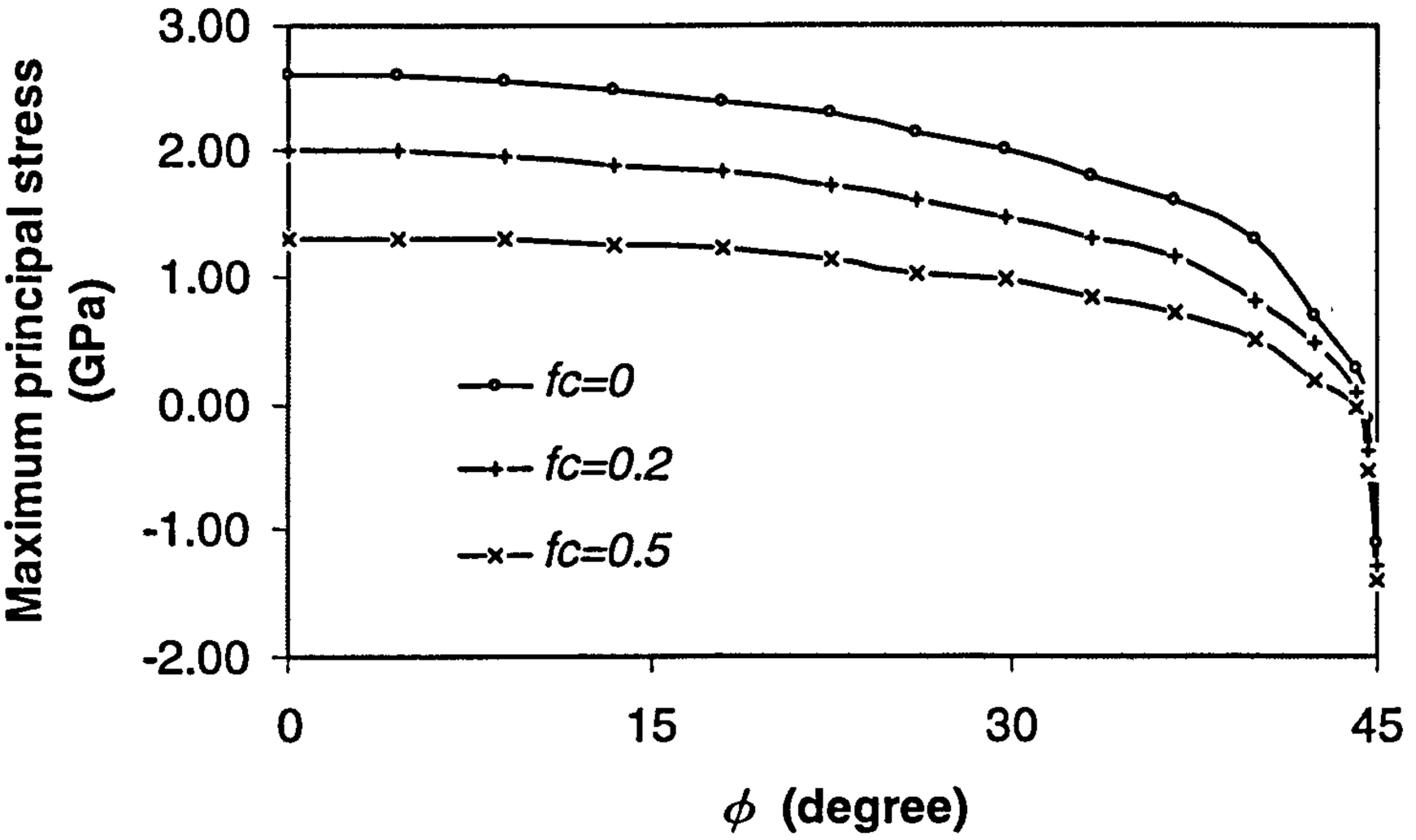

Figure 5.28 Principal stress against ϕ along the crack front (Case 2, $x = 0.047$ mm, crack gap = 0).

The origin in figures 5.25 and 5.27 represents the crack tip, and negative coordinates represent the stresses on the crack face. Figures 5.25 and 5.26 show the case of x = 0.347 mm where the crack front is fully beneath the contact circle. Figures 5.27 and 5.28 show the case of x = 0.047 mm where most of the crack face is under the contact circle except the crack front. There is no change in the stress distributions when the coordinates > 0 (non-crack zone). However, the stresses on the crack face are changed significantly when approaching the crack tip from the ball surface. Several features emerge in figures 5.25 to 5.28: (1) the maximum principal stress is non-negative near the crack tip and exists along the whole crack front; (2) it exists whether $f > 0$ or $f < 0$; (3) it decreases with the increase of the crack face friction coefficient f_c. The maximum value occurs at approximately 5 μm from the crack tip. The results in the present study predict that the tensile stress near the crack tip will trigger subsurface branch cracks. If crack propagation is of this characteristic, then these subsurface cracks will occur on the fracture surface, and will inherit the geometry of the original crack front. On the other hand, the radius of the branch crack should be very close to that of the original ring crack.

If the fatigue spall formation is only due to the original ring crack propagation, then the observed spall contour should be the half ellipse only. However, an ellipse spall is always found. The possible reason for this is that the subsurface branch cracks formed on the lower crack face propagate in a direction opposite to the direction of the original crack growth. The branch crack growth is driven by mode I stress intensity arising from the stress field where the contact circle moves to another side.

5.4.2 On the upper crack face

Figures 5.29 and 5.30 show the stress distributions on the upper crack face for the contact circle lying in a coordinate of x = 0.467 mm, which shows how friction coefficients f_c and f influence the stress distributions. Again, the directions of principal stresses are determined in terms of the analysis of Eigen vectors. Maximum principal trajectories at any points along the crack front are approximately orthogonal to the first and second tangential directions at the corresponding point.

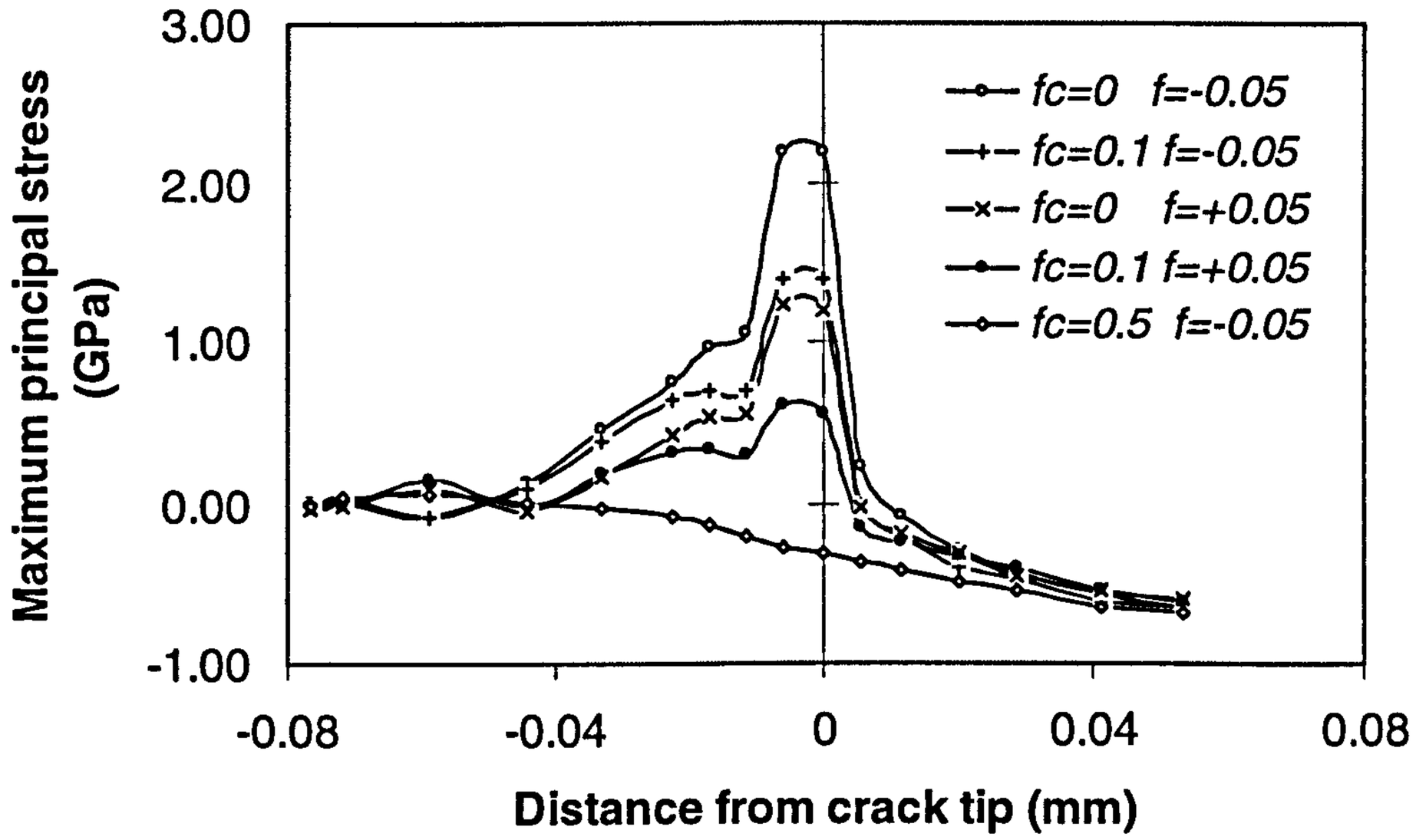

Figure 5.29 Principal stress variations across the crack tip at the plane $\phi = 0^{o}$ (Case 2, $x = 0.467$ mm, crack gap = 0).

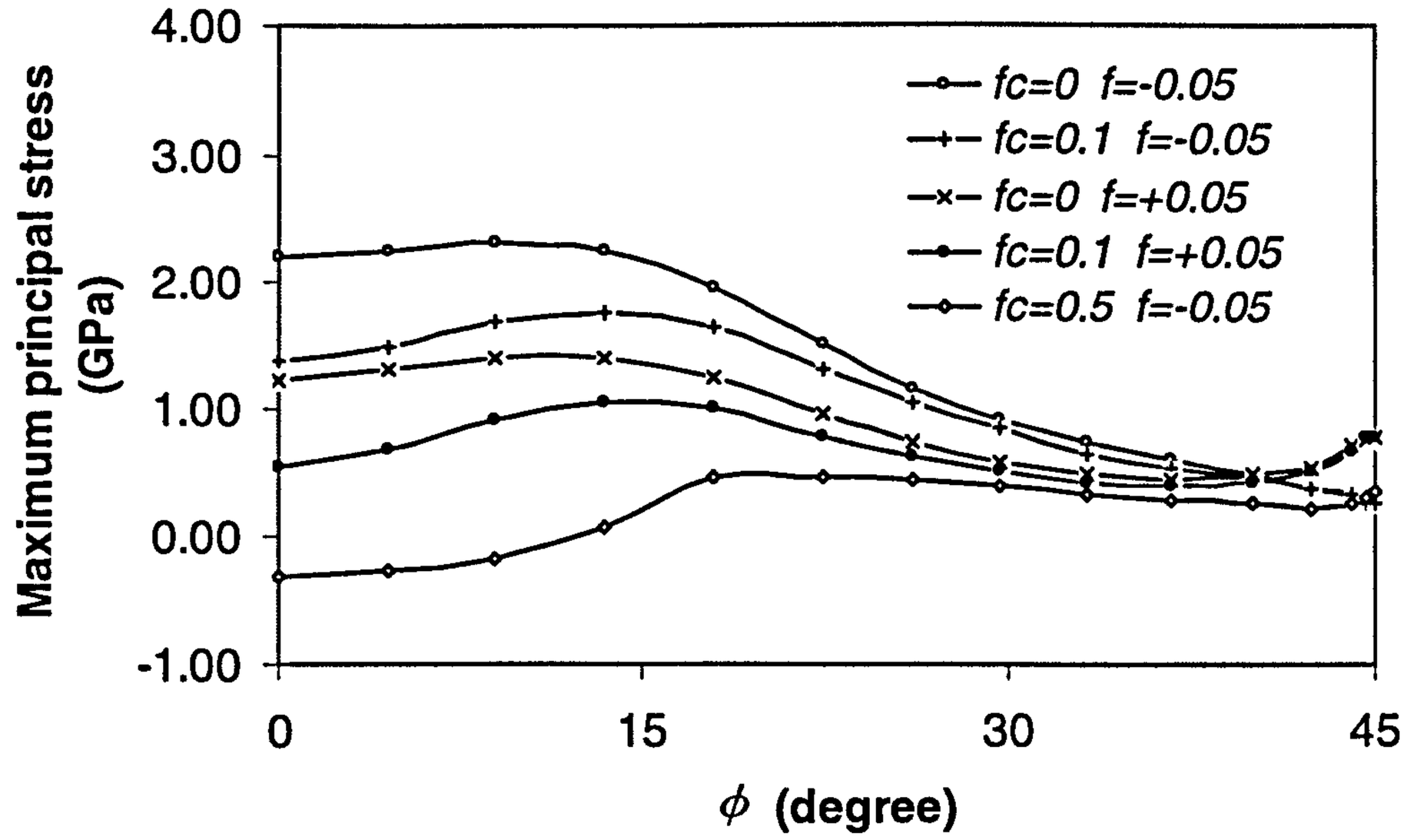

Figure 5.30 Principal stress against ϕ along the crack front (Case 2, $x = 0.467$ mm, crack gap = 0).

As in figure 5.25, the origin represents the crack tip, and negative coordinates represent the stresses on the crack face. There is practically no change in the stresses in the non-crack area. However, the stress distributions on the crack face vary significantly when approaching the crack tip from the ball surface to the crack tip. It is found that the non-negative stress occurs near the crack tip, and the value is sensitive to the change of the crack face friction coefficient and traction direction. This stress value decreases with the increase of the crack face friction coefficient (f_c). When the crack face friction coefficient exceeds 0.5 there is no change (as normal with no cracks). It is not difficult to imagine that the crack faces will be interlocked when the crack face friction coefficient exceeds a certain value. The results indicate that the stresses on the upper crack face are high enough to initiate the subsurface branch cracks on the upper crack face. The crack formed on the upper crack surface will grow back to the surface to cause the fatigue spall. It is evident how the fatigue spall is formed in brittle materials. According to the analysis of stresses (x, y and z components), these subsurface branch cracks propagate mainly in perpendicular to the tangential direction corresponding to the point at which the crack is generated. Consequently, the branch cracks formed on the upper crack face will grow back to the surface. It can be concluded that the branch crack growth is one of the causes which lead to the final sheet separation.

Experimental observations show that failure modes in high viscosity oil are the same as in low viscosity oil but the fatigue life is different. Fatigue life in high viscosity oil is longer than that in low viscosity oil. The calculated results indicate that fatigue life increases with the increase of the crack face friction coefficient (f_c) in that the more f_c decreases the greater the possibility of the formation of both secondary surface cracks and subsurface branch cracks. The use of higher viscosity oil inhibits the amount of fluid that can enter a crack, and friction forces acting between the faces of the crack increase. The experimental results agree well with the prediction in terms of the numerical analysis.

CHAPTER 6

DISCUSSION AND CONCLUSIONS

6.1 DISCUSSION

Ring crack defects are routinely found on finished ceramic ball surfaces. The dimension of the ring crack is very close to the in-service contact area and any minor variation in geometry attitude of a ring crack on the contact track may result in a significant change in rolling contact fatigue (RCF) performance. The modified four-ball machine experiments show that the RCF life performance is extremely sensitive to the crack location in relation to the contact path and fatigue spall happens only at a few crack locations. The possibility of a surface ring crack being in the contact region is two percent. If the crack location effect is considered, the failure probability resulting from the surface ring crack will be 0.5 percent only. This result indicates that the traditional statistics analysis is no longer suitable for the fatigue performance assessment of the ceramic balls with surface ring crack defects if using the conventional test methods.

To describe precisely location geometry influences, the geometrical attitude of a ring crack on the contact track is presented by two parameters: δ and β. The parameter δ represents the distance of the centre of the crack circle to the central line of the contact track. The parameter β is the angle of the chord of ring crack to the central line. The experimental results indicate that the RCF life decreases as β increases, and increases as δ increases no matter what type of lubricants are adopted. The locations which may lead to fatigue failure are when $\beta = 90^{\circ}$ and $\delta <= 0.5a$ or when $\beta = 45^{\circ}$ and $\delta = 0$. The worst location in the RCF life performance is when $\delta =$ 0 and $\beta = 90^{\circ}$. If surface ring cracks are not in easy failure locations, it is difficult to cause fatigue failure in limited testing time (10^8 fatigue cycles) for the maximum contact load of 5.58GPa. For the same crack location, the RCF life is dependent upon the lubricant type. High viscosity lubrication (gear oil) exhibits long fatigue life, compared with the case of low viscosity oil (gas turbine oil).

A three-dimensional boundary element model associated with crack growth is developed to study the driving force of surface ring crack propagation. The calculated

results indicate that the K_I stress intensity is mainly responsible for ring crack growth. Fracture mechanics analysis indicates that the reason for RCF life difference with the crack locations is that the different crack locations have different stress intensity factor values, which govern the crack propagation behaviour. The stress intensity factors along the crack front are very sensitive to the ring crack orientation. In addition, the calculated stress intensities are also sensitive to the surface traction direction. The influence of crack geometry on the stress intensity factors is studied through four typical crack surfaces. The calculated results indicate that the stress intensity factors are affected by the geometry. Fracture mechanics analysis quantitatively confirms that ring crack propagation is affected markedly by the crack location within the contact path. There is a good correlation between numerical analysis and experimental studies. As a result, the RCF performance of silicon nitride rolling elements can be predicted through fully numerical fracture mechanics analysis.

Crack front growth depends upon ring crack location due to different crack locations corresponding to different SIF values. The calculated result shows that the crack propagates towards the material and will not grow along the ring crack circle. The prediction based on the numerical calculations has been verified by extensive experimental studies, which have been discussed in Chapter 3, Section 3.3.

Spalling fatigue failure in rolling contact is complex due to Hertzian loading in a cyclic fashion. The purpose of the stress intensity analysis is to answer the possibility of ring crack propagation under rolling contact. The calculated results show that the crack front can be propagated and will be governed by K_I stress intensity. The K_I stress intensity decreases as the crack depth increases. This result predicts that crack growth will be arrested at a certain depth. Experimental observation shows that the original ring crack growth is downwards conical. If a fatigue spall that results from rolling contacts is due to propagation of the original ring crack, then it seems very difficult to explain the final sheet separation. Of course, stress intensities propagating a crack are mandatory to a fatigue spall formation. To explain the sheet separation, the lubricant hydrostatic pressure was assumed to prise the crack open and to force the crack to grow back to the surface (Kaneta and Murakami 1987). It is questionable whether enough fluid is available to force the crack open due to the thickness of the film under

the contact loading (Bower 1988). It is believed that the nature of a fatigue spall can be revealed provided that the stress field arising from the crack face contacts is fully understood.

To interpret the failure processes, a three-dimensional boundary element model of crack face contact is developed to study the failure mechanisms of ceramic surface ring crack in rolling contacts. The calculated results show that surface ring crack fatigue failure involves complex mechanics processes. They are (1) original ring crack propagation along the main growth path until arrested (0.15 mm in radius); (2) secondary surface crack initiation when the crack gap > 0.2 μm; and (3) subsurface branch crack nucleation and growth. Figure 6.1 illustrates the processes of the spalling fatigue failure. Figure 6.2 shows the mechanisms of the fatigue spall formation. Comprehensive experiments have been carried out and results agreed well with the numerical analysis.

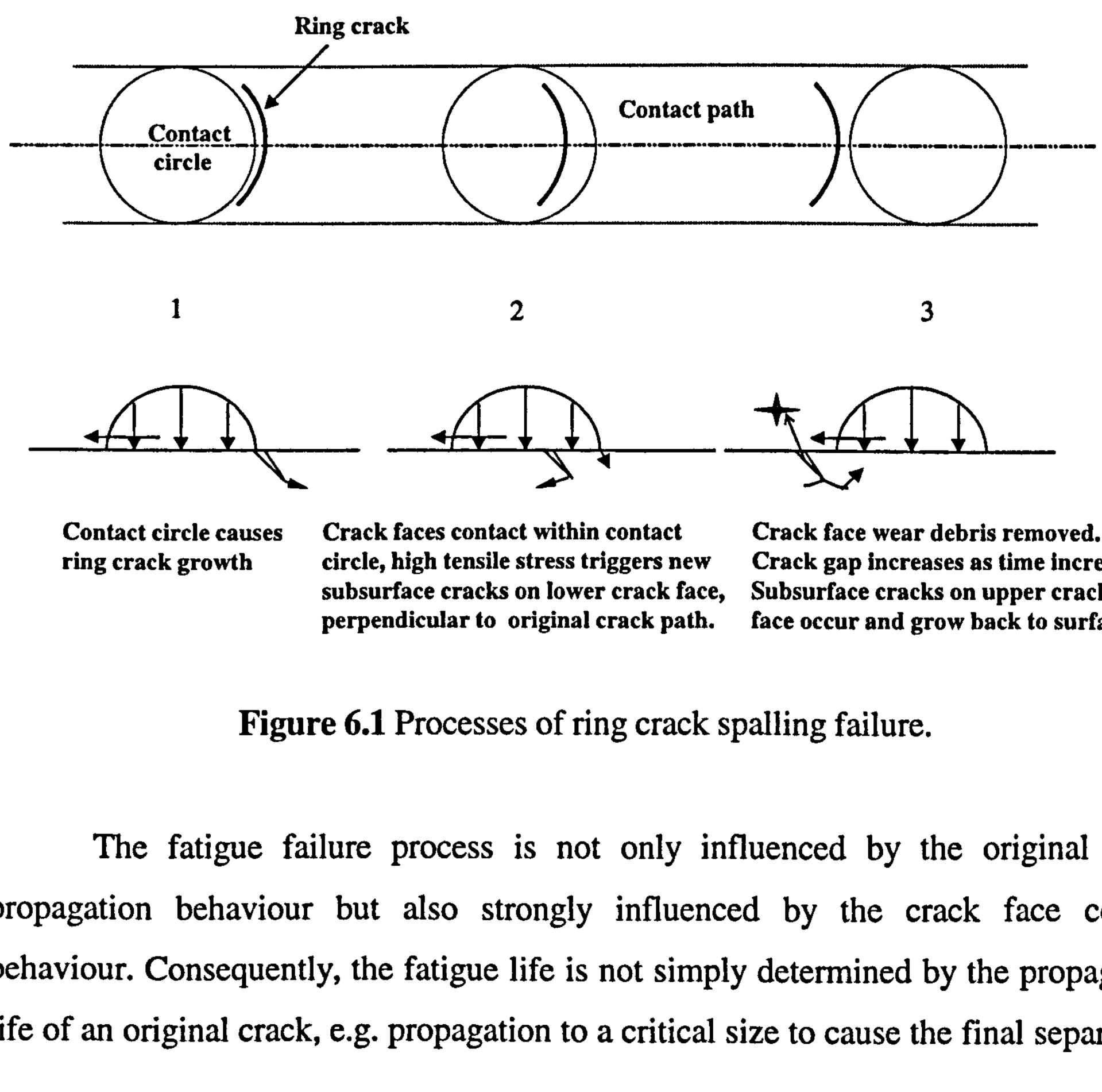

Figure 6.1 Processes of ring crack spalling failure.

The fatigue failure process is not only influenced by the original crack propagation behaviour but also strongly influenced by the crack face contact behaviour. Consequently, the fatigue life is not simply determined by the propagation life of an original crack, e.g. propagation to a critical size to cause the final separation.

Secondary surface cracks play a dominant role in spalling failure. The existence of the original ring crack is a necessary condition for the formation of the secondary surface cracks. The spalling fatigue failure life of silicon nitride rolling elements involves two parts: (1) crack growth required for a certain size and (2) fatigue cycles required for the spall sheet separation. There exists a period in which the crack stays the same size. During this period, the crack experiences a cyclic surface loading and the crack gap increases due to the crack face friction. Secondary surface cracks will be formed if the crack gap reaches a critical value.

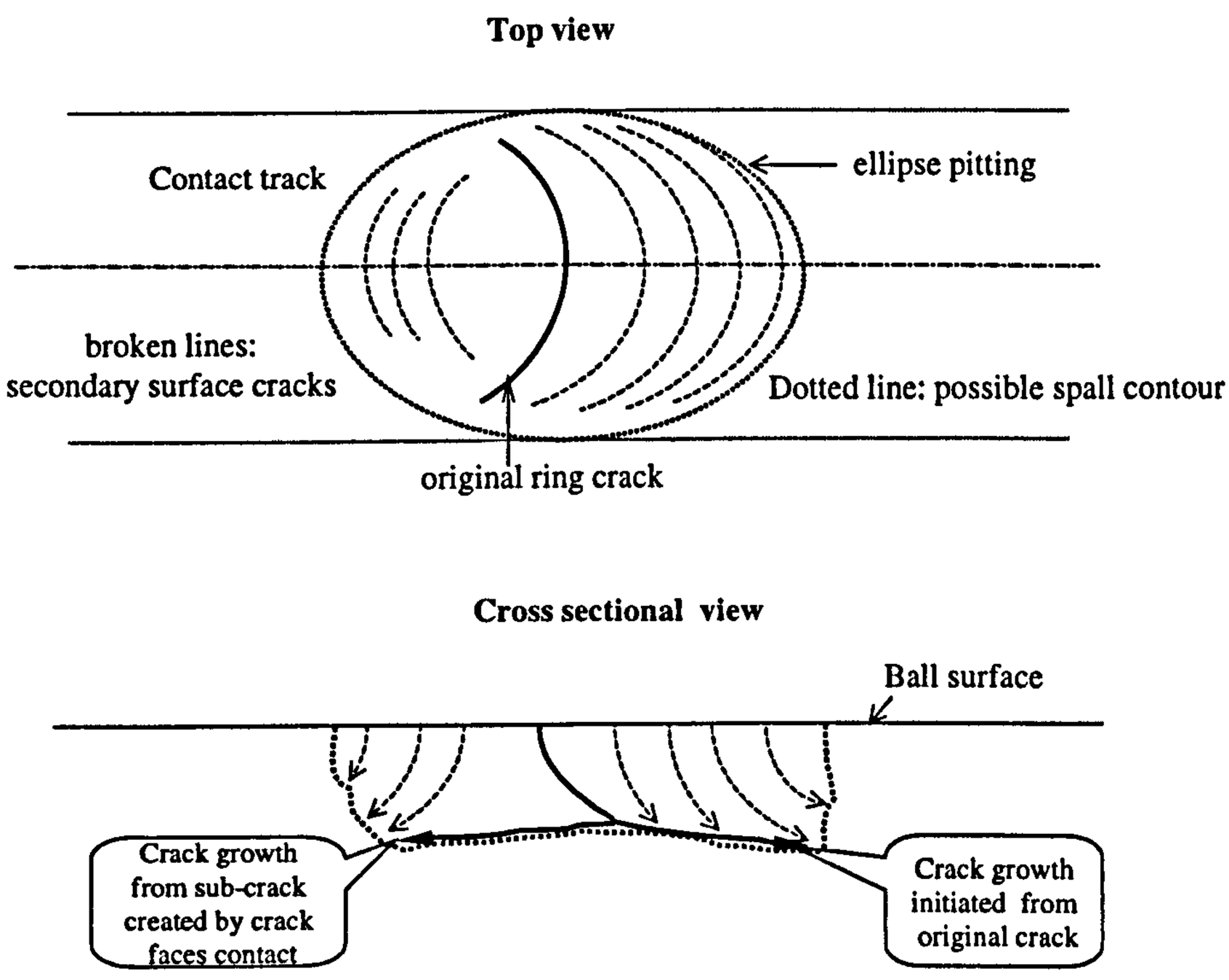

Figure 6.2 Mechanisms of the ceramic fatigue spall formation.

The formation of secondary surface cracks depends mainly on the crack gap, crack dimensions and crack face friction coefficient. The formation of secondary surface cracks increases with the increase of the crack gap and crack depth and decreases with the increase of crack face friction coefficient. The secondary surface cracks are formed when the crack gap reaches a certain value. These cracks propagate

conically away from the surface and meet the main crack path to lead to the formation of a fatigue spall.

Subsurface branch cracks which are formed on the upper crack face, are another important factor which cause the final spall sheet separation. The formation of subsurface branch cracks is sensitive to crack face friction coefficient. The possibility of the formation of the branch cracks decreases with the increase of the crack face friction coefficient. These branch cracks may be able to propagate towards the surface to cause a fatigue spall. Subsurface branch cracks can also be generated on the lower crack face, which may propagate in a direction opposite to the direction of the main crack growth so that the other half of an ellipse spall is formed. The crack nucleation also increases with the decrease of the friction coefficient.

6.2 CONCLUSIONS

(1) Rolling contact fatigue (RCF) life performance of silicon nitride bearing elements is found to be markedly sensitive to the crack location and fatigue spall happens only at a few crack locations. RCF life decreases as β increases, and increases as δ increases.

(2) A quantitative three-dimensional boundary element model has been developed which can be used to determine the geometry of acceptable surface ring cracks.

(3) Stress intensity factors (SIF) along the crack front can provide all of the necessary information to determine the state of a surface ring crack. RCF life performance can be predicted by a simulation analysis through comparing SIF on the crack front to K_{IC} and ΔK_{th}.

(4) Experimental observations show that there is no significant crack propagation along the original ring crack circle on the ball surface. Crack propagation in rolling contact is underneath the surface, and is dependent upon the point location along the crack front.

(5) Fatigue failure processes arising from the surface ring cracks are not only influenced by original crack propagation behaviour but also strongly influenced by crack face contact behaviour. Crack face friction coefficients significantly affect the RCF performance and failure modes.

(6) Secondary surface cracks play a dominant role in the formation of spalling failure. Increasing the crack gap and depth increases the formation of secondary surface cracks.

(7) A spalling non-catastrophic fatigue failure mode is identified in the cases of surface ring cracks and line defects.

6.3 FURTHER WORK

It is found that the RCF life increases with the increase of crack face friction coefficients. Study of the influence of varying the crack penetration properties of the lubricant is needed. Experiments using grease lubrication and powerful penetration lubricants are required.

Interaction of the crack faces with the trapped lubricants and the consequent influence on the wear properties of the rough crack faces are required. This also has important implications for the determination of the formation of secondary surface cracks.

It is suggested that a comprehensive understanding of crack propagation under rolling contact is required. This is necessary for the rolling bearing life design and prediction. Experimental results based on conventional techniques are not well suited to crack propagation behaviour in rolling contact.

APPENDIX 1

ROLLING CONTACT FATIGUE TEST MACHINE

Many test-rig types are used to study rolling contact fatigue performance of ceramics. Typically, in such tests, a detector coupled with a shutdown device is used to monitor the vibration of the assembly. When a pre-set vibration level is exceeded, indicating the formation of a spall or excessive uneven wear, the test is automatically stopped and the lifetime of the test is recorded. Or, tests are suspended at different times to study the wear rate. Failure modes could be changed according to contact geometry (Hadfield and Stolarski 1995). The experimental evaluation of silicon nitride should be conducted on a number of model tests before predicting its performance for rolling element applications. The characteristics of various types of rolling contact fatigue test methods are summarised below.

A1.1 The modified four-ball machine

A model contact consisting of three lower balls driven by a fourth contacting upper ball simulates conditions within a standard deep-groove ball bearing. The upper ball models the bearing race, while the cup simulates the bearing outer race and the three planetary balls represent the balls within a ball bearing. The loading geometry is shown in figure A1.1. The machine has a proven history as being useful to investigate the rolling contact fatigue resistance of materials under various tribological conditions. Previously, this machine has been mainly used as an accelerated method to measure the rolling contact fatigue of bearing steels by various research staff. Barwell and Scott (1956), Krivoshein (1960) and Scott (1963) used the machine to evaluate the influence of lubrication type on steel ball rolling contact fatigue. The Institute of Petroleum gathered various papers (Tourret and Wright 1977), which describes various test results, ball dynamics and kinematics using the modified four-ball machine.

The RCF performance of hot-pressing silicon nitride bearing materials has been studied in the past by Scott et al. (1971) and Scott and Blackwell (1973), using this machine. Recently, Hadfield et al. (1993a), Hadfield et al. (1993b), Hadfield

(1998) have used the modified four-ball machine to simulate the rolling contact in hybrid ball bearings.

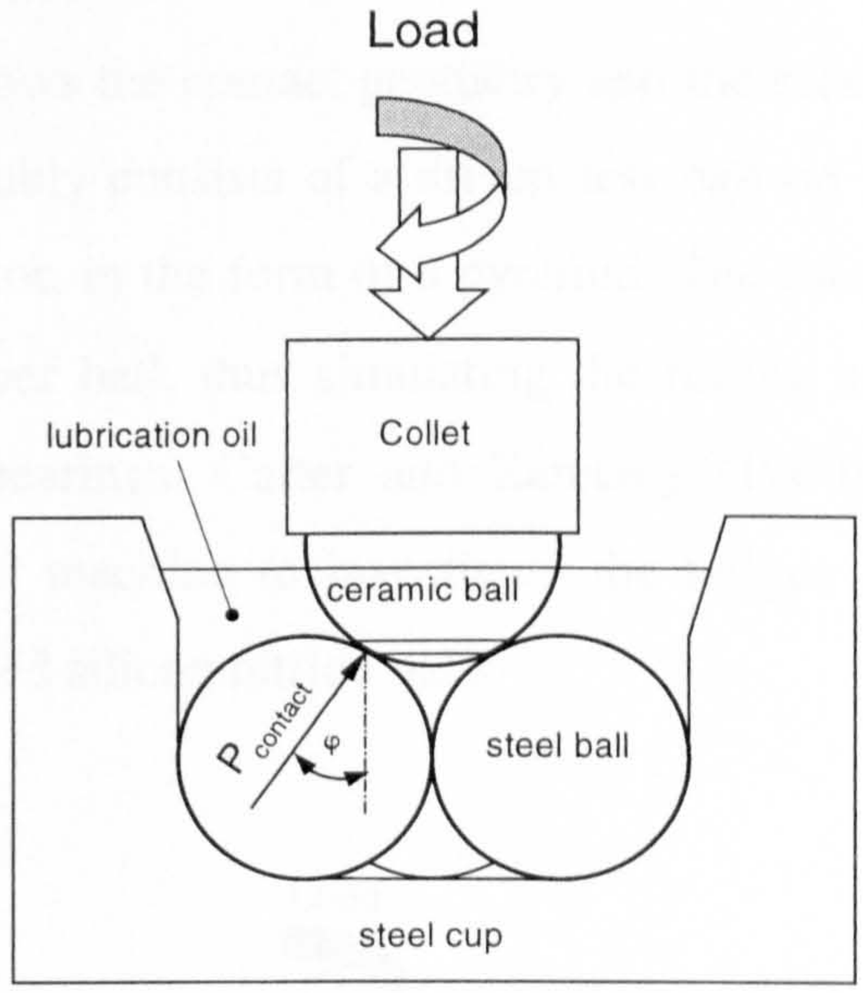

Figure A1.1 Loading configuration of four-ball machine

The upper-ball stress cycle factor '*L*' may be calculated from equation (A1.1) (Tourret and Wright 1977). This parameter is used to assess the total number of upper-ball stress cycles per machine spindle revolution.

$$\text{Stress cycles per rev } (L) = z\left(\frac{R_A + 2R_P}{2(R_A + R_P)}\right) \qquad \text{(A1.1)}$$

Hence $$L = 3\left(\frac{6.35 + 2(6.35)}{2(6.35 + 6.35)}\right)$$

Therefore $$L = 2.25$$

Hence, for example, two million stress cycles applied to the upper-ball, require 0.889 million machine spindle revolutions.

A1.2 Five-ball machine

Figure A1.2 shows the contact geometry and the rotating mechanisms of the test rig. The test assembly consists of a driven test ball on top of four lower balls positioned by a separator, in the form of a pyramid. The four lower balls rotate in a race driven by the upper ball, thus simulating the rolling and sliding produced in angular contact ball bearings. Carter and Zaretsky (1960), Parker and Zaretsky (1975) used a five-ball machine to investigate the fatigue life of high-speed ball bearings with hot pressed silicon nitride balls

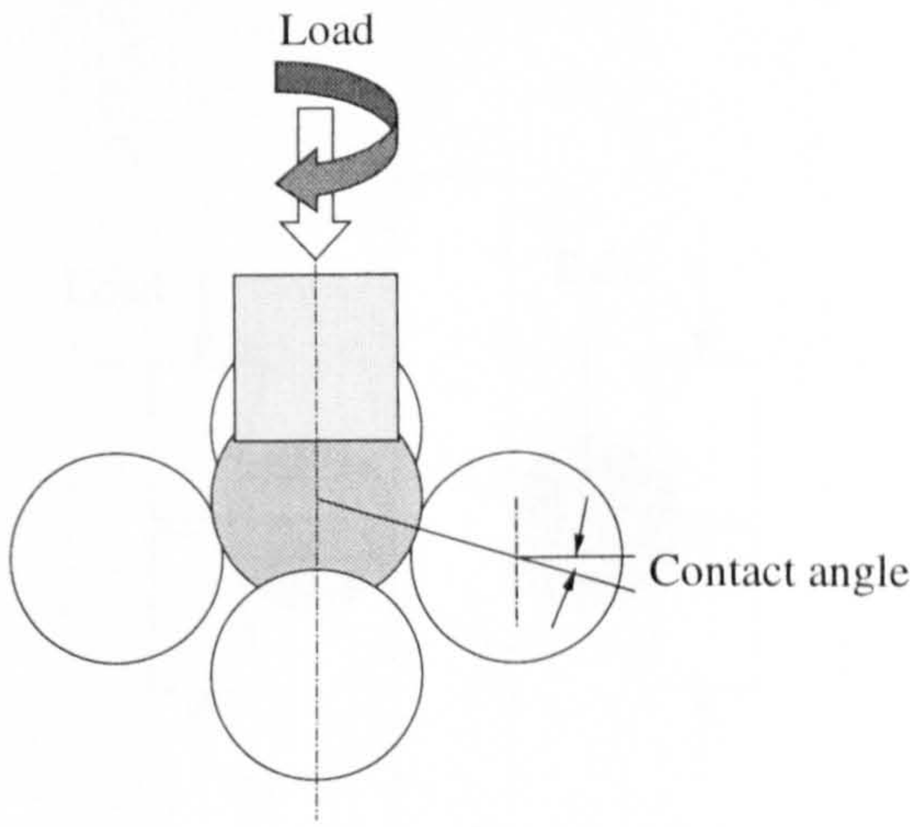

Figure A1.2 Loading configuration of five-ball machine

A1.3 Ball-on-plate machine

The ball-on-plate machine was used by Fujiwara et al. (1989) and Kikuchi et al. (1984), to investigate the rolling contact fatigue performance of silicon nitride. Figure A1.3 shows a cross section view of the test rig. The test unit has a unidirectional thrust bearing configuration, which consists of three balls or rollers equally spaced at 120° by a retainer and loaded between a stationary flat washer and

a rotating grooved washer. The rotating washer produces ball motion and serves to transmit load to the balls (or rollers) and the flat washer.

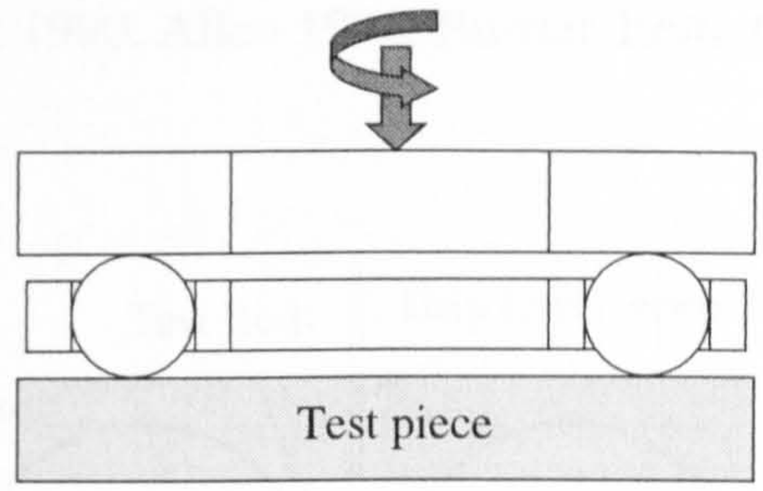

Figure A1.3 Loading configuration of ball-on-plate machine

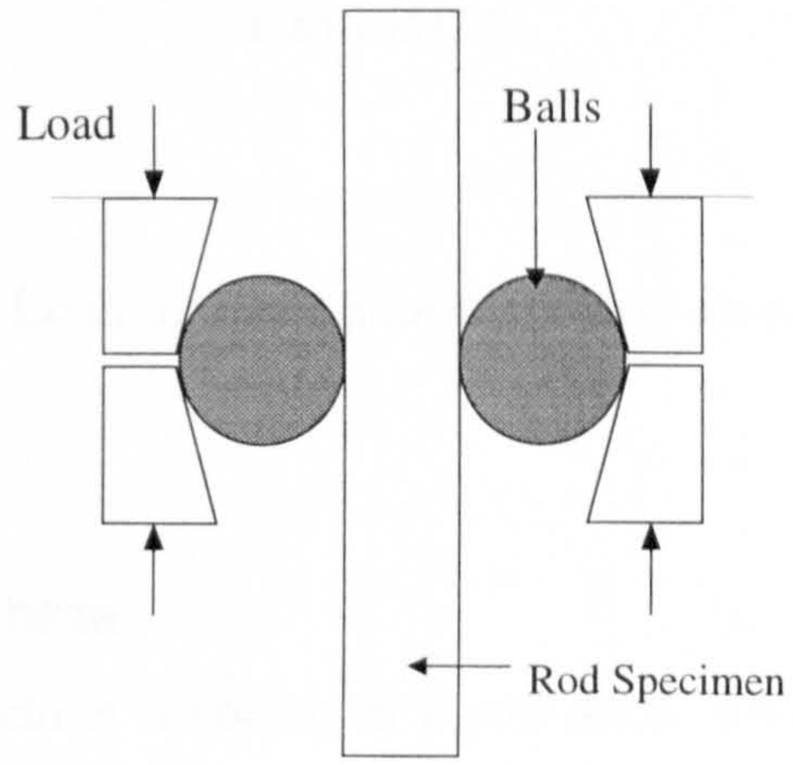

Figure A1.4 Loading configuration of ball-on-rod machine

A1.4 Ball-on-rod machine

Figure A1.4 shows the loading geometry of the ball on rod type testing machine. Three steel balls, 12.7 mm in diameter, orbit a rotating 9.53 mm diameter cylinder test specimen. The thrust load on the bearing cups is applied mechanically by forcing the upper cup towards the lower cup with three precalibrated coil springs

in the assembly. The rod specimen is rotated by a direct-drive electric motor mounted in line with the specimen below the table. The three balls are, in turn, driven by the rod and rotate around the rod. Lubricant is supplied by drip feeding onto the top of the rod. The machine has been employed to study rolling contact wear performance (Lucek 1990, Allen 1994, Burrier 1996, Chao et al. 1998).

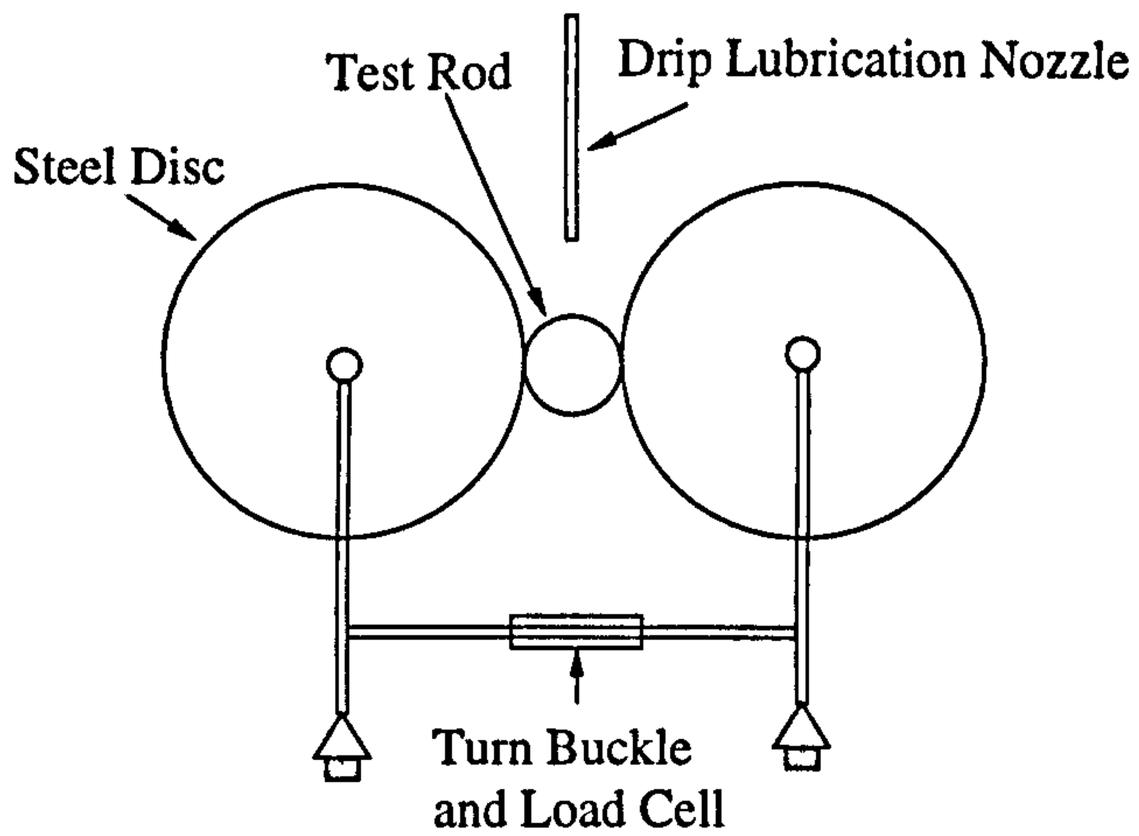

Figure A1.5 Loading configuration of disc-on-rod machine

A1.5 Disc-on-rod machine

A disc-on-rod machine is shown in figure A1.5. Two steel disks, 177.7 mm in diameter and 12.7 mm thick, are pressed against the test specimen which is held in a spindle and driven at 10000 rpm. The test specimen is a 76 mm long, straight cylinder with a 9.52 mm diameter. With the known geometry, the contact stresses as a function of load can be calculated. The machine provides a means of rapid testing in nearly pure rolling contact. The specimen receives 1,200,000 stress cycles per hour when driven at 10,000 rpm. Earlier work using this machine was performed by Baumgartner (1974), Lucek and Cowley (1978).

A1.6 Contacting ring machine

The contact ring machine has been used by Akazawa and Kato (1988), Braza et al. (1989) and Akazawa et al. (1986). Figure A1.6 shows a diagram of the test rig, which uses two disk-shaped specimens rotating against each other on their outer surfaces. Geometry of the test specimen can be disks or rings which can be mounted on shafts. The contacting outer surface of the specimens can be both flat or, one specimen may have a flat surface while the other has a toroidal surface. The rotational speeds of the two disks (ring) can be controlled individually with separate motors or using the gear mechanism; thus, rolling contact with differing amount of sliding (slippage) at the interface can be generated. Typically the load is applied using a compressed coil spring or dead weight loading systems. Tests can be conducted in either dry or lubricated conditions. Profiles of the wear scars on the contact surfaces can be used to estimate the wear volume.

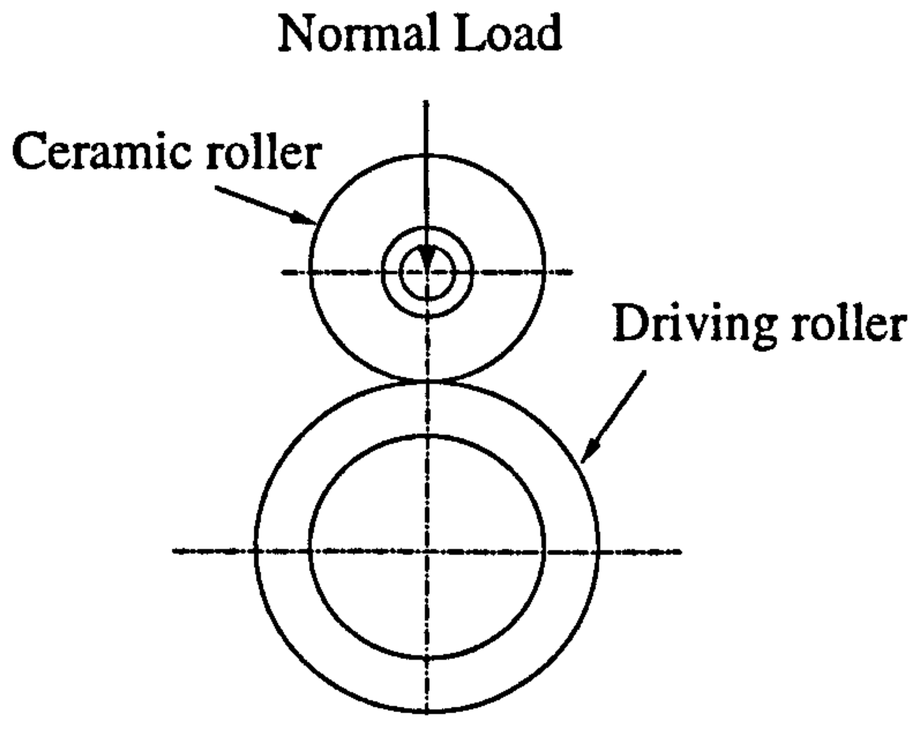

Figure A1.6 Loading configuration of contacting ring machine.

APPENDIX 2

MECHANICAL PROPERTIES

Table A2.1 Mechanical properties of silicon nitride with different processing routes

Processing route	Density (g/cm^3)	Flexural strength (MPa)	Fracture toughness (MPa $m^{1/2}$)	Elastic modulus (GPa)	Poisson's ratio	Hardness (GPa)
Sintered	3.2	600	4.5	276	0.24	14
Hot-pressed	3.2	800	5.0	317	0.28	20
Reaction-bound	2.5	210	3.6	165	0.22	10
Sintered reaction-bound	3.3	825	-	297	0.28	19
Hot isostatic pressing	3.2	1000	6.0	310	0.28	20

Table A2.2 Typical properties of engineering ceramics and bearing steel

Material	Density (g/cm^3)	Elastic modulus (GPa)	Hardness (kg/mm^2)	Toughness (MPa $m^{1/2}$)	Failure mode
Silicon nitride	3.2	315	1400 - 1800	4 - 7	Spalling
Silicon carbide	3.1	420	2000 - 2400	2 - 4	Fracture
Alumina	3.9	390	1800 - 2000	3 - 5	Fracture
Zironia	5.8	210	1100 - 1400	8 - 12	Spalling
Steel*	7.8	200	1000	> 16	Spalling

* Standard bearing steel AISI 52100, or aircraft bearing steel- M50 high speed steel

APPENDIX 3

THE MANIPULATOR FOR LOCATING BALL SURFACES

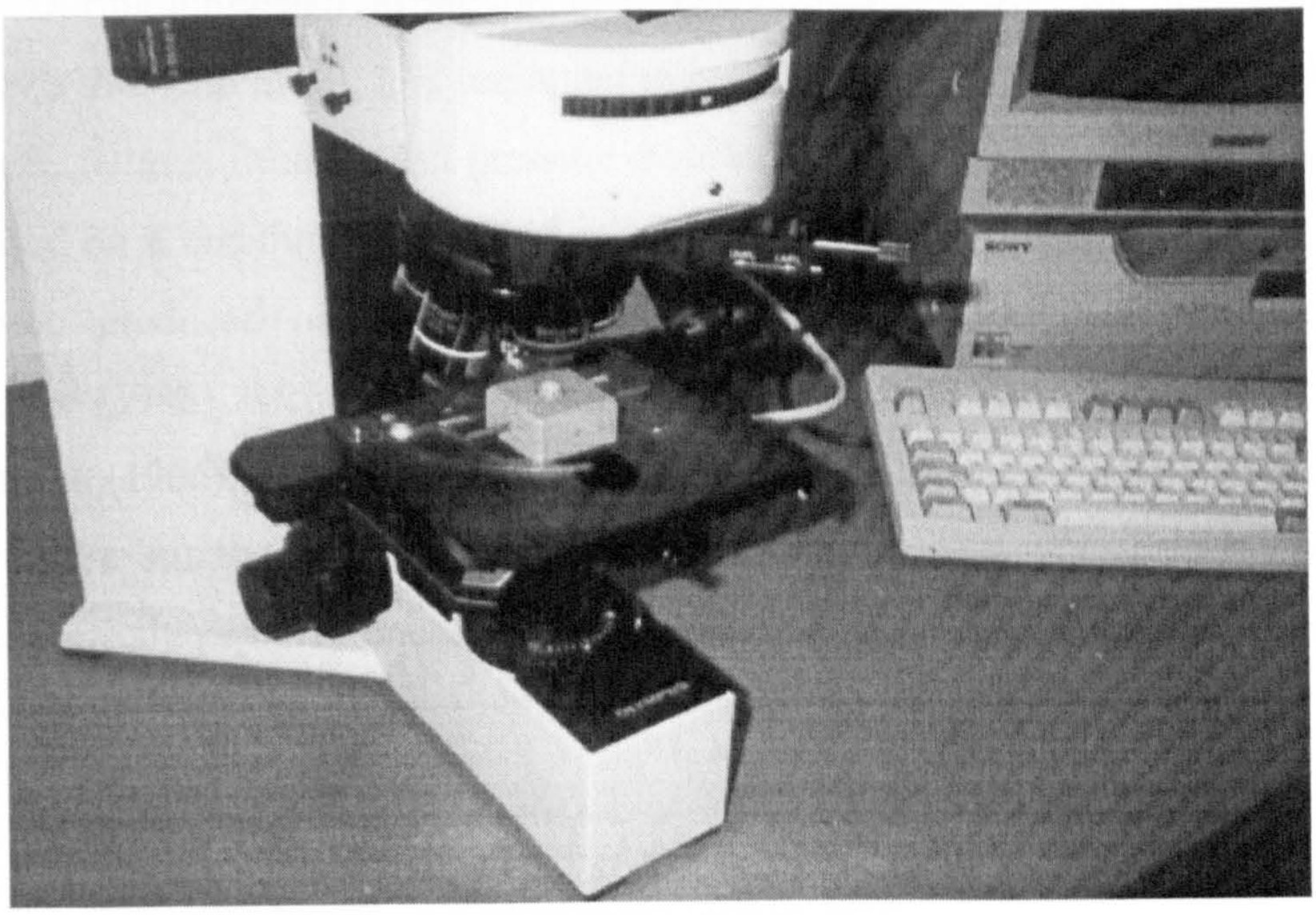

Figure A3.1 Manipulator for locating ball surfaces

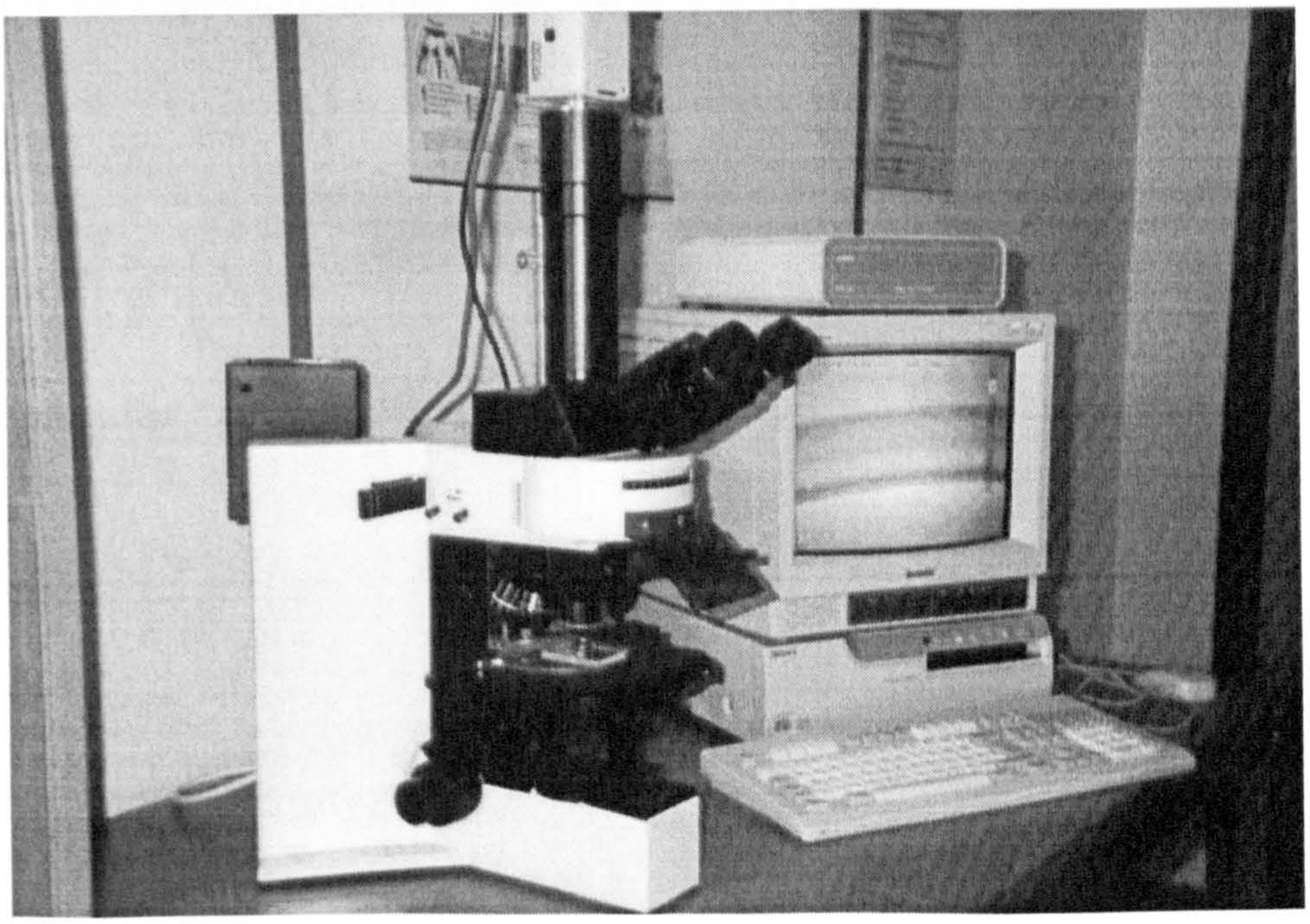

Figure A3.2 Platform for supporting microscopy detection

APPENDIX 4

THEORETICAL LUBRICATION REGIME

During lubricated testing the upper ball is separated from the three planetary balls by a thin film of oil. It is important to calculate this film thickness as it affects the wear, fatigue, friction, and pressure distribution. Calculations of film thickness are based on a combination of fluid mechanics and materials science. Much work has been produced on elasto-hydrodynamic lubrication, notably by Hirst and Richmond (1988), Archard (1973), Tallian (1972), Hirano et al. (1971), Dowson and Higginson (1966), and Archard and Kirk (1960). The magnitude of separation between the surfaces and the lubrication regime is calculated using the classical Elasto-Hydrodynamic Lubrication (EHL) equation (A4.1) developed by Hamrock and Dowson.

$$H_{\min} = 3.63U^{0.68}G^{0.49}W^{-0.073}(1-e^{-0.68k}) \qquad \text{(A4.1)}$$

$H_{\min}$ is dimensionless minimum film thickness, and U, G, W and k are dimensionless parameters for speed, materials, load and ellipticity respectively, ie.

$$G = \xi E^{'}$$

$$k = \left(\frac{R_y}{R_x}\right)^{2/\pi}$$

$$U = \frac{\eta_0 u}{E^{'} R_x}$$

$$W = \left(\frac{P}{E^{'} R_x^2}\right)$$

where η_0 = viscosity (Ns/m^2)

u = mean surface velocity in x (motion) direction (m/s)

E' = effective elastic modulus (N/m^2)

ξ = pressure viscosity (m^2/N)

P = Total load (N)

R_x = effective radius in x (motion) direction (m)

R_y = effective radius in y (motion) direction (m)

The minimum film thickness (h_{min}) is found from the product of the dimensionless minimum film thickness parameter (H_{min}) and effective ball radius.

$$h_{min} = H_{min} R_x \tag{A4.2}$$

The minimum lubricant film thickness, together with the surface roughness, determines when the full fluid lubrication begins to break down. It is useful to define the ratio

$$\lambda = h_{min} / \sigma^* \tag{A4.3}$$

where σ^* is the composite r.m.s. roughness of the two surfaces, defined by

$$\sigma^* = \sqrt{R_{q1}^2 + R_{q2}^2} \tag{A4.4}$$

R_{q1} and R_{q2} are the r.m.s. roughness values for each surface.

The value of λ provides a measure of how likely, and how severe, asperity interactions will be in lubricated sliding. For $\lambda > 3$, a full film will separate the two surfaces, asperity contact will be negligible and both friction and wear should be low. However, in the range of $1 < \lambda < 3$, then some contact of asperities will occur and this lubrication condition is called partial or mixed EHL. In this lubrication regime the friction forces start to rise quite rapidly, especially if the sliding speed falls or the normal load increases. At extremely high loads or low sliding speeds, when $\lambda < 1$ severe surface damage occurs on sliding and the damage can only be mitigated by the use or presence of boundary lubricants.

The film thickness may be evaluated using the following physical properties:

$\xi \approx 2.3$ E-8 m^2/N

$\eta_0 = 0.027$ Ns/m^2

$u = 1.92$ m/s

$R_x = 3.175$ E-3 m

$E' = 331$ GPa

$P = 490$ N

$k = 1.0$

Then using the equation (A4.1)

$$H_{min} = 3.63\ (4.93\text{ E-}11)^{0.68}\ (7613)^{0.49}\ (1.4685\text{E-}4)^{-0.073}\ (1-e^{-0.68}) = 2.667\text{ E-}5$$

Using (A4.2), actual minimum film thickness is:

$$h_{min} = (2.667\text{ E-}5)\ (3.175\text{E-}3) = 8.468\text{ E-}8\text{ m}$$

The lambda ratio may then be calculated using a surface r.m.s roughness value of 0.01 μm for both contacting balls. Then using equations (A4.3) and (A4.4)

$$\lambda = \frac{h_{min}}{\sqrt{R_{q1}^2 + R_{q2}^2}} = 8.468\text{ E-}8\ /\ ((10\text{E-}9)^2 + (10\text{E-}9)^2)^{0.5} = 5.98$$

This result implies that the experiment under the conditions described is operating with a full-film lubrication.

APPENDIX 5

THE DUAL BOUNDARY ELEMENT METHOD

The dual boundary element method (Portela et al. 1992) is based on dual equations, which are the displacement and traction boundary integral equations. Application of the dual boundary element method to three-dimensional crack growth analysis was presented by Mi and Aliabadi (1992), Mi and Aliabadi (1994) and Mi (1996). The formulation of the displacement and stress integral equations reported here, follow Cruse (1977). The Somigliana's identity relating the displacements u_i at an internal point X' to the displacement u_j and traction t_j on the surface Γ is given by

$$u_i(X') = \int_\Gamma U_{ij}(X', x) t_j(x) d\Gamma(x) - \int_\Gamma T_{ij}(X', x) u_j(x) d\Gamma(x) \qquad \text{(A5.1)}$$

where $i, j = 1, 2, 3$; $U_{ij}(X', x)$ and $T_{ij}(X', x)$ are the Kelvin displacement and traction fundamental solution respectively. Differentiating (A5.1) with respect to X_k' and using the Hooke's law yields the Somigliana's identity for stresses at an interior point X':

$$\sigma_{ij}(X') = \int_\Gamma U_{kij}(X', x) t_k(x) d\Gamma(x) - \int_\Gamma T_{kij}(X', x) u_k(x) d\Gamma(x) \qquad \text{(A5.2)}$$

where $U_{kij}(X', x)$ and $T_{kij}(X', x)$ contain derivatives of $U_{ij}(X', x)$ and $T_{ij}(X', x)$ respectively.

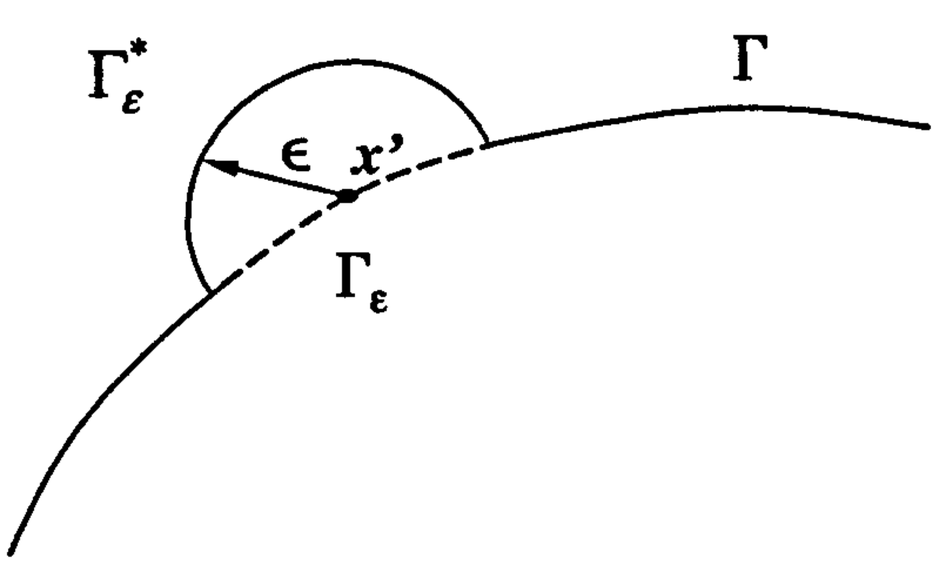

Figure A5.1 Source point x' located on the surface surrounded by a sphere.

The direct boundary element formulation relating the boundary displacements to boundary tractions can be obtained from (A5.1) by considering the limiting process as an internal point goes to the boundary, (i.e. $X' \rightarrow x$). For a body represented as shown in figure A5.1, the integral equation (A5.1) can be written as

$$u_i(x') = \lim_{\varepsilon \to 0} \int_{\Gamma - \Gamma_\varepsilon + \Gamma_\varepsilon^*} U_{ij}(x', x) t_j(x) d\Gamma(x) - \lim_{\varepsilon \to 0} \int_{\Gamma - \Gamma_\varepsilon + \Gamma_\varepsilon^*} T_{ij}(x', x) u_j(x) d\Gamma(x) \qquad \text{(A5.3)}$$

where Γ_ε^* represents the surface of a spherical inclusion of radius ϵ. As $\epsilon \rightarrow 0$, Γ_ε^* tends to Γ_ε. In (A5.3), the first integral contains the singular integrand of the order $O(1/R)$ and is integrable as an improper integral. The second integral in (A5.3) contains a strongly singular integral of the order $O(1/R^2)$ and is regularised with the first term of a Taylor's expansion of the displacements, about the source point, to give

$$\begin{aligned}
&\lim_{\varepsilon \to 0} \int_{\Gamma - \Gamma_\varepsilon + \Gamma_\varepsilon^*} T_{ij}(x', x) u_j(x) d\Gamma(x) \\
&\quad = \lim_{\varepsilon \to 0} \int_{\Gamma - \Gamma_\varepsilon} T_{ij}(x', x) u_j(x) d\Gamma(x) \\
&\quad + \lim_{\varepsilon \to 0} \int_{\Gamma_\varepsilon^*} T_{ij}(x', x) [u_j(x) - u_j(x')] d\Gamma(x) \\
&\quad + u_j(x') \lim_{\varepsilon \to 0} \int_{\Gamma_\varepsilon^*} T_{ij}(x', x) d\Gamma(x) \qquad \text{(A5.4)}
\end{aligned}$$

where the first integral on the right hand side of (A5.4) is an improper integral which is treated in a Cauchy principal sense; the second integral vanishes to zero because of the requirement of displacement continuity, (i.e. Hölder-continuous) and the last integral results in a jump in displacement given by $\alpha_{ij}(x')u_j(x')$. Finally the displacement boundary equation can be written as

$$c_{ij}(x')u_j(x') + \int_{\Gamma} T_{ij}(x', x)u_j(x)d\Gamma(x) = \int_{\Gamma} U_{ij}(x', x)t_j(x)d\Gamma(x) \qquad \text{(A5.5)}$$

where $-\!\!\!\!\!\!\int$ denotes Cauchy principal value integral and $c_{ij}(x') = \delta_{ij} + \alpha_{ij}(x')$, ($\delta$ is the Kronecker delta).

The traction boundary integral equation is obtained by taking the limiting form of the interior stress equation (A5.2), as an internal point goes to the boundary, in a same way as the displacement formulation. In absence of body force and assuming continuity of both strains and traction at x' on a smooth boundary, the stress boundary integral equation can be given by

$$\frac{1}{2}\sigma_{ij}(x') + \int_{\Gamma} U_{kij}(x', x)t_k(x)d\Gamma(x) = -\!\!\!\!\!\!\int_{\Gamma} U_{kij}(x', x)t_k(x)d\Gamma(x) \qquad \text{(A5.6)}$$

and, the traction boundary integral equation is given by

$$\frac{1}{2}t_j(x') + n_i(x')\,=\!\!\!\!\!\!\int_{\Gamma} T_{kij}(x', x)u_k(x)d\Gamma(x) = n_i(x')\,-\!\!\!\!\!\!\int_{\Gamma} U_{kij}(x', x)t_k(x)d\Gamma(x) \qquad \text{(A5.7)}$$

where $n_j(x', x)$ denotes the component of outward unit normal to the boundary at x'. The symbol $=\!\!\!\!\!\!\int$ stands for the Hadamard principal value integral. Equations (A5.5) and (A5.7) constitute the basis of the dual boundary element method.

APPENDIX 6

DEFORMATION CONTOURS OF THE CONTACT ZONE

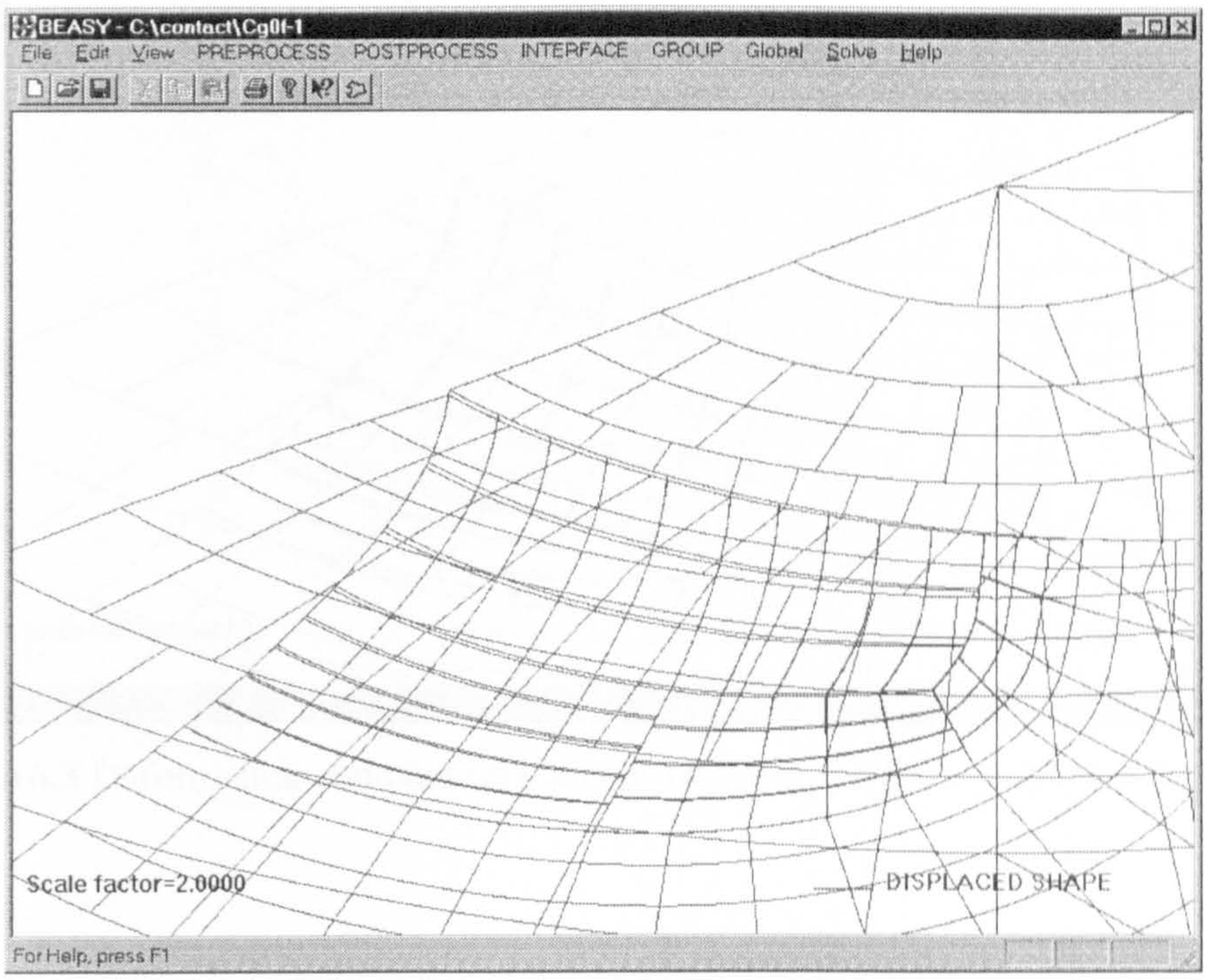

Figure A6.1 Deformation contours (crack gap = 0, f_c = 0.1, f = -0.05, x = 0.047 mm).

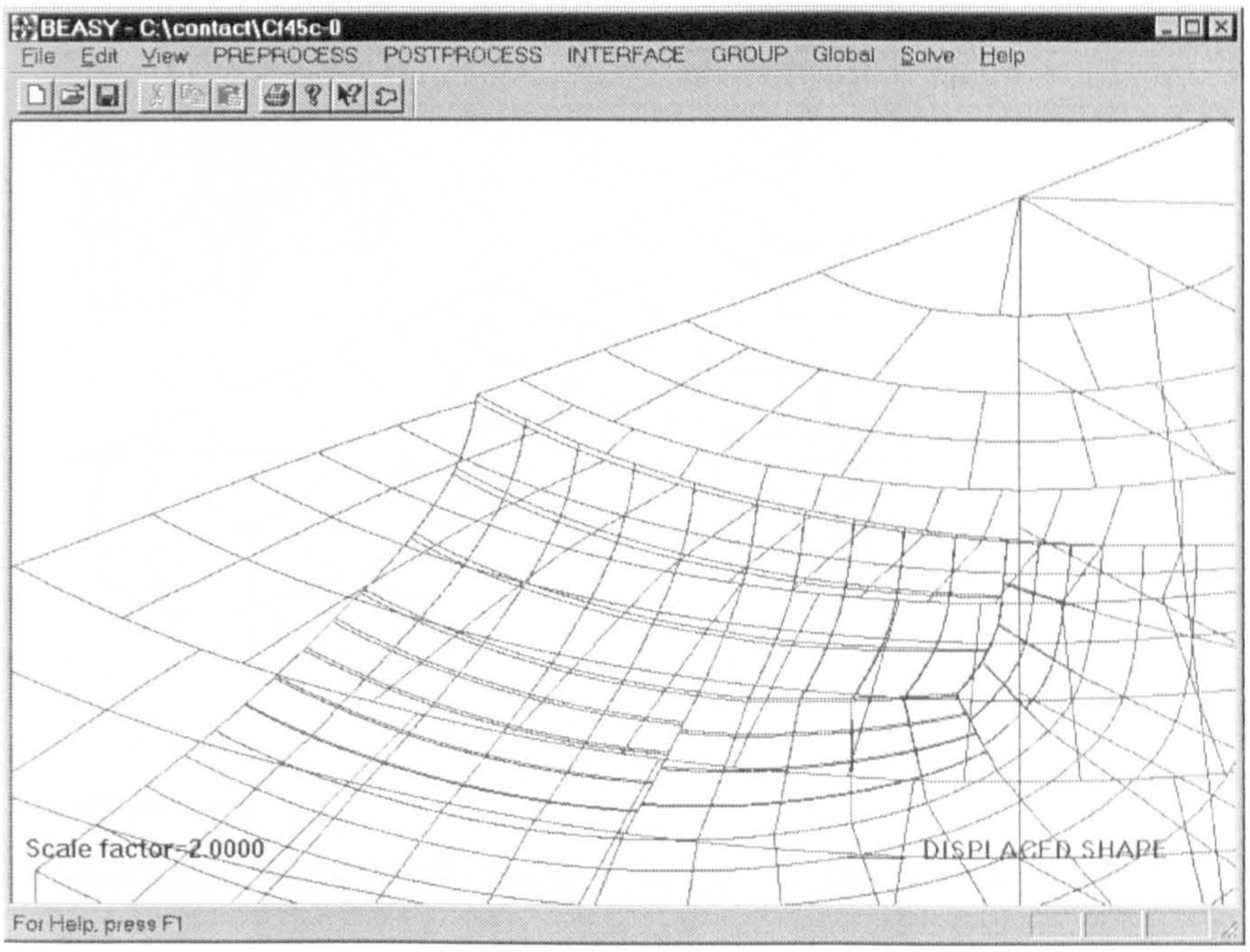

Figure A6.2 Deformation contours (crack gap = 0, f_c = 0, f = -0.05, x = 0.047 mm).

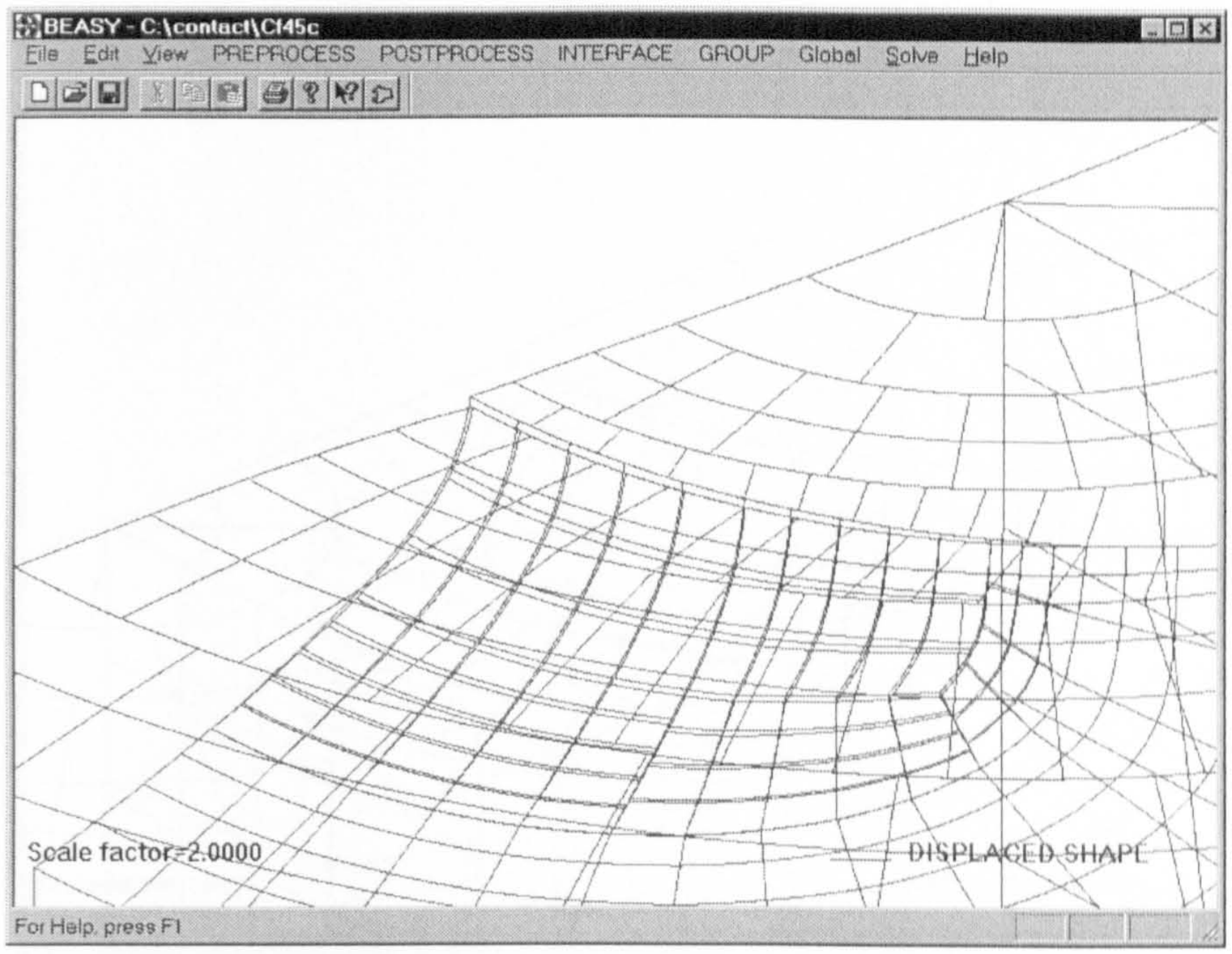

Figure A6.3 Deformation contours (crack gap = 0.5μm, $f_c = 0$, $f = -0.05$, $x = 0.047$ mm).

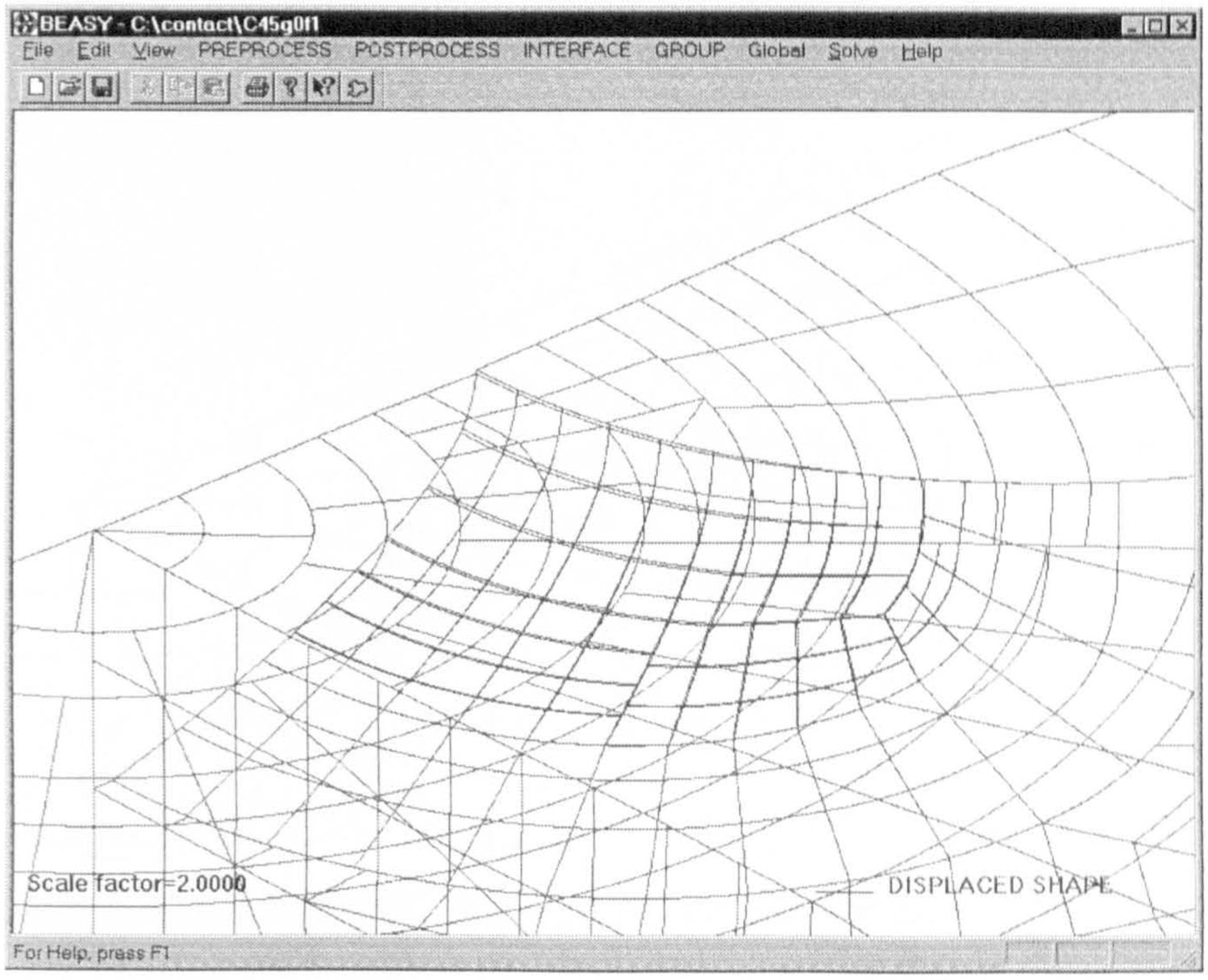

Figure A6.4 Deformation contours (crack gap = 0, $f_c = 0.1$, $f = -0.05$, $x = 0.347$ mm).

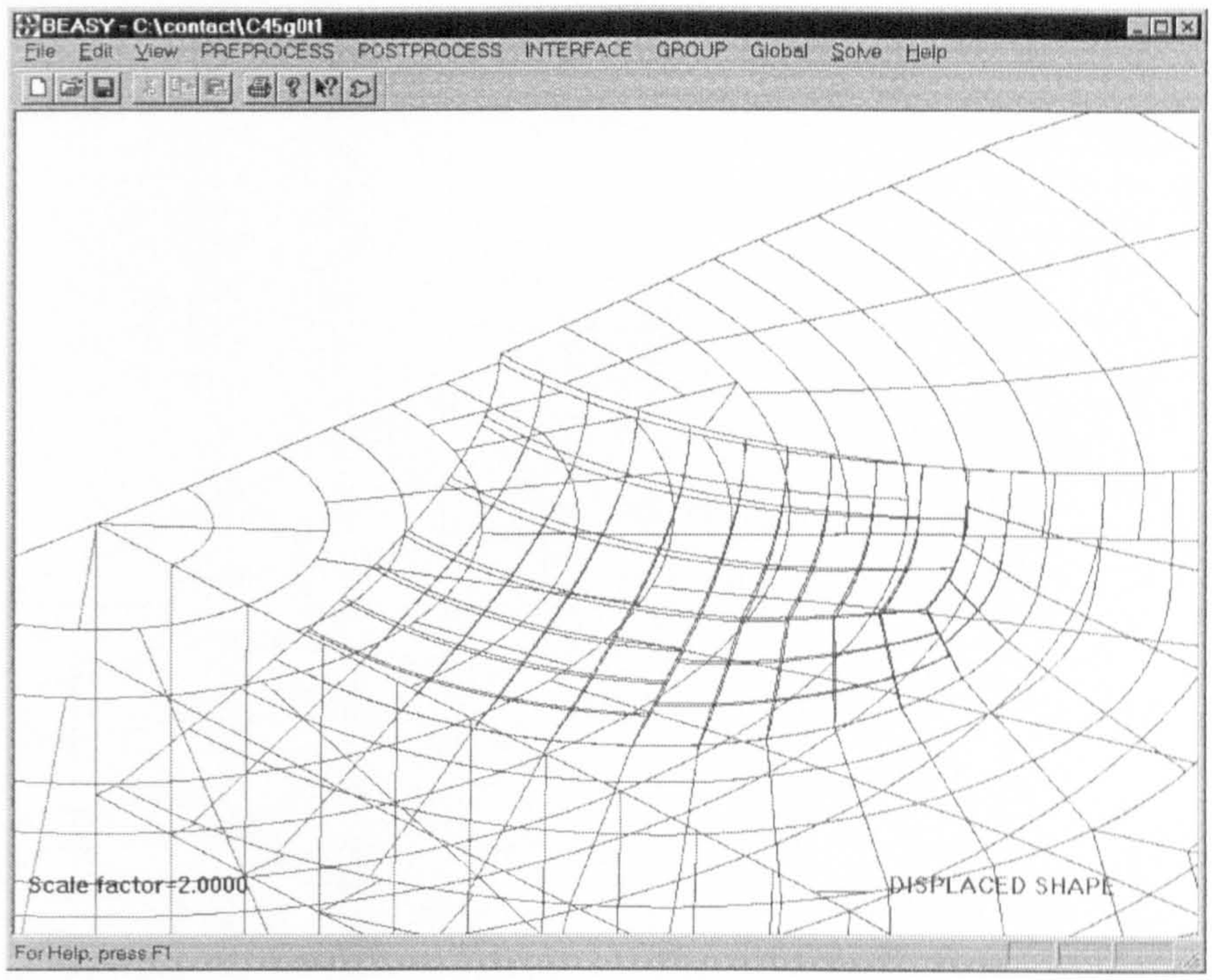

Figure A6.5 Deformation contours (crack gap = 0, $f_c = 0$, $f = -0.05$, $x = 0.347$ mm).

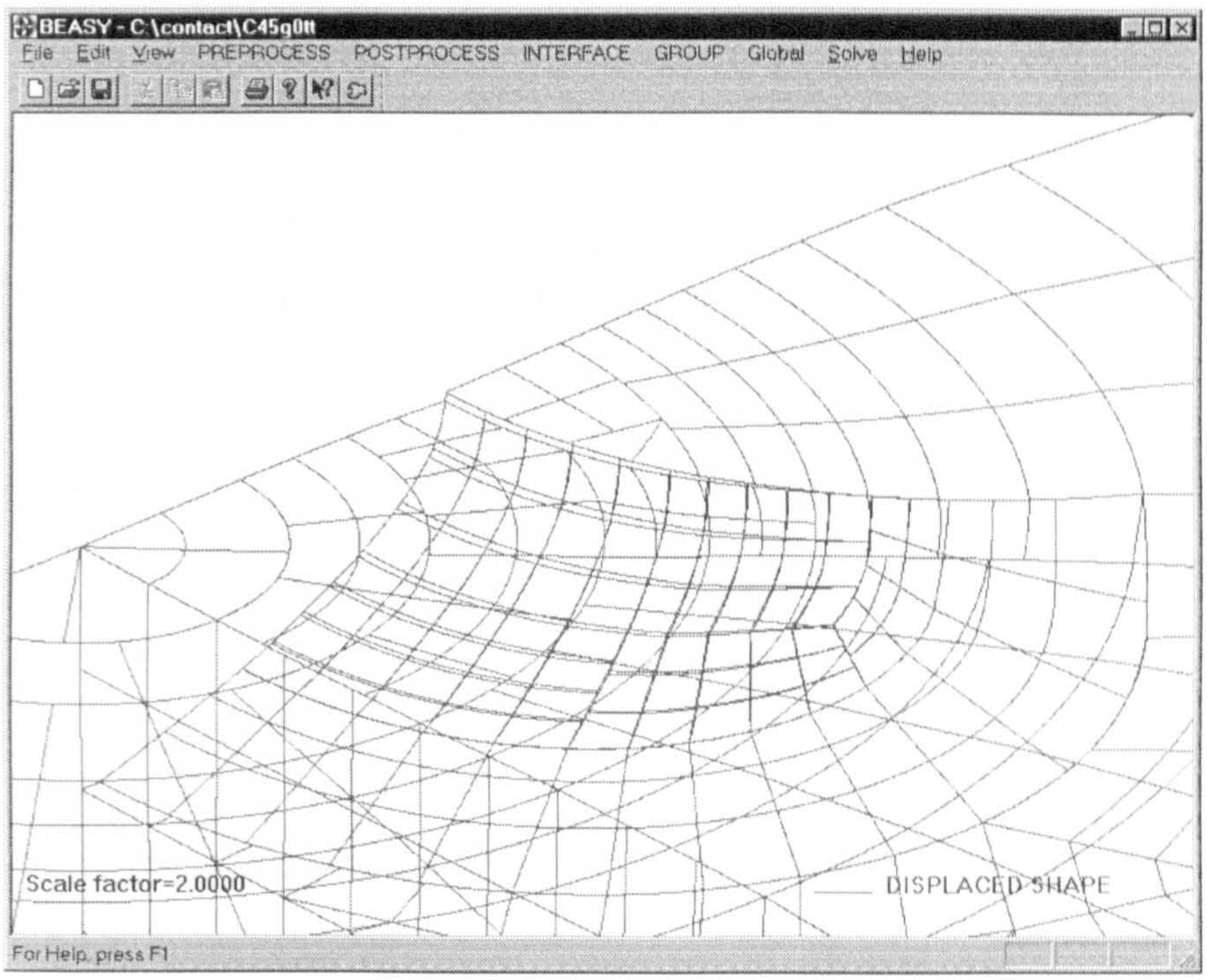

Figure A6.6 Deformation contours (crack gap = 0, $f_c = 0$, $f = +0.05$, $x = 0.347$ mm).

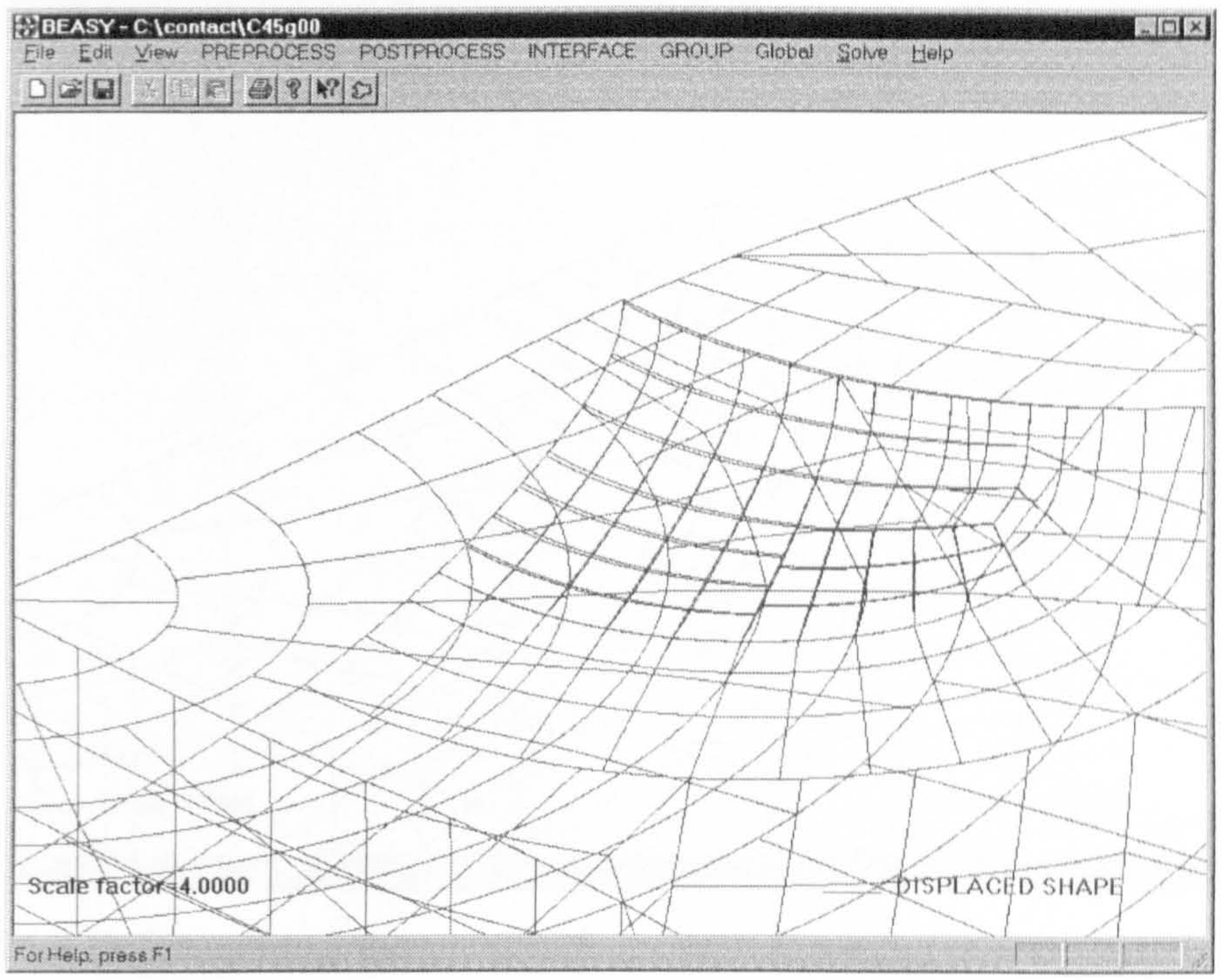

Figure A6.7 Deformation contours (crack gap = 0, f_c = 0, f = -0.05, x = 0.467 mm).

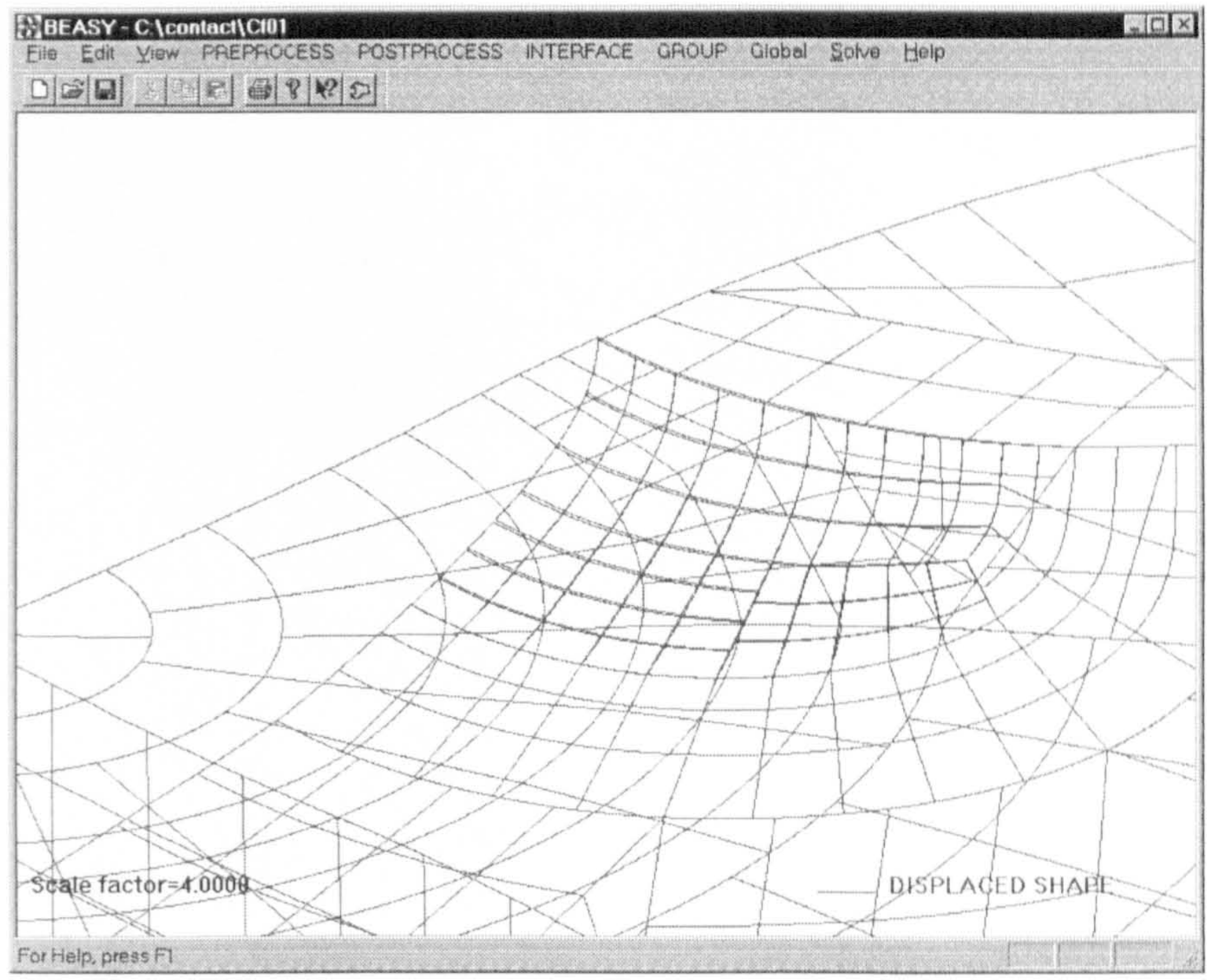

Figure A6.8 Deformation contours (crack gap = 0, f_c = 0.1, f = -0.05, x = 0.467 mm).

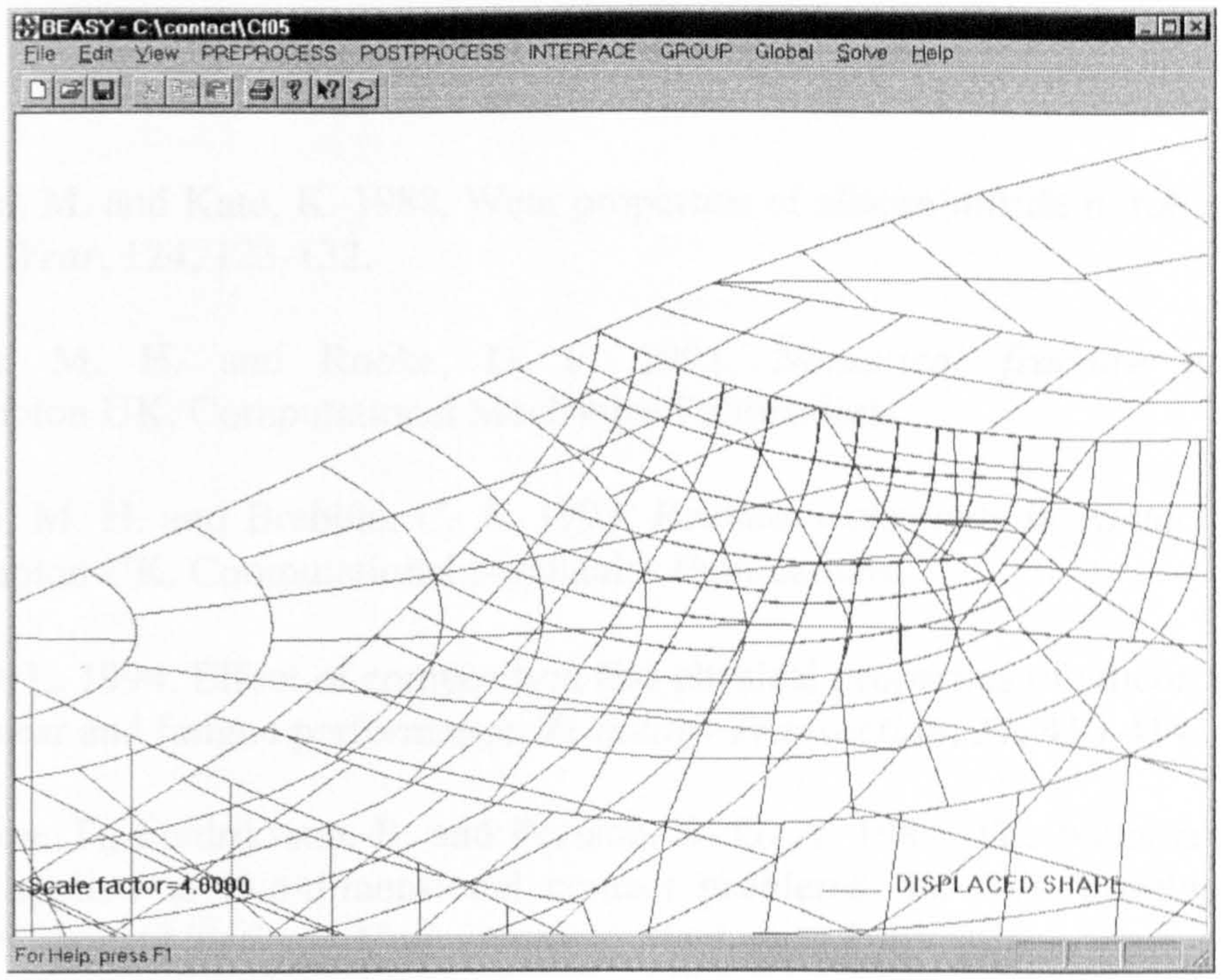

Figure A6.9 Deformation contours (crack gap = 0, f_c = 0.5, f = -0.05, x = 0.467 mm).

REFERENCES

Akazawa, M. and Kato, K. 1988. Wear properties of silicon nitride in rolling sliding contact. *Wear*, 124, 123-132.

Aliabadi, M. H. and Rooke, D. P. 1991. *Numerical fracture mechanics.* Southampton UK, Computational Mechanics Publications.

Aliabadi, M. H. and Brebbia, C. A. 1993. *Boundary elements in contact analysis.* Southampton UK, Computational Mechanics Publications.

Allen, D. L. 1994. Effect of composition and physical properties of silicon nitride on rolling wear and fatigue performance. *Tribology Transaction*, 37, 410-414.

Andersson, T., Fredriksson, B. and Persson, B. G. A. 1980. The boundary element method applied to two-dimensional contact problems. In: *New developments in boundary element methods*. Computational Mechanics Publications.

Aramaki, H., Shoda, Y., Morishita, Y. and Sawamoto, T. 1988. The performance of ball bearings with silicon nitride ceramic balls in high speed spindles for machine tools. *Journal of Tribology*, 110, 693-698.

Archard, J. F. 1973. Elastohydrodynamic lubrication of real surface. *Tribology* (February), 8-14.

Archard, J. F. and Kirk, M. T. 1960. Lubrication at point contact. *Proc. Roy. Soc. Lond. A*261, 532-549.

Barwell, F. T. and Scott, D. 1956. Effect of lubricant on pitting failure of ball bearings. *Engineering*, July 6, 9-12.

Baumgartner, H. R. 1974. Evaluation of roller bearings containing hot-pressed silicon nitride rolling elements. In: Burke, J. J., Gorum, A. E. and Katz, R. N. (eds.) *Ceramics for high performance applications*. Chestnut Hill MA, Brook Hill Publishing. 713-727.

Bar-On, I. and Beals, J. T. 1990. Fatigue in silicon nitride bend bars. In: Kitagawa, H. and Tanaka, T. (eds.) *Fatigue 90: Proceedings of 4th International conference on fatigue and fatigue thresholds*. Edgbaston, Materials and Component Engineering Publications. 793-798.

Bethune, B. J. 1971. The surface cracking of glassy polymers under a sliding spherical indenter. *J. Mater. Sci.*, 11, 199-205.

Bhushan, B. and Sibley, L. B. 1981. Silicon nitride rolling bearings for extreme operating conditions. *ASLE Transactions*, 25(4), 417-428.

Bower, A. F. 1988. The influence of crack face friction and trapped fluid on surface initiated rolling-contact fatigue cracks. *Journal of Tribology; Transactions of the ASME*, 110(4), 704-711.

Braza, J. F., Cheng, H. S. and Fine, M. E. 1989a. Silicon nitride wear mechanisms: rolling and sliding contact. *Tribology Transactions*, 32(4), 439-446.

Braza, J. F., Cheng, H. S., Fine, M. E., Gangopadhyay, A. K., Keer, L. M. and Worden, R. E. 1989b. Mechanical failure mechanisms in ceramic sliding and rolling contacts. *Tribology Transactions*, 32(1), 1-8.

Brebbia, C. A., Telles, J. C. F. and Wroble, L. C. 1984. *Boundary element Techniques*, Berlin, New York, Tokyo, Springer-Verlag.

Bryant, M. D., Miller, G. R. and Keer, L. M. 1984. Line contact between a rigid indenter and a damaged elastic body. *Q. J. Mech. Appl. Math. 37(3)*, 468-478.

Burrier, H. I. 1996. Optimising the structure and properties of silicon nitride for rolling contact bearing performance. *Tribology Transactions*, 39(2), 276-285.

Carter, T. L. and Zaretsky, E. V. 1960. Rolling contact fatigue life of a crystallized glass ceramic. *NASA TN D-259*.

Chao, L.-Y., Lakshminarayanna, R., Iyer, N., Lin, G.-Y. and Shetty, D. K. 1998. Transient wear of silicon nitride in lubricated rolling contact. *Wear*, 223, 58-65.

Chaudhri, M. and Phillips, M. A. 1990. Quasi-static indentation cracking of thermally tempered soda-lime glass with spherical and Veckers indenters. *Phil. Mag. A*62(1), 1-27.

Computational Mechanics BEASY 1998. *BEASY user guide*. Southampton UK.

Cruse, T. A. 1977. Mathematical formation of the boundary integral equation methods in solid mechanics. *Report No. AFOSR-TR-77-1002*. Pratt and Whitney Aircraft Group.

Cundill, R. T. 1990. Rolling element bearings into 21st century. In: *Proceedings of IMechE Seminar*, London.

Cundill, R. T. 1997. Impact resistance of silicon nitride balls. In: *6th international symposium on ceramic materials & components for engines*, Arita, Japan.

Dauskardt, R. H., James, M. R., Porter, J. R. and Ritchie, R. O. 1992. Cyclic fatigue crack growth in a SiC-whisker-reinforced alumina ceramic composite: long crack and small crack behaviour. *J. Am. Ceram. Soc.*, 75(4), 759-771.

Dowson, D. and Higginson, G. R. 1966. *Elasto-Hydrodynamic Lubrication.*

Pergamon Press.

Faber, K. T. and Evans, A. G. 1983. Crack deflection processes II - experiment. *Acta Metall*, 31(4), 577-584.

Fleming, J. R. and Suh, N. P. 1977. Mechanics of crack propagation in delamination wear. *Wear*, 44, 39-56.

Frank, F. C. and Lawn, B. R. 1967. On the theory of Hertzian fracture. *Proc. Roy. Soc. Lond. A*299, 291-306.

Fujiwara, T., Yoshioka, T., Kitahara, T., Koizumi, S., Takebayashi, H. and Tada, T. 1989. Study on load rating property of silicon nitride for rolling bearing material. *Journal of JSLE International Edition* 10, 81-86.

Gerstle, W. H. 1986. Finite and boundary element modelling of crack propagation in two- and three- dimensional using interactive computer graphics. PhD thesis. Cornell University, Ithaca NY.

Hadfield, M. 1998. Failure of silicon nitride rolling elements with ring crack defects. *Ceramics International*, 24(5), 379-386.

Hadfield, M. and Stolarski, T. A. 1995a. The effect of the test machine on the failure mode in lubricated rolling contact of silicon nitride. *Tribology International*, 28(6), 377-382.

Hadfield, M. and Stolarski, T. A. 1995b. Observations of delamination fatigue on precracked ceramic elements in rolling-contact. *Ceramics International*, 21(2), 125-130.

Hadfield, M. and Stolarski, T. A. 1995c. Observations of lubricated rolling contact fatigue on silicon nitride rods. *Ceramics International*, 21(1), 13-19.

Hadfield, M., Stolarski, T. A. and Cundill, R. T. 1993a. Failure modes of ceramics in rolling contact. *Proc.R. Soc. Lond., A*443, 607-621.

Hadfield, M., Stolarski, T. A., Cundill, R. T. and Horton, S. 1993b. Failure modes of ceramic elements with ring crack defects. *Tribology International*, 26(3), 157-164.

Hadfield, M., Stolarski, T. A., Cundill, R. T. and Horton, S. 1993c. Failure modes of pre-cracked ceramic elements under rolling-contact. *Wear*, 169(1), 69-75.

Hadfield, M., Tobe, S. and Stolarski, T. A. 1994. Subsurface crack investigation on delaminated ceramic elements. *Tribology International*, 27(5), 359-367.

Hadfield, M. 1992. Rolling contact fatigue of ceramics. PhD thesis. Brunel University, London.

Hamburg, G., Cowley, P. and Valori, R. 1981. Operation of an all-ceramic mainshaft roller bearing in J-402 gas turbine engine. *J. ASME, Lubrication Engineering*, 37(7), 407-415.

Hills, D. A. and Ashelby, D. W. 1979. A fracture mechanics approach to rolling contact fatigue. *Tribology International*, 115-119.

Hirano, F., Sakai, T. and Kamitani, T. 1971. On a significant property of lubricants concerning rolling fatigue and scoring. *Proc Instn Mech Engrs*, C66, 86-96.

Hirst, W. and Richmond, J. W. 1988. Traction in elasto-hydrodynamic contacts. *Proc Instn Mech Engrs*, 202(C2), 129-144.

Hu, S., Chen, Z. and Mecholsky, J. J. 1996. On the Hertzian fatigue cone crack propagation in ceramics. *International Journal of Fracture*, 79, 295-307.

Ichikawa, M., Takamatsu, T., Matsuo, T., Okabe, N. and Abe, Y. 1995a. Intra-ball and inter-ball variability of ring crack initiation load of silicon nitride bearing balls. *JSME International Journal, Series A, Mechanics and Material Engineering*, 38(2), 231-235.

Ichikawa, M., Takamatsu, T., Shindou, N., Okabe, N. and Abe, Y. 1995b. Ring crack initiation load of silicon nitride bearing balls. *JSME International Journal, Series A, Mechanics and Material Engineering*, 38(2), 226-230.

Irwin, G. R. 1957. Analysis of stresses and strains near the end of a crack traversing a plate. *Trans. ASME J. Appl. Mech.*, 24, 361-364.

Jahanmir, S. 1994. *Friction and wear of ceramics*. New York, Basel, Hong Kong, Marcel Dekker, Inc.

Johnson, K. L. 1985. *Contact mechanics*. Cambridge, Cambridge University Press.

Kaneta, M. and Murakami, Y. 1987. Effects of oil hydraulic pressure on surface crack growth in rolling sliding contact. *Tribology International*, 20(4), 210-217.

Kato, K. 1990. Tribology of ceramics. *Wear*, 136, 117-133.

Keer, L. M. and Bryant, M. D. 1983. A pitting model for rolling contact fatigue. *Journal of Lubrication Technology-Transactions of the ASME*, 105(2), 198-205.

Keer, L. M., Bryant, M. D. and Haritos, G. K. 1982. Subsurface and surface cracking due to Hertzian contact. *Journal of Lubrication Technology-Transactions of the ASME*, 104(3), 347-351.

Keer, L. M. and Worden, R. E. 1990. A qualitative model to describe the microchiping wear mode in ceramic rollers. *Tribology Transactions*, 33, 411-417.

Kikuchi, K., Yoshioka, T., Kitahara, T., Ozaki, K., Nakayama, K. and Fujiwara, T. 1984. Rolling contact fatigue life of ceramics for rolling bearing materials. *J. JSLE Int. Ed.*(5), 137-142.

Kim, S. S., Kato, K., Hokkirigawa, K. and Abe, H. 1986. Wear mechanism of ceramic materials in dry rolling friction. *Transactions of the ASME*, 108, 522-526

Krivoshein, G. S. 1960. On evaluating the effect of lubricants on the fatigue pitting of steel. *Industr. Lab.*, 26, 405-7

Lawn, B. R. 1967. Partial cone crack formation in a brittle material loaded with a sliding spherical indenter. *Proc. R. Soc. Lond.*, A299, 307-316.

Lee, S. K. and Lawn, B. R. 1999. Contact fatigue in silicon nitride. *Journal of the American Ceramic Society*, 82(5), 1281-1288.

Li, C. W. and Yamanis, J. 1989. Super tough silicon nitride with R-curve behaviour. *Ceram. Eng. Sci. Proc.*, 10, 632-645.

Li, Y. Z. and Hills, D. A. 1991. The Hertzian cone crack. *Journal of Applied Mechanics-Transactions of the ASME*, 58(1), 120-127.

Lucek, J. W. 1990. Rolling wear of silicon nitride bearing materials. *ASME paper No.* 90-GT-165.

Lucek, J. W. and Cowley, P. E. 1978. Investigation of the use of ceramic material in aircraft engine bearings. *Dept. of Navy, Code AIR-52032A*. Washington.

Man, K. W. 1994. *Contact mechanics using boundary elements*. Southampton UK, Boston USA, Computational Mechanics Publications.

Mi, Y. 1996. Three-dimensional analysis of crack growth. *Topics in Engineering*, 28, Computational Mechanics Publ., Southampton, UK.

Mi, Y. and Aliabadi, M. H. 1992. Dual boundary element method for three-dimensional fracture mechanics analysis. *Engineering Analysis with Boundary Elements*, 10, 161-171.

Mi, Y., and Aliabadi, M. H. 1994. Three-dimensional crack growth simulation using BEM. *Computer & Structure*, 52, 871-878

Miller, G. R., Keer, L. M. and Cheng, H. S. 1985. On the mechanics of fatigue crack growth due to contact loading. *Proc. R. Soc. Lond.*, *A*397(1813), 197-209.

Miner, J. R., Grace, W. A. and Valori, R. 1981. Demonstration of high-speed gas turbine bearings using silicon nitride rolling elements. *Lubr. Eng.*, 37, 462-478.

Morrison, F. R., McCool, J. I. and Yonushonis, T. M. 1984. The load-life relationship for M50 steel bearings with silicon nitride ceramic balls. *J. of ASLE, Lubrication Engineering*, 40, 153-159.

Mouginot, R. and Maugis, D. 1985. Fracture indentation beneath flat and spherical punches. *J. Mater. Sci.*, 20, 4354-76.

Newman, J. C. and Raju, I. S. 1986. *Computational methods in the mechanics of fracture*. In: Atluri, S. N. (ed). Amsterdam, North Holland.

Niku, S. M., Adey, R. A. and Baynham, J. M. W. 1991. Contact analysis using BEASY: Theory and application. In: Brebbia, C. A. (ed.) *Boundary element technology VI*. Southampton UK, Computational Mechanics Publications.

Ohgushi, K. and Ichikawa, M. 1996. Fracture mechanics study of ring crack initiation in ceramics by sphere indentation. *JSME International Journal, Series A: Mechanics and Material Engineering*, 39(4), 489-495.

Paris, P. and Erdogan, F. 1963. A critical analysis of crack propagation laws. *ASME Jour. Basic Eng.*, 85 528-534.

Parker, R. and Zaretsky, E. V. 1975. Fatigue life of high-speed ball bearings with silicon nitride balls. *Trans. of the ASME, J. of Lub. Tech.* (July), 350-357.

Portela, A., Aliabadi, M. H., and Rooke, D. P. 1992. The dual boundary element method: effective implementation for crack problems. *Int. J. Num. Meth. in Eng.*, 23, 1269-1287.

Reece, M. and Guiu, F. 1991. Indentation fatigue of high-purity alumina in fluid environments. *J. Am. Ceram. Soc.*, 74(1), 148-154.

Ritchie, R. O. and Dauskardt, R. H. 1991. Cyclic fatigue of ceramics - a fracture mechanics approach to subcritical crack-growth and life prediction. *Nippon Seramikkusu Kyokai Gakujutsu Ronbunshi - Journal of the Ceramic Society of Japan*, 99(10), 1047-1062.

Ritchie, R. O., Gilbert, C. J. and McNaanry, J. M. 2000. Mechanics and mechanisms of fatigue damage and crack growth in advanced materials. *International Journal of Solids and Structures*, 37, 311-329.

Roesler, F. C. 1956. Brittle fracture near equilibrium. *Proc. Phys. Soc. Lond.*, B69, 981-1012.

Rosenfield, A. R. 1980. A fracture mechanics approach to wear. *Wear*, 61, 125-132.

Scott, A., Blackwell, J. and McCullagh, P. J. 1971. Silicon nitride as a rolling bearing material - A preliminary assessment. *Wear*, 17, 73-82.

Scott, D. 1963. Study of the effect of lubricant on pitting failure of balls. *IMechE, Lub. and Wear Convention*, 463-468.

Scott, D. and Blackwell, J. 1973. Hot pressed silicon nitride as a rolling bearing material - A preliminary assessment. *Wear*, 24, 61-67.

Sih, G. C. and Cha, B. C. K. 1974. A fracture criterion for three-dimensional crack problems. *Engineering Fracture Mechanics*, 6, 699-723.

Sih, G. C. 1991. *Mechanics of fracture initiation and propagation*, New York, Kluwer Academic Publishers.

Suh, N. P. 1977. An overview of the delamination theory of wear. *Wear*, 44, 1-16.

Tada, H., Paris, P. C. and Irwin, G. R. 1985. *Stress analysis of cracks handbook*, St. Louis, MO , Paris Publications Inc.

Tallian, T. E. 1972. The theory of partial elasto-hydrodynamic contacts. *Wear*, 21, 49-110.

Thomsen, N. B. and Karihaloo, B. L. 1996. Subsurface and surface cracks under contact loading in transformation-toughened ceramics. *J. Mech. Phys. Solids*, 44(2), 207-231.

Tillett, J. P. A. 1956. Fracture of glass by spherical indenters. *Proc. Phys. Soc.*, B69, 47-54.

Tourret, R. and Wright, E. P. 1977. *Rolling contact fatigue: performance testing of lubricants*, London , Heyden & Son Ltd.

Ueda, K. 1989. Deformation and fracture of ceramics in contact stress field. *Journal of Japanese Society of Tribologists*, 34(2), 82-87.

Warren, P. D., Hills, D. A. and Dai, D. N. 1995. Mechanics of Hertzian Cracking. *Tribology International*, 28(6), 357-362.

Warren, R. 1978. Measurement of the fracture properties of brittle solids by Hertzian indenters. *Acta Metall*, 26, 1759-1769.

Wilshaw, T. R. 1971. The Hertzian fracture test. *J. Phys. D: Appl. Phys.*, 4, 1567-1581.

BIBLIOGRAPHY

Akazawa, M., Kato, K. and Umeya, K. 1986. Wear properties of silicon nitride in rolling contact. *Wear*, 110, 285-293.

Andersson, M. 1996. Stress distribution and crack initiation for an elastic contact including friction. *International Journal of Solids and Structures*, 33(25), 3673-3696.

Bar-On, I., Baratta, F. I. and Cho, K. 1996. Crack stability and its effect on fracture toughness of hot-pressed silicon nitride beam specimens. *J. Am. Ceram. Soc.*, 79, 2300-2308.

Bower, A. F. and Fleck, N. A. 1994. Brittle fracture under a sliding line contact. *J. Mech. Phys. Solids*, 42(9), 1375-1396.

Brebbia, C. A. and Dominguez, J. 1992. *Boundary elements: An introductory course*. Southampton UK and Boston USA, Computational Mechanics Publications.

Cai, H., Kalceff, M. A. S. and Lawn, B. R. 1994. Deformation and fracture of mica-containing glass-ceramics in Hertzian contacts. *J. Mater. Res.*, 9(3), 762-770.

Chang, C. C. and Mear, M. E. 1996. A Boundary element method for two-dimensional linear elastic fracture analysis. *International Journal of Fracture*, 74(3), 219-251.

Chang, F., K., Comninou, M., Sheppard, S. and Barber, J. R. 1984. The subsurface crack under conditions of slip and stick caused by a surface normal force. *Journal of Applied Mechanics, Transactions of the ASME*, 51, 311-316.

Chantikul, P., Anstis, G. R., Lawn, B. R. and Marshall, D. B. 1981. A critical evaluation of indentation techniques for measuring fracture toughness II - strength methods. *Journal of the American Ceramic Society*, 64(9), 539-543.

Chen, S., Farris, T. N. and Chandrasekar, S. 1993. Experimental and boundary element analysis of Hertzian cone cracking. *American Society of Mechanical Engineers, Aerospace Division (Publication) AD*, 36, 135-150.

Chen, S. Y., Farris, T. N. and Chandrasekar, S. 1995. Contact mechanics of Hertzian cone cracking. *International Journal of Solids and Structures*, 32(3-4), 329-340.

Chen, Z., Cuneo, J. C., Mecholsky, J. J. and Hu, S. F. 1996. Damage processes in Si_3N_4 bearing material under contact loading. *Wear*, 198(1-2), 197-207.

Cheng, W., Cheng, H. S., Mura, T. and Keer, L. M. 1994. Micromechanics modelling of crack initiation under contact fatigue. *Journal of Tribology, Transactions of the ASME*, 116(1), 2-8.

Chiang, S. S. and Evans, A. G. 1983. Influence of a tangential force on the fracture of two contacting elastic bodies. *Journal of the American Ceramic Society*, 66(1), 4-10.

Chiang, Y., Brinie, D. P. and Kingery, W. D. 1997. *Physical ceramics*, New York, Chichester, Toronto, Brisbane, Singapore , John Wiley & Sons, Inc.

Dill, S. J., Bennison, S. J. and Dauskardt, R. H. 1997. Subcritical crack growth behaviour of borosilicate glass under cyclic loads: evidence of a mechanical fatigue effect. *Journal of the American Ceramic Society*, 80(3), 773-776.

Dusza, J. and Steen, M. 1999. Fractography and fracture mechanics property assessment of advanced structural ceramics. *International materials reviews*, 44(5), 165-215.

Eberhardt, A. W. and Kim, B. S. 1998. Crack face friction effects on mode II stress intensities for a surface-cracked coating in two-dimensional rolling contact. *Tribology Transactions*, 41(1), 35-42.

Ebert, F. J. 1990. Performance of silicon nitride components in aerospace bearing applications. *ASME*, 90-GT-166.

Evans, A. G. 1980. Fatigue in Ceramics. *International Journal of Fracture*, 16(6), 485-498.

Fischer, T. E. 1990. Friction and wear of ceramics. *Scripta Metallurgica et Materlala*, 24, 833-838.

FischerCripps, A. C. 1997. Predicting Hertzian fracture. *Journal of Materials Science*, 32(5), 1277-1285.

FischerCripps, A. C. and Lawn, B. R. 1996. Stress analysis of contact deformation in quasi-plastic ceramics. *Journal of the American Ceramic Society*, 79(10), 2609-2618.

Fleming, J. R. and Suh, N. P. 1977. The relationship between crack propagation rates and wear rates. *Wear*, 44, 57-64.

Gilbert, C. J., Dauskardt, R. H. and Ritchie, R. O. 1995. Behaviour of cyclic fatigue cracks in monolithic silicon-nitride. *Journal of the American Ceramic Society*, 78(9), 2291-2300.

Gilbert, C. J. and Ritchie, R. O. 1998. Transient fatigue-crack growth behaviour following variable-amplitude loading in a monolithic silicon nitride ceramic. *Engineering Fracture Mechanics*, 60(3), 303-313.

Goryacheva, I. G. 1998. *Contact mechanics in tribology*. Kluwer Acad.Publrs.

Green, D. J. 1998. *An Introduction to the mechanical properties of ceramics*. Cambridge, Cambridge University Press.

Hanson, M. T. and Keer, L. M. 1992. An analytical life prediction model for the crack propagation occurring in contact fatigue failure. *ASLE Trans.*, 35, 451-461.

Hutchings, I. M. 1992. *Tribology - Friction and Wear of Engineering Materials*, London, Sydney, Auckland, Arnold.

Johnson, K. L., O'Connor, J. J. and Woodward, A. C. 1973. The effect of the indenter elasticity on the Hertzian fracture of brittle materials. *Proc. R. Soc. Lond. A.*, 334, 95-117.

Kaneta, M., Suetsugu, M. and Murakami, Y. 1986. Mechanism of surface crack growth in lubricated rolling sliding spherical contact. *Transactions of ASME*, 53(June), 354-360.

Kaneta, M., Yatsuzuka, H. and Murakami, Y. 1985. Mechanism of crack growth in lubricated rolling sliding contact. *ASLE Transactions*, 28(3), 407-414.

Kelly, A. and Macmillan, N. H. 1986. *Strong solids*, Oxford, Oxford University Press.

Kim, D. K., Jung, Y. G., Peterson, I. M. and Lawn, B. R. 1999. Cyclic fatigue of intrinsically brittle ceramics in contact with spheres. *Acta Materialia*, 47(18), 4711-4725.

Kishimoto, H. 1991. Cyclic fatigue in ceramics. *JSME International Journal*, 34(4), 393-403.

Kishimoto, H., Ueno, A. and Matsunaga, A. 1998. Cyclic-fatigue crack initiation and propagation in smooth alumina specimens. *Journal of American Ceramics Society*, 81(1), 55-60.

Kocer, C. and Collins, R. E. 1998. Angle of Hertzian cone cracks. *Journal of the American Ceramic Society*, 81(7), 1736-1742.

Kossowsky, R. 1974. Defect detection in hot-pressed silicon nitride. In: Burke, J. J., Gorum, A. E. and Katz, R. Z. (Eds.) *Ceramics for High Performance Applications*. Brook Hill Publishing, Chestnut Hill, MA, 665-685.

Kuo, C. H., Keer, L. M. and Bujold, M. P. 1997. Effects of multiple cracking on crack growth and coalescence in contact fatigue. *Journal of Tribology-Transactions of the ASME*, 119(3), 385-390.

Lawn, B. 1993. *Fracture of brittle solids. 2nd edition.* Cambridge, Cambridge University Press.

Lawn, B. R. 1998. Indentation of ceramics with spheres: a century after Hertz. *J. Am. Ceram. Soc.*, 81(8), 1977-1994.

Lawn, B. R., Lee, S. K., Peterson, I. M. and Wuttiphan, S. 1998. Model of strength degradation from Hertzian contact damage in tough ceramics. *Journal of the American Ceramic Society*, 81(6), 1509-1520.

Lawn, B. R., Padture, N. P., Guiberteau, F. and Cai, H. 1994. A model for microcrack initiation and propagation between Hertzian contacts in polycrystalline ceramics. *Acta Metall. Mater.*, 42(5), 1683-1693.

Lee, S. K. and Lawn, B. R. 1998. Role of microstructure in Hertzian contact damage in silicon nitride II, strength degradation. *J. of the Am. Ceram. Soc.*, 81(4), 997-1003.

Lee, S. K., Wuttiphan, S. and Lawn, B. R. 1997. Role of microstructure in Hertzian contact damage in silicon nitride I, mechanical characterisation. *J. Am. Ceram. Soc.*, 80(9), 2367-2381.

Marshall, D. B., Evans, A. G., Khuri, B. T., Tien, J. W. and King, G. S. 1983. The nature of machining damage in brittle materials. *Proc. R. Soc. Lond*, A385, 461-475.

Mukai, D. J. 2000. An analysis of a near-surface crack branching under a rigid indenter. *Journal of Tribology-Transaction of the ASME*, 122, 23-29.

Murakami, Y. 1987. *Stress Intensity Factors Handbook*, Oxford, New York, Beijing, Frankfurt , Pergamon Press.

Murakami, Y., Kaneta, M. and Yatsuzuka, H. 1985. Analysis of surface crack propagation in lubricated rolling contact. *ASLE Transactions*, 28(1), 60-68.

Murakami, Y., Sakae, C. and Inchimaru, K. 1994. Three-dimensional fracture mechanics analysis of pit formation mechanism under lubricated rolling sliding contact loading. *ASLE Trans.*, 37, 445-454.

Otsuka, A., Sugawara, H. and Shomura, M. 1996. A test method for mode II fatigue-crack growth relating to a model for rolling contact fatigue. *Fatigue & Fracture of Engineering Materials & Structures*, 19(10), 1265-1275.

Plint, M. A. 1967. Traction in elasto-hydrodynamic contacts. *Proc Instn Mech Engrs*, 182(14), 300-307.

Rooke, D. P. and Cartwright, D. J. 1976. *Compendium of stress intensity factors*, London, H.M.S.O.

Rose, L. R. F. 1987. The mechanisms of transformation toughening. *Proc. R. Soc. Lond.*, A412, 169-197.

Sheppard, S., Barber, J. R. and Comninou, M. 1985. Short subsurface cracks under conditions of slip and stick caused by a moving compressive load. *Journal of Applied Mechanics - Transactions of the ASME*, 52(4), 811-817.

Sheppard, S., Barber, J. R. and Comninou, M. 1987. Subsurface cracks under conditions of slip, stick, and separation caused by a moving compressive load. *J. Appl. Mech.*, 54, 393-398.

Thouless, M. D., Evans, A. G., Ashby, M. F. and Tutchinson, J. W. 1987. The edge cracking and spalling of brittle plates. *Acta Metall*, 35(6), 1333-1341.

Trevelyan, J. 1994. *Boundary elements for engineers: theory & application*, Southampton UK , Computational Mechanics Publications.

Wachtman, J. B. 1996. *Mechanical properties of ceramics*, New York Chichester Brisbane Toronto Singapore, John Wiley & Sons, Inc.

Way, S. 1935. Pitting due to rolling contact. *ASME Journal of Applied Mechanics*, 2, A49-A58.

Xu, H. H. K., Jahanmir, S., Ives, L. K., Job, L. S. and Ritchie, K. T. 1996. Short crack toughness and abrasive machining of silicon nitride. *Journal of the American Ceramic Society*, 79(12), 3055-3064.

Yoffe, E. H. 1986. Stress field of radial shear traction applied on elastic half-space. *Philos. Mag.*, A 54(1), 115-29.

Zeng, K., Breder, K. and Rowcliffe, D. J. 1992. The Hertzian stress field and formation of cone cracks: 1. Theoretical approach. *Acta Metallurgica Et Materialia*, 40(10), 2595-2600.